The Pennsylvania State University
The Graduate School
Department of Ceramic Science

CHARACTERIZATION OF FERROELECTRIC SURFACES AND THIN FILMS BY SPECTROSCOPIC ELLIPSOMETRY

A Thesis in
Ceramic Science
by

Susan Elizabeth McKinstry

Submitted in Partial Fulfillment
of the Requirements
for the Degree of

Doctor of Philosophy

August 1992

We approve the thesis of Susan Elizabeth McKinstry.

Date of Signature

Robert E Newnham
May 28, 1992
Robert E. Newnham
Alcoa Professor of Solid State Science
Thesis Advisor
Chair of Committee

K. Vedam
28 May 1992
Kuppuswamy Vedam
Professor Emeritus of Physics

28 May 1992
Carlo G. Pantano
Professor of Materials Science and Engineering

5/28/92
Altaf H. Carim
Assistant Professor of Ceramic Science
and Engineering

David Green
6/9/92
David J. Green
Professor of Ceramic Science and Engineering
In Charge of Graduate Programs in
Ceramic Science and Engineering

ABSTRACT

Spectroscopic ellipsometry has been utilized as a tool for investigating surfaces and thin films of ferroelectric materials. Using this technique, the thickness and properties of the anomalous surface layers formed on a $BaTiO_3$ single crystal and a PLZT ceramic specimen as a function of surface preparation were characterized. It was found that mechanical polishing produces a damaged surface layer which probably consists of a combination of amorphous material and second phases embedded during polishing. The depth of the damaged region varies with the polishing procedure, but can be made as thin as 200Å. Chemical etching was found to roughen the surface, but again, the depth of the anomalous layer could be made quite thin (~300Å).

Spectroscopic ellipsometry was also used to depth profile both the optical properties and the microstructural inhomogeneities of ferroelectric films prepared by the sol-gel method, rf sputtering, and Molecular Ion Beam Reactive Sputtering (MIBERS). It was found that many film deposition techniques engender remanent structural features (including voids distributed inhomogeneously throughout the film thickness and surface roughness) which decrease the apparent dielectric constant and increase the apparent coercive field of the films. The effect of such incorporated porosity on the bulk properties overwhelms changes due to intrinsic size effects. A model relating the net electrical properties of such thin films to their structural inhomogeneities has been developed and used to predict the presence of extrinsic size effects in ferroelectric thin films.

In addition, spectroscopic ellipsometry has been utilized to follow reactions in film/substrate systems during the annealing of as-deposited films. It has been shown that appearance of structural inhomogeneities typically occurs between 550 and 600°C, and that this is largely coincident with crystallization of the perovskite phase. Results on the *in-situ* annealing of sol-gel and MIBERS PZT films have been presented.

TABLE OF CONTENTS

LIST OF FIGURES

LIST OF TABLES

ACKNOWLEDGEMENTS

During the course of this thesis, I have benefitted tremendously from the guidance and insight of Dr. R. E. Newnham, and I would like to thank him for his contributions both to this thesis and to my growth as a scientist. I am also very grateful to Dr. K. Vedam for graciously "adopting" me into the the ellipsometry group and permitting me to benefit from his equipment and his experience in the field. His support in many ways made this thesis possible.

I would also like to thank Dr. H. Adachi, Dr. K. Kushida, K. Udayakumar, J. Chen, and H. Hu for providing thin film samples, and H. McKinstry for the computer interfaces used in furnace control. Technical discussions with Dr. P. Chindaudom, G. Fox, K. Udayakumar, J. Chen, Dr. A. Bhalla, and Dr. S. Krupanidhi were especially helpful, and are gratefully acknowledged. The critical reading of the fifth chapter of this thesis by Dr. R.W. Collins was also greatly appreciated. In particular, however, I would like to thank Dr. Pongpan Chindaudom, who not only made many contributions to this work, but was a good friend in the process.

Financial support from the National Science Foundation, Corning Inc., the NASA Space Grant Program, and Penn State is gratefully acknowledged.

Finally, I would like to thank my husband and family for their love and support throughout the past several years.

CHAPTER 1

INTRODUCTION

The field of ferroelectric thin films has burgeoned over the last few years due to the surge of interest in film-based ferroelectric memories, electrooptic switches, pyroelectric detectors, and high frequency piezoelectric transducers. While tremendous progress has been made in the film deposition technology, it is clear from a review of the literature that there is still considerable variability in the electrical properties of these materials. Although much of the scatter can be traced to differences in the preparation conditions, it is difficult to unambiguously ascertain the role of each processing variable in determining the net properties. Among the factors responsible for irreproducibility in thin films are variations in [1] the film density or microstructure (especially that associated with columnar growth of vapor deposited films), [2] the degree of crystallinity and the crystal phase of the material, [3] the chemistry of the film, either within the film plane or through the thickness, [4] any stresses imposed on the film by the substrate, and [5] environmental instability of the deposit.

Unlike other thin film systems, however, in ferroelectric materials, changes in film properties associated with processing variables may be augmented by intrinsic changes in the electrical properties as the thickness and particle size are decreased. Many materials, when made small in at least one dimension, display properties which differ from those shown by the bulk. The divergence of these size-dependent properties from their macroscopic values is often referred to as a "size effect." Very fine metallic particles, for example, liquify below the bulk melting temperature. Similarly, superconducting and superfluid transitions have been shown to depend on size (Ido 1976, Hlasnik et al. 1985, Watson 1966, Chainer et al. 1980, Guyon and Mitescu 1972, Kjaldman et al. 1978). In a comparable way, for ferroelectric materials, both the presence of domain walls and the ferroic transition itself are influenced by crystallite size and the geometrical dimensions of the phase. While this has not previously been critical to most applications, for both thin film and small particle-based devices, finite specimen size and large surface area/volume ratios may play an important role in determining the properties of ferroelectric materials.

Consequently, in studying either ferroelectric surfaces or thin films, it is desirable to have some means of sample characterization which is capable of distinguishing the different mechanisms contributing to deviation from bulk properties. In an attempt to move toward this goal, this thesis describes the use of spectroscopic ellipsometry to investigate the role of both intrinsic and processing-induced size effects in ferroelectric single crystal and thin film specimens.

1.1 Introduction to Size Effects

Beginning with work on the melting behavior of metals, it has been reported that many phase transitions are susceptible to size effects. The melting point of bulk gold, for example, is 1337.58 K, but this temperature drops rapidly for grain sizes below 100Å (see Fig. 1.1). This decrease in the phase transition temperature has been attributed to the change in the ratio of surface energy to volume energy as a function of particle size. Thus, for spherical particles of radius r, the melting temperature can be predicted from (Takagi 1954):

$$\Delta U\, dV - \Delta S T_r\, dV - \sigma\, dA = 0$$

where ΔU and ΔS are the changes in internal energy and entropy on melting, σ is the interfacial energy between the liquid and the solid, and T_r is the melting temperature of the particle. If ΔS and ΔU are temperature independent, then the difference between the bulk and small particle melting temperatures is inversely proportional to the particle

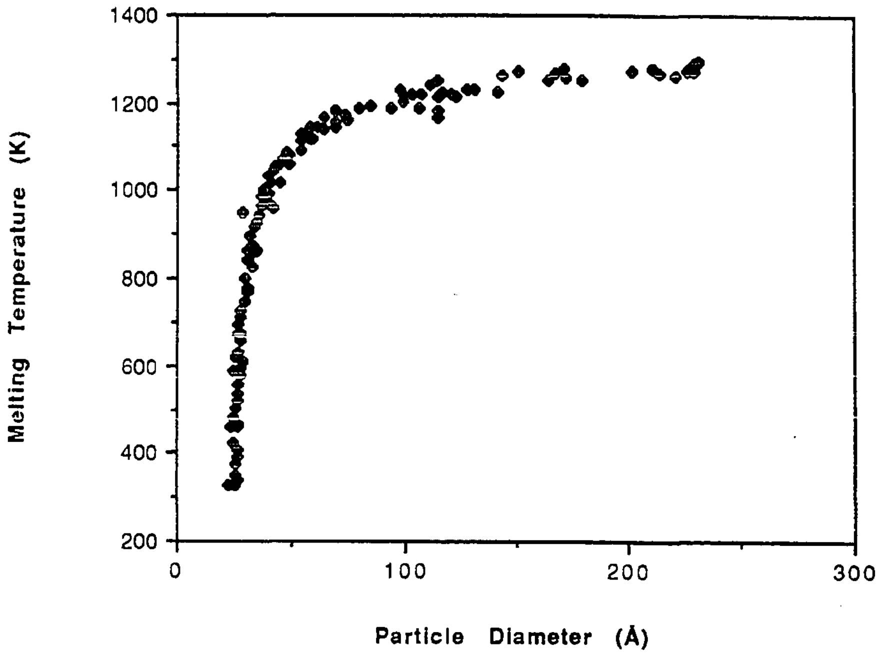

Fig. 1.1: The melting temperature of gold particles as function of particle diameter (after Buffat and Borel 1976)

radius according to:

$$\frac{T_o - T_r}{T_o} = \frac{2\sigma}{\rho L r}$$

where L is the heat of fusion, ρ is the density, and T_0 is the bulk melting point.

It is interesting that many types of equilibrium phase transitions display comparable size effects. In addition to the data on gold particles, the melting temperatures of copper (Gladkich et al. 1966), tin (Blackman and Curzon 1959), indium (Boiko et al. 1969), lead and bismuth (Takagi 1954) particles and thin films have all been shown to be size dependent. Similarly, the superconducting transition depends on size both intrinsically (Ido 1976, Hlasnik et al. 1985, Guyon and Mitescu 1972), and extrinsically, if the stress exerted on the superconducting phase is different at different sizes (Watson 1966). Superfluid transitions in He-impregnated powder compacts and thin films also depend on either the film thickness or the size of the pore diameter (Chainer et al. 1980, Guyon and Mitescu 1972, Kjaldman et al. 1978).

The phenomenology of both superfluids and superconductors can be described as a perturbation of the normal state free energy function by an expansion in terms of the order parameter Θ:

$$G_{super} = G_{normal} + \frac{1}{2}\alpha\,\Theta^2 + \frac{1}{4}\beta\,\Theta^4 + \frac{1}{6}\gamma\,\Theta^6 + \kappa\,(\nabla\Theta)^2$$

where α, β, γ, and κ are constants and $\nabla\Theta$ is the gradient of the order parameter. For superfluids and superconductors, Θ is an "effective wave function" of the superfluid, and the degree of superconducting order (where $\Theta^*\Theta$ = the concentration of superconducting electrons), respectively (Ginzburg 1958, 1961, Ashcroft and Mermin 1976). Transitions between the high and low temperature phases are governed by the series expansion in terms of the order parameter. However, a description of size effects in these materials requires that at least the gradient term be added. When this is done, the phenomenological description can also be used to describe transitions as a function of size (Ginzburg 1958, Kriss and Rudnick 1970, Guyon and Mitescu 1972).

In the same way, this type of expansion, with some terms proportional to the volume and others to the surface area, has been used to describe transitions between the para- and ferro- states of ferromagnets and ferroelectrics. The order parameters for these materials are the spontaneous magnetization and polarization. Consequently, it is projected that as the volume of a ferroic material diminishes, it will also be subject to size effects. While later authors have added additional terms to the free energy function for ferroelectrics to better describe the behavior of thin wafers and films, this general conclusion remains.

1.1.1 Size Effects in Ferroic Materials

These predictions in conjunction with a variety of experimental data have led to the postulation that there are four regimes expected in the size dependence of ferroic properties (Fig. 1.2). In large crystallites, several equivalent domain states exist, and motion of the domain walls under applied fields leads to hysteresis. As the size is reduced, however, the number and type of domain walls should diminish, leading to stable single domain particles. At yet smaller sizes the material remains single domain, but the domain direction is not fixed in time. Finally at sufficiently small sizes a reversion to non-ferroic behavior is expected at the point where there are simply too few unit cells to sustain cooperative behavior. Similar transitions with size should occur in secondary ferroics.

Beginning with the larger end of the size spectrum: when prepared as large grain ceramics, ferroic ceramics exhibit complex domain structures, often with several types of domain walls. The domain wall energy in these materials is proportional to the surface area of the boundaries. For large-grained ferroics, this additional energy can be

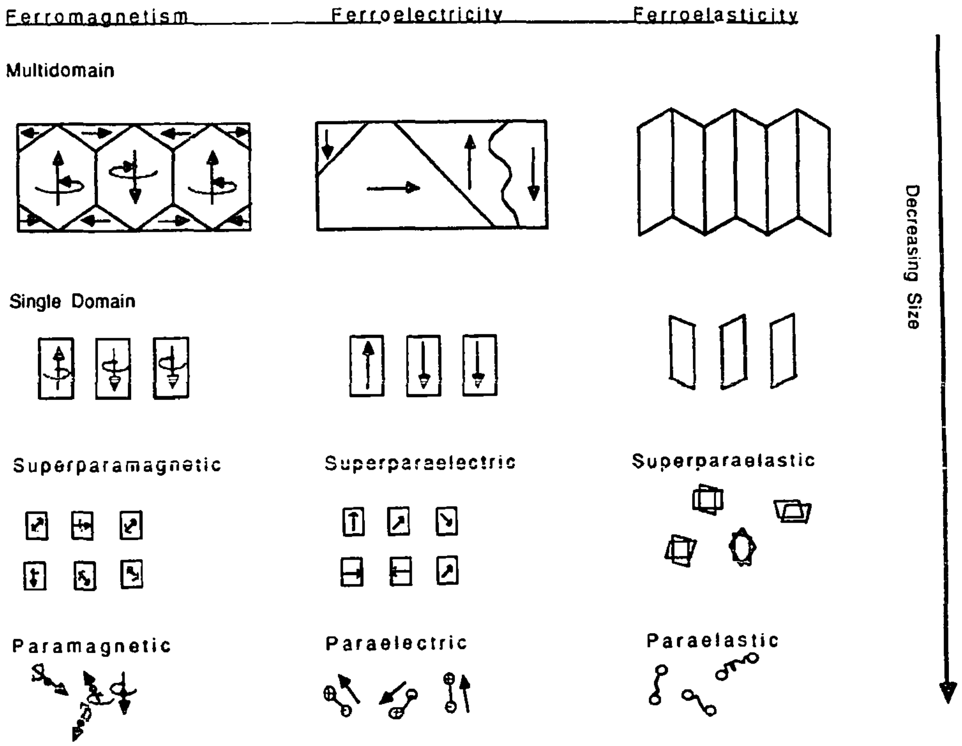

Fig. 1.2: Transitions in ferroic materials as a function of size

supported by a decrease in the depolarization energy associated with the volume of the crystal (Lines and Glass 1977). However, as the size of the system decreases, the volume free energy necessarily decreases as well, and it becomes increasingly difficult to support the free energy term associated with domain walls (Kittel 1946). Consequently, the number of domains is expected to diminish as first one, then the other, types of domain walls are eliminated. The transition from polydomain to single domain behavior is well-documented in a number of ferromagnets. Pure iron suspended in mercury, for example, shows a critical size for conversion to single domain behavior at ~23 nm and $Fe_{0.4}Co_{0.6}$ at a critical size of ~28 nm (Kneller and Luborsky 1964). This is in good agreement with calculations by Kittel, who suggested 20 nm as the minimum size for multidomain behavior in magnets (Kittel 1946). Results for acicular agglomerates of γ - Fe_2O_3 particles separated by non-magnetic grain boundaries are also consistent with these estimates; Berkowitz et al. (Berkowitz et al. 1968) report that the stable single domain range at room temperature is centered at ~40 nm.

Although the loss of multidomain behavior in ferroelectric ceramics is known to occur for much larger grain sizes (~several tenths of a micron), it is also clear that the stress state in a monolithic body containing domains is considerably more complex than that for isolated particles. Consequently, the changes in ferroic properties as a function of size in ferroelectric powders are expected to follow the ferromagnetic analog more closely. Lee et al. (1988) have reported that in 0-3 $PbTiO_3$ / polymer composites, there is a significant drop in the ability to pole the composites when the filler particle size is decreased below ~200 nm. They attributed this to the transition from multi to single domain behavior. It is not clear from their data, however, either how wide the particle size distribution is, or whether the volume fraction of crystalline material in the powder changed with particle size. There is a need for further studies in this area.

At still smaller sizes, ferroic materials undergo a phase change to the high temperature prototype group. In the case of ferromagnetic particles, this has been correlated with the size at which the anisotropy energy holding the magnetization oriented in a fixed direction is on the order of the thermal energy (Jacobs and Bean 1963). As a result, the spin direction is randomized with time, leading to an unmagnetized, but highly orientable single domain crystal. Thus, a magnet in this size regime is characterized by a zero net magnetization, the disappearance of a magnetic hysteresis loop, extremely high magnetic susceptibilities, and a symmetry which is, on average, higher than that of the ferromagnetic phase. Iron exhibits superparamagnetic behavior at particle sizes near 7 nm (Kneller and Luborsky 1964), γ - Fe_2O_3 at ~30 nm (Berkowitz et al. 1968), and $BaFe_{12-2x}Ti_xCo_xO_{19}$ at 15 - 35 nm depending on the stoichiometry and the degree of particle shape anisotropy (Kubo et al. 1985). Some commercial ferrofluids have particle size distributions which span the transition between ferromagnetic and superparamagnetic states (Fertman 1990).

A similar mechanism has been proposed to explain the dielectric and elastic properties of relaxor ferroelectrics (Cross 1987, Viehland et al. 1990). Compositions including many of the $A(B'_{1/2},B''_{1/2})O_3$ and $A(B'_{2/3},B''_{1/3})O_3$ exhibit micro polar regions (typically 2 - 30 nm in size) of 1:1 ordering on the B sublattice dispersed in a disordered matrix. It has been suggested that as a result of this nanostructure, the spontaneous polarization in these materials is also subdivided into very small local regions. Thus, a lead magnesium niobate ceramic can be regarded as a collection of disordered, but highly orientable dipoles. The result, much like the case of superparamagnetism, is a high dielectric permittivity over a broad temperature range, even though the net spontaneous polarization is zero. Because of the long range of the electric fields induced by the local dipoles, however, there is more interaction between the local electric dipoles than was present in the ideal superparamagnet. Consequently, the superparaelectric behavior in relaxor ferroelectrics is modulated by coupling between local moments, so that a spin glass model is necessary to completely describe the phase transition behavior (Viehland et al. 1990). Evidence for the importance of the size of the microregions is given in experiments on materials which can be ordered by heat treatment. As the scale of the ordered regions grow beyond a certain size, the material reverts to ordinary ferroelectric (or antiferroelectric) behavior with a well defined transition temperature and a non-dispersive dielectric response.

As yet, direct observation of superparaelectric behavior in particulate ordinary ferroelectrics has not been documented. Recently, however, several investigators have attempted to determine the critical size for reversion to the high temperature prototype symmetry (Ishikawa et al.1988, Uchino 1990, Saegusa et al. 1989). As in the case of the melting of metal particles, as the particle size is decreased, the transition temperature drops markedly (see Fig. 1.3). While at larger sizes the high symmetry phase is the ordinary paraelectric phase, as the size of the ferroelectric particles becomes small enough that thermal energy can disorder the dipoles, there should be a transition from paraelectric to superparaelectric particles. The reported results indicate that unconstrained $BaTiO_3$ particles show the transition to a cubic phase near 80 - 120nm (Uchino 1990, Miller 1991) whereas $PbTiO_3$ is stable in the tetragonal form to ~10 - 20nm (Ishikawa et al. 1988, Lee et al. 1988). Because it is difficult to characterize the electrical properties of such small particles, it is not known if and when the high symmetry particles actually become superparaelectric. $NaNO_2$, on the other hand, shows only some broadening in the DTA characteristic for the ferroelectric phase transition with no change in the transition temperature for particle sizes down to 5nm. While it is an order-disorder ferroelectric, and so might have different size dependence for the properties than would a displacive ferroelectric, it is interesting that there in no evidence for superparaelectricity even at particle sizes of 5 nm.

It is also possible to shift the critical size for reversion to high temperature symmetry with changes in the processing. Residual strains, in particular, have been shown to drastically affect the properties of $BaTiO_3$ (Jyomura et al. 1980, Schoijet 1964). Kanzig (Kanzig 1955), for example, demonstrated that mechanical strain

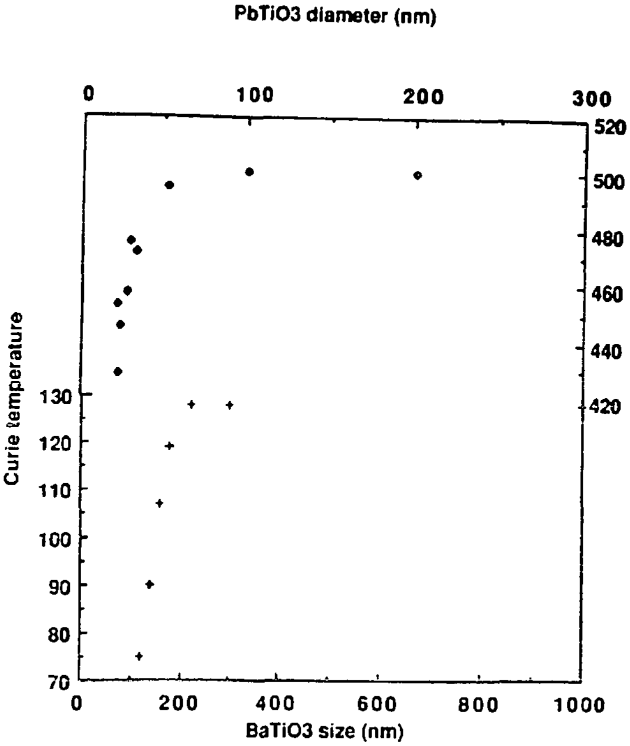

Fig. 1.3: Curie temperature as a function of particle size for $PbTiO_3$ and $BaTiO_3$ powders (after Ishikawa and Uchino, respectively)

induced by grinding $BaTiO_3$ powders produces a tetragonally distorted layer 10 nm thick at the surface above the Curie temperature. By annealing the milled powders at 1100°C, however, Schoijet was able to eliminate this without greatly altering the grain size (Schoijet 1964). Thus, it is not surprising that heavily milled $BaTiO_3$ powders with an average radius of ~10 nm have been shown to possess permanent dipole moments (Bachmann and Barner 1988).

Saegusa et al. examined the solid solution between $BaTiO_3$ and $PbTiO_3$ to determine the critical size for stabilization of the cubic phase to room temperature as a function of composition. Assuming that crystallinity and stoichiometry were maintained for the smallest sizes, their data suggests that the critical size is not a linear function of composition (Saegusa et al. 1989). It would be tremendously interesting to follow the magnitude of the polarization as a function of temperature in such powders to see how its magnitude is affected by particle size.

Although the general outline of size effects expected in films are similar to those demonstrated in ferromagnetic particles, it would not be surprising for the boundaries between different regions to shift along the size axis for different geometries. Kittel was one of the first to explore this possibility in ferromagnetic materials (Kittel 1946). He calculated that in a film where the preferred magnetization is perpendicular to the major surface, the multi to single domain transition should occur near 300nm, an order of magnitude larger than the same transition in a particulate material. If, however, there is either no anisotropy or the easy magnetization direction falls in the film plane, new types of domain walls may appear and persist down to very small sizes (Cullity 1972).

The transition to superparamagnetic behavior is apparently suppressed in comparatively perfect thin films produced in high vacuum systems, probably because the large two dimensional area raises the volume energy above the available thermal energy, even for very thin films. As a result, regular ferromagnetic behavior persists in much thinner films (down to ~ 0.5 nm for Ni films sandwiched between non-magnetic layers [Beauvillain 1986]). In such samples, the ferromagnetic transition temperature also drops rapidly for films < 1.5 nm thick.

Films which grow as discrete islands of magnetic material rather than continuous layers or which consist of magnetic particles isolated from each other by non-magnetic hydride or oxide layers, on the other hand, should behave like particulate systems (undergoing superparamagnetic transitions appropriate for the primary magnetic particle size). This type of behavior has been confirmed in ferromagnetic films which became superparamagnetic at apparent thicknesses of 2.7 nm (where the film actually consisted of 5-10 nm islands (Prutton 1964). It is interesting that no change in the Curie temperature was noted before the onset of thermal randomization of the spins.

Given this information, what can be predicted about the behavior of ferroelectric thin films? First, for an unelectroded film it seems likely that ferroelectricity will remain stable at least down to thicknesses of ~100nm for $BaTiO_3$, and possibly considerably lower for $PbTiO_3$ films. This is in accord with several theoretical predictions for size effects in thin ferroelectric wafers. In that work it was shown that when space charge effects (which will be considered in the following section) are discounted, the onset of intrinsic size effects is projected to fall in the tens to hundreds of Ångstroms range (Binder 1981).

Multidomain configurations should also remain stable down to very small sizes. Corroborating evidence for this is suggested by TEM studies of thinned ferroelectric ceramics and single crystals where, provided the grain size is large enough, domains can be detected in wafers below 100 nm thick (Tanaka and Honjo 1964). When, however, the grain size in the film falls below some critical limit, the density of domains will probably decrease in a manner similar to that shown in ceramics (Arlt 1985).

Finally, as in the case of the magnetic films, unless there is some extrinsic mechanism for forming discrete polar microregions, the onset of superparaelectricity should be depressed by the relatively large volume of ferroelectric.

1.1.2 One-Dimensional Size Effects at Ferroelectric Surfaces

The theoretical justification for both size effects and changes in the electrical properties at the surface of a ferroelectric material can be visualized as follows. Ferroelectricity differs from other cooperative phenomena in that a surface requires termination of the electrical polarization. In one dimension this can be pictured schematically as:

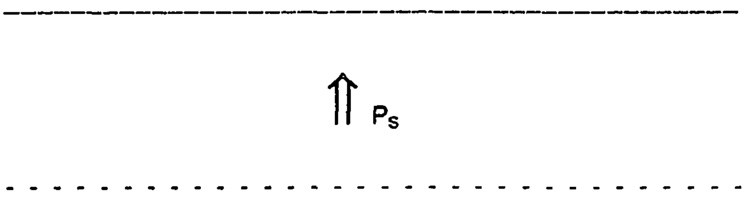

If it were possible to truncate the material so that the spontaneous polarization was maintained right up to the ferroelectric/air interface, then at the surface there would be a discontinuity in the dielectric displacement. However, the normal component of the displacement must be continuous across an interface, so such a situation cannot exist unless there is an accumulation of charge at or near the surface which is sufficient to compensate the polarization. When there is no top electrode and the material is an insulator, on the other hand, the spontaneous polarization itself must decay as the surface is approached to eliminate the discontinuity in the displacement (Binder 1981).

Two principal types of theoretical treatments have been proposed to treat the question of how ferroelectrics will behave in this one-dimensional situation. In the first of these, the ferroelectric is assumed to have no electrodes on the surface, so that all of the compensation for the surface polarization must be done within the ferroelectric itself. This question has been addressed several times by authors using different expansions for the free energy of the system (Ivanchik 1962, Kholodenko 1963, Binder 1981, Gitel'son et al. 1977). Among the most complete of these is Binder's phenomenological description, in which the energy difference between the ferroelectric and paraelectric phases is written as

$$F = \int_0^L \left(\frac{1}{2} A P^2 + \frac{1}{4} B P^4 + \frac{1}{2} C \left(\frac{dP}{dz}\right)^2 - \frac{1}{2} E_d P\right) dz + \frac{1}{2} C \lambda^{-1} (P_1^2 + P_L^2)$$

where F = Free Energy, P = polarization, z is along the thickness direction, A, B, and C are constants, E_d is the depolarization field resulting from inhomogeneities in P, λ is the extrapolation length, L is the thickness of the film, and P_1 and P_L are the order parameters at the two surfaces (Binder 1981). The integral contains contributions to the volume free energy of the ferroelectric with no electric field applied, including the standard Devonshire expansion of the polarization, the correlation energy, and the depolarization energy. The remaining term is the bare surface contribution. Order of magnitude calculations based on this type of formalism lead to the prediction that ferroelectric properties will be modified substantially only very close to the surface for large crystals and at very small thicknesses for wafers or films (~tens of nm). Unfortunately, it is difficult to measure some of the necessary material properties experimentally, so more accurate estimations will depend on new techniques for determining surface properties.

The second approach addresses the situation where the ferroelectric is electroded. In agreement with the studies on unelectroded crystals, Batra and Wurfel have shown that when the conductivity of the electrodes is insufficient to completely compensate the polarization, the transition temperature of the ferroelectric is depressed, the spontaneous polarization levels are decreased and for thin films ferroelectricity becomes unstable (Batra et al. 1973a,b). In marked contrast to the previous case, however, they suggest that for a ferroelectric with semiconducting electrodes, size effects will become noticeable for films on the order of microns thick. This was verified experimentally with a triglycine sulfate film electroded asymmetrically with doped silicon on one side and gold on the other (Wurfel and Batra 1973, Wurfel et al. 1973). Since the carrier concentration of positive and negative species in the semiconductor are not equivalent, it was possible to completely destabilize the polarization direction for which compensation could not be achieved. Consequently, for 100Hz cycling, the film behaved as a polar, not a ferroelectric material. When, however, the semiconducting electrode was illuminated with high intensity light, more minority carriers were available to compensate the spontaneous polarization, and a full hysteresis loop could be achieved (Wurfel and Batra 1973).

A number of authors have also shown that in unelectroded, semiconducting crystals the depolarizing field can become sufficiently large at small platelet thicknesses that ferroelectricity is unstable (Lines and Glass 1977, Kholodenko 1963, Ivanchik 1962). The size at which this is calculated to occur depends on the assumptions used in the theory, but they typically fall around 10-20 nm (Vendik 1984, Ivanchik 1962).

In comparison to these theoretical predictions, experimental studies on bulk ferroelectrics have shown that near the specimen surface, the materials display anomalous properties over depths which are estimated to range from tens of Ångstroms to tens of microns. The upper end of this size scale points to a second, and perhaps more important, cause of size effects in ferroelectric materials.

1.1.3 Extrinsic Size Effects in Ferroelectrics

Unfortunately, in addition to the intrinsic size effects expected for all ferroelectric materials, several extrinsic, processing-related phenomena can also result in apparently size-dependent deviations from bulk properties. Mechanically damaged regions left after polishing, for example, introduce low permittivity regions at the sample surface. As the material is thinned, these anomalous layers become a progressively larger fraction of the overall thickness, and begin to dominate the measured dielectric constant, ε. The result is a thickness dependent ε which is unrelated to actual changes in the material properties. Similarly, several other processing artifacts can also cause extrinsic size and surface effects. Among these are nonstoichiometry at the surface due to either volatility of one component during firing (Thacher 1977), preferential leaching of one constituent during etching or cleaning (Utech 1990), reaction between the material and ambient gases (Utech 1990), or gradients in impurity concentrations associated with the crystal growth (Triebwasser 1960). This last point is especially important in examining literature data on surface layers in Remeika "butterfly twin" $BaTiO_3$ crystals, where impurities such as Pt and F are not homogeneously distributed through the crystal thickness (Triebwasser 1960, Tongson 1981). Charge injection from the electrodes during poling, or space charge layers formed as a result of electric field concentrations bridge the gap between intrinsic and extrinsic phenomena and can also result in large changes in the electrical properties.

Although the existence of surface layers on ferroelectrics has been confirmed by a variety of techniques, interpretation of the experimental results has been complicated by the fact that the observational methods have been indirect. That is, the surface-layer properties could only be inferred from deviations of surface-sensitive material parameters from the corresponding bulk values. Thus, it was typically necessary to estimate a value for the layer thickness, t, to calculate its dielectric constant, ε, or vice versa. Discrepancies in the value chosen naturally led to wide variations in the deduced properties. This, as much as differing sample preparation conditions, accounts for the scatter in reported values for t and ε of the surface layer. Moreover, without a direct knowledge of both parameters and their change with temperature (and hence with polarization), it is very difficult to distinguish the mechanism dominating deviation from bulk properties.

Ferroelectric thin films are particularly prone to processing-induced defects. Included among these are microstructural heterogeneities, variations in crystalline quality, and mechanical stresses imposed on the film by the substrate. It is critical to note that the first two of these, which in the opinion of the author accounts for the majority of the "size effects" observed in thin film properties, are, in fact, size independent. It is fortuitous, then, that many film preparation techniques produce films that are defective and would remain defective even if macroscopic samples could be fabricated.

1.1.4 Size Effects in Ferroelectric Films

The experimentally observed size effects reported in the ferroelectric thin film literature fall into four major categories: an increase in the coercive field, a decrease in the remanent polarization, a depression in the dielectric constant, and a smearing of the paraelectric/ferroelectric transition over values expected from bulk materials of the same composition. Typical data on the first two observations are listed in Table 1.1, the third is depicted in figure 1.4 and the fourth point is discussed by Biryukov et al. (1984). One point which is immediately apparent from Table 1.1 and a perusal of literature data is that deviations from bulk properties are nearly universal, but the thickness at which the properties begin to diverge and the magnitude of the disparity is

Table 1.1: Representative data for the remanent polarization and coercive field on $BaTiO_3$, $PbTiO_3$, and PZT thin films.

Material	P_r (μC/cm^2)	E_c (kV/cm)	Reference
Single crystal $PbTiO_3$	~55 - 75	6.75	Gavrilyachenko et al. 1970
Sol-gel $PbTiO_3$	3.37	54.8	Kuang et al. 1990
Sputtered (001) $PbTiO_3$	55	75	Yamaka et al. 1988
Sputtered (001) $PbTiO_3$	35	160	Iijima et al. 1986
Sputtered or CVD $PbTiO_3$	12	250	Okuyama and Hamakawa 1985
CVD (001) $PbTiO_3$	14.1	20.16	Yoon et al. 1989
bulk PZT 58/42	45	17	Sreenivas and Sayer 1988
Sol-gel PZT	36		Payne 1990
Sol-gel PZT 53/47	12	150	Nagata et al. 1990
Sol-gel PZT 52/48	35		Udayakumar et al. 1990
Sol-gel PZT	18-20	50-60	Dey and Zuleeg 1990
Sol-gel PZT 40/60	6.6	26.7	Yi et al.1988, 1991
Sputtered PZT 90/10	13.9	60.0	Okamura et al. 1990
Sputtered PZT 58/42	30.0	25	Sreenivas and Sayer 1988
Sputtered PZT 65/35, weak (100)	12.5	90	Croteau et al. 1987
Sputtered PZT 65/35	3.6	33	Croteau et al. 1987
Sol-gel PLZT 2/54/46	28.5	190	Wu and Sayer 1988
Single crystal $BaTiO_3$	26	1	Jaffe, Cook, Jaffe 1971
Polycrystalline $BaTiO_3$	8	3	Jaffe, Cook, Jaffe 1971
Sputtered $BaTiO_3$	0.8	3	Nagatomo and Omoto 1987
Screen-printed $BaTi_{0.95}Sn_{0.05}O_3$	1.7 - 2.8	25	Loposzko et al. 1980
Sputtered (001) $BaTiO_3$	7	60	Surowiak et al. 1989
Sputtered $BaTiO_3$, weak (101)	16	20	Surowiak et al. 1989

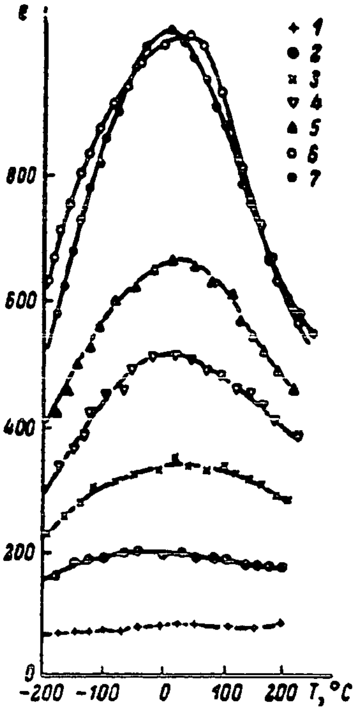

Fig. 1.4: Temperature dependence of ε for (Ba,Sr)TiO3 films. Film thickness (μm) 1) 0.1; 2) 0.33; 3) 0.5; 4) 1.0; 5) 2.0; 6) 5.0; 7) 8.2 (after Gitel'son et al. 1977)

strongly dependent on the preparation conditions. Consequently, films produced at one laboratory may display marked size effects, while others of the same composition and thickness possess bulk properties.

The reasons for this type of discrepancy lie in the variety of mechanisms causing the apparent size effect. These include microstructural heterogeneities, variations in crystalline quality, mechanical stresses imposed on the film by the substrate, space charge effects, and finally intrinsic size effects.

Inhomogeneity in the film microstructure can take the form of incorporated porosity, surface and interface roughness, or variations in the grain size. In particular, many ferroelectrics grown by vapor deposition processes are columnar, and should be expected to have low densities (see Fig. 1.5). This, in turn, could appreciably lower the dielectric constant, and if there was poor coupling between the grains, would increase the coercive field as well (Jiang 1990). Even in films that appear dense, Dudkevich et al. have shown that the microstructure may change continuously as a function of film thickness (Dudkevich et al. 1981). Thus, for sputtered $Ba_{0.85}Sr_{0.15}TiO_3$ films, thinner films tend to be composed of small particles (15 nm for a 4 nm thick film) where thicker films show a distribution of grain sizes ranging from the very fine particles deposited next to the substrate to larger grains at the film surface (200 - 300 nm for a film 2000 nm thick). Given this type of microstructural heterogeneity, it is no wonder that many properties appear to be dependent on film thickness. As the absolute grain size at any given thickness would also be expected to be a sensitive function of both the deposition conditions and any post annealing, samples prepared at different laboratories would behave differently.

A second significant influence on thin film properties is the crystalline quality of the ferroelectric material. It is well known from the chemical preparation literature that the loss of clear X-ray diffraction peaks is coupled to the disappearance of the paraelectric-ferroelectric phase transition. Unfortunately, many film deposition

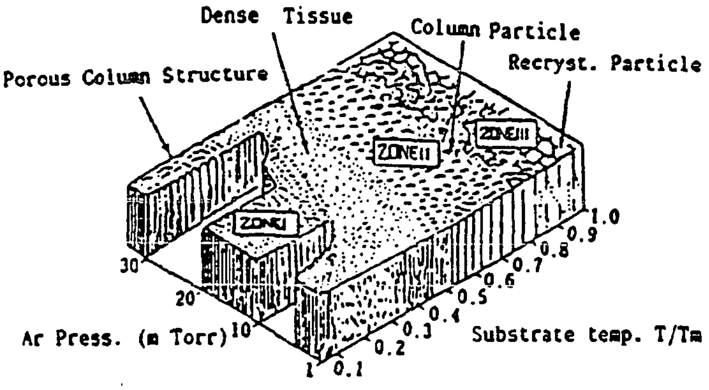

Fig. 1.5: Relation between the gas pressure and the normalized substrate temperature for sputtered films (after Thornton 1977)

techniques also result in poor crystallinity. During sputtering, for example, the growing film is subjected to bombardment by high energy ions. While this can be advantageous in terms of providing additional energy to the deposit and increasing the surface mobility, heavy bombardment, particularly at low substrate temperatures, can also introduce high defect concentrations. In chemically prepared thin films, on the other hand, low annealing temperatures can be insufficient to fully crystallize the ferroelectric phase.

Fast neutron irradiation of $BaTiO_3$ single crystals (neutron energy ≥ 50 keV), for example, eventually introduces sufficient defects that the material transforms into a metastable cubic state with an expanded lattice parameter (Wittels and Sherrill 1957). Having undergone this transition, no displacive transformation to the tetragonal, ferroelectric, state can be detected at temperatures above 78K. Although the bulk still displays some long range order, the X-ray peaks are broadened by a factor of five over the unirradiated crystal, and it is not unlikely that the surface was completely amorphized. Annealing to 1000°C is required before the lattice parameter relaxes back to its initial value. Unfortunately, in many thin films, annealing temperatures are kept as low as possible to minimize changes in stoichiometry. While this may help maintain the perovskite structure, it is probable that 500 - 700 °C is insufficient to fully crystallize amorphous or badly damaged films. It is interesting that many authors working with either vacuum deposited or chemically prepared thin films report modifications of the perovskite structure with a slightly expanded cubic unit cell (Naka et al. 1974).

In one of the most complete characterizations of the actual crystallinity of ferroelectric films, Surowiak et al. measured lattice strains in sputter-deposited $BaTiO_3$ films. They found that films which had experienced heavy bombardment during growth tended to have more heavily deformed crystallites (i.e. the mean microdeformation $\Delta d/d$ was as large as 0.01 - 0.005) and small coherent scattering sizes. Larger, less defective crystallites ($\Delta d/d < 0.005$) could be formed when the growth conditions were not as rigorous (Surowiak et al. 1989). Differences between the two types of films were readily apparent in the electrical properties: lower $\Delta d/d$ values were associated with high remanent polarizations, piezoelectric constants close to single crystal values, and relatively narrow phase transitions. This last point was examined by Biryukov et al. who demonstrated that films with large lattice strains should be expected to show diffuse phase transitions (Biryukov et al. 1984). It is important to note that poorly crystallized films from any preparation method will probably display low remanent polarization, lowered dielectric and electromechanical coupling constants, and diffuse phase transitions.

It is not at all surprising that mechanical stresses should also affect thin film properties. As in most ferroic materials, the appearance of the order parameter at the transition temperature is accompanied in perovskite ferroelectrics by a spontaneous strain. The domain structure, then, should be heavily influenced by the types of strains present in the film. In a similar way, stresses in heteroepitaxial films have been shown to alter the equilibrium domain structure (Besser et al. 1971). Forsbergh has also shown that two dimensional stresses can stabilize the ferroelectric phase to higher temperatures in bulk materials (Forsbergh 1954), and this mechanism could well operate in thin films when there is good cohesion between the substrate and the film.

The primary difference between size effects in ferromagnetic materials and ferroelectric materials is that in the electrical analog, it is necessary to compensate the polarization at the surface of the material. Batra et al. have shown that in a ferroelectric which is slightly conducting or electroded with a material with a low carrier density, tremendous depolarization fields or space charge migration can be generated even in comparatively thick films (~1 μm). These can shift the phase transition temperature, lower the magnitude of the spontaneous polarization, and even destabilize the ferroelectric phase in the film (Batra et al. 1973a,b).

Despite all of these opportunities for extrinsic size effects, there is evidence that films which are prepared carefully can display near bulk properties to very small thicknesses. In work on sol-gel PZT films, Udayakumar (Udayakumar et al. 1990), for example, showed that room temperature dielectric constants of ~1300 could be maintained for films >300nm thick (see Fig. 1.6). The bulk remanent polarization was retained to 450 nm, and remained finite, though reduced, in films 190nm thick (see Fig. 1.7).

In work on rf sputtered $BaTiO_3$ films, Dudkevich et al. showed that the size of the coherent scattering region, D, within their films was more important than the thickness in determining the macroscopic electrical properties. Consequently, the dielectric constant increased markedly as the coherent scattering size grew larger than ~30 nm. When D reached 50 nm, room temperature dielectric constants of >1000 were achieved, and some indication of a dielectric constant peak could be detected at the Curie temperature (Dudkevich et al. 1981).

As shown in Table 1.1, several other recent papers have also demonstrated that it is possible to achieve bulk or near bulk properties for several members of the perovskite family.

1.2 Statement of the Problem

As the field of ferroelectric thin films grows, it will become increasingly important to examine the role of size effects on the expected properties. While intrinsic size effects similar to those demonstrated in ferromagnetic analogs will act as lower limits to the size of ferroelectric devices, in many cases extrinsic, processing-induced contributions overshadow the fundamental size restrictions. Because of the sheer number of factors which can influence apparently size dependent properties, it is imperative that the characterization technique employed be capable of distinguishing

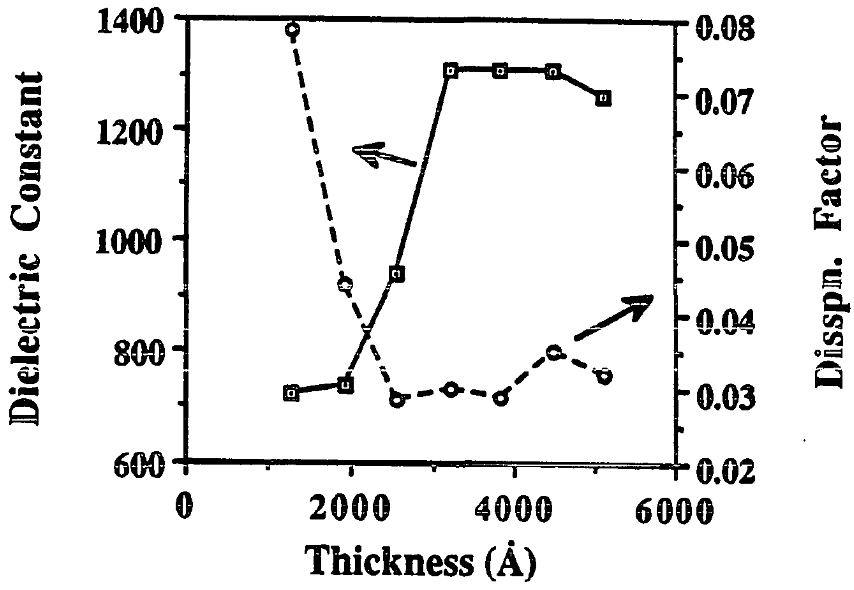

Fig. 1.6: Dielectric constant and dissipation factor vs. thickness for a sol-gel PZT film (after Udayakumar et al. 1990)

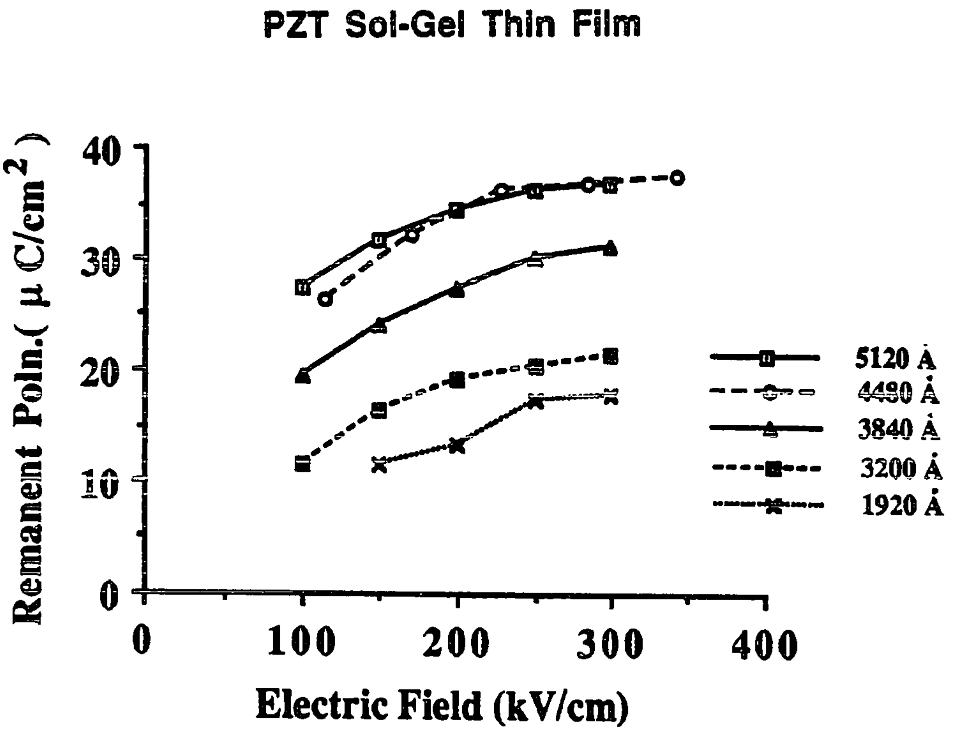

Fig. 1.7: Polarization vs. electric field for sol-gel PZT films of varying thickness (after Udayakumar et al. 1990)

intrinsic and extrinsic causes for the overall "size effects." Only in this way will it be possible to fully understand the relationship between processing and properties in ferroelectric films.

There are few techniques which allow this flexibility. A review of the available direct measurements for both polarization and space charge distributions has been given by Lang and Das-Gupta (Lang and Das-Gupta 1986). They list two principal techniques: sectioning of the sample surface or sectioning of a sandwich structure followed by analysis of the individual layers, and introduction of a modulated thermal or shock wave and deconvolution of the derived pyro or piezoelectric response. The first is impractical for this thesis in light of the impossibility of preparing layers on the fine scale over which the polarization was expected to vary at the surface of a bulk single crystal. The second has been used primarily in analysis of inhomogeneously poled (or charged) polymer films, where the distribution in the polarization occurs on the scale of microns. Consequently, the estimated resolution of the technique (~1-4 µm, Sessler et al. 1982) was sufficiently high to provide useful information on the spatial variation of the polarization and space charge. However, this is coarser than the phenomena expected in ceramic systems. In addition, the elastic stiffness and the speed of sound is higher in ceramics than in polymers, which would further reduce the resolution for acoustic systems. It is also expected that the thermal technique would be limited in probing the very-near-surface region. Furthermore, it is not at all clear whether microstructural variations like those expected in some thin films could be properly handled with these measurements.

A second possibility for obtaining information on a layer thickness and its dielectric properties is an optical technique. Of these, spectroscopic ellipsometry is the most promising as it involves measurement of both the intensity and phase of the reflected light at each wavelength. In contrast, standard transmission-reflection measurements handle only the intensity of the light, and so contain inherently less information. Although ellipsometry has in the past been limited to characterization of samples in which at least one component was absorbing, it was shown recently that the technique can be extended to transparent materials with no loss in accuracy (Chindaudom 1991). The depth resolution of the technique is typically in the Ångstrom range, and in previous experiments the agreement with cross-sectional transmission electron microscopy has been very good (McMarr 1985). Given a sufficient refractive index contrast between film and substrate, the depth resolution is even greater, and sub-monolayer coverages can be analyzed. For transparent materials like the ferroelectrics used in this study, the effective penetration depth of light is effectively infinite over the wavelength range utilized, so the entire depth of a film several microns in thickness can be sampled and profiled. Thus, spectroscopic ellipsometry is one of the few surface science tools which can be used to study phenomena over the scale of Ångstroms to microns. This is particularly advantageous in the current study due to the wide thickness range over which surface and size effects are reported to appear.

However, the primary advantage of spectroscopic ellipsometry as a characterization tool for ferroelectrics is that, unlike other indirect techniques, it is possible to determine both the thickness of an anomalous region at the surface of a crystal or a film and the refractive index of the layer. As the refractive index is related to the spontaneous polarization, this should allow the polarization to be tracked as a function of depth. In contrast to other indirect techniques, the data is sufficiently overdetermined that a small number of parameters describing the surface properties (for example, the thicknesses of any surface layers and the optical properties of those layers, the degree of surface roughness, the surface polarization, the rate at which the polarization changes as the surface is approached, and the number of charge carriers at the surface) can be determined using several hundred independent data points. Moreover, the technique is non-destructive and non-invasive.

Despite these attractive features, only a few cursory studies on the characterization of ferroelectrics by spectroscopic ellipsometry have been performed. While it was shown that ellipsometry is sensitive to the surface layers on both single crystal and ceramic specimens, no attempt was made to depth profile the material to determine the cause (Afanasjev 1985, Thacher 1977). This is largely due to previous limitations on the technique in the measurement of transparent samples. Recently, however, new methods for handling this problem have been developed (Chindaudom 1991, Jellison and Sales 1991, Jellison and Modine 1990) and the first has been incorporated into one of The Pennsylvania State University spectroscopic ellipsometers. Consequently, this thesis concerns the application of spectroscopic ellipsometry to the study of ferroelectric materials.

Given the above review of size effects in ferroelectric materials, it is clear that there remain several questions concerning the mechanisms responsible for changes in properties with size and the scale over which each acts. The motivation for this thesis was to address these questions as follows:

1) To develop spectroscopic ellipsometry as a characterization tool for ferroelectric surfaces and thin films. To accomplish this, computer code capable of simulating the effect of each variable of interest on the ellipsometric spectra needs to be developed. It is hoped that in this way, the sensitivity of spectroscopic ellipsometry to different phenomena can be determined, and guidelines concerning the optimization of sensitivity (via intelligent choice of the material under study or experimental conditions) for a given situation can be promulgated.

2) To study the surface of a $BaTiO_3$ single crystal so that the role of preparation conditions on the thickness and electrical properties of any anomalous layer present can be determined. After characterization of several surfaces, data from the most nearly ideal will be examined for changes in either the polarization or the number of mobile charge carriers as a function of temperature. This should allow investigation of such

fundamental quantities as the correlation length for ferroelectricity and the role of depolarizing fields and space charge layers on the properties of ferroelectric surfaces.

3) To characterize ferroelectric films prepared by different methods with spectroscopic ellipsometry. This should allow the mechanisms dominating size effects in these materials to be studied, along with the role of processing in controlling structure-microstructure-property relationships. Such information will be useful both from the standpoint of improving film preparation procedures and as it will permit comparisons between the size effects in ferroelectric thin films and those manifested in single crystals.

CHAPTER 2

INTRODUCTION TO ELLIPSOMETRY AND ELLIPSOMETER CALIBRATION

Ellipsometry is fundamentally a technique designed to measure both the amplitude and phase of a beam of light reflected from a sample surface. In a rotating analyzer instrument like that utilized in this thesis, a beam of light of a known wavelength and a known (and constant) polarization state is incident on the specimen. On reflection, the polarization state of the light is changed in a way which depends on the depth profile of the dielectric function of the sample. A complete description of the polarization state is obtained by rotating the analyzer continuously and sampling the intensity of the light incident on the detector at discrete points during the 360° rotation. For spectroscopic measurements, the wavelength is subsequently changed and the process is repeated.

In section 2.1 of this chapter, the use of spectroscopic ellipsometry as a characterization tool for depth-profiling the homogeneity of samples is discussed. Following that, description of the configuration and calibration of the ellipsometer utilized in these studies is given in section 2.2.

2.1 Depth Profiling of Sample Surfaces with an Ideal Rotating Analyzer Ellipsometer

The Jones matrix representation of an ellipsometer with ideal components in the polarizer-sample-analyzer configuration is

$$\begin{bmatrix} E_u \\ E_v \end{bmatrix} = \begin{bmatrix} 1 & 0 \\ 0 & 0 \end{bmatrix} \begin{bmatrix} \cos A & \sin A \\ -\sin A & \cos A \end{bmatrix} \begin{bmatrix} r_{par} & 0 \\ 0 & r_{perp} \end{bmatrix} \begin{bmatrix} \cos P & -\sin P \\ \sin P & \cos P \end{bmatrix} \begin{bmatrix} 1 \\ 0 \end{bmatrix} E_o$$

where P and A correspond to the angles made by the polarizer and the analyzer transmission axes with respect to the x-y reference frame of the sample, r_{par} and r_{perp} are the reflection coefficients for light polarized parallel and perpendicular to the plane of incidence, E_o is the initial electric field at the light source, and E_u and E_v are the electric field components in the analyzer reference frame. The complex ratio

$$\rho = \frac{r_{par}}{r_{perp}}$$

thus contains all of the information from the sample.

For a perfect interface between two isotropic materials, the reflection coefficients can be defined as

$$r_{par} = \frac{n_1 \cos \phi_0 - n_0 \cos \phi_1}{n_1 \cos \phi_0 + n_0 \cos \phi_1}$$

$$r_{perp} = \frac{n_0 \cos \phi_0 - n_1 \cos \phi_1}{n_0 \cos \phi_0 + n_1 \cos \phi_1}$$

where n_1 and ϕ_1 are the complex refractive index and refraction angle in the substrate and n_o and ϕ_o are the complex refractive index and incidence angle of the beam in the ambient. When, however, there are one or more intermediate layers separating the substrate from the ambient, reflections at each interface contribute to the net reflection coefficients. For the configuration shown in Fig. 2.1, the layer closest to the substrate can be regarded as a film of thickness $d_{x-1} = d_{film}$ separating the substrate from an "ambient" with the refractive index $n_{x-2} = n_{amb}$. For this portion of the system, the reflection coefficients are:

$$r_{par} = \frac{r_{1par} + r_{2par} e^{-2i\beta}}{1 + r_{1par} r_{2par} e^{-2i\beta}}$$

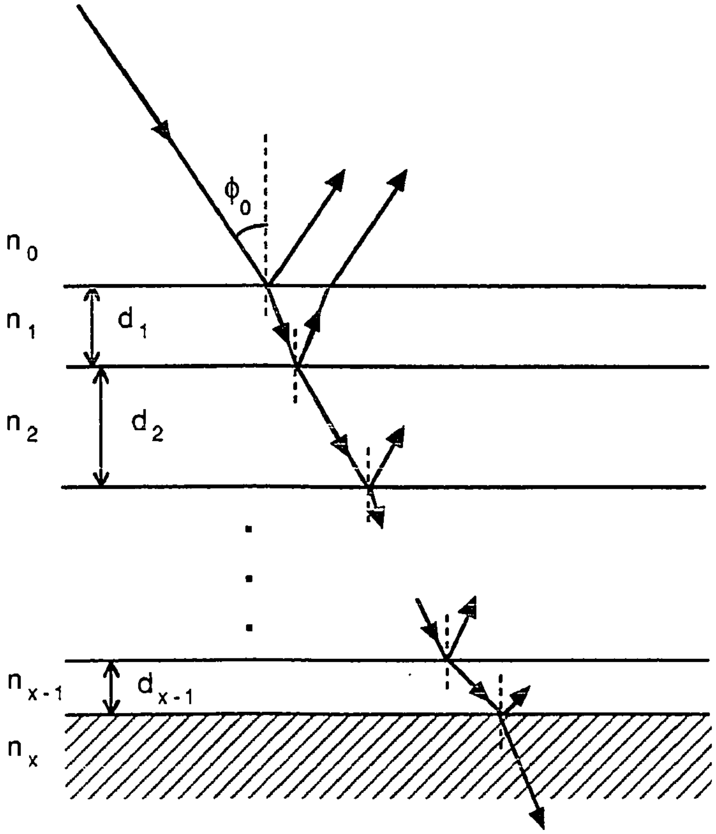

Fig. 2.1: Representation of a multilayer film configuration

$$r_{perp} = \frac{r_{1perp} + r_{2perp}\, e^{-2i\beta}}{1 + r_{1perp}\, r_{2perp}\, e^{-2i\beta}}$$

when all of the materials are isotropic. In this equation, the subscript "1" refers to reflection from the upper surface of the film, and "2" to the lower surface. β is defined as:

$$\beta = 2\pi \left(\frac{d_{film}}{\lambda}\right) \left(n_{film}^{2} - n_{amb}^{2} \sin \phi_{amb}\right)^{\frac{1}{2}}$$

where λ is the wavelength of the light in vacuum and ϕ_{amb} is the angle of incidence of the light on the final film. This can be calculated by applying Snell's law successively in each layer if the initial angle of incidence is known. Once the net reflection coefficients for the bottom film have been calculated, the process can be iterated to find r_{par} and r_{perp} for the next layer, using n_{x-3} as the refractive index of the "ambient" and n_{x-2} and d_{x-2} to describe the optical properties and thickness of the new film. In this case, the bottom film and the substrate can be treated as an "effective substrate" with the reflection coefficients calculated in the previous step. During the final calculation for the topmost film, the net reflection coefficients for the entire multilayer stack are calculated.

When one or more of the layers in the system is anisotropic, the situation becomes more complicated. Yeh has described a matrix method to handle this situation for non-magnetic materials which are not optically active (Yeh 1979). In his formalism, the electric field distribution within any layer is described as a sum of four partial waves. For layers stacked in the z direction, the electric field distribution in the n^{th} layer is described by:

$$E = \sum_{\sigma=1}^{4} A_{\sigma}(n)\, p_{\sigma}(n)\, e^{i\,[\alpha x + \beta y + \gamma_{\sigma}(n)(z - z_n) - \omega t]}$$

where $A_\sigma(n)$ is a column vector containing the four complex amplitudes, p_σ is the polarization of the waves, and the wave vectors are $k_\sigma = \alpha x + \beta y + \gamma_\sigma z$. The magnetic field distribution is given by

$$H = \sum_{\sigma=1}^{4} A_\sigma(n)\, q_\sigma(n)\, e^{i[\alpha x + \beta y + \gamma_\sigma(n)(z - z_n) - \omega t]}$$

where

$$q_\sigma(n) = \frac{c\, k_\sigma(n)}{\omega\mu}\, p_\sigma(n)$$

and ω is the light frequency, c is the speed of light in vacuum, and μ is the magnetic permeability. As for the isotropic case, the x and y components of the electric and magnetic field must be continuous at each interface. This is used to define a set of dynamical, D(n), propagation, P(n), and transfer matrices, $T_{n-1,n}$, which in turn are used to describe light propagation in a multilayer stack, via:

$$\begin{bmatrix} A_1(0) \\ A_2(0) \\ A_3(0) \\ A_4(0) \end{bmatrix} = T_{0,1}\, T_{1,2}\, T_{2,3} \cdots T_{N-1,N}\, T_{N,\mathrm{sub}} \begin{bmatrix} A_1(\mathrm{sub}) \\ A_2(\mathrm{sub}) \\ A_3(\mathrm{sub}) \\ A_4(\mathrm{sub}) \end{bmatrix}$$

Once these are defined, the ellipse of polarization describing the light reflected from the multilayer stack can be defined (Yeh 1980, Allara and Parikh 1989, Parikh and Allara 1992).

It is clear that for both anisotropic and isotropic multilayer films, it is not possible to invert the ellipsometric information directly to completely characterize the dielectric constant and thickness of each layer. Consequently, a modelling procedure is performed to fit calculated values of Δ and Ψ to the experimentally determined values. It is this modelling which permits depth profiling of complex samples. The modelling procedure is described more fully in Chapter 3.

2.2 PSU Ellipsometer: Alignment and Operation

All measurements described in this thesis were made on a rotating-analyzer spectroscopic ellipsometer built at The Pennsylvania State University (Mariner 1981, McMarr 1985). The basic configuration has been described elsewhere (McMarr 1985, Aspnes and Studna 1975) and was modified only slightly to facilitate alignment of the optics (see. Fig. 2.2). The pinhole used to define the beam prior to the sample had a 2mm diameter During operation, an IBM PS/2 model 30 computer was utilized to step the monochromator, change the filters, monitor the intensity as a function of analyzer angle, and convert the raw data to values for the ellipsometric angles Δ and Ψ. Both the analyzer rotation speed and the high voltage on the photomultiplier tube were controlled independently, the first by a crystal oscillator (which maintained a constant analyzer rotation speed of 33.5 Hz) and the second by an autonomous feedback circuit designed to adjust the voltage, and hence the detector sensitivity, according to measured values of the integrated signal strength. The latter permitted accurate measurements of low strength signals in comparatively short times.

Alignment of the system was accomplished by mounting a HeNe laser on the optical rails in place of the detector and tracing the light beam backwards to the source, centering components in the beam path. Final adjustments were made after remounting the photomultiplier tube by positioning mirrors to maximize the signal intensity and minimize the differences between signals for analyzer positions 180° apart (i.e. the difference between equivalent positions in the two optical cycles per mechanical cycle of the analyzer).

Once alignment was complete and calibration for non-idealities in the optics and detection system had been made (see section 2.2.1), the sample was inserted into the beam path and aligned by adjusting tilts corresponding to rotation around the x and y axes in the laboratory reference frame and translation in the z direction (Mariner

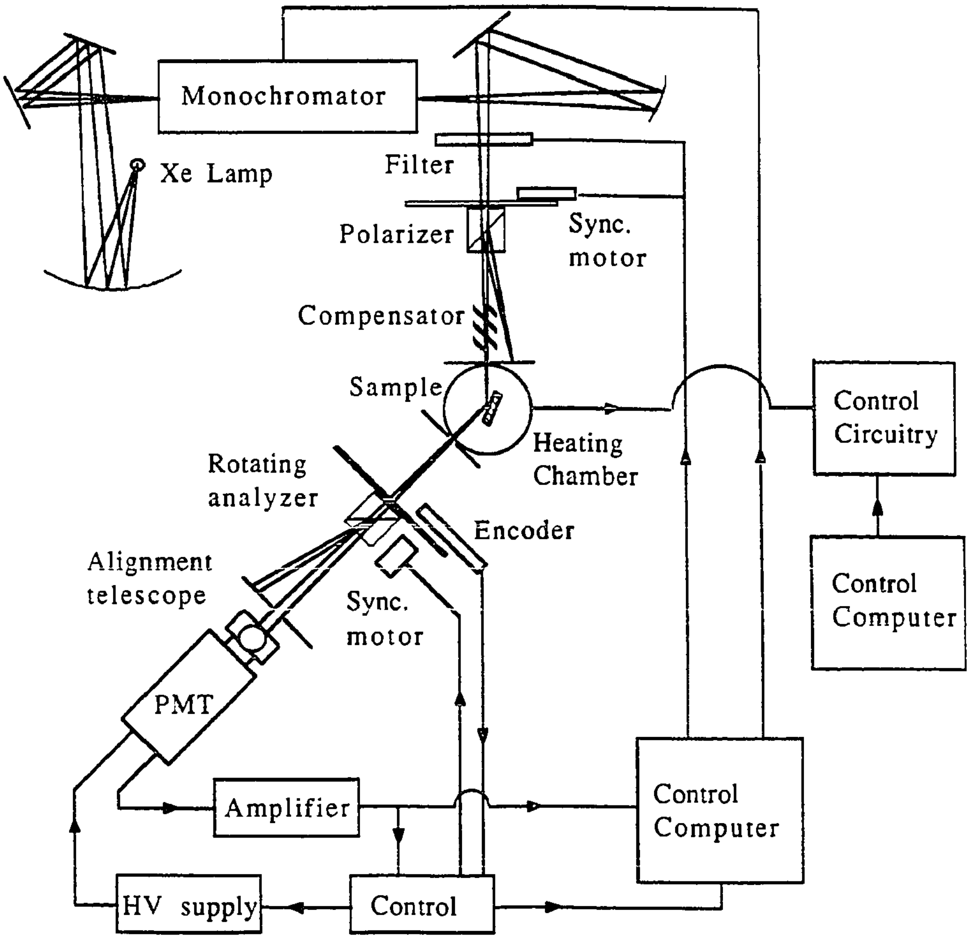

Fig. 2.2: Schematic of the rotating analyzer ellipsometer utilized in this work

1981). The reflected light intensity was then measured as a function of analyzer position at 90 positions during a 360° rotation. To minimize errors due to random intensity fluctuations, data from 100 to 250 turns of the analyzer were averaged prior to any mathematical manipulation of the data.

In terms of the measured polarizer and analyzer positions, P and A, the light detected at the photomultiplier can be described in Jones matrix algebra as:

$$\begin{bmatrix} E_u \\ E_v \end{bmatrix} = \begin{bmatrix} 1 & -i\gamma_A \\ 0 & 0 \end{bmatrix} \begin{bmatrix} \cos(A - A_s) & \sin(A - A_s) \\ -\sin(A - A_s) & \cos(A - A_s) \end{bmatrix} \begin{bmatrix} r_{par} & 0 \\ 0 & r_{perp} \end{bmatrix} \mathrm{X}$$

$$\begin{bmatrix} \cos(P - P_s) & -\sin(P - P_s) \\ \sin(P - P_s) & \cos(P - P_s) \end{bmatrix} \begin{bmatrix} 1 \\ i\gamma_P \end{bmatrix} E_o$$

when optical activity and misalignment of the polarizing components are included. Here, A_s is defined as the angle between the azimuth of the analyzer and the x axis in the sample (laboratory) reference frame when the measured angle A is zero. Similarly P_s is the calibration for the exact angular position of the polarizer with respect to the same reference for $P = 0$. γ_P and γ_A are the optical activity coefficients for the polarizer and analyzer. A_s, P_s, γ_P, and γ_A are characteristic of the system and can be determined from the calibration technique described in Section 2.2.1. Assuming these quantities are known, this leaves the electric vector of the light in the analyzer reference frame, $\begin{bmatrix} E_u \\ E_v \end{bmatrix}$, as a function of the Fresnel reflectivity coefficients of the sample r_{par} and r_{perp}. On squaring this expression, the intensity incident on the PMT, I, for a rotating-analyzer ellipsometer is shown to be given by

$$I = I_o\,(1 + \alpha \cos 2A(t) + \beta \cos 2A(t))$$

where A(t) is the time dependent analyzer position and I is a general description of elliptically polarized light. A Fourier transform of the intensity data yields α and β as the second order coefficients.

The ellipse characteristic of the reflected light can also be described in terms of the two mode parameters, Q and a, where

Q = the angle between the x axis and the longest dimension of the ellipse and

$$a = \frac{\text{semi - major axis}}{\text{semi - minor axis}}$$

(see Fig. 2.3). As described by Aspnes (Aspnes 1974) the two descriptions are related through

$$a = \frac{\pm\sqrt{1-\zeta^2}}{1+\zeta} \qquad \zeta = \eta\sqrt{\alpha^2+\beta^2}$$

$$Q = \frac{1}{2}\tan\frac{\beta}{\alpha} + \frac{\pi}{2}u(-\alpha)\,\mathrm{sgn}(\beta)$$

where $u(x) = 0$ for $x < 0$ and 1 for $x \geq 0$.

By convention the ellipsometric angles Δ and Ψ are defined from the complex reflectivity ratio, $\rho = r_{par}/r_{perp}$ as

$$\rho = \tan\Psi\, e^{i\Delta}$$

Since ρ can also be expressed as

$$\rho = \frac{[\cot(Q - A_s) - ia]\,[\tan(P - P_s) + i\gamma_P]}{[1 + ia\cot(Q - A_s)]\,[1 - i\gamma_P\tan(P - P_s)]}$$

it follows that

$$\tan\Delta = \frac{\rho_{imag}}{\rho_{real}} \qquad \tan\Psi = \sqrt{\rho_{real}^2 + \rho_{imag}^2}$$

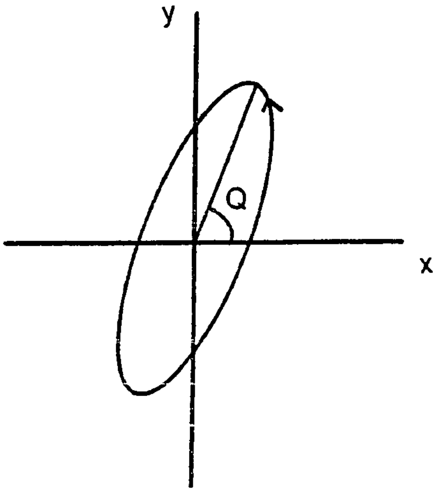

Fig. 2.3: The ellipse of polarization of the reflected light beam

2.2.1 Calibration For First Order Errors in the Optics

To determine values for the system constants A_s, P_s, γ_A, and γ_P (see section 2.2), the ellipsometer was calibrated following the procedure developed by Aspnes (Aspnes 1974). A highly reflecting gold sample was aligned at $\phi = 70°$ to give minimum values for the point and zone differences at the polarizer angle for measurement. With the analyzer spinning, the polarizer was then stepped at small increments over 6 - 10° ranges around "0°" and "90°."

A highly absorbing material like gold reflects incident linearly polarized light as linearly polarized light if the incident beam is either parallel or perpendicular to the plane of incidence. Moreover, the reflected beam should be 100% modulated, so that the minimum of the ac amplitude is equal to the dc background. For a system with optically active polarizers and analyzers (i.e. quartz Rochon prisms) the polarization rotation shifts the maximum modulation away from P_s to some nearby angle P_1. Since, however, P_1 is the minima in the residual $R(P) = 1 - \alpha^2 - \beta^2$, the true value for P_s can be calculated as

$$P_s = P_1 - \frac{\gamma_A \tan\Psi + \gamma_P \cos\Delta}{\sin\Delta}$$

Once P_1 is known, A_1 can be calculated from

$$A_1 = \frac{1}{2}\tan^{-1}\left(\frac{\beta}{\alpha}\right) \text{ at } P = P_1$$

and

$$A_s = A_1 - \frac{\gamma_P \cot\Psi + \gamma_A \cos\Delta}{\sin\Delta}$$

Using the data from P near 90°, A_s and P_s were calculated again as a check on the calibration and then the two values were averaged. Although γ_A and γ_P can also be determined from this calibration, they were always close to the theoretical value

$$\gamma = 0.0010 \left(\frac{h\nu}{eV}\right)$$

where eV is the energy of the radiation in electron volts. In general, the better the calibration, the closer that γ_A and γ_P approached the optical activity values calculated from the dispersion equation.

2.2.2 Calibration of the Detection System

In addition to the standard calibration for eliminating first order errors in the alignment of the optics, it was found that two additional steps were required to achieve accurate data for transparent samples. It should be noted that these additional procedures constitute a calibration of the polarization detection system, and as such are also sample independent.

2.2.2.1 Dark Current Correction

This comparatively simplistic correction was designed to minimize the importance of background light on the precision of the measured values for Δ and Ψ. With the beam from the monochromator blocked, the gain on the photomultiplier tube was manually adjusted to various PMT voltages between 700 and 1100V, and the signal detected was averaged over 50 mechanical cycles of the analyzer. (During a measurement the feedback loop would adjust the voltage between 600 and 1200 V). At room temperature, a measurable signal was detected for PMT voltages above ~700 - 800V (see Fig. 2.4) and with a high gain, the total dark current contribution to the signal could account for up to 30% of the observed minimum signal intensity as a function of analyzer angle in a straight through measurement. Not surprisingly, for transparent samples, where the minimum signal level is typically quite low, and the

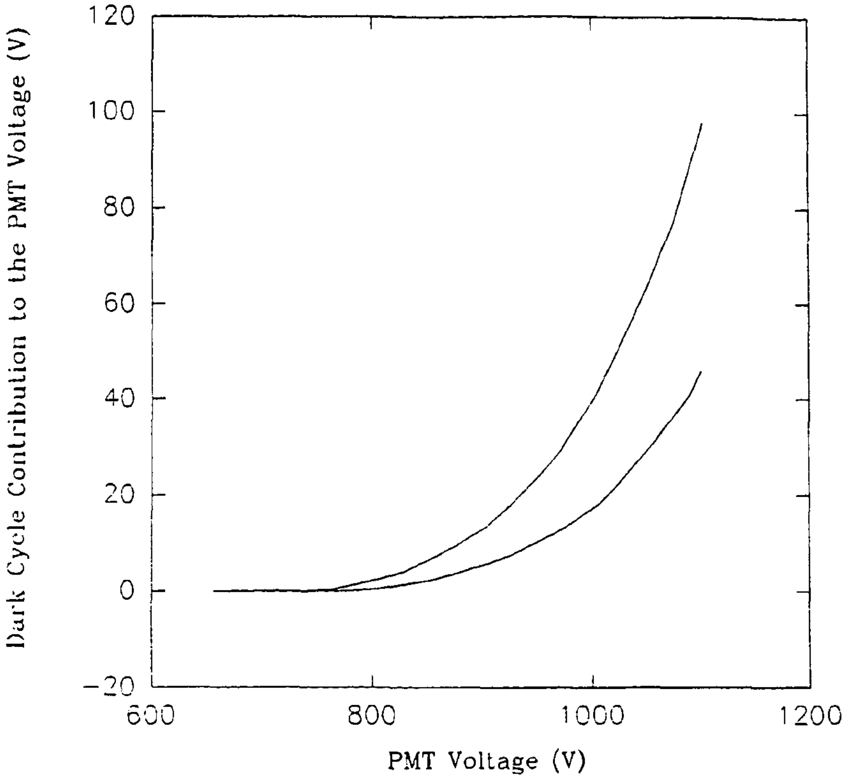

Fig. 2.4: Measurement of the dark current

low overall light intensity leads to high PMT voltages (~700 - 1200 V), the dark signal can result in considerable distortion of the ellipse describing the polarization state of the reflected beam.

Dark current correction became especially important during high temperature measurements, where glow from the furnace contributed to the ambient light levels. The photomultiplier became sensitive to this additional light at ~ 400°C, even before it could be detected by eye. Above this temperature, the dark current increased dramatically with further temperature rises, until at ~ 550°C the cherry glow of the furnace made alignment very difficult.

To minimize this source of error, the dark current was measured before all experimental data runs by blocking the incident beam and detecting the signal at different PMT sensitivities. This data was then fit to a fifth order polynomial as a function of PMT voltage. During the run, the dark cycle contribution to the signal could then be calculated and subtracted from all of the raw data. For the most accurate spectra, the time between dark current measurement and data collection was minimized, as the observed dark current was a sensitive function of both the room temperature and the amount of time that high voltage had been applied to the photomultiplier tube / amplifier system.

2.2.2.2 η Correction

As discussed in section 2.2, the measured intensity of light contains both dc and ac components with respect to the analyzer angle A. While in an ideal detection system, the static and dynamic intensity levels are detected with the same sensitivity, more generally, I must be expressed as:

$$I = I_o (1 + \eta\alpha \cos 2A + \eta\beta \sin 2A)$$

(Aspnes and Studna 1975) where η relates to the difference in gain for the dc and ac signals and is generally not equal to unity.

In order to measure η, the detector arm of the ellipsometer was rotated to the straight-through position and a neutral density filter was inserted into the beam before the polarizer. α and β were determined in the ordinary fashion and then η was calculated at a given PMT voltage as:

$$\eta = \frac{1}{\sqrt{\alpha^2 + \beta^2}}$$

The neutral density filter was then rotated to absorb/reflect a different proportion of the incident beam, allowing η to be calculated at different PMT voltages.

Uncorrected for the dark current, η curves upward sharply as the signal intensity drops (Fig. 2.5). When, however, the dark cycle contribution is subtracted from the raw intensities, η was found to be a linear function of the PMT voltage (Fig. 2.6). Although the value of η was found to drift somewhat (up to 0.001) with the length of time high voltage had been applied to the detector, the slope remained approximately constant. Such variations in η were calculated to produce changes in Ψ of ~.05° for vitreous silica. For materials with a higher refractive index (and consequently higher reflectivities) the error due to this source was much smaller, on the order of 0.015° in Ψ for $BaTiO_3$.

It is important to note that both these corrections are sample-independent, being determined from measurements made in the PA configuration. As a test of the utility and necessity of the corrections, a vitreous silica sample was inserted into the beam path, and Δ and Ψ were measured. Fig. 2.7 shows the comparison between this data and Ψ calculated from a set of reference oscillators for glassy SiO_2 (Malitson 1965). Over the whole wavelength range, Ψ was within ± 0.01°, leading to an accuracy in the refractive index derived from the experimental data of ± 0.001. For contrast, uncorrected data taken on the same sample is also shown.

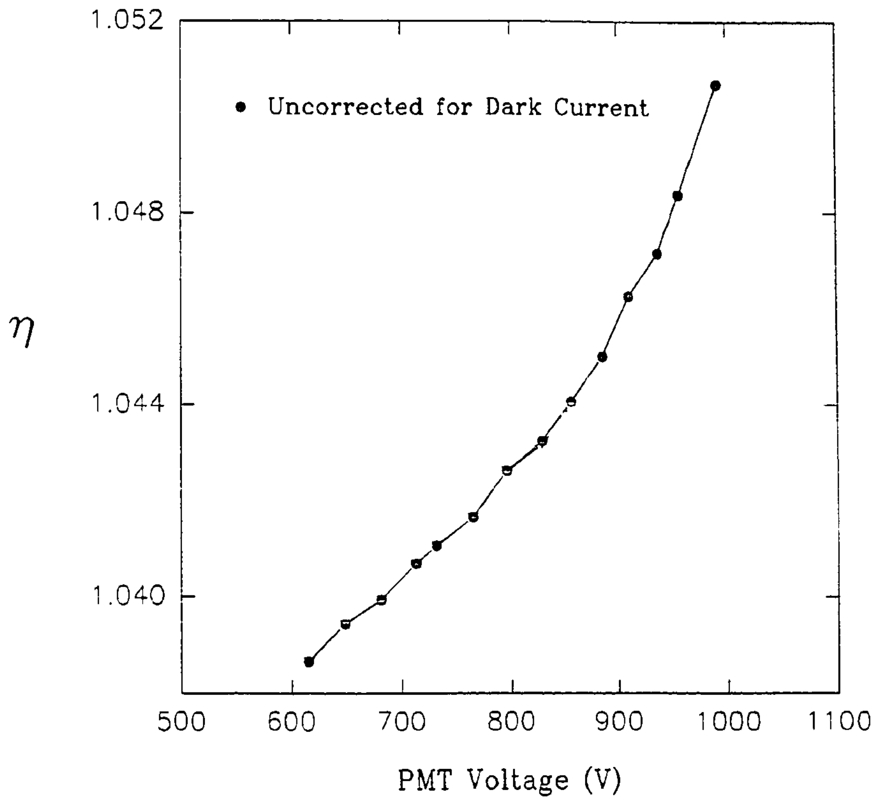

Fig. 2.5: The η parameter measured without dark cycle correction

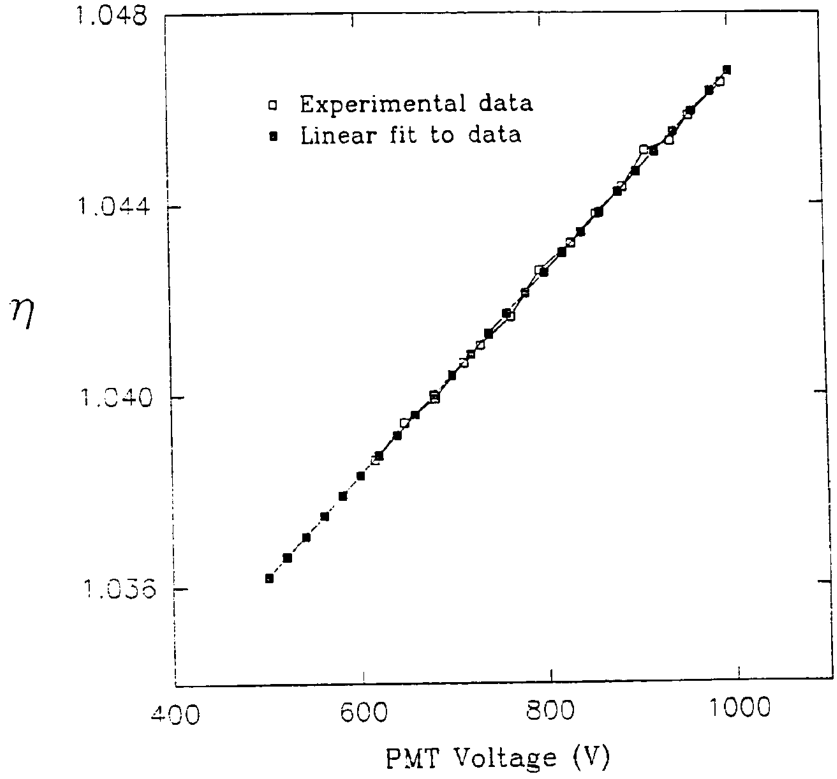

Fig. 2.6: η corrected for the dark current

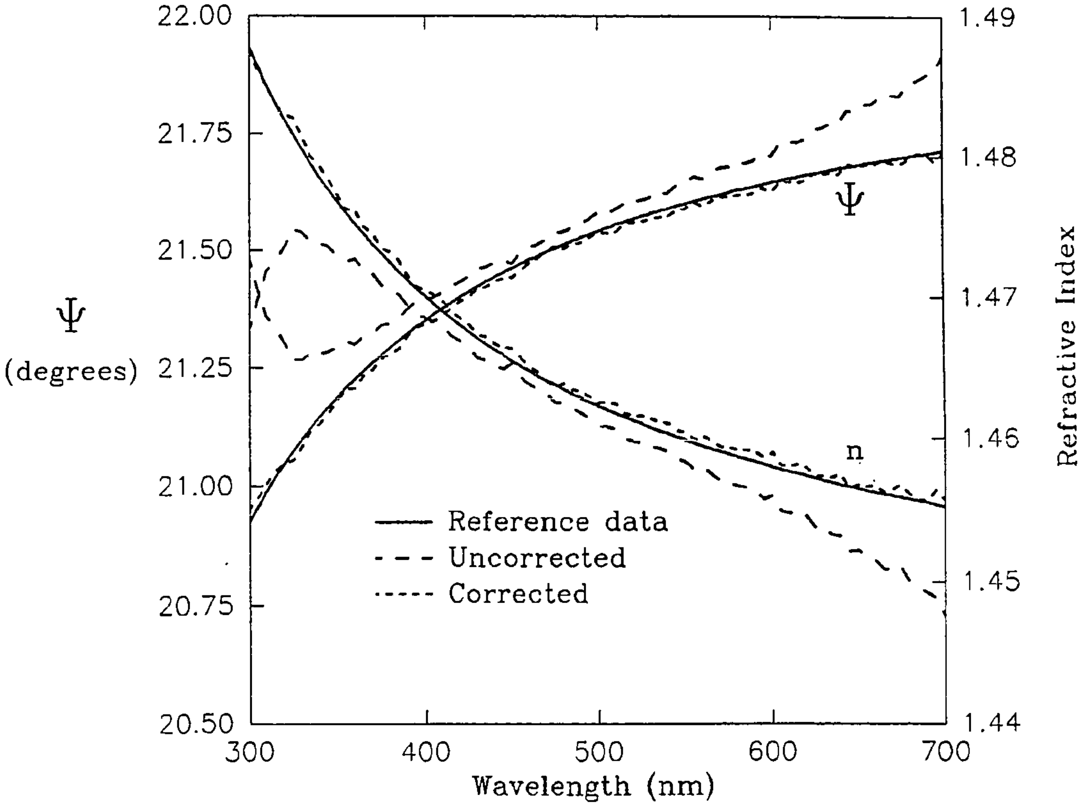

Fig. 2.7: Comparison between reference and experimental values for Ψ and n of a vitreous silica sample

2.2.2.3 Effective Source Calibration of the Achromatic Compensator

Despite this accuracy in Ψ, there is a large inherent inaccuracy in Δ when Δ approaches 0° or 180°, as it does for transparent film/transparent substrate systems (Chindaudom 1991). To artificially induce a Δ near 90°, where the system accuracy is considerably higher, a compensator was added to the standard ellipsometric configuration. The three-reflection quarter wave plate described by King and Downs (King and Downs 1969) acts as a nearly achromatic compensator throughout the wavelength range 300 - 800 nm, and so was used in all spectroscopic measurements. To correct for the remaining wavelength dependent errors introduced by the compensator, a two-measurement, effective source calibration was utilized. The ellipsometer detection arm was first swung into the straight-through position and Δ and Ψ were measured over the entire spectral range of interest in the polarizer - compensator - analyzer configuration. This allows a complete description of the polarization of the light striking the sample surface at every wavelength. Then, the sample was inserted in the beam path, aligned at the desired angle of incidence, and measured over the same wavelength range to obtain a spectrum containing lumped information on the sample properties and the source polarization. The change in the light polarization due to reflection from the sample itself, the quantity of interest, could then be calculated from:

$$\tilde{\rho} = \frac{\tilde{r}_p}{\tilde{r}_s} = \frac{\dfrac{E_{2p}}{E_{1p}}}{\dfrac{E_{2s}}{E_{1s}}} = \frac{\tan\Psi_2}{\tan\Psi_1} e^{i(\Delta_2-\Delta_1)}$$

$$= \frac{(\cot Q_2 - i\, a_2)(1 + i\, a_2 \cot Q_2)}{(1 + i\, a_2 \cot Q_2)(\cot Q_2 - i\, a_2)}$$

where ρ is the complex reflectivity ratio. The subscript 1 signifies the straight-through measurement and 2 the measured reflection from the sample.

It is important to note that since both experimental measurements are performed with Δ near 90°, where the ellipsometric data is very accurate, the derived value of Δ for the sample also possesses high accuracy. As discussed by Chindaudom (Chindaudom 1991), exact determination of the system accuracy in Δ is not possible due to the lack of a perfect sample. However, examination of the rms deviation between calculated and experimental Δ values for a vitreous silica sample led to an estimated accuracy of 0.03° for transparent materials. This is equivalent to the accuracy claimed by other workers for measurements on opaque samples where Δ is above 15°. Moreover, the effective source correction did apparently eliminate all of the wavelength dependent errors in Δ for Δ near either 0 or 180°.

A second attractive feature of this method is that it permits a complete effective calibration for the compensator over the entire spectral range in 20 minutes, a significant improvement over other techniques in which time-consuming calibrations are required at each wavelength of interest.

2.3 Furnaces for the Ellipsometer

2.3.1 Low Temperature Windowless Heating Chamber

In order to probe the behavior of the surface layer of $BaTiO_3$ as a function of the bulk polarization, a windowless sample chamber capable of maintaining temperatures between 20 and 200° C was designed for the ellipsometer. As shown in Fig. 2.8, the temperature is controlled by circulating heated oil through a coil of copper tubing around the sample. This heating source was chosen for its temperature stability; the oil temperature itself had a large thermal mass, and so provided a stable radiative heat source suitable for heating large single crystals which could not be exposed to rapid temperature fluctuations.

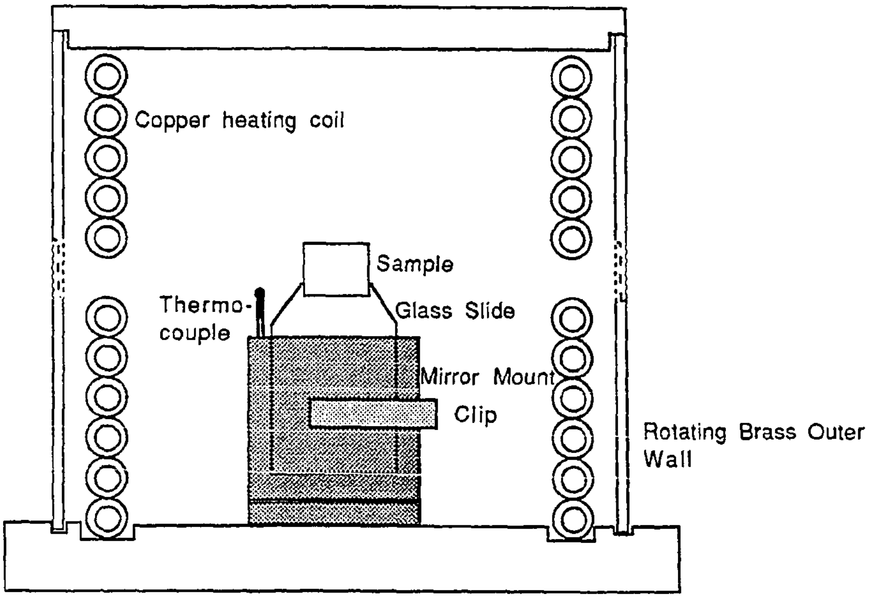

Fig. 2.8: Heating chamber based on circulating hot oil, and sample mount

The outer shell of the chamber consisted of two slotted brass cylinders which could be rotated with respect to one another. Each was milled with a wide and a narrow slot. When the large opening in one was superimposed over the small gap in the other (and vice versa) two windowless 1/4" x 1/2" slots were obtained for incidence angles between 55 and 80°. By minimizing the size of the holes in the outer shell in this manner, the temperature was stable to ±0.2°C over the course of a data collection cycle. It is also important to note that as the chamber is windowless, no additional corrections for the ellipsometer optics were required.

In order to control the chamber temperature and heating rates, the existing control circuit on the Tamson oil bath (Neslab Instruments) was modified to permit an Apple II computer to override the on/off signals to the quartz heater. As shown in Fig. 2.9, a Fluke digital thermometer was used to continuously read the temperature of a thermocouple placed within half an inch of the sample. At one second intervals, the temperature reading was passed to the computer via an Adalab digital interface card (Interactive Microscience Inc.), and a running average was performed for the previous 20 readings. This average was compared to the setpoint, and a decision on whether or not to power the oil bath heater was made. The contact thermometer on the oil bath was left intact to act as a failsafe against overheating. Ramps were controlled by updating the setpoint every 20 seconds according to the desired heating or cooling rate. In this way, stable heating rates between 0.1°C/min and 2°C/min could be attained. With Dow Corning 550 fluid (a silicone oil) the working temperature range for this heater was 21 to 200°C.

2.3.2 High Temperature Furnace

In order to extend the temperature range accessible on the ellipsometer, a second electrical resistance furnace was built. As shown in Fig. 2.10, a kanthal-wire wrapped

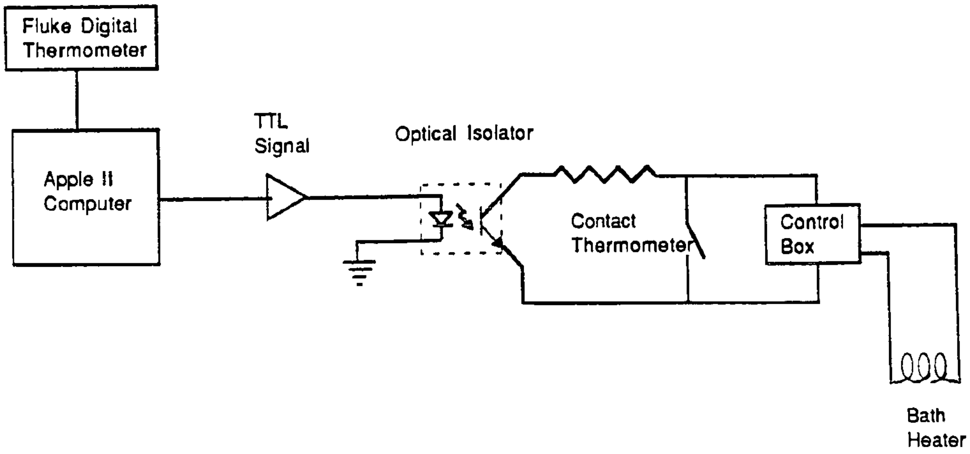

Fig. 2.9: Control circuit for the oil bath

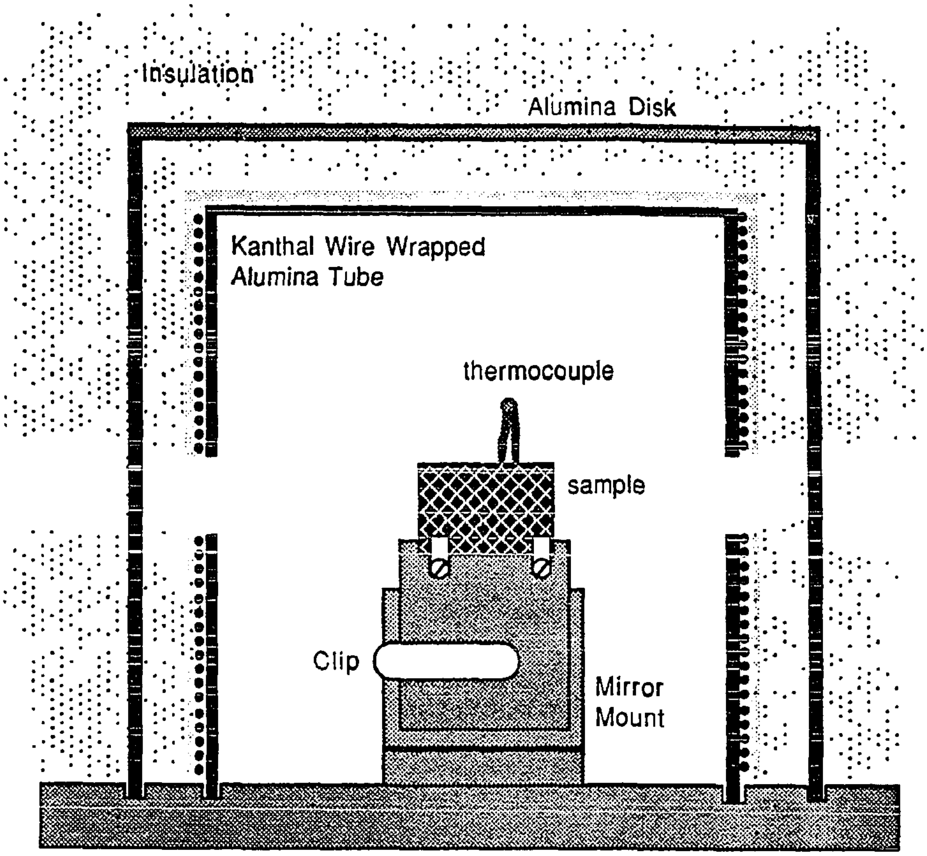

Fig. 2.10: Electrical resistance furnace and sample mount

alumina tube was used as the heat source. This was powered by TTL logic-triggered, on-off signals from a solid state relay (Omega Inc. 25 amp dc solid state relay) as shown in Figure 2.11. Again, the Apple computer was used to control the setpoint to allow both controlled ramp rates and constant temperature soaks. The total power dissipated through the furnace was limited by a variac set between 10 and 50 V, which passed a current between one and five amperes through the kanthal wire. Temperatures between 25 and 700°C could be achieved easily under these conditions, where the upper limit was controlled by melting of the aluminum mirror mount. However, a practical upper limit for in situ ellipsometric measurements was 500°C, where glow from the furnace significantly decreased the signal/noise ratio. Typically, with this furnace temperatures could be maintained within ± 2 °C of the setpoint and ramps between one and 10°C/min could be achieved.

In order to prevent warping of the rotating outer shells used for the low temperature heating chamber at extreme temperatures, two monolithic outer cylinders were machined for fixed incidence angles of 70 and 80°. Both these brass cylinders and the baseplate were subsequently electroplated with nickel to minimize oxidation of the copper and vaporization of the zinc at elevated temperatures. Then the inner and outer shells were insulated with zircar felt, and the outside insulation was reinforced by thick fiberfrax insulation. In this way, the total heat lost to the surroundings was quite small, and none of the ellipsometer components were heat damaged.

To insure that changing the temperature of the chamber did not affect the quality of the ellipsometric data, a sapphire plate with one side polished was aligned in the ellipsometer, and measurements were made at an incidence angle of 80° every 100°C up to 400°C. Without changing the sample position the chamber was then heated to 500°C, held for 0.5 hours and cooled to 350°C for measurement, to eliminate errors from furnace glow. This was repeated for 600°C. Prior to each measurement, the sample was realigned to counteract drift in the sample holder position with temperature. As shown

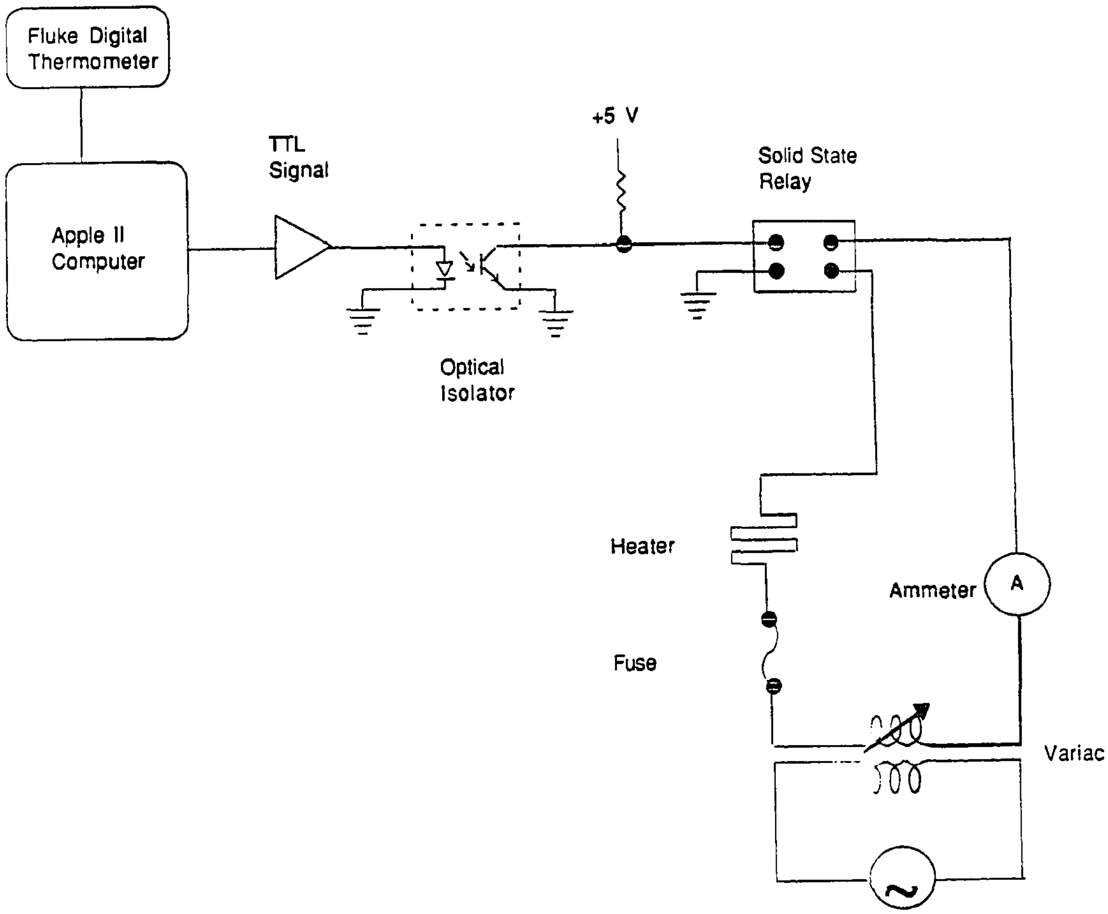

Fig. 2.11: Control circuit for the electrical resistance furnace

in Figure 2.12, Δ and Ψ do not change appreciably over the entire temperature range. Data for 400°C are not shown as an incomplete correction for the dark current resulted in high Δ values. Excluding the 400°C spectra, the maximum deviations for Δ and Ψ values between runs are ±0.10° and ±0.03° respectively. The standard deviation of the data from the average values for $\Delta(\lambda)$ and $\Psi(\lambda)$ are considerably lower, being 0.025° and 0.013°, respectively. Although the maximum errors are larger than the stated errors at room temperature (see sections 2.2.2.2 and 2.2.2.3), the additional error can be attributed to changes in the tilt around the horizontal axis of the sample with changes in temperature. It should be possible to eliminate the variations in Δ and Ψ with temperature by adding a slot to the furnace so that an alignment laser could be utilized at higher temperatures.

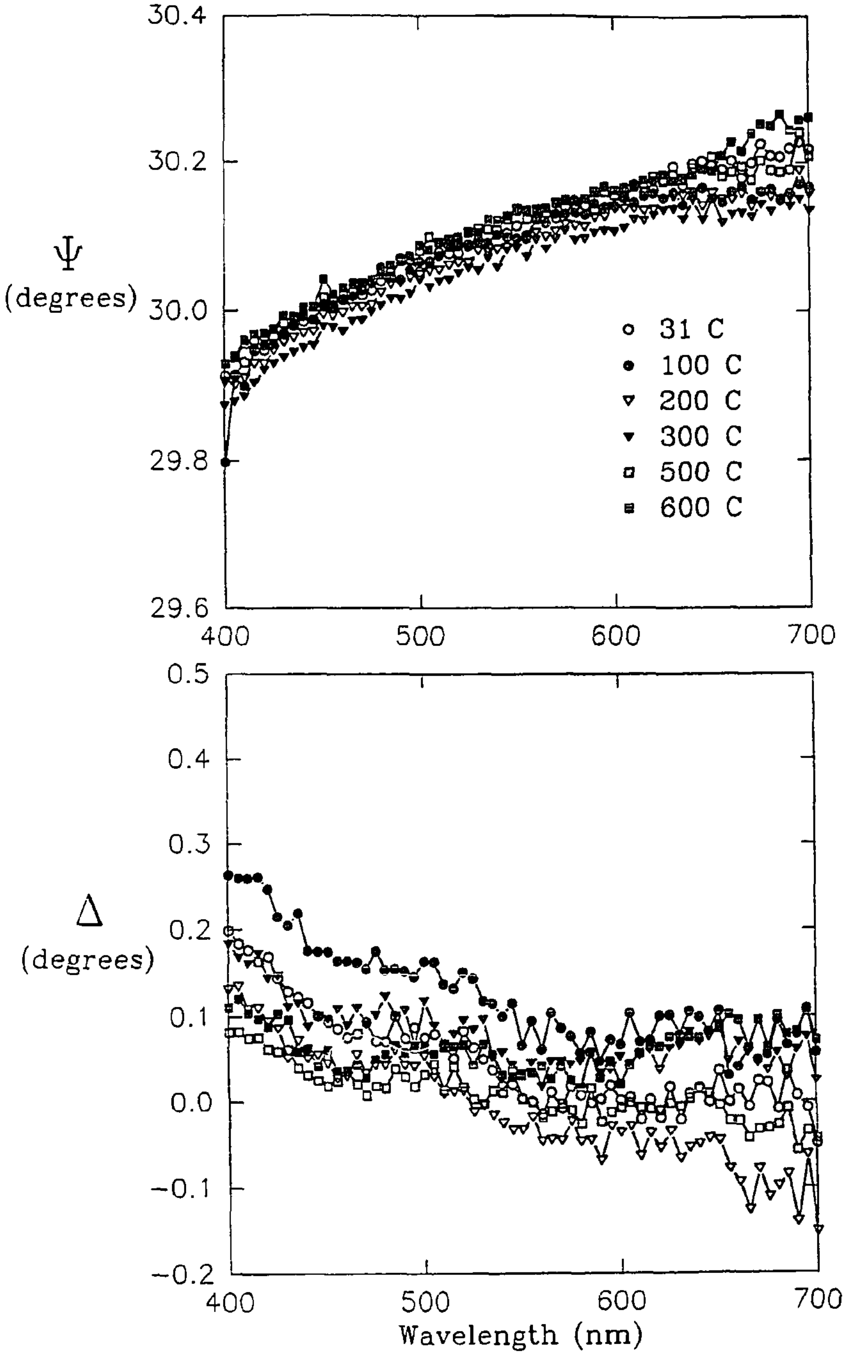

Fig. 2.12: Δ and Ψ of a sapphire wafer as a function of temperature

CHAPTER 3

EXPERIMENTAL PROCEDURE

3.1 Single Crystal Preparation

Because all of the samples investigated in this thesis were transparent throughout the visible spectrum, the penetration depth for incident light is effectively infinite. Typically in an ellipsometric measurement it is assumed that all of the light is absorbed in some finite (and small) depth in the material. However, with transparent materials, if the front and back faces of the sample are both parallel and non-absorbing, light reflected from the back surface and retransmitted through the front (see Fig. 3.1) will be added to the desired reflection from the front surface. Because it is impossible to separate the two contributions after the fact, this leads to tremendous distortions in observed values for Δ and Ψ. For example, data taken on a virgin soda-lime-silica cover slip showed that reflections from the back face led to errors in Δ and Ψ of ~11° and 2.2° respectively in the transparent region. Only below 300 nm, where the intrinsic absorption of the glass prevented light from reaching the back surface, did Ψ approach the value expected for that composition.

As these errors are larger than the deviations expected from the presence of surface layers on single crystal ferroelectrics it was imperative to remove them. For thick single crystal samples this was done by wedging the back face during polishing to induce non-parallelism. This in turn physically separates the two reflections by 2 - 10 mm at the diaphragm for wedge angles of 1 - 6°.

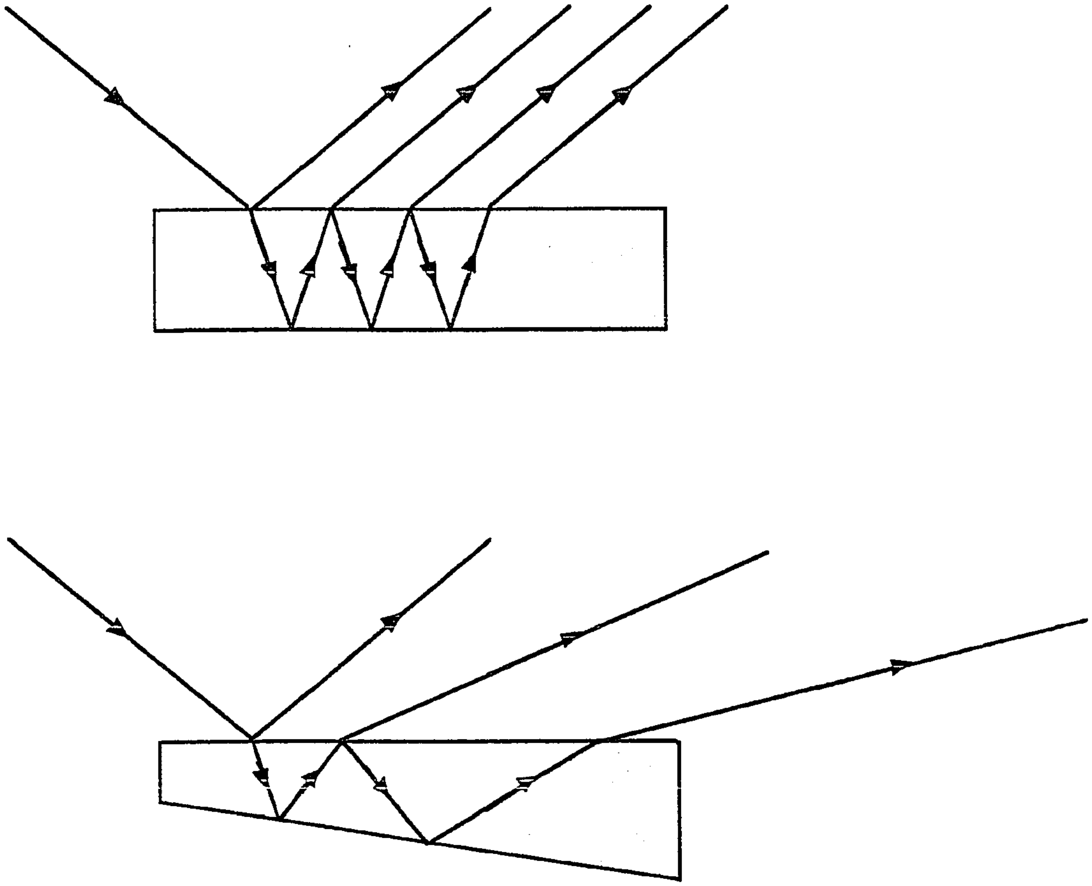

Fig. 3.1: Interference between light rays reflected from the front and back surfaces of a transparent material

3.1.1 $BaTiO_3$

A single crystal of $BaTiO_3$ (1 cm x 1 cm x 2mm) was obtained from Sanders Incorporated (Nashua, New Hampshire). These crystals are grown by the top-seeded solution technique from a TiO_2 rich melt. Previous measurements have demonstrated that such crystals incorporate significantly lower impurity levels than do Remeika butterfly twins (typically in the ppm range rather than at a 1 - 2% level). Excellent dielectric and optical data have been reported by Camlibel et al. (1970) and Wemple et al. (Wemple 1970, Wemple et al. 1968).

After orienting with a Laue X-ray camera, one large face was rough polished so that the surface normal was within 0.5° of <001> family of axes. The optic axes in different twins were then aligned by electroding and poling the sample under an electric field of 3 - 5 kV/cm for periods ranging from 15 minutes to several hours. Elimination of the 90° twins was confirmed with conoscopic imaging under a polarizing microscope. Prior to measurement the sample was cleaned thoroughly with acetone to remove organic contamination. It was then mounted on the ellipsometer, aligned, and cleaned repeatedly until the values of Δ and Ψ had stabilized.

Since this thesis hinges on the relation between surface layers and processing, more specific descriptions of individual surface preparations are detailed in the following sections.

3.1.2 Polishing

Because $BaTiO_3$ has no convenient cleavage plane perpendicular to the optic axis, it was necessary to polish a smooth, well-oriented face before any subsequent processing could be done. The polishing schedule detailed in Table 3.1 was designed so that each step removed a layer thickness 3-5 times the diameter of the previous abrasive. This, in

Table 3.1: Polishing procedure for the $BaTiO_3$ crystal

Grit	Time	Substrate
9µm Al_2O_3	until flat	glass
5µm Al_2O_3	30 min	glass
3µm Al_2O_3	30 min	glass
1µm diamond	45 min	paper on rotating brass wheel
0.25µm diamond	45 min	paper on rotating brass wheel
0.05µm γ- Al_2O_3	30 min	nylon on rotating glass plate

turn, should insure that the final surface quality was the product of only the previous step rather than the accumulation of damage generated throughout the entire polishing cycle. As the resultant depth of mechanically - induced damage or amorphization scales with both the minimum grit size utilized (Struers) (see Fig. 3.2) and the abrasive hardness, the final polishing was done with a soft 0.05μm γ-Al_2O_3. Kerosene was used as the lubricant to avoid leaching of the surface barium on exposure to water (Utech 1990). In order to separate the reflections from the two faces as discussed in section 3.1 the reverse side was subsequently polished at a slight angle to the first face.

3.1.3 Sputtering

In order to remove any organic contamination remanent from the polishing, the crystal was subsequently sputtered with low energy Ar ions in an oxygen ambient. Sputtering conditions are given in Table 3.2.

Table 3.2: Ion beam sputtering conditions

Sputtering voltage:	60 V
Sputtering time:	45 min
Sputtering pressure:	4 x 10^{-4} torr
Ar ions passed through gun:	5 standard cc/min
Oxygen flow through chamber:	5 standard cc/min

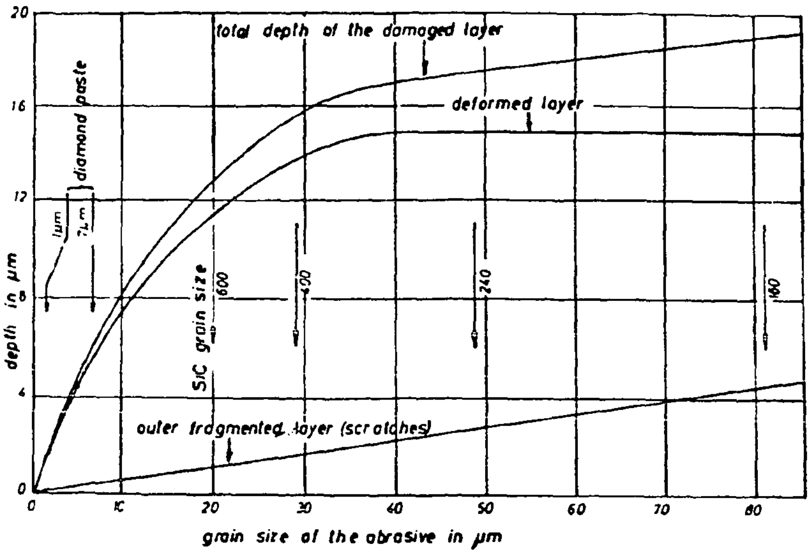

Fig. 3.2: Polishing damage depth as a function of grit size

3.1.4 Chemical Etching

Although chemical etching is frequently regarded as a comparatively non-destructive surface preparation technique for ferroelectrics (particularly useful in stripping off damaged layers attributed to lapping and grinding [Jyomura et al. 1980]), very little work has been done to insure that in fact these etchants dissolve $BaTiO_3$ stoichiometrically. Incongruent dissolution is observed in many multicomponent oxides, including many glass compositions (Paul 1977, Doremus1985) and the 123 superconductor (Bansal and Sankuhl 1988, Frase et al. 1987). This is expected to be particularly marked in the titanium based perovskites as while alkaline earth cations are easily complexed and dissolved, TiO_2 is exceptionally stable in aqueous solution, dissolving only at very low or very high pH values (Baes and Mesmer 1976, Utech 1990). The tendency towards leaching of Ba from $BaTiO_3$ has been confirmed by Utech (Utech 1990) and was shown to be particularly marked under acidic conditions.

In an effort to move away from aqueous acid-base chemistry, Br_2 in methanol, a standard etchant used in the preparation of smooth surfaces in the semiconductor industry (Aspnes and Studna 1981) was investigated at dilutions ranging from 0.05 to 50 volume % bromine. (Note that above concentrations of 10%, bromine - solvent mixtures are known to be explosive if stored in a tightly capped container: caution should be utilized in their handling [Bretherick 1986]). However, no appreciable mass loss was observed at any concentration. Similarly, acids diluted in organic solvents either left the surface completely untouched, or in the case of HF : methanol, left a cloudy film which probably corresponded to the redeposition of $BaCO_3$ on exposure of the leached Ba to atmospheric water and CO_2 (Utech 1990, Bansal and Sandkuhl 1988).

Because the primary difficulty in the dissolution was the inability to form a soluble titanium complex, several strong complexing agents were investigated. $EDTA^{4-}$ is known to be a very strong complexing agent (Bailar et al. 1984) and it has been shown to etch PZT 5A ceramics. However, when a 1 Molar solution of ethylene diamine tetraacetic acid (EDTA) in KOH : water (pH = 9.5) was used to etch $BaTiO_3$ single crystals, mass loss was detected only on irregularly-shaped specimens, not on (001) polished samples. Thus, while not particularly useful in the present study, EDTA solutions may eventually have some interest as anisotropic etches for Ti-based perovskites.

The etchant finally chosen to dissolve the surfaces of $BaTiO_3$ single crystals was a 1:1:3 mixture of hydrochloric acid, hydrogen peroxide, and deionized water. Addition of H_2O_2 to the etchant promoted the formation of a water-soluble titanium-peroxide complex which significantly enhanced the rate of Ti removal. Although the precise species formed is unknown, a progressive yellowing of the supernatant suggests that that it is one of the colored 1:1 Ti:peroxy complexes reported previously for acidic solutions (Fox et al. 1990). DC plasma emission spectroscopy was used to assay the barium and titanium concentrations in the leachate and confirm dissolution of the titanium. It was found that in spite of the soluble titanium complex, barium was still leached preferentially from the crystal. Ba:Ti ratios of 2.65 : 1 were typical. The resulting surfaces were smooth for etching times under 15 minutes and did not have the cloudy surface characteristic of redeposited $BaCO_3$. This last may also be due to the presence of peroxide, as H_2O_2 has been shown in other studies to suppress the formation of carbonate phases in aqueous solutions (Fox et al. 1990).

3.1.5 Laser Ablation

Laser ablation was investigated as a surface preparation technique because it should provide an uncontaminated, near equilibrium surface which would be ideal for studies on the intrinsic properties of a polar surface. Prior to the ablation, the crystal was repolished to eliminate the surface roughness introduced during chemical etching.

Then, ten to twenty pulses from a krypton fluoride excimer laser (Lambda Physics EMG 150) with a beam density between 70 and 235 mJ/cm^2 were focused onto the sample. In all cases this left the crystal surface bluish - colored, probably as a result of reducing the titanium to the 3^+ state (Weyl and Marboe 1967). Further attempts to lower the beam density and prevent dissociation on the surface were not successful.

3.2 Thin Film Samples

In order to investigate the importance of surface effects on relatively pristine samples, ferroelectric thin films were obtained from a number of sources. Data on the deposition conditions, film and substrate composition and polarization orientation are given for each sample in Table 3.3. More complete descriptions are given in Chapter 5 for individual samples.

As the transparent substrates used in this thesis were usually less then 0.5 mm thick, it was not possible to wedge the back to physically separate reflections from the two major surfaces of the substrate. Hence, whenever possible, the back of the substrate was roughened and painted with a flat black paint to artificially absorb light which reached the back face. In some of the higher temperature measurements, however, paint could not be used, as the organic component burned out and contaminated the sample. For those measurements only samples which gave the same Δ and Ψ readings with and without painting the back surface were utilized.

3.3 SIMS Data

All SIMS data were collected by Vincent Bojan with a Cameca IMS - 3F Secondary Ion Mass Spectrometer using the experimental conditions listed in Table 3.4. In order to obtain sufficient sensitivity to all of the elements of interest, it was necessary to gold-

Table 3.3: Summary of the thin film preparation conditions.

Sample	**Preparation**	**Source**
(111) PLT on (0001) Sapphire	rf - planar magnetron sputtered from a $Pb_{0.8}La_{0.2}Ti_{0.93}O_3$ target at a substrate temperature of 580°C. Input rf power of 200W for a target 100mm in diameter. Final composition near $Pb_{0.8}La_{0.2}Ti_{0.95}O_3$.	Hideaki Adachi, Matsushita Electric Industrial Co., Ltd. Central Research Laboratories Moriguchi, Osaka 570, JAPAN
(001) $PbTiO_3$ on (100) $SrTiO_3$	Prepared by sol-gel from alkoxide precursors. Annealed at 700°C for 4 hours.	Keiko Kushida, Materials Research Laboratory, the Pennsylvania State University
<101> PZT on $(1\bar{1}02)$ Sapphire <101> PZT on (0001) Sapphire Polycrystalline PZT on Pt-coated Si	Multi-ion-beam reactively sputtered $PbZr_{0.5}Ti_{0.5}O_3$. Substrate temperature = 100°C, post-deposition anneal at 650°C for 2 hr.	Hongxing Hu, Materials Research Laboratory
As-deposited PZT on Pt-coated Si and Sapphire substrates	Multi-ion-beam reactively sputtered $PbZr_{0.5}Ti_{0.5}O_3$. Substrate temperature ~ 100°C.	Hongxing Hu, Materials Research Laboratory, the Pennsylvania State University.
As-deposited sol-gel PZT on Sapphire	Spin-coated $PbZr_{0.5}Ti_{0.5}O_3$. Heated to 400°C after each coating.	Jiayu Chen, Materials Research Laboratory, the Pennsylvania State University
As-deposited sol-gel PZT on Pt-coated silicon	Spin-coated $PbZr_{0.5}Ti_{0.5}O_3$. Heated to 200°C - 400°C after each coating.	Jiayu Chen and K.R. Udayakumar, Materials Research Laboratory, the Pennsylvania State University

Table 3.4: Operating conditions for the Cameca IMS - 3F SIMS system.

Primary Current:	50 nA $^{18}O^-$
Primary Beam Diameter:	~ 100 μm
Raster:	250 μm
Primary Accelerating Voltage:	-12.5 kV - 5 kV
Sample Bias:	+ 4.5 kV
Contrast Aperture:	150 μm
Imaged Field:	150 μm

All slits wide open

Shroud cooled with liquid nitrogen

coat the crystal to prevent charging of the insulating surface under bombardment with the $^{18}O^-$ probe ions. Knock-in, a process where the primary beam propels surface material deeper into the sample, was found to be a problem at an accelerating voltage of -12.5 kV, so measurements were repeated at -5kV.

3.4 Computer Modeling of Data

Although direct inversion of ellipsometric data to calculate optical properties can be used in a limited number of instances, in general if the refractive index of the film and substrate are similar, direct inversion leads to the incorporation of tremendous errors (Gustin 1987). Rather than using that approach, then, modeling to fit the data was done by postulating a geometry for the specimen described by a small number of parameters representing, for example, the refractive index and its dispersion, the thickness of any layers present, the volume fraction of second phase in any layer, the decay length of the polarization, or the concentration of free carriers present. In each case it was assumed that the sample could be subdivided into a number of planar layers, where within any plane the optical properties were homogeneous. It is important to remember that in an ellipsometric measurement, the initially circularly light beam strikes the sample obliquely, and is elongated in one dimension. Thus, with the PSU spectroscopic ellipsometer used in this thesis, for angles of incidence between 55° and 80°, the actual specimen area sampled ranges from 2mm x ~5mm to 2mm x ~1cm. All of the modelling results represent values averaged over the entire sampled area.

The program used to model ellipsometric data on isotropic materials was developed by Dr. Vedam's research group at the Materials Research Laboratory. In outline, the program consists of a search over parameter space for the values which lead to the best approximation of experimental Δ and Ψ data. Following an initial grid search to obtain reasonable starting values for each parameter, final optimization for the parameters was performed using a commercial nonlinear least squares routine. The Levenberg-Marquadt algorithm ZXSSQ from the International Machine Subroutine Library outputs both the best-fit values for all of the parameters in the model and an approximation of the Jacobian for the system. This is subsequently used to calculate the 90% confidence limits for each variable.

For most cases, including all of the thin films analyzed in this thesis, the best values for the parameters in any given model were determined by minimizing

$$\sum_{i}^{m} \{(\tan \Psi_{exp} - \tan \Psi_{calc})_i^2 + (\cos \Delta_{exp} - \cos \Delta_{calc})_i^2\}$$

for all m data points at one temperature. Here, the subscripts "exp" and "calc" refer to the experimental and calculated values of the ellipsometric parameters, respectively. For some of the single crystal data taken without a compensator, however, the experimentally determined values were inaccurate, and only Ψ values were used in the fitting. This eliminated the large relative error inherent in Δ for values approaching 0 or 180° (de Nijs and van Silfhout 1988). In this case the minimization was done over

$$\sum_{i}^{m} (\Psi_{exp} - \Psi_{calc})_i^2$$

or

$$\sum_{i}^{m} (\tan \Psi_{exp} - \tan \Psi_{calc})_i^2$$

Nee and Bennett (Nee and Bennett 1988) have shown that fitting to Ψ alone still gives accurate values for the refractive index in the characterization of materials with very low absorption coefficients. $BaTiO_3$ and the other oxide crystals examined in this thesis do qualify for this criterion throughout the majority of the visible spectrum. As a check, however, for these samples the results were later confirmed with experiments in which a compensator was added to the ellipsometer to artificially induce Δ near 90° so that data for both Ψ and Δ could be fit.

Comparisons between different models were facilitated by the unbiased estimator of the mean-square deviation between the experimental and the calculated values, σ. σ is defined as

$$\sigma = \frac{1}{m - p - 1} \left[\text{Sum of the squares of the errors} \right]^{1/2}$$

where p is the number of parameters required in the model, and acts as an estimate of the goodness of fit for the model.

The best model was then chosen by considering simultaneously the following five conditions:

1) A physically reasonable model
2) A small value for the unbiased estimator σ
3) Good agreement between calculated and experimental Ψ values
4) Reasonable values for the 90% confidence limits on all parameters
5) Low values for the cross-correlation coefficients

Appendix A contains the computer code developed in this work to fit the experimental Δ and Ψ spectra for anisotropic materials. As in the isotropic case, the beginning consists of a grid search over parameter space to find a set of parameters for which σ is minimized. These values were then input as starting values to the Levenberg-Marquadt routine ZXSSQ. On output from the minimization routine, the best fit values for all of the parameters were written to a file along with the 90% confidence limits and σ. Finally, best-fit Δ and Ψ spectra were calculated.

The subroutine handling the propagation of light in anisotropic materials was written by Allara and Parikh (Allara and Parikh 1989, Parikh and Allara 1992) following the 4 x 4 formalism of Yeh (Yeh 1979, 1980). This routine required input data in the form of (ε_1, -ε_2) for the dielectric functions ($\varepsilon_1 + i\varepsilon_2$). All of the computer code was written and compiled using Microsoft Fortran 020 for the Macintosh computer using double precision floating point numbers. Due to the need to handle large matrices of double precision complex numbers, execution of the computer code required a math coprocessor and extended memory.

3.4.1 Reference Optical Property Data

Because the majority of the possible surface layers were projected to result in small perturbations from the reflectivity of a hypothetical ideally-terminated crystal, it was imperative that accurate data for the optical properties of all known phases be utilized. To this end, only transmission experiments were used as sources for reference data on ferroelectric phases, as all prior reflection measurements contains systematic errors due to the presence of uncharacterized surface layers. While this was necessary, it has the unfortunate consequence of limiting reference data to wavelengths where the sample is still transparent enough to permit accurate detection of a transmitted beam. During modelling, then, dispersion relations were extended no more than 50nm below the lowest energy reference data.

3.4.1.1 $BaTiO_3$

Much of the early published data on the optical properties of $BaTiO_3$ were derived from single crystals prepared by the Remeika method. This technique entails growth from a KF flux in platinum crucibles, and results in thin platelets which contain up to a few percent of incorporated potassium, fluorine, platinum, and frequently iron (DiDomenico and Wemple 1968, Ducharme et al. 1987, Godefroy et al. 1981). Such impurities result in a lower transition temperature, slightly different values for the spontaneous polarization, increased refractive indices, and impurity-based absorption in the near ultraviolet (Wemple 1970).

For this thesis, reference optical properties for $BaTiO_3$ were confined to literature reports on transmission experiments (i.e. minimum deviation experiments with a prism) with pure, melt-grown single crystals. Although the elimination of reflectance measurements limited the reference data set to wavelengths at which the absorption was not too high (~>350 nm), reflectance techniques are generally surface sensitive and should be susceptible to large errors due to the presence of surface layers. Data for the dispersion of refractive indices and absorption coefficients were taken from the published data of DiDomenico and Wemple (DiDomenico and Wemple 1968, Wemple et al. 1968). The non-linear least squares routine ZXSSQ from the IMSL subroutine library was utilized to fit this data to the two-oscillator model utilized by Johnston (Johnston 1971). Below the Curie temperature, the complex refractive indices for bulk $BaTiO_3$ were well - described by

$$n^2 = 1 + \frac{S_\varepsilon \lambda_\varepsilon^2}{1 - \left(\frac{\lambda_\varepsilon}{\lambda}\right)^2 + 2i\, G_\varepsilon \left(\frac{\lambda_\varepsilon}{\lambda}\right)} + \frac{S_\gamma \lambda_\gamma^2}{1 - \left(\frac{\lambda_\gamma}{\lambda}\right)^2 + 2i G_\gamma \left(\frac{\lambda_\gamma}{\lambda}\right)}$$

where:

$S_\varepsilon = 14.79 \times 10^{-6}\ \mathrm{nm}^{-2}$

$\lambda_{\varepsilon a} = 301.3$ nm

$\lambda_{\varepsilon c} = 284.0$ nm

$G_\varepsilon = .01342\ \mathrm{nm}^{-2}$

$S_\gamma = 154.5 \times 10^{-6}$

$\lambda_\gamma = 137.7$ nm

$G_\gamma = -.02600$

Following Johnston (Johnston 1971), only the position of the near oscillator was considered to be polarization dependent:

$$\lambda_{\varepsilon a} - \lambda_{\varepsilon c} \propto P^2$$

As a first approximation, all of the temperature dependence in the refractive indices was ascribed to the temperature dependence of the polarization. Consequently n_a is considered to be a function of wavelength only, and not a function of temperature. While this is not strictly true, measurements of the ordinary index by Burns and Dacol (1985) and Wemple (Wemple 1970) show changes only on the order of 0.002 between 25 and 120°C. Accurate values for the polarization on melt-grown crystals were taken from Camlibel et al. (Camlibel et al. 1970)

3.4.1.2 Other Materials

Wherever possible, reference data were used to describe the optical properties of other materials used in this thesis. For single crystal alumina, the oscillator given by Malitson was used to describe the dispersion of the ordinary index (Malitson 1962). Reference data on the extraordinary index as reported by Jeppesen was fit to a simple single term Sellmeier dispersion relation (Jeppesen 1958). Because the literature values for both dn/dT are so small, room temperature data for the refractive indices of sapphire were used at all temperatures. Similarly, reference oscillators for $SrTiO_3$ and $PbTiO_3$ were taken from papers by Toyoda (Toyoda 1985) and the CRC Handbook on Optical Materials (CRC), respectively.

Several platinum-coated silicon wafers prepared under different conditions were used as substrates for the deposition of ferroelectric thin films. It was found that ellipsometric data on the different substrates were sufficiently variable and difficult to model with reference data for platinum, that it was advisable to record Δ and Ψ spectra for each substrate type. This data was then inverted analytically to establish reference values for ε_1 and ε_2 for that substrate.

When the refractive index of an insulating film was unknown, as for example, with the PZT films, it was modelled using a single term oscillator

$$n^2 = A(1) + \frac{A(2)\lambda^2}{\lambda^2 - A(3)^2 - 2\imath\lambda A(4)}$$

where the A(i) were constants obtained during the modelling. A(1) was typically fixed to 1.0.

3.4.2 Algorithm for Space Charge Modelling

Experiments designed to determine the nature of the charge carriers in $BaTiO_3$ have not yet established unequivocally whether the conduction should be attributed to small polarons or free carriers (Lines and Glass 1977). Because the latter is both well understood and easily described using the Drude theory, in this work, space charge accumulation was modelled by superimposing a collection of free carriers over the dielectric function for insulating $BaTiO_3$. This method has been used previously in ellipsometric studies to calculate the effect of heavy doping on the optical properties of semiconductors (Aspnes et al. 1984). At each wavelength, the modification of the dielectric function was described by

$$\varepsilon_m = \varepsilon_i - \frac{E_p^2}{E\,(E - \imath\Gamma)}$$

where ε_m is the modified complex dielectric constant, ε_i is the dielectric constant of the insulating material, E_p is the plasma energy, E is the energy of the incoming light, and Γ is a damping factor (Aspnes et al. 1984). Both the ordinary and extraordinary components of ε were assumed to be modified by the same factor, so that the fitting parameters introduced by modelling for space charge were E_p, Γ, and the thickness of the charge accumulation region. For $BaTiO_3$, Γ always converged to zero, and allowing it to vary resulted in unrealistic values for the 90% confidence limits. Consequently, for most of the modelling, Γ was set to zero.

3.4.3 Algorithm for Modelling Internal Electric Fields

When an electric field is applied to a ferroelectric, the optical properties are modified via the electrooptic effect. Consequently, in order to model the effect of an internal electric field (for example, one established by the presence of depolarizing fields), it was necessary to know the electrooptic coefficients of $BaTiO_3$ as a function both of temperature and wavelength. Unfortunately, the only published dispersion data for the electrooptic coefficients were obtained on Remeika crystals, and so were expected to be strongly influenced by the impurities present in the sample (Johnston 1971). To circumvent the lack of experimental data, the dispersion equation for $BaTiO_3$ was modified so that the positions of both the a and c near oscillators were dependent of the electric field, i.e.

$$\lambda_{ea} = C(P_{ind})$$

$$\lambda_{ec} = C' \, (P_s + P_{ind})$$

where $P_{ind} = \varepsilon_o(K_c - 1)E$ and K_c is the dielectric constant along the c axis (Johnston 1971, Lines and Glass 1977). Ducharme's values for the electrooptic coefficients of melt grown $BaTiO_3$ at 515 nm were used to calculate the constants (Ducharme et al. 1987). Even at modest electric fields, C' differed from the zero field case, so both constants were calibrated to Ducharme's values as a function of E. Low frequency dielectric constants were taken from the paper of Camlibel et al. (Camlibel et al. 1970). Output from this modelling program includes the strength of the electric field and the thickness over which the field is present.

3.4.4 Algorithm for Polarization Gradient Modelling

If the conductivity of the crystal is sufficiently small, then as discussed in Chapter 1, the polarization should decay from its bulk value P_{max}, to a smaller P_0 as the surface is approached. For simplicity, this falloff was assumed to have an exponential form with a decay constant τ.

$$P = P_{max} - (P_{max} - P_o)e^{-d/\tau}$$

where P_{max} is a function of temperature and d is the depth into the surface. For a surface polarization of 0 C/m^2, this leads to the refractive index profile shown in Fig. 3.3.

In order to calculate Δ and Ψ for this profile, the surface of the material was subdivided into layers parallel to the surface. As the refractive index changes most quickly near the surface, the layers were spaced closely near the $BaTiO_3$ - air interface, and more widely further into the bulk of the material. It was necessary to adopt this approach, rather than a larger number of equally spaced layers, to avoid making the calculation prohibitively time consuming. To insure that the profiles were treated the same way for different values of the decay constant, the layer thicknesses were all scaled to the dropoff in P. First, the polarization was subdivided into equally spaced increments from P_o to P_{max} and the high frequency dielectric constants were calculated from the dispersion relation given in section 3.4.1.1. The corresponding depths into the surface, d(i), were then calculated from equation 3.7, and from these the thicknesses of the individual layers were defined as t(i) = (d(i) + d(i-1))/2 - summed thickness of the previous layers. A schematic representation of this approach is given in Fig. 3.4.

If too few layers are used to describe the system, then the relatively large changes in the refractive indices between layers result in interference fringes, and the calculated Δ and Ψ values oscillate around the true solution as a function of wavelength. In simulations, it was shown that these oscillations could be eliminated by subdividing the gradient into 50 layers for τ values less than ~10,000Å.

Because all of the variation in the refractive indices with polarization is confined to the extraordinary index, the magnitude of the change in the ellipsometric parameters

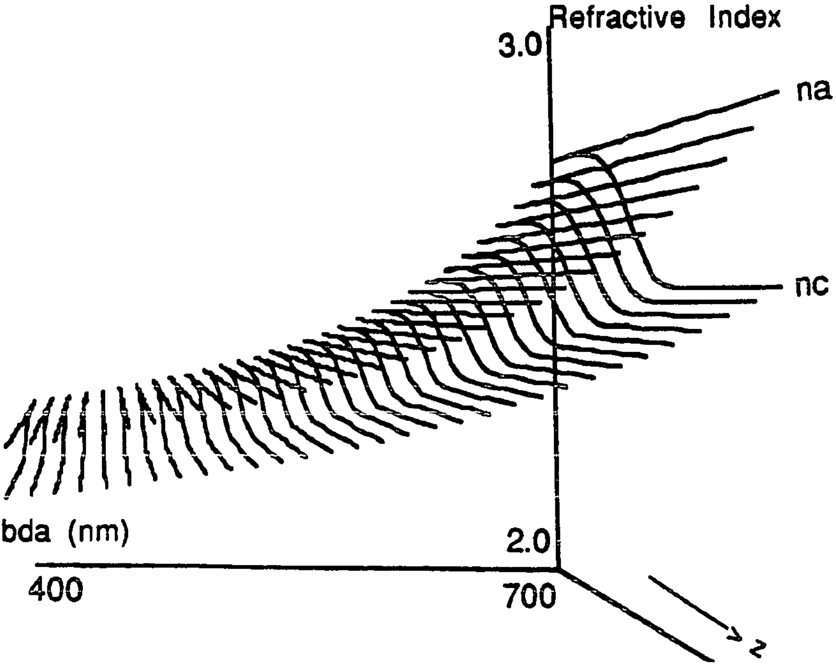

Fig. 3.3: Depth profile of the refractive index of a $BaTiO_3$ crystal with a polarization gradient

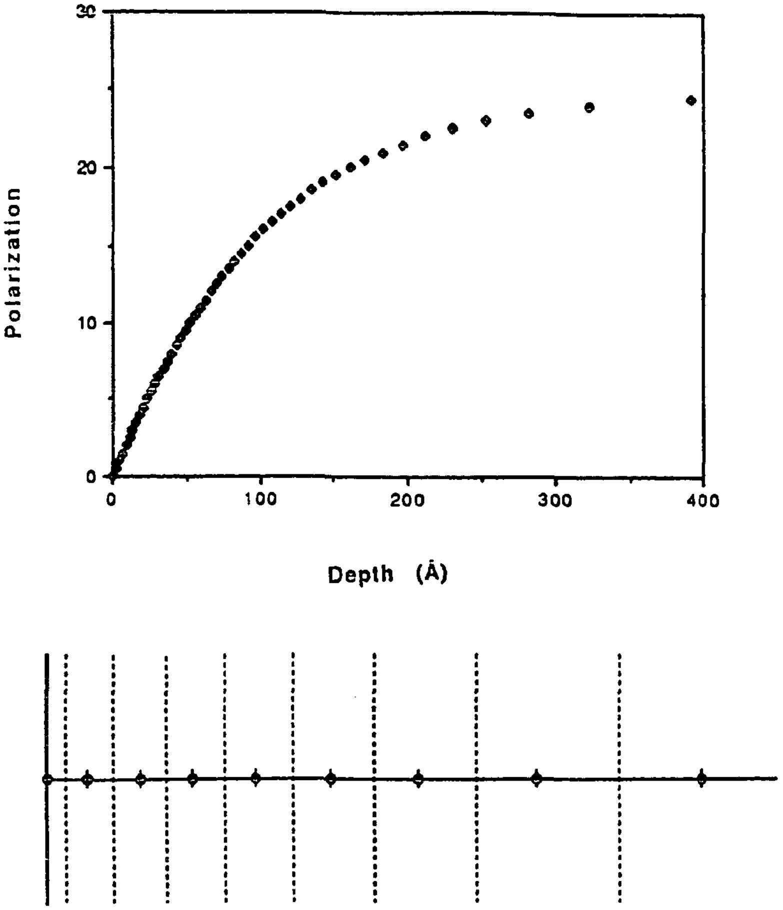

Fig. 3.4: Subdivision of the polarization and the layer thicknesses utilized in modelling polarization gradients at the surface of a $BaTiO_3$ crystal

for a polarization gradient in $BaTiO_3$ is small. This is particularly true for rapid decays in the polarization (see Fig. 3.5). Assuming that the gradient could be detected if the change in Ψ were > 0.05°, the minimum value of the decay length that could be determined ellipsometrically is ~ 50 - 100Å. While this is larger than typical quotations for the depth sensitivity of spectroscopic ellipsometry, it reflects the fact that the depth variation of the dielectric function in such a case is small and occurs only along the spontaneous polarization direction. Sensitivity to a gradient in the polarization would be improved in a material, such as $PbTiO_3$, in which both of the refractive indices demonstrate a large polarization dependence. In contrast, the huge difference between the dielectric functions of either a metal or a semiconductor and an oxide make spectroscopic ellipsometry sensitive to submonolayer oxide coatings on pristine absorbing substrates.

The algorithm in Appendix B allows this polarization gradient to be superimposed over geometrical layers describing the inhomogeneities in the system, for example the presence of surface roughness.

3.4.5 Discussion of 90% Confidence Limits

All of the modelling parameters are returned from the fitting program with the 90% confidence interval for the variable. Throughout this thesis, these numbers are reported as the best-fit parameter ± the 90% confidence limit for that parameter. Statistically, the confidence interval means that if a large number of ellipsometric spectra from the same sample were fitted, the confidence interval would contain the true value of the parameter 90% of the time (Devore 1982). Consequently, a confidence interval is not necessarily a measure of local variations in the physical structure of the sample, e.g., an output thickness of 120 ± 5Å does not guarantee that over the area

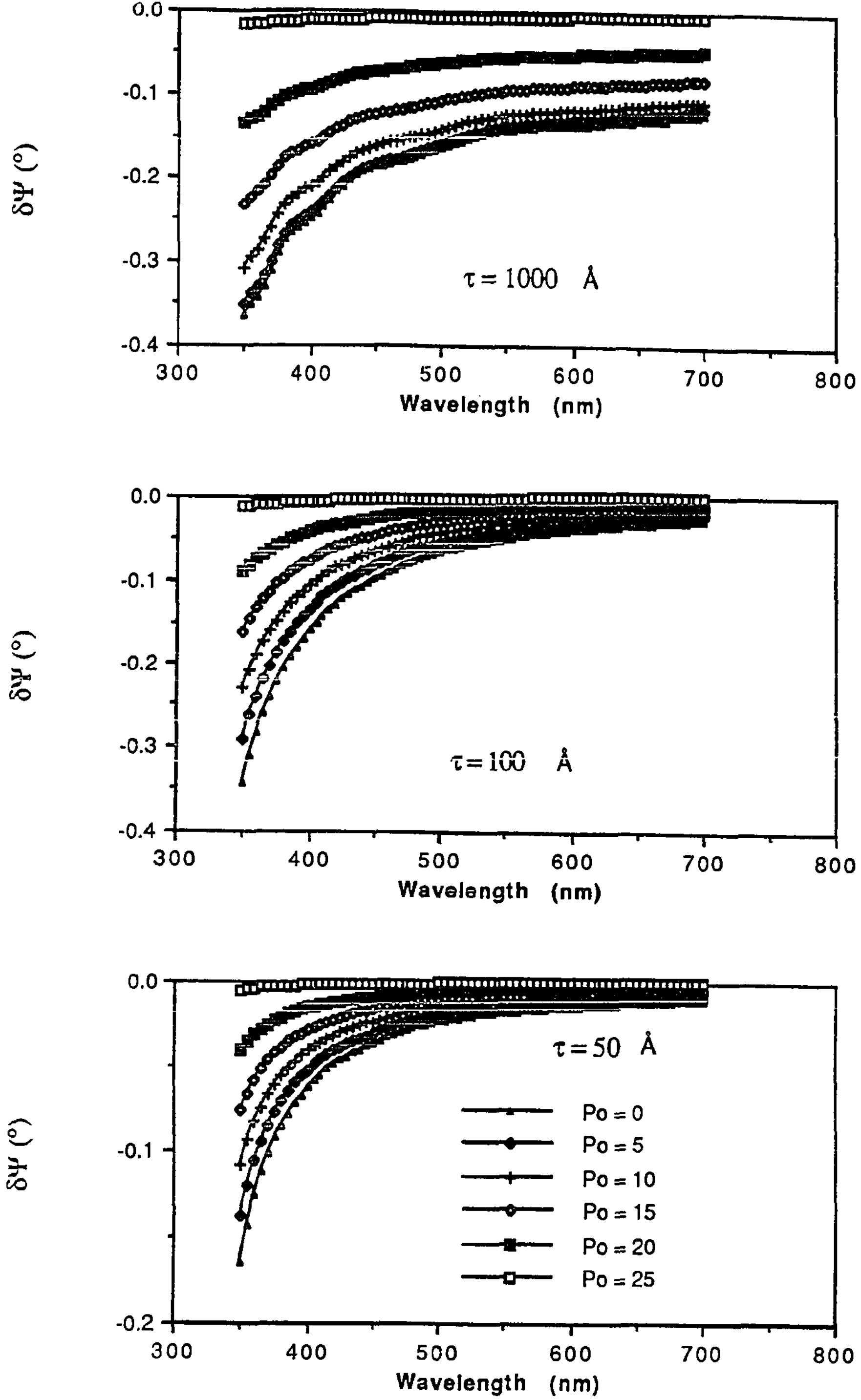

Fig. 3.5: $\delta\Psi$ ($\Psi_{\text{ideally terminated surface}} - \Psi_{\text{polarization gradient}}$) calculated for $BaTiO_3$ as a function of the surface polarization, P_o, and and the decay length, τ

sampled, the thickness ranges from 115 to 125Å. In fact, variations in the thickness could be either larger or smaller than this.

The 90% confidence limits also serve, along with σ and the correlation coefficients, as a means of estimating the statistical validity of the model chosen. Thus, while a perfect fit to the experimental data could be achieved by using a very large number of fitting parameters, excessive correlation between parameters, large uncertainties in the magnitude of any parameter, or a failure to lower σ are indications that statistically, the number of fitting parameters is not justified.

CHAPTER 4

STUDIES ON SINGLE CRYSTAL AND CERAMIC SPECIMENS

Many techniques have been utilized over the years to investigate the properties of ferroelectric surfaces. As most of these were indirect, however, information on the thickness and electrical properties of the anomalous region near the surface is limited. Spectroscopic ellipsometry, SE, while still indirect, does permit a depth profile of the optical properties of a sample in the near surface region, and so should be useful in re-examining the question of surface layers on ferroelectric crystals. This chapter details the use of spectroscopic ellipsometry in the characterization of the surfaces of bulk ferroelectric materials. Sections 4.1 and 4.2 describe the SE characterization of a mechanically polished and chemically etched (001) $BaTiO_3$ crystal, respectively. In both cases, the Δ and Ψ spectra show easily measured differences between the experimental data and those expected for an ideally terminated $BaTiO_3$ crystal (i.e. one where the bulk properties are maintained up to the surface). These are consistent with the formation of a low dielectric constant surface layer. Although details on the properties of the anomalous layer vary with the specific surface preparation conditions, it seems to be possible to prepare crystals with defective layers only a few hundred Ångstroms thick. Finally, the role of the surface finish quality in controlling the ellipsometrically-determined refractive index of a transparent PLZT 9.5/65/35 prism is discussed in section 4.3.

4.1 Mechanically Polished Single Crystal $BaTiO_3$

A top-seeded melt-grown crystal was polished as described in section 3.1.2, and poled to eliminate 90° twins. This latter point was checked using both conventional polarizing microscopy and conoscopic imaging. SE measurements were made at room temperature both with and without an achromatic compensator. As expected, Δ values near 0 or 180° were inaccurate when measured without the compensator. To eliminate this error, data taken without a compensator were modelled using the Ψ spectrum only, whereas data taken with the compensator were modelled using both tanΨ and cosΔ spectra to define the residual.

The design of the oil bath did not permit measurements to be made in the straight-through position with the sample in place on the sample mount, so all data at elevated temperatures were collected without the compensator. As a result, these data were also modelled using the Ψ spectrum only. At any single temperature, measurements were made at four angles of incidence, 56°, 60°, 75°, and 80°. The chamber was subsequently heated to the next higher temperature and the cycle was repeated. To prevent accidental cracking of the crystal due to thermal gradients, the ramp rates on both heating and cooling were maintained at ≤ 0.1°C/min.

The Δ and Ψ spectra at all temperatures were found to be shifted in a manner consistent with the formation of a low dielectric constant layer on the crystal surface. (see Fig. 4.1). No interference oscillations due to the surface layer were obvious. Several possibilities for the properties of the layer were pursued using the room temperature data, including (i) an effective medium approximation for roughness, (ii) a layer in which only the polarization differed from the bulk, and (iii) a single oscillator of unknown strength, position and damping. In all cases, (001) $BaTiO_3$ was assumed to be the substrate. Agreement with the experimental data was not improved by allowing the optic axis of the crystal to tilt away from the surface normal.

An attempt was made to check for possible contamination of the surface with organic phases by exposing the sample to a 60eV Ar ion beam as described in section 3.1.3. On "cleaning" the surface with the low voltage bombardment, the ellipsometric spectra shifted towards those expected for the ideal termination of the $BaTiO_3$ lattice (see Fig. 4.2). As the sputtering voltage used is below the threshold at which any of the

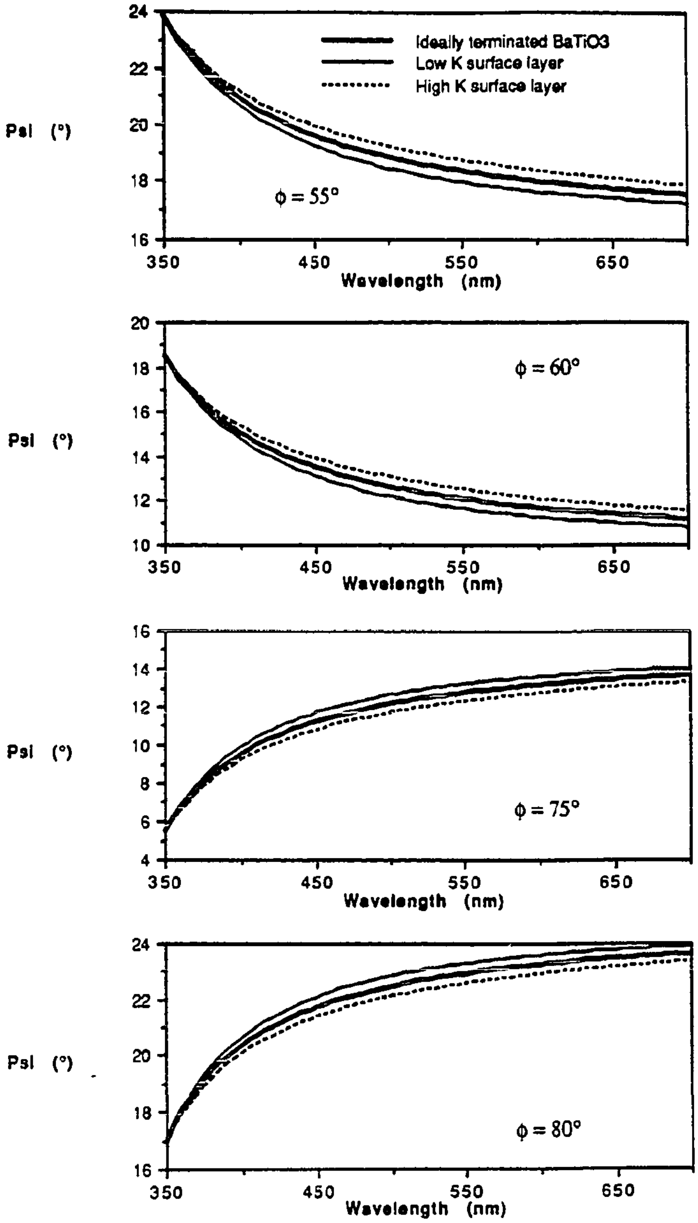

(a)

Fig. 4.1: Calculated and experimental ellipsometric data for mechanically polished $BaTiO_3$ (a) Modelled data showing the effect of higher and lower dielectric constant surface layers on Ψ (b) Ellipsometric data for a mechanically polished $BaTiO_3$ crystal and modelled spectra of an ideally terminated (001) face

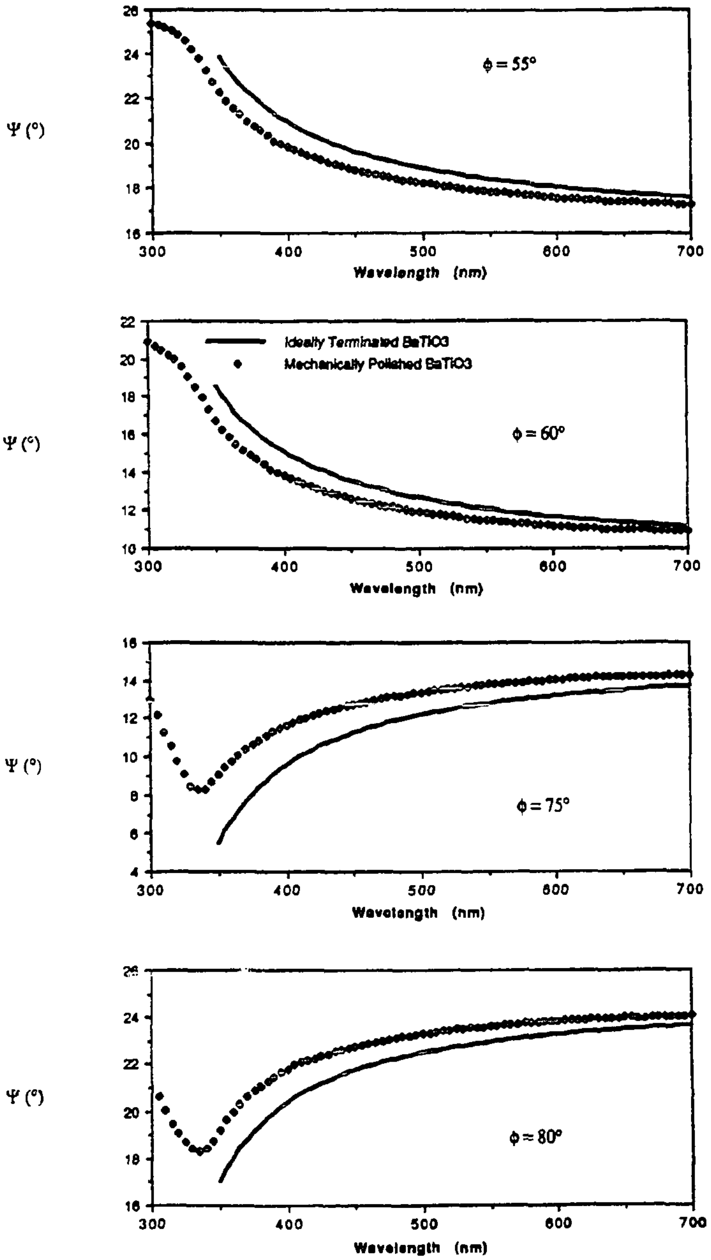

(b)

Fig. 4.1: Continued

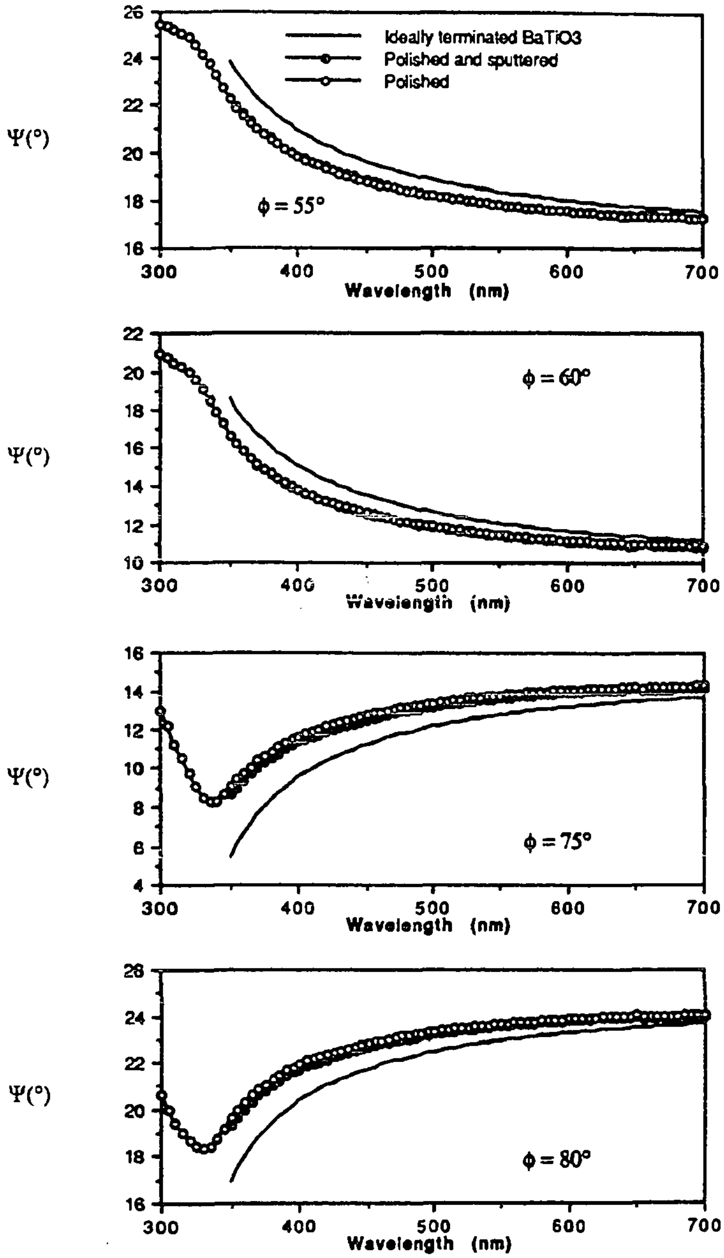

Fig. 4.2: Ellipsometric data for mechanically polished $BaTiO_3$ before and after low voltage ion beam sputtering

cations should be dislodged, these changes are probably associated with the removal of embedded organic species. (The sputtering threshold for $BaTiO_3$ is ~200eV [Krupanidhi 1990]).

From studies on the properties of lapped $(Pb_{0.8}Ba_{0.1}Sr_{0.1})(Zr_{0.8}Ti_{0.2})O_3$ ceramic specimens, Jyomura et al. (1980) concluded that mechanically polished ferroelectrics possess a non-ferroelectric surface layer in addition to residual roughness. Indirect evidence for the existence of the layer included lowered remanent polarization and dielectric constant values, and a decrease in the squareness of the hysteresis loops, all of which were dependent on the quality of the surface finish. Following chemical etching (and hence removal of the damaged layer) the electrical properties converged on higher ε and P_r values, and became independent of the initial surface preparation conditions.

Their observations were explained in terms of a low dielectric constant surface layer. The thickness of the anomalous layer was estimated at 2, 0.65, and 0.15 μm for samples lapped with 16μm SiC, 5μm SiC, and 1 μm diamond, respectively. This depth of the damaged layer was roughly comparable to the depth of the surface roughness after lapping (~2.2μm, 0.55μm, and 0.02μm for the three corresponding lapping conditions). The capacitance of the surface layer was found to be approximately temperature independent. Physically, these results were attributed to the presence of a non-ferroelectric, non-crystalline surface layer resulting from polishing damage.

This interpretation is supported by the current results on polished and sputtered single crystal $BaTiO_3$ surfaces. Although the ellipsometric results can be modelled well with the addition of a layer of either surface roughness or an oscillator with unknown properties at the crystal surface (see Fig. 4.3), it is unlikely that the low energy bombardment utilized could significantly alter the degree of surface roughness (typically >200 eV ions are required to initiate sputtering of $BaTiO_3$ [Krupanidhi 1990]). Consequently, while the ellipsometric spectra are influenced to some extent by

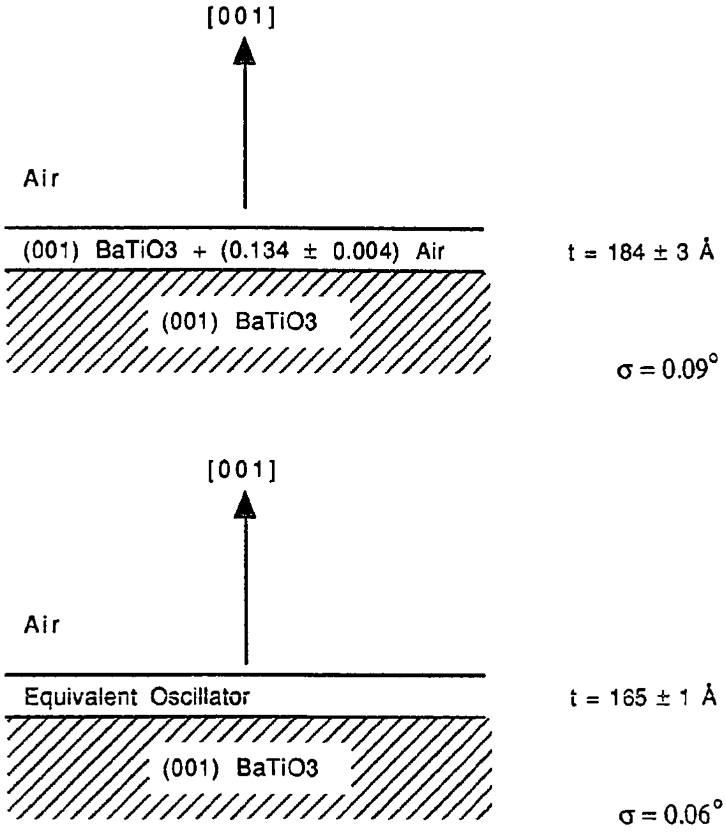

Fig. 4.3: Models for mechanically polished $BaTiO_3$ (using Ψ only)

the presence of some residual roughness at the crystal surface, the oscillator model is probably more realistic. Under this assumption, the defective layer was found to be ~165Å thick (140 - 180Å in different spots on the crystal), and the refractive index was depressed considerably below either value for bulk $BaTiO_3$ (see. Fig. 4.4). This thickness falls at the lower end of the range estimated by other workers for the surface layer on polished $BaTiO_3$ but is in line with Jyomura's data for finely polished ceramic specimens (Jyomura et al. 1980). Again, as discussed in section 3.4.5, the "error bars" shown in Fig. 4.3 and elsewhere in this thesis for all of the parameters are 90% confidence limits, rather than indications of local variations in the thickness of the anomalous layer. Consequently, they are a statistical description of the surety with which the average value for any parameter can be determined over the entire sampled area (~2mm x 1 cm).

It is also probable that the interface between the surface layer and the unperturbed $BaTiO_3$ shown in Fig. 4.3 (and similar ones elsewhere in this thesis) is not atomically abrupt, but is actually graded somewhat. Attempts were made to model the SE data for mechanically polished $BaTiO_3$ with two or more surface layers, but this was found to produce unacceptable correlation between parameters, and very large 90% confidence limits. In general, as a graded layer becomes thicker, or the dielectric function contrast between the layers increases, it becomes possible to model the system with an increased number of layers (see for example, the work of Chindaudom [Chindaudom 1991]). Due to the thinness of the perturbed region on the mechanically polished $BaTiO_3$ crystal in this work, however, such a subdivision into more than one layer was not possible. Consequently, the models shown in Fig. 4.3 constitute statistically valid interpretations of the SE data on the basis of the fewest possible free parameters.

Using the single oscillator model, data for high temperatures were also fitted, allowing the strength, position, and damping of the oscillator as well as the layer thickness to vary in each case. Results for the surface layer thickness and dispersion curves as a function of temperature are shown in Fig. 4.4, along with the unbiased estimator of the fits. The data collection cycle was then repeated on a different region of the sample. Values for the parameters and their temperature dependence were nearly identical to those shown above. Following sputter cleaning of the surface with 60eV Ar ions in an oxygen ambient, the refractive index increased by 0.04 while the layer thickness remained approximately constant (see Fig. 4.5). At the same time, the imaginary component of the refractive index of the surface layer decreased, suggesting that the surface cations were not reduced during the sputtering.

In Fig. 4.4 it is clear that both the surface layer thickness and its refractive index are approximately temperature independent between 20 and 100°C, confirming that the surface layer is not associated entirely with the bulk polarization. Moreover, the significant depression of the surface layer refractive index below either n_a or n_c for bulk $BaTiO_3$ suggests that the surface is not solely cubic perovskite. This was supported by Ion Surface Scattering experiments, in which contamination from both carbon (probably as an organic compound) and aluminum (probably as residue from the polishing media) was detected in the top few Ångstroms of the sample. However, no evidence for long range changes in either the cation stoichiometry or organic content was determined by SIMS for mechanically polished crystals. This can be seen in Fig. 4.6, in which it is apparent that all of the significant changes in composition occur at the transition from the gold overcoat (utilized to minimize charging) to the $BaTiO_3$ crystal. Following penetration of the metal layer, there is an exponential decay in the concentrations of C, Al, Au, and H which is attributable to knock-in of those species from the surface by the energetic sputtering ions. Unfortunately, the high concentration of Al in the gold overcoat made it impossible to determine whether the Al tail was associated with knock-in from the gold layer or contamination in the $BaTiO_3$ associated with γ-

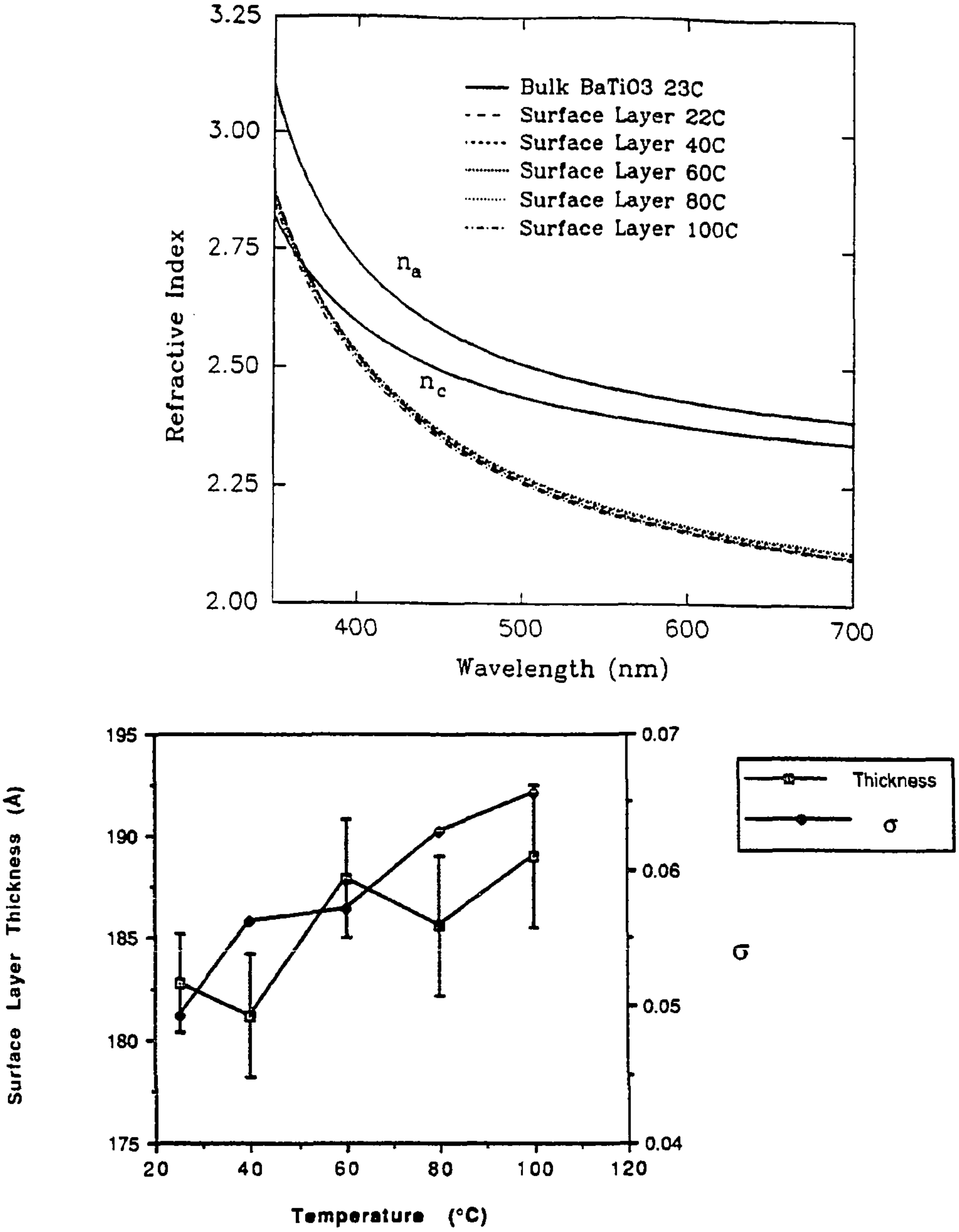

Fig. 4.4: Refractive index and thickness of the surface layer on a mechanically polished $BaTiO_3$ crystal as a function of temperature. The unbiased estimator for the fit, σ, is also shown

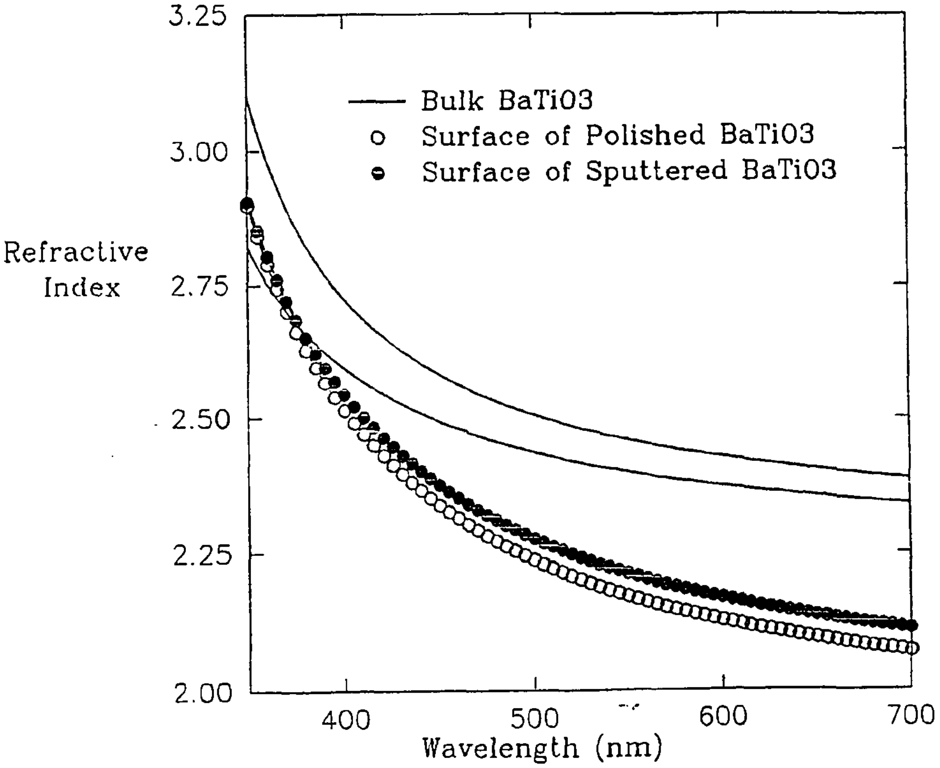

Fig. 4.5: Comparison of the surface layer refractive index of mechanically polished $BaTiO_3$ before and after ion beam sputtering

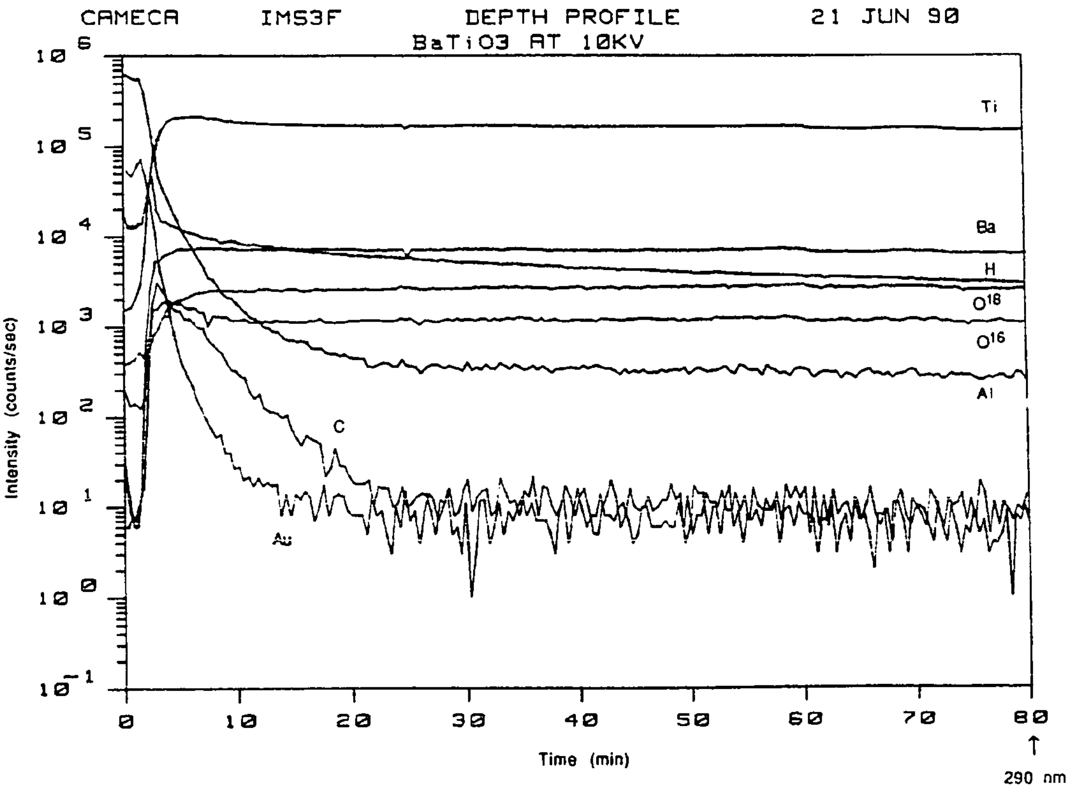

Fig. 4.6: SIMS compositional depth profile of a mechanically polished $BaTiO_3$ surface

Al_2O_3 embedded during polishing. It is also clear in the figure that there is no observable change in the Ba/Ti ratio at depths greater than a few hundred Ångstroms. This is in agreement with the ellipsometric results, which did not indicate the existence of a thick defective region.

The lack of correlation between the bulk polarization and the mechanically polished surface, coupled with the results following sputtering suggest that the observed depression in the refractive index of the surface (and hence in its dielectric properties) is probably related to polishing damage and the introduction of second phase contamination rather than an intrinsic change in the ferroelectric properties at the surface. It is likely that the low refractive index for the observed surface layer of a mechanically polished (001) $BaTiO_3$ crystal is due to a combination of damage to the crystal (i.e. amorphization), contamination from second phases embedded during polishing, and residual roughness. While the depth of this layer will vary with the quality of the polished surface, it is possible to produce damaged layers which are optically less than a couple hundred Ångstroms thick.

4.2 Chemically Etched Single Crystal $BaTiO_3$

Although considerable work has been performed on the nature of the surface layers on etched $BaTiO_3$ crystals (Chynoweth 1956, Miller and Savage 1958, 1960, Bhide et al. 1965), these studies utilized crystals grown by the Remeika method. Such crystals are known to contain large concentrations of aliovalent impurities which tend to be concentrated most heavily near the sample surface (Tongson et al. 1981). In addition, etching was frequently performed under conditions likely to result in nonstoichiometric surface layers. Hence it is not surprising that the surface behavior in such samples was dominated by the presence of space charge. In contrast, comparatively little data are available in the literature concerning the surface behavior of "pure" $BaTiO_3$ ceramics or crystals.

In this work, a top-seeded solution-grown $BaTiO_3$ crystal was etched in a mixture of hydrogen peroxide, hydrochloric acid, and deionized water. Following this treatment, the surface was somewhat rougher to the eye in reflected light; prolonged or repeated etches resulted in clearly perceptible "hazing" of the polished surface. The higher roughness values were manifested in the ellipsometric spectra as a further deviation from the Ψ curves expected for a perfectly terminated $BaTiO_3$ crystal. This is apparent in Fig. 4.7, where data for the mechanically polished, polished and sputtered, and chemically etched crystal is shown. At the same time, Δ also moved several degrees further away from the 0 or 180° limit expected for an unperturbed, insulating bulk sample. As for the mechanically polished sample, data was collected at angles of incidence of 56°, 60°, 75°, and 80° for each temperature.

Three classes of behavior were observed on heating an etched crystal depending on how the crystal had been poled. Following mechanical poling to eliminate 90° twins (though not 180° domains) the Δ and Ψ spectra showed modest variations with temperature up to 115°C (see Fig. 4.8) Similarly, the effective refractive index determined by direct inversion is only slightly temperature dependent (Fig. 4.8b). In contrast, after electrical poling, the Δ and Ψ spectra and the effective n changed considerably on heating (Fig. 4.9). On cooling, the spectra usually remained near the highest temperature values, although in one instance, after prolonged poling at elevated temperatures, the curves approximately retraced those on heating. When hysteretic behavior was observed, the high temperature values were then stable with time (see Fig 4.9). In all cases, the hysteresis in Δ and Ψ scaled with the angle of incidence, so that the smallest effect was observed at 56° and the hysteresis was greatest for the highest angles of incidence. The data shown in Figs. 4.8 and 4.9 were all collected at $\phi = 80°$, where the largest hysteresis was observed.

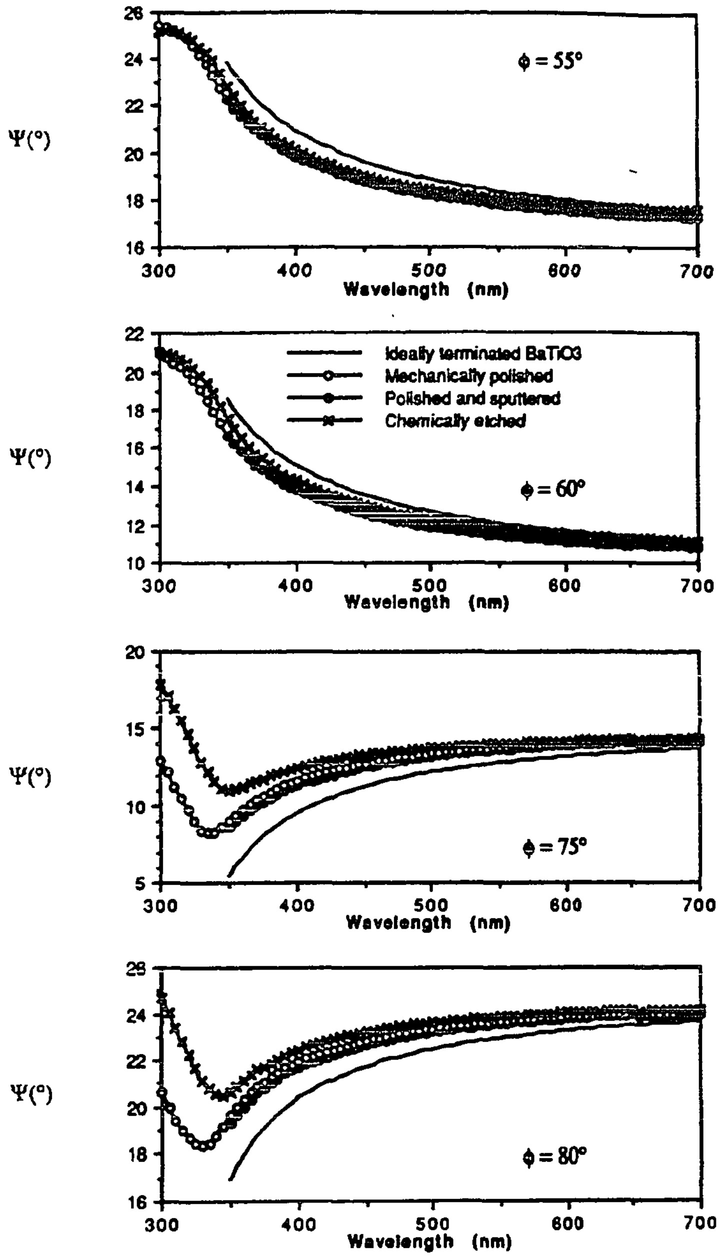

Fig. 4.7: Experimental data for the mechanically polished, polished and sputtered, and chemically etched $BaTiO_3$ with reference data for an ideally terminated crystal. The incidence angles 55°, 60°, 75°, and 80° are shown

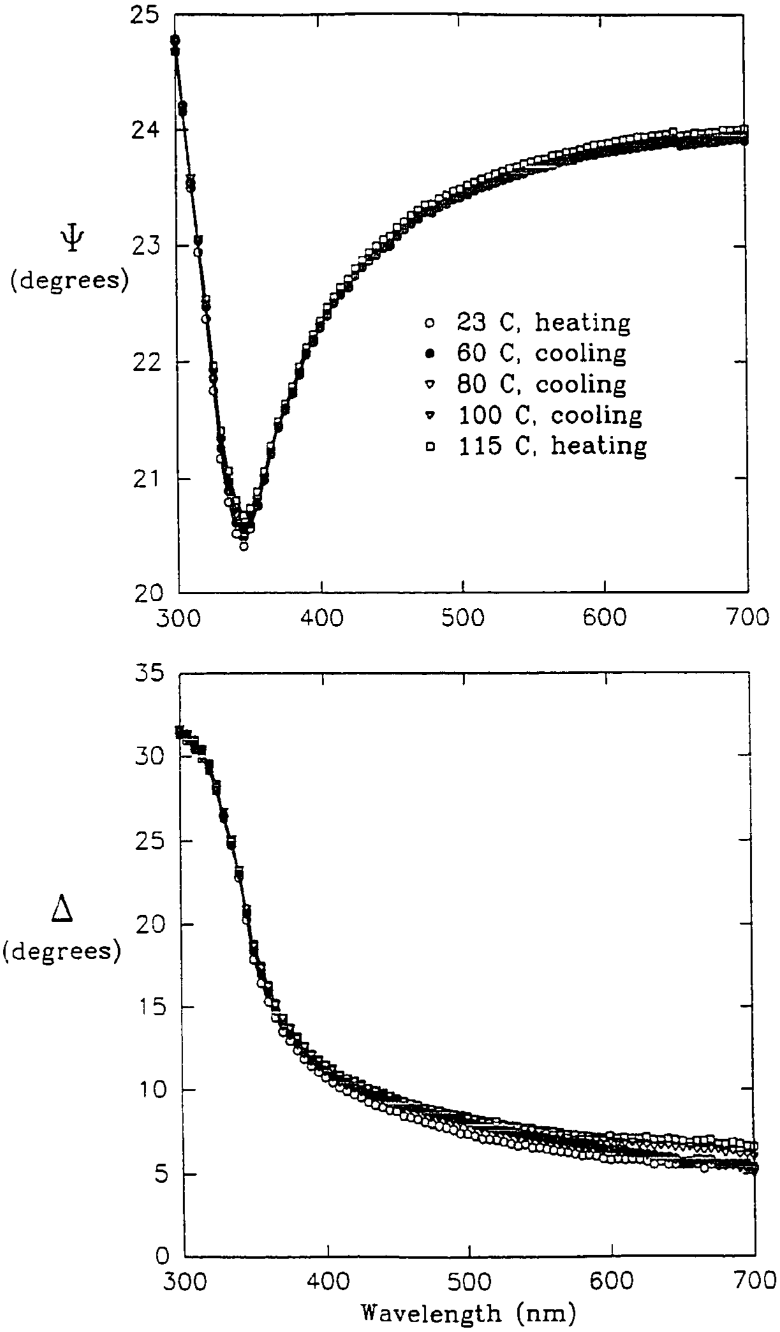

(a)

Fig. 4.8: Experimental data for a chemically etched BaTiO3 crystal with 180° twins. (a) Δ and Ψ as a function of temperature. (b) Effective n determined by direct inversion.

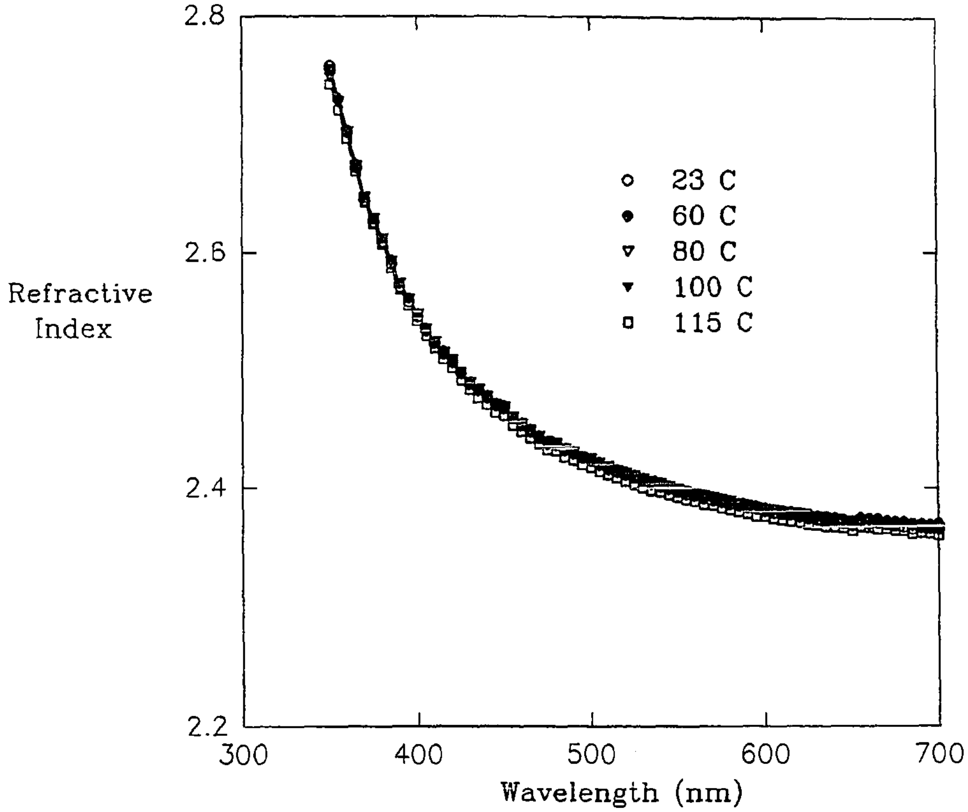

(b)

Fig. 4.8: Continued

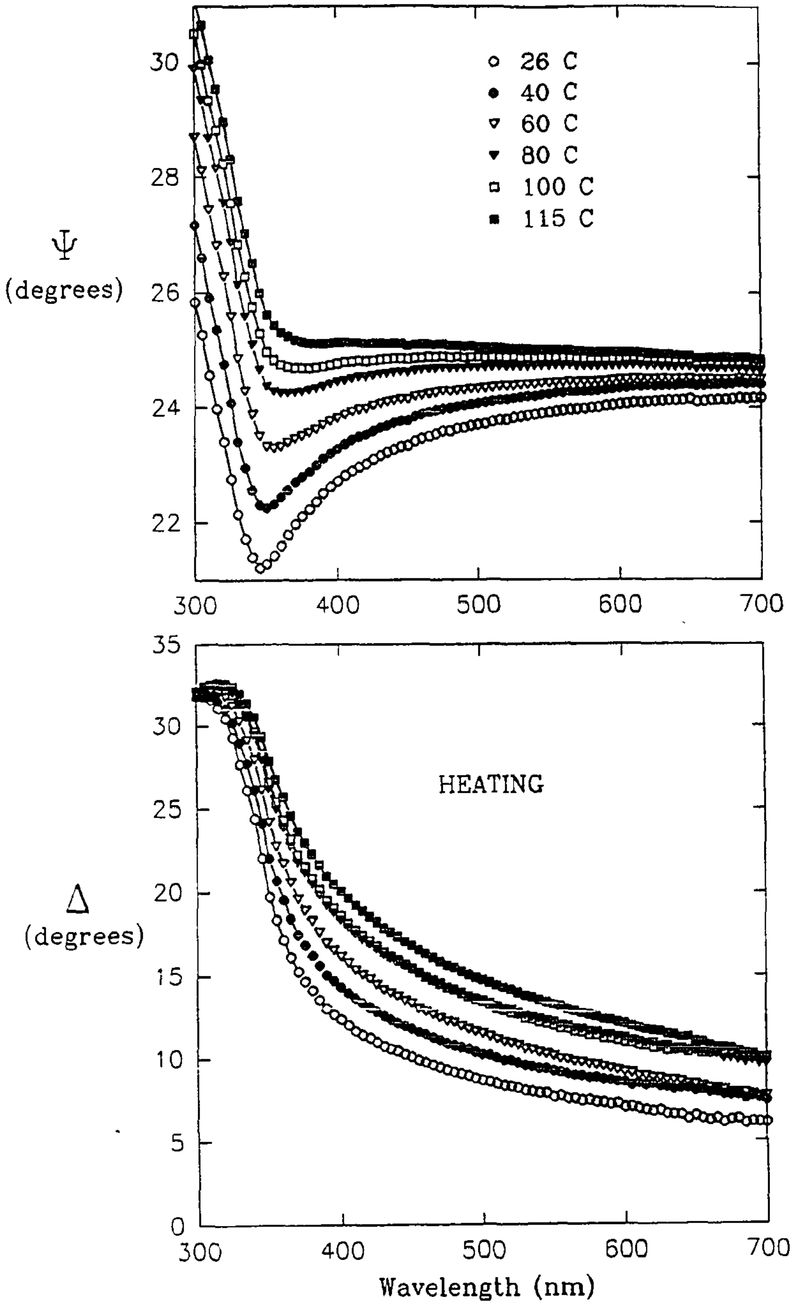

(a)

Fig. 4.9: Δ and Ψ as a function of temperature for a chemically etched $BaTiO_3$ crystal with the polarization pointing into the measured surface (a) heating and (b) cooling (this data was taken during the same run as shown in part a). (c) Effective n determined by direct inversion

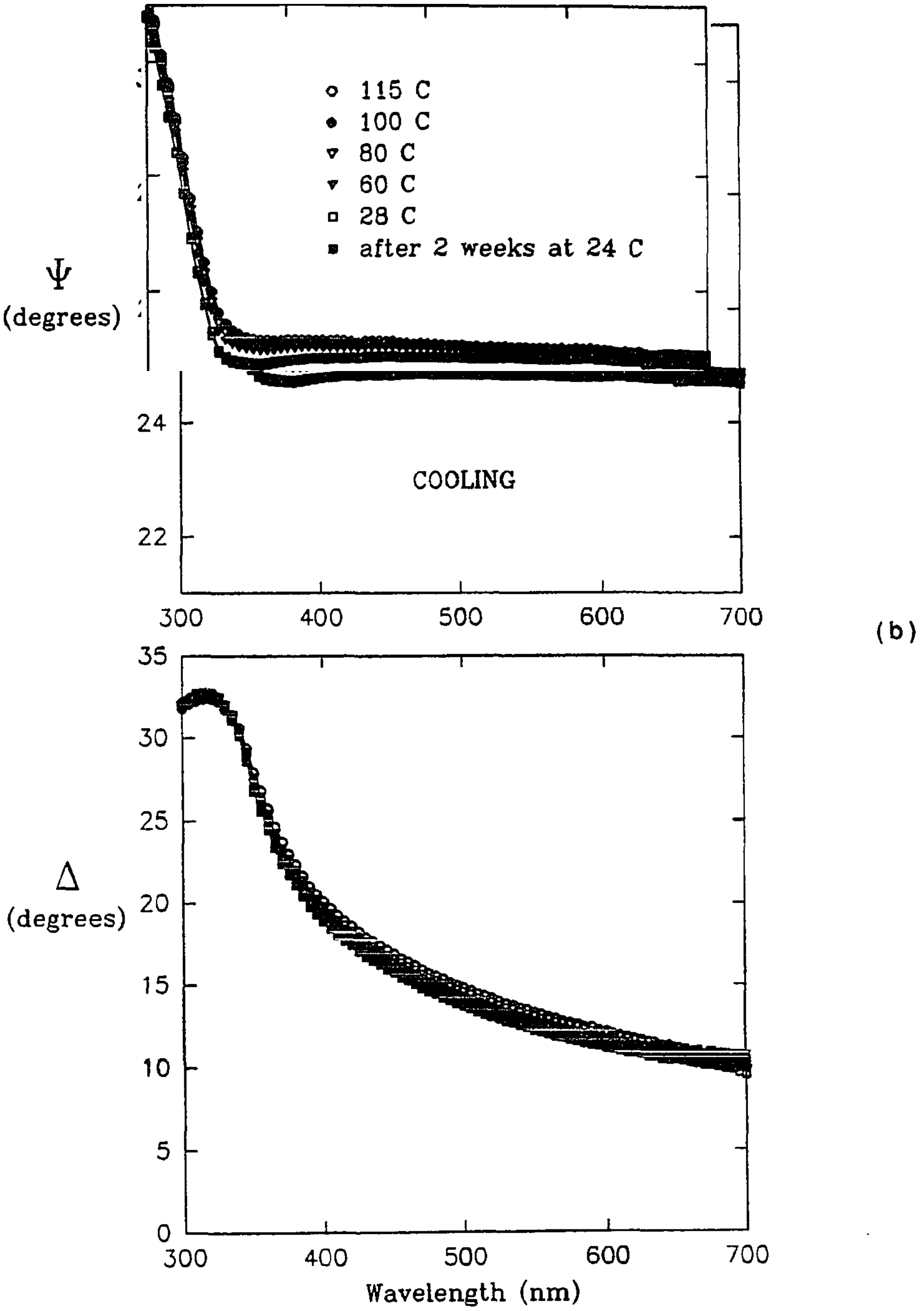

Fig. 4.9: Continued

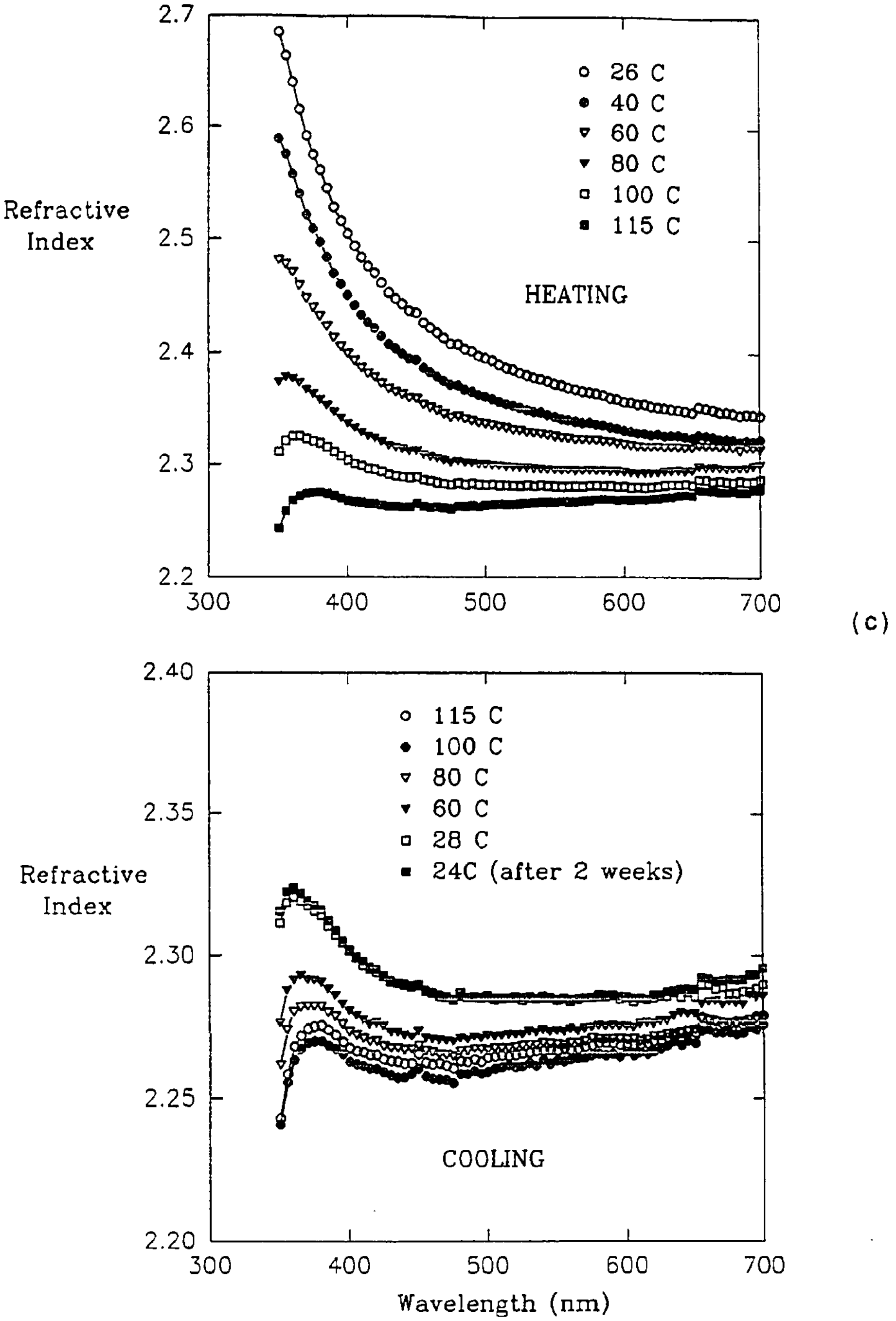

Fig. 4.9: Continued

If a sample which demonstrated hysteretic behavior as a function of temperature was reheated without re-poling, the initial large changes in Δ and Ψ on heating were not repeated. The hysteresis could, however, be restored by re-poling the sample. The direction and magnitude of the shift in the curves with temperature was considerably larger than that expected on the basis of the known temperature dependence of the refractive indices of (001) $BaTiO_3$. It was also independent of whether the polarization was directed towards or away from the measured surface. No evidence was found for the generation of macroscopic 90° twins during heating runs, although some 180° domain reversal occurred (as determined from d_{33} measurements before and after heating). In addition, as for the polished sample, the SIMS experiments on etched $BaTiO_3$ did not show any change in the concentration of the components as a function of depth beyond that attributable to knock-in (Fig. 4.10). Again, the large composition changes apparent in Fig. 4.10 are associated with penetration of the gold overcoat.

If the data were modelled as a layer of roughened $BaTiO_3$ on (001) $BaTiO_3$, these changes were accommodated by allowing the thickness and the volume fraction of air in the roughened layer to increase with temperature and (most often) saturate near the highest temperature values (see Fig. 4.11). This is clearly unphysical. Attempts were made to eliminate the temperature dependence of the physical parameters defining the roughness by incorporating additional phenomena into the modelling. Among the possibilities considered were the presence of space charge or high electric fields in the sample and a-domains at the sample surface. As can be seen in Fig. 4.12, it was not possible to eliminate the temperature dependence of the apparent roughness with either of the first two possibilities. Thus, while the $BaTiO_3$ surface may be influenced by the presence of space charge concentration or internal electric fields, these factors do not control the hysteresis in the ellipsometric spectra. Due to the much larger changes in the extraordinary index with temperature, however, allowing a-domains to form on the surface mitigated the temperature dependence of the roughness layer somewhat.

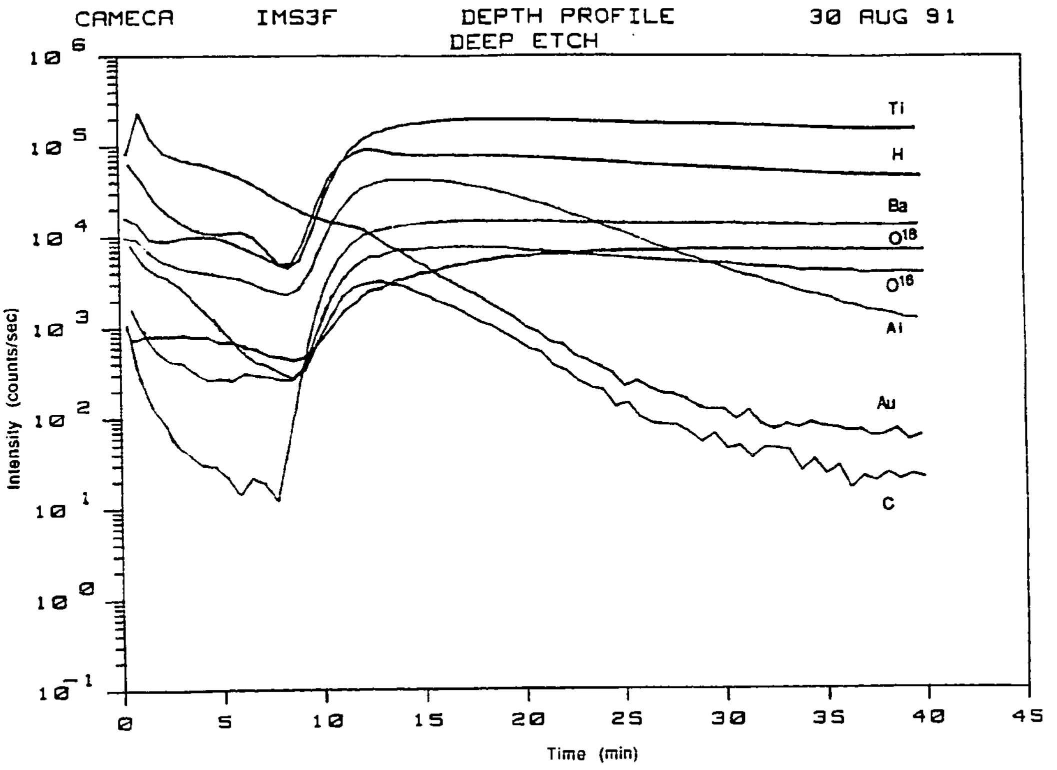

Fig. 4.10: SIMS depth profile of a heavily etched $BaTiO_3$ crystal

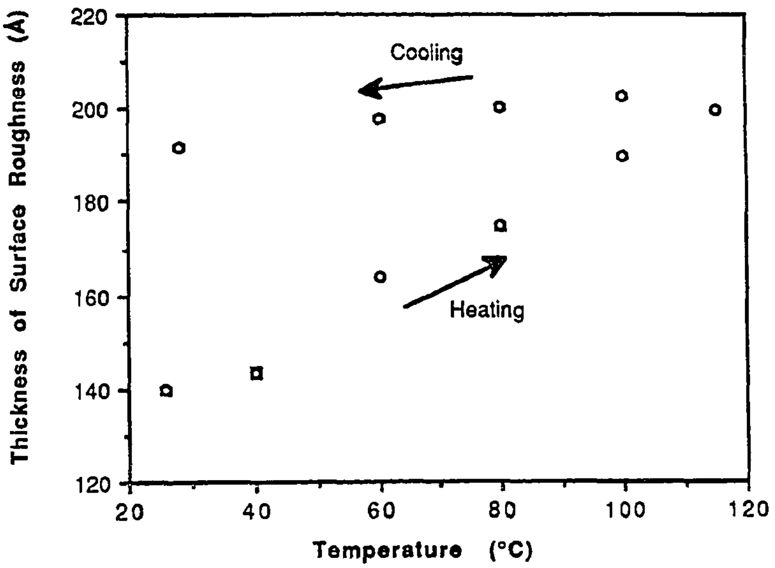

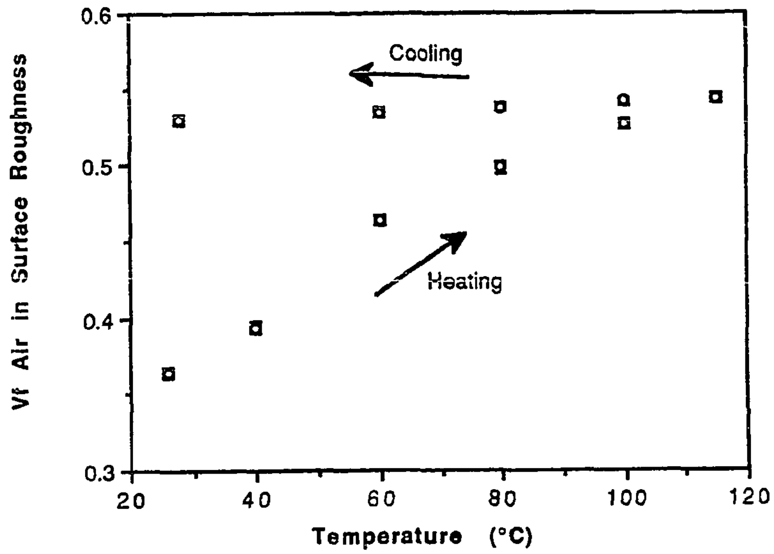

Fig. 4.11: Hysteresis in the apparent roughness of an etched $BaTiO_3$ crystal measured as a function of temperature after polishing away from the measured surface

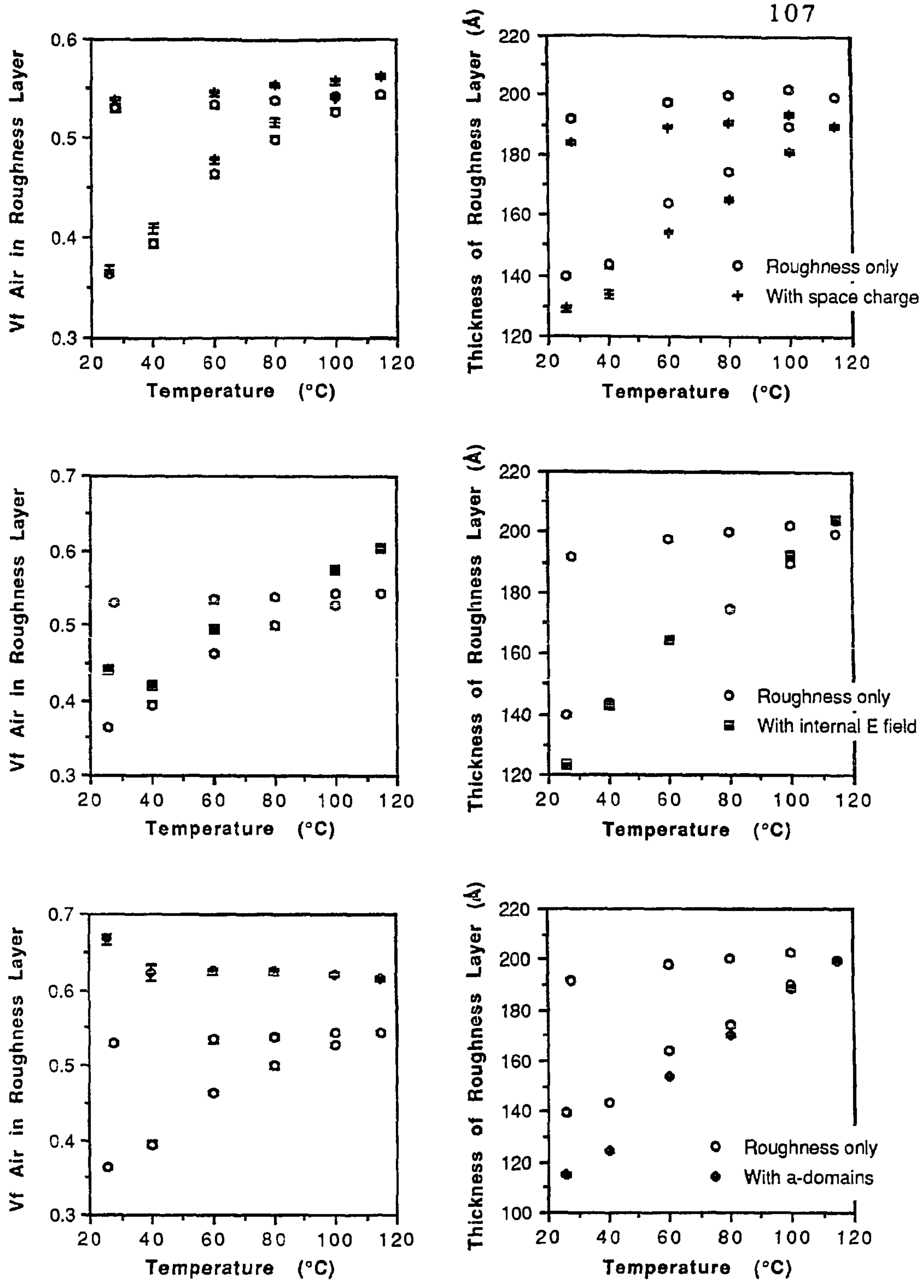

Fig. 4.12: Modelling of a well-poled etched (001) $BaTiO_3$ crystal

Physically, it is believed that the substantial temperature dependence of Δ and Ψ spectra for the poled $BaTiO_3$ single crystal was associated with either the presence of bulk defect dipoles or the existence of 90° domains near the sample surface. Defect dipoles would tend to align under the influence of a strong electric field, but would not be expected to disorder thermally in exactly the same way as the spontaneous polarization. Consequently, on heating the sample, a progressive disordering of the dipoles could lead to the substantial temperature dependence of Δ and Ψ. Once thermal randomization occurred, the defect dipoles would not reorder unless re-exposed to a high internal or external electric field. This would account for the observed hysteresis in the ellipsometric data on temperature cycling of the sample. As the dipoles respond to external electric fields, they are probably similar to those observed in "hard" PZT compositions. Typically, those would be due to oxygen vacancies in the perovskite lattice generated during the processing. "Hard" defects of this type would also account for the observed difficulty in repeatedly switching the polarization direction of the $BaTiO_3$ crystal at room temperature.

As suggested previously, the presence of a domains also partially eliminates the temperature dependence of the apparent roughness. It is not clear, however, why poling of the sample should result in a layer of reversed domains at the surface.

In previous work on PZT and PLZT materials, Afanasjev et al. (1985) reported differences in the Ψ spectra for the opposite faces of poled ceramic samples. This was attributed to surface phenomena, and variation in the space charge layer formation was projected as a likely cause for the discrepancies between the two measurements. In the current work on $BaTiO_3$, however, because of the interrelation between the absolute magnitudes of Δ and Ψ and the poling conditions, the differences between spectra for samples poled towards and away from the measured sample face could not be attributed unambiguously to the surface. As a result, it was not possible to confirm Afanasjev's conclusions.

To avoid complications due to the large temperature dependence of Δ and Ψ of well-poled sample, more extensive modelling was performed primarily on samples which did not show anomalously large variations in the spectra with temperature. Among the possibilities considered in these models were (i) the presence of a-domains in the surface region, (ii) the existence of a gradient in the spontaneous polarization, and (iii) the existence of space charge at the sample surface.

4.2.1 Modelling with a-Domains at the Surface

Several investigators (Subbarao et al. 1957, Lezgintseva 1965) have suggested that the domain structure of $BaTiO_3$ crystals and ceramics can differ in the surface and the bulk of the material. For many surface preparation conditions, c-domains (i.e. those with the polarization perpendicular to the crystal face) were shown to form preferentially near the surface (Subbarao et al. 1957). Because the crystal is uniaxial, the presence of this type of domain cannot be detected optically, and would not affect modelling of the single crystal data. Nevertheless, to account for the possibility of partial switching to a-domains at the surface, additional modelling was performed by superimposing a layer of "polycrystalline" material over the layer of surface roughness for the etched $BaTiO_3$ crystal. Again, c-axis oriented $BaTiO_3$ was used as the substrate. The dielectric function for this overlayer was approximated by a polycrystalline average of the ordinary and extraordinary ε components.

An example of the best fit model of this type is shown in Fig. 4.13 alongside the one and two-layer roughness model without a-domains. As can be seen, the higher refractive indices of the "polycrystalline" material required a larger volume fraction of air in the layer of roughness. While modelling the data with switched domains resulted in approximately the same σ value as the two-layer roughness model, the volume

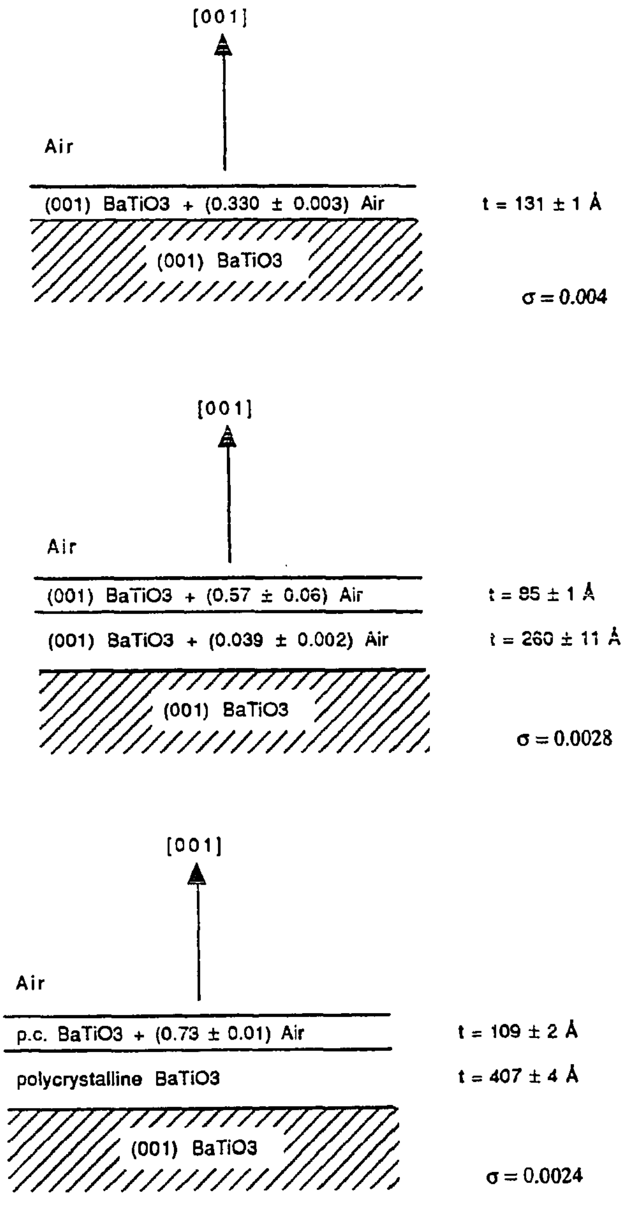

Fig. 4.13: Modelling of chemically etched $BaTiO_3$ with and without a-domains at the surface

fraction of air in the layer of surface roughness is strongly temperature dependent (see Fig. 4.14). This is not physically reasonable. Consequently, it is believed that the presence of a-domains at the surface of etched, un-electroded top-seeded melt-grown $BaTiO_3$ was not confirmed by the optical data.

4.2.2 Polarization Gradient Modelling

In order to investigate the possibility of a decay in the spontaneous polarization at the surface of an etched crystal, the near surface region was subdivided into 50 layers at points along an exponentially decaying polarization as described in section 3.4.4. This was superimposed over the existing surface roughness. Due to the large number of layers involved, these models were very time consuming, typically requiring a week to fit for the four parameters involved (the thickness and volume fraction of air in the surface roughness, the surface polarization and the decay length, τ, of the polarization gradient) using a dedicated computer with a math coprocessor running at 25 MHz. As a result, a less exhaustive survey was conducted for these models than for others discussed in this thesis. Nevertheless, the best fit parameters consistently yielded decay lengths on the order of 150 ± 90Å. This is very close to the dimension at which simulations suggest that ellipsometry becomes insensitive to the presence of a gradient in the polarization. The calculated values for the surface polarization were typically negative, again implying that if a polarization gradient exists in the crystal, either the current assumptions utilized in the modelling are a poor description, or the scale is sufficiently small that ellipsometry cannot properly characterize it. In any event, there is no proof on the basis of the current modelling for supposing a polarization gradient within an unelectroded, reasonably pure crystal exists with a scale extending beyond ~100Å.

The ellipsometrically-obtained value for τ is on the same order as other estimates of the correlation length for ferroelectricity in the paraelectric phase of

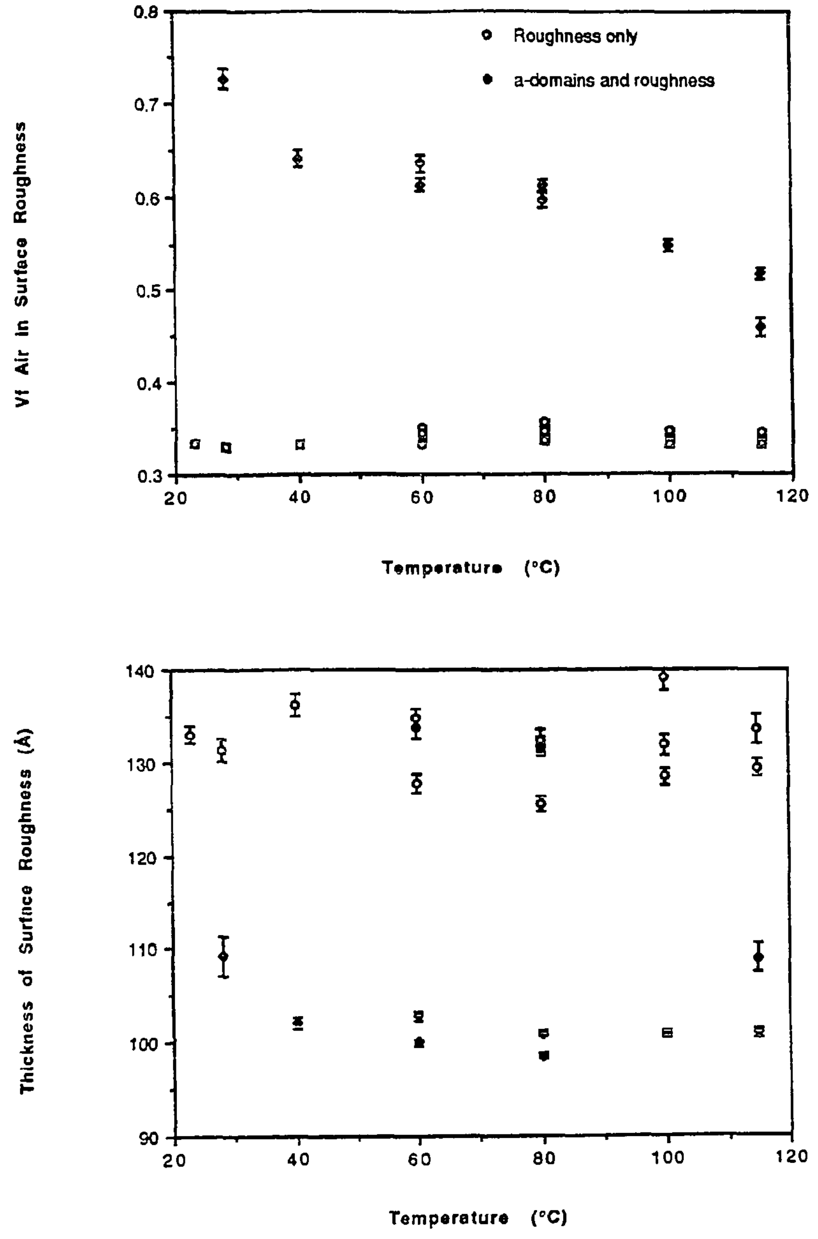

Fig. 4.14: Temperature dependence of the surface roughness of an etched $BaTiO_3$ crystal when modelled with and without a-domains at the surface

$BaTiO_3$. Yamada et al. (Yamada et al. 1969) and Comes et al. (Lambert and Comes 1969, Comes et al. 1968) for example, have estimated the correlation length at ~20 and 40 - 100Å, on the basis of inelastic neutron scattering and X-ray data, respectively. Similarly, the correlation volume for ferroelectricity (which is related, though not equivalent to, the cube of the correlation length, having been normalized to the dielectric constant) has been estimated at ~10^4 - 10^5 Å^3 (Wemple 1970). As discussed by Kretschmer and Binder (1979), the decay in the polarization at the surface of a ferroelectric should be on the order of the correlation length for ferroelectricity in insulating materials in which space charge effects can be neglected. This suggests that for many practical applications, intrinsic changes in the polarization may be negligible down to very small sizes (i.e. where the small dimension is on the order of tens to hundreds of unit cells).

4.2.3 Space Charge Modelling

The data was also modelled by adding a layer of space charge to the rough $BaTiO_3$ surface. It was found that when a geometry comparable to that shown in Fig. 4.13 was utilized (with the layer of polycrystalline material replaced with a space charge-rich (100) $BaTiO_3$), σ dropped by approximately one half from the value modelled with one layer of roughness alone. Moreover, in contrast to modelling with two layer of surface roughness, or the presence of a-domains and roughness at the surface, the parameters describing the surface roughness were approximately temperature independent (see Fig. 4.15). It can also be seen in that figure that as the temperature is increased, E_p, which is related to the concentration of charge carriers, decreases. This is a realistic possibility if the charge is, in fact, localized near the surface to compensate the spontaneous polarization.

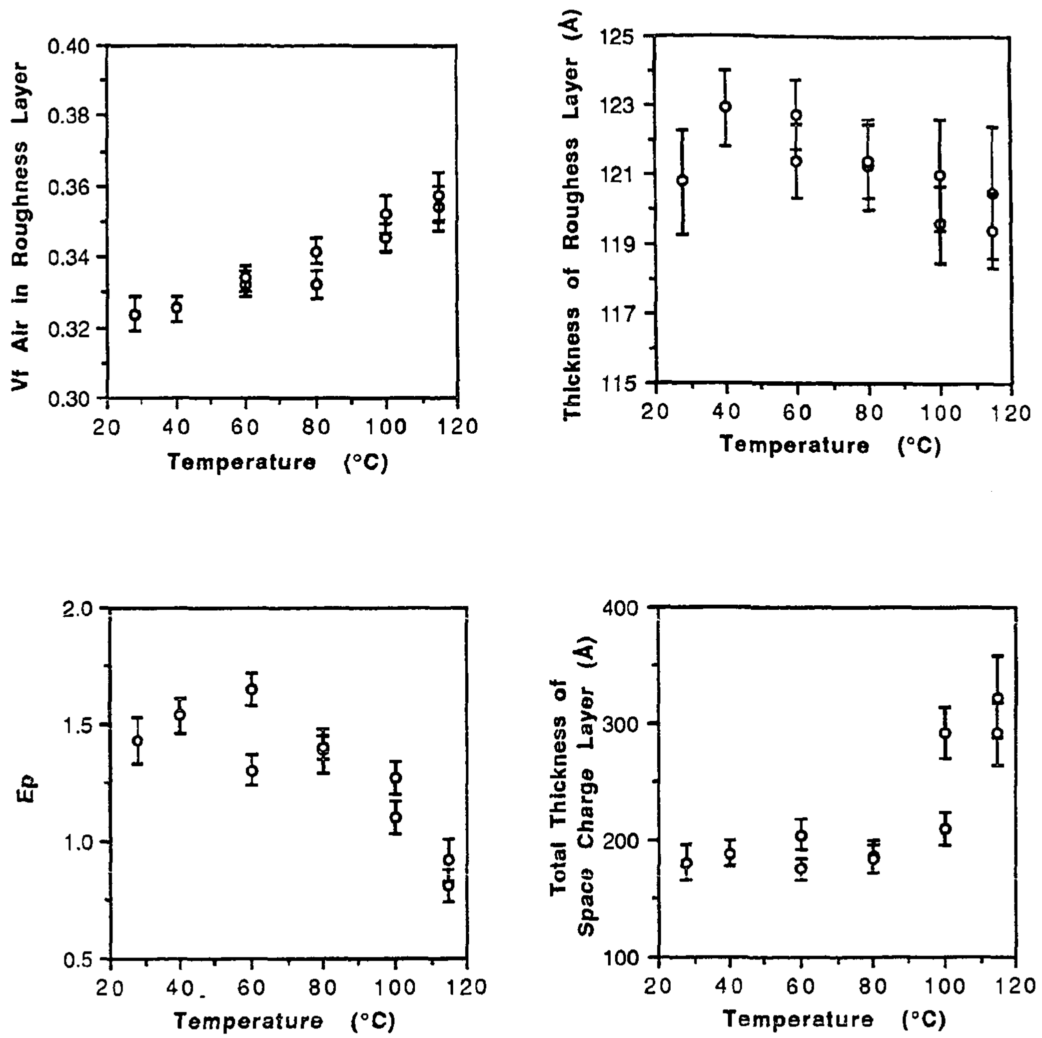

Fig. 4.15: Space charge modelling of chemically etched $BaTiO_3$

In light of this modelling, it is believed that the surface of chemically etched $BaTiO_3$ which did not show large hysteresis in the ellipsometric data with temperature is best described as a roughened material which may have an accumulation of free carriers concentrated at the surface. There is no definitive optical evidence for the presence of a gradient in the polarization as the surface is approached. Consequently, if there is a polarization gradient, it is probably contained within a very thin surface layer.

4.3 Polished 9.5/65/35 Prism

Some SE measurements on a 9.5/65/35 PLZT prism have been reported by Furman (1987). He reported changes in the apparent "k" of the sample (determined by assuming the sample was homogeneous and directly inverting the ellipsometric data) with variations in the surface preparation. In that work, mechanical polishing was found to result in a high "k" value which could be partially relieved either by annealing the sample at 800°C, presumably recrystallizing the surface, or lightly etching the sample face. Prolonged etching was found to increase the apparent "k" value due to roughening of the surface. While the trends indicated by Furman are probably correct, no attempt was made to depth profile the anomalous layer. Moreover, as measurements were made without a compensator, substantial error is expected in the absolute "k" values.

In the current work, a comparable 9.5/65/35 PLZT ceramic prism, also prepared by Eugene Furman, was examined. The bulk refractive index of the same prism was determined by the minimum deviation method at several wavelengths. These data were then fit by an oscillator model assuming zero absorption and used as reference data in the ellipsometric modelling. One sample face was polished with 1 μm diamond paste using kerosene as a lubricant, cleaned in acetone, and measured at an angle of incidence of 80° with the achromatic compensator in place. The process was then repeated after repolishing with 0.25μm and 0.05 μm γ- Al_2O_3. As was the case for the $BaTiO_3$ sample, no distinct interference oscillations associated with the surface layer were present in any of the data sets.

Fig. 4.16 shows both the experimental data for the prism and reference spectra calculated from the minimum deviation data. It is clear from the figure that as the surface finish is improved, deviation of the ellipsometric spectra from the bulk data decreases. This is borne out in direct inversions of the data to obtain the effective refractive index of the specimen assuming that it can be treated as a homogeneous material (see. Fig. 4.17).

Thacher has reported that direct inversion of ellipsometric data for PLZT prisms yields poor agreement with minimum deviation data (Thacher 1977). It can be seen in Fig. 4.17 that this is strongly dependent on the quality of the surface finish. Thus, the effective refractive index following the 1μm polish is, in agreement with Thacher's conclusions, both low and too dispersive relative to the transmission data. In contrast, the dispersion curves for the sample following the 0.25μm and especially the 0.05μm polishing steps match the bulk data reasonably well.

The finite values for Δ in each case, however, confirm the existence of a surface layer with properties different from the bulk for all of the surface treatments examined. Modelling the system with a layer of roughness over the reference data for the bulk of the prism resulted in negative thicknesses for the surface roughness when the sample was polished with 0.25μm or 0.05μm grit. Consequently, this type of model was abandoned. Reasonable fits could be obtained in all cases, however, by describing the optical properties of the surface layer with an oscillator and permitting the layer thickness to vary. Fig.4.18 shows the best fit models for this geometry, and the refractive indices of the oscillators describing the surface. As suggested by Jyomura et al. (1980) with respect to $(Pb_{0.8}Ba_{0.1}Sr_{0.1})(Zr_{0.8}Ti_{0.2})O_3$ samples, the depth of the

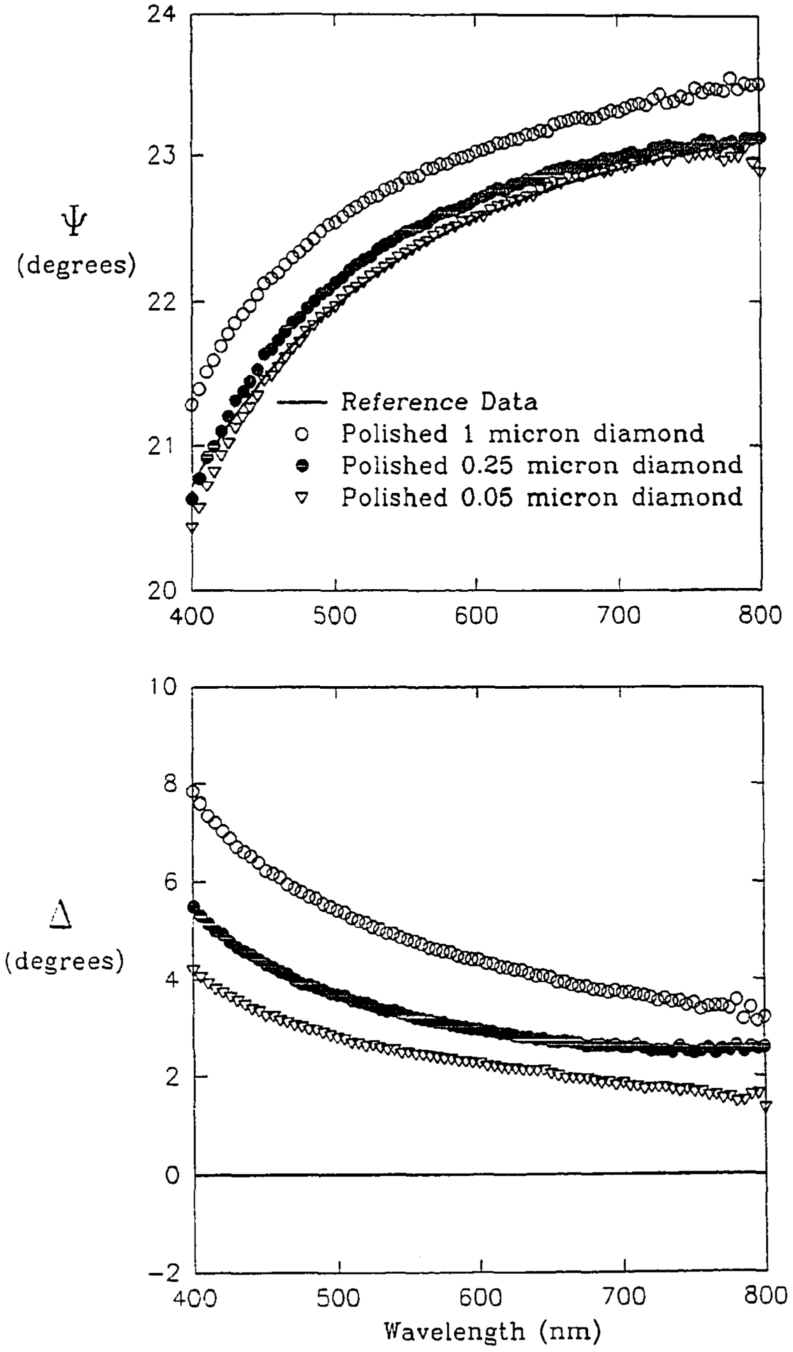

Fig. 4.16: Experimental and reference spectra for a 9.5/65/35 PLZT prism

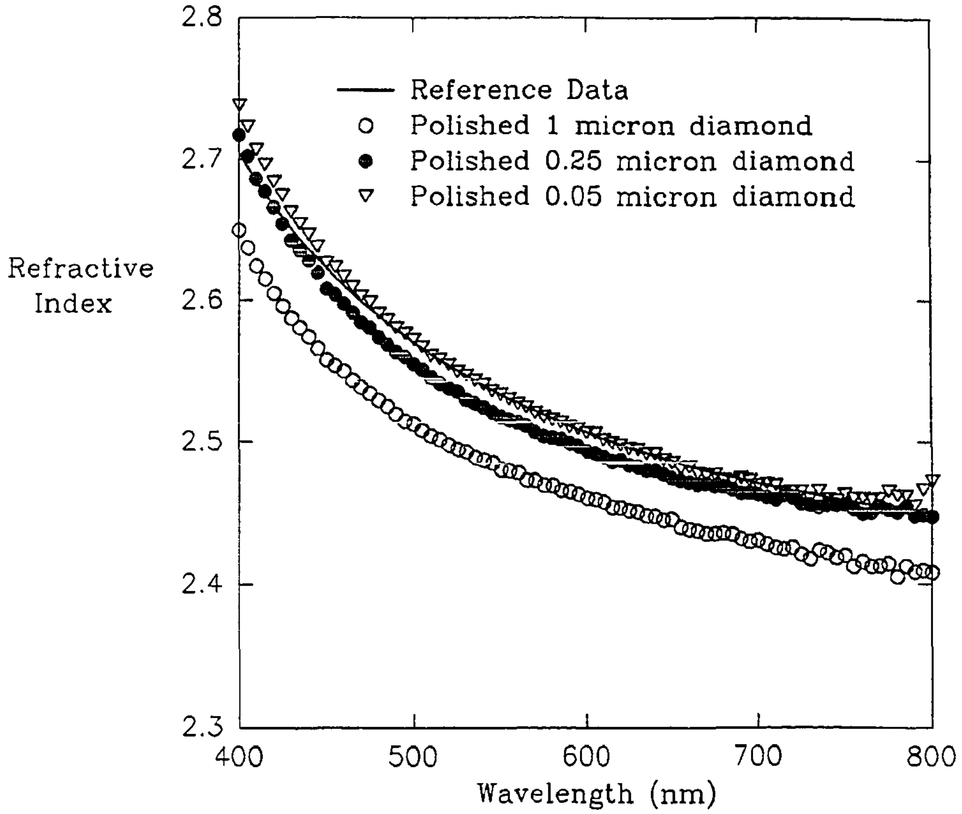

Fig. 4.17: Direct inversion of ellipsometric spectra assuming a homogeneous sample in order to obtain the effective refractive index of a polished PLZT prism

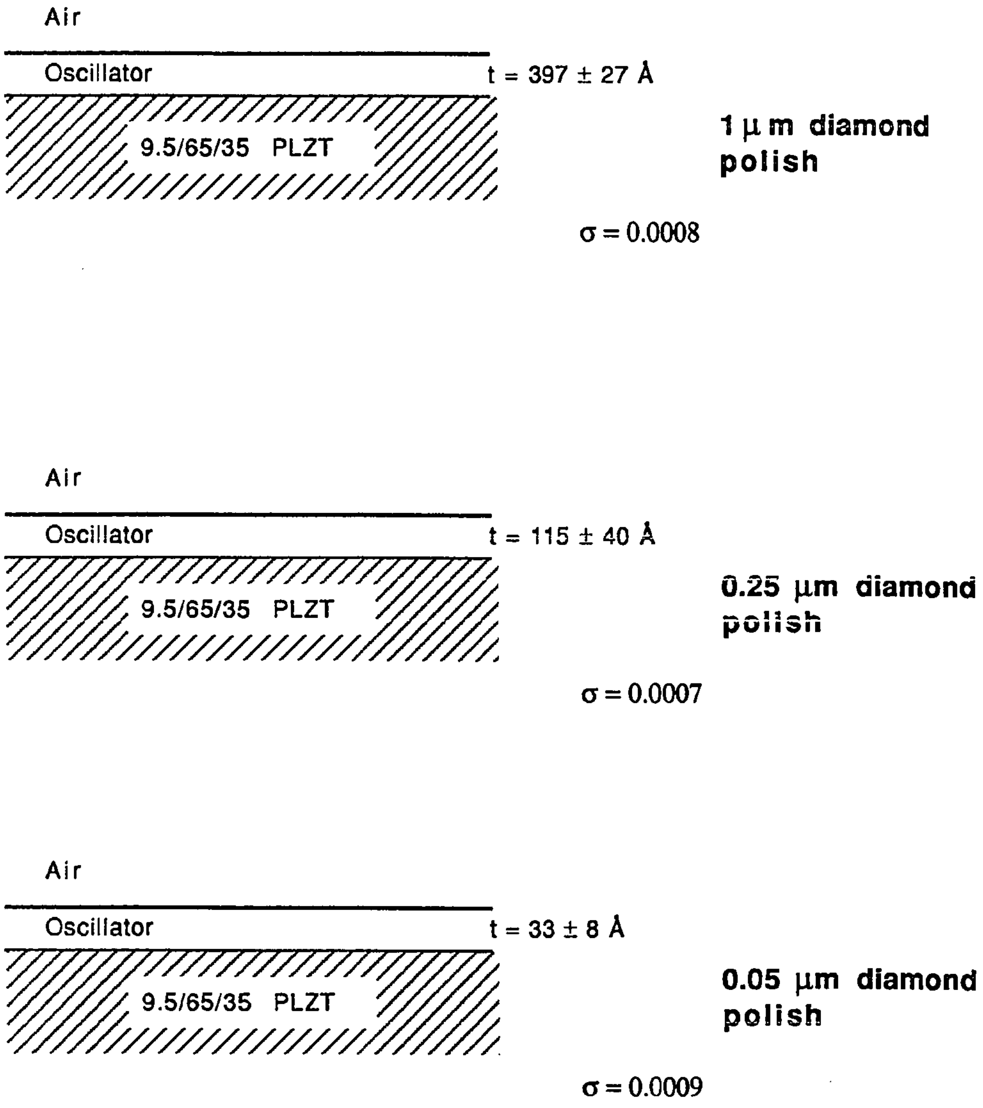

Fig. 4.18: Modelling of the damaged layer on a PLZT prism as a function of the quality of the surface finish. (a) Best fit models for the surface layer on PLZT. (b) Surface layer refractive indices for the three different surface finishes

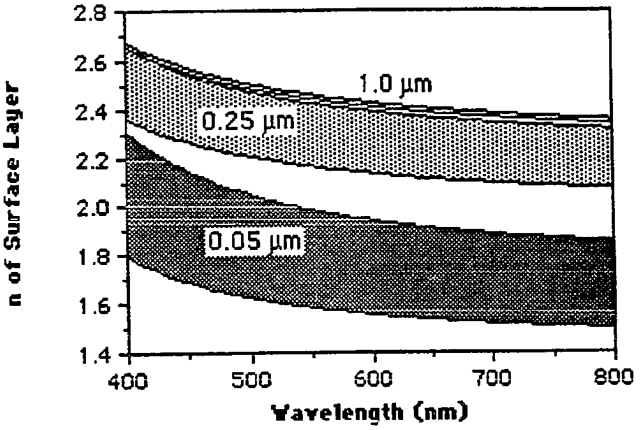

(b)

Fig. 4.18: Continued

damaged layer decreases with the polishing powder grit size. At the same time, the refractive index of the surface layer progressively decreased. Thacher describes as possible mechanisms for surface layer formation on PLZT materials lead loss, polishing damage, and any of the "various suggestions for the surface layer on $BaTiO_3$." The strong link between the layer properties in the polishing procedure demonstrated here suggests that mechanical damage is the dominant mechanism for lapped or polished materials.

In conclusion, it is possible to utilize spectroscopic ellipsometry to measure the bulk refractive index of ferroelectric materials, provided the quality of the surface finish is sufficiently high. One useful measure of the validity of the inversion process as a means of approximating transmission data on transparent materials is the magnitude of the Δ parameter. In general, the less influence the surface layer exerts on the ellipsometric spectra, the more closely Δ will approach 0° or 180° for transparent samples.

Conversely, investigation of surface layers on materials for which bulk reference data are available can also be performed ellipsometrically. As for the $BaTiO_3$ samples discussed earlier, the major contributor to defective surface layers on PLZT materials is damage introduced during the processing rather than fundamental changes in the ferroelectric properties at the surface. As suggested earlier, the existence of a surface layer of some type can often be confirmed visually by the presence of substantial Δ values, even when the curve for Ψ closely approximates that expected from bulk data. Consequently, characterization of either bulk or surface properties in transparent ferroelectric materials is greatly aided by the ability to measure Δ accurately throughout the spectral range.

CHAPTER 5

THIN FILM CHARACTERIZATION

During the course of this work, ferroelectric thin films prepared by several different techniques were characterized by spectroscopic ellipsometry. The results of these analyses have been subdivided into four major sections and will be presented in this chapter. Section 5.1 contains the depth profiles of epitaxial and well-oriented perovskite films prepared on single crystal substrates. There was no indication of a reaction between any of the oxide substrates and the ferroelectric films for any of the preparation methods investigated. In addition, it was shown that a high degree of X-ray orientation via lattice matching with the substrate is not, of itself, a guarantee of microstructural perfection for the film. In section 5.2 a comparison between Multi-Ion-Beam Reactively Sputtered (MIBERS) films on single crystal sapphire and platinum-coated silicon substrates is given, followed by a description of the film microstructure and its evolution as a function of *in-situ* annealing in the ellipsometer. The effect of the microstructure on the apparent dielectric constant and coercive field of an otherwise perfect film is subsequently discussed. Following that, section 5.3 reports results on *in-situ* annealing of sol-gel PZT films on Pt-coated silicon substrates. It is believed that the maximum values for the refractive indices of these films is governed by a competition between densification of the film and lead loss as a function of annealing time and temperature. Lastly, a series of sol-gel PZT films with thicknesses ranging from 500 to 4500Å is examined in section 5.4. The utility of spectroscopic ellipsometry in characterizing unknown, inhomogeneous films as a function of thickness is discussed.

5.1 Epitaxial and Oriented Films on Single Crystal Substrates

Lead lanthanum titanate films prepared on sapphire substrates by rf magnetron sputtering were kindly provided by H. Adachi of Matsushita Electric Co., Ltd. The film composition was ~ 20/0/100 for a 28/0/100 powder target, with a small degree of variability between depositions. In describing the composition, the notation x/y/1-y is used to indicate the addition of x mole percent La_2O_3 to $Pb(Zr_yTi_{1-y})O_3$. Such films were shown to be epitaxial with lattice matching between the {111} planes of the perovskite lattice and the basal plane (0001) of the sapphire substrate. Previous measurements on these films demonstrated exceptional electrical, piezoelectric, and electrooptic properties (Adachi et al. 1986).

SE data were taken on these films as a function of temperature at a fixed angle of incidence of 80°. Modelling was done using the anisotropic room temperature dielectric function for sapphire, and an isotropic damped oscillator of the form discussed in section 3.4.1.2 for the film. Anisotropy was not included in the film, despite the high degree of orientation, as $PbTiO_3$ has a fairly low initial birefringence (~0.03 - 0.01 between 400 and 700 nm)(Kleemann et al. 1986), and the addition of lanthanum has been shown to decrease the birefringence still further in La-modified lead zirconate titanate (PLZT) materials (Land et al. 1974). Given the large La content in the film, it was judged that the standing birefringence would be quite low and the isotropic approximation should be a good one.

With this film, as with the remainder of those discussed in this chapter, several geometries were tried to determine whether inhomogeneities were important in modelling the optical data. Included among the possibilities were surface roughness and/or a low density layer located either near the film/substrate interface or at some point in the middle of the film. Once an initial geometry was chosen, additional layers were incorporated into the model to mimic either graded changes or further inhomogeneities. The process was stopped when no further reduction in σ could be achieved without increasing the 90% confidence intervals unrealistically.

Figure 5.1 shows the best fit to the experimental data of the $(Pb,La)TiO_3$ film between 400 and 750 nm, in addition to the variation of all of the parameters with temperature. Structurally, the film is quite homogeneous, with only a thin layer of roughness superimposed over the bulk of the film. No reaction layer between the film and the substrate could be detected. In particular, there is no indication of the Ti and TiO_2 segregation near the substrate discussed by Tomashpolski (1978a, b) for $BaTiO_3$ films deposited at high temperatures on sapphire. Such layers would also be inconsistent with the observation of epitaxy between the film and the substrate.

A comparison of the calculated refractive index of the lower layer with literature data (Fig. 5.2) shows that the general level of n is comparable to that of single crystal $PbTiO_3$, suggesting that the bulk of the film is dense. The additional dispersion of the lanthanum-doped film is consistent with previous reports for the effect of La additions on the refractive index of glasses (Rawson 1980). As is typical of perovskite ferroelectrics, the refractive index increases slightly with temperature. No anomaly in the refractive index is observed for the lead lanthanum titanate film on passing through the transition temperature range (~110 - 140°C) (Fig. 5.2b), which is reasonable in light of the comparatively small spontaneous polarization and the breadth of the transition range.

The comparatively high values for k shown in Fig. 5.2b are due in part to failure of the oscillator model to completely describe the absorption edge. If the data set is progressively truncated to eliminate the high energy measurements and remodelled, the parameter A(4), which controls the imaginary part of the dielectric function, decreases continuously. As a result, the calculated k values also decrease throughout the spectral range (see part c of the same figure). At the same time the modelled refractive index was independent (within the 90% confidence limits) of the width of the data set. The

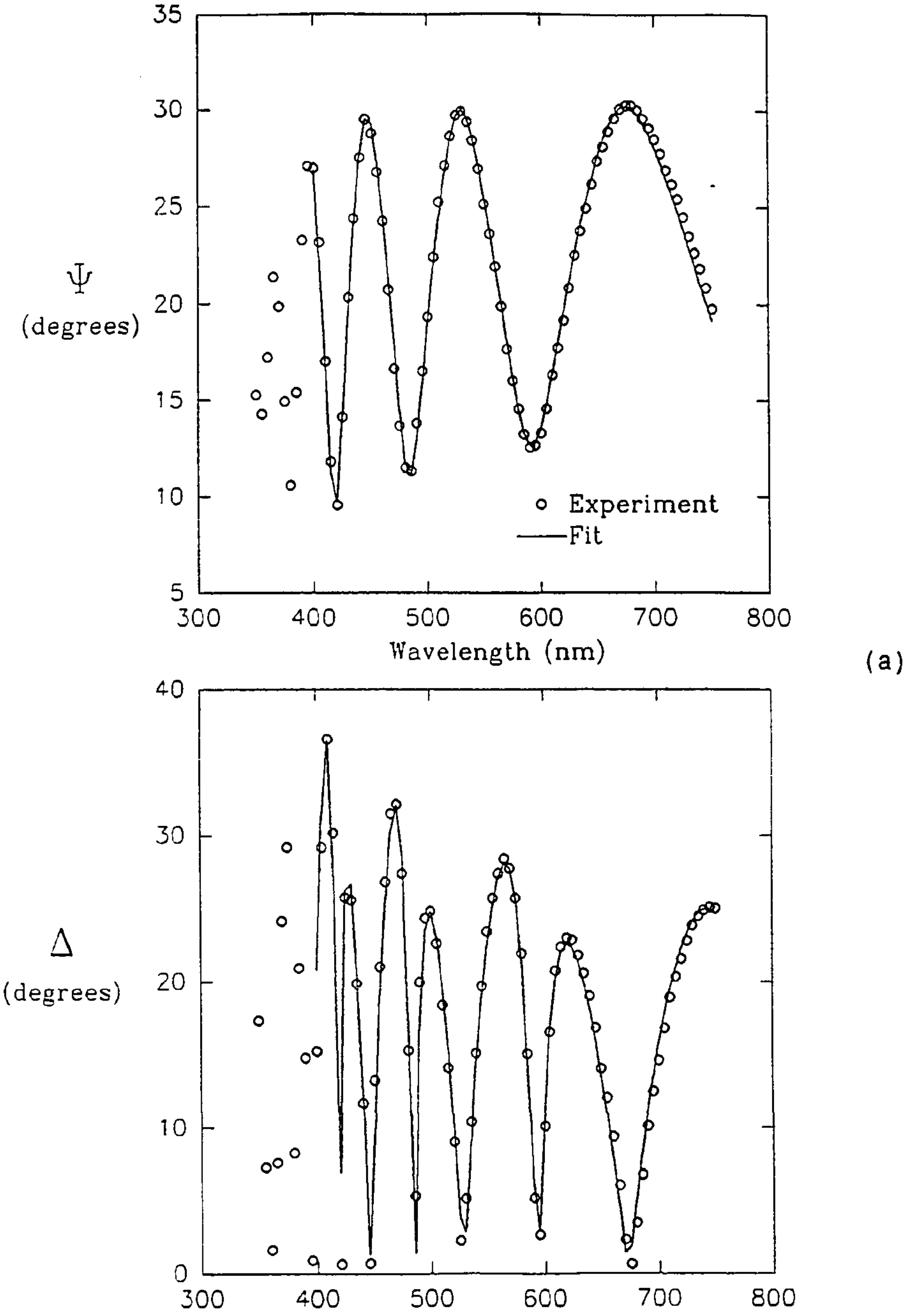

Fig. 5.1: Modelling for an epitaxial (Pb,La)TiO_3 film on (0001) sapphire. (a) Comparison of modelled and experimental ellipsometric spectra. (b) Model and change in the modelling parameters and σ as a function of temperature

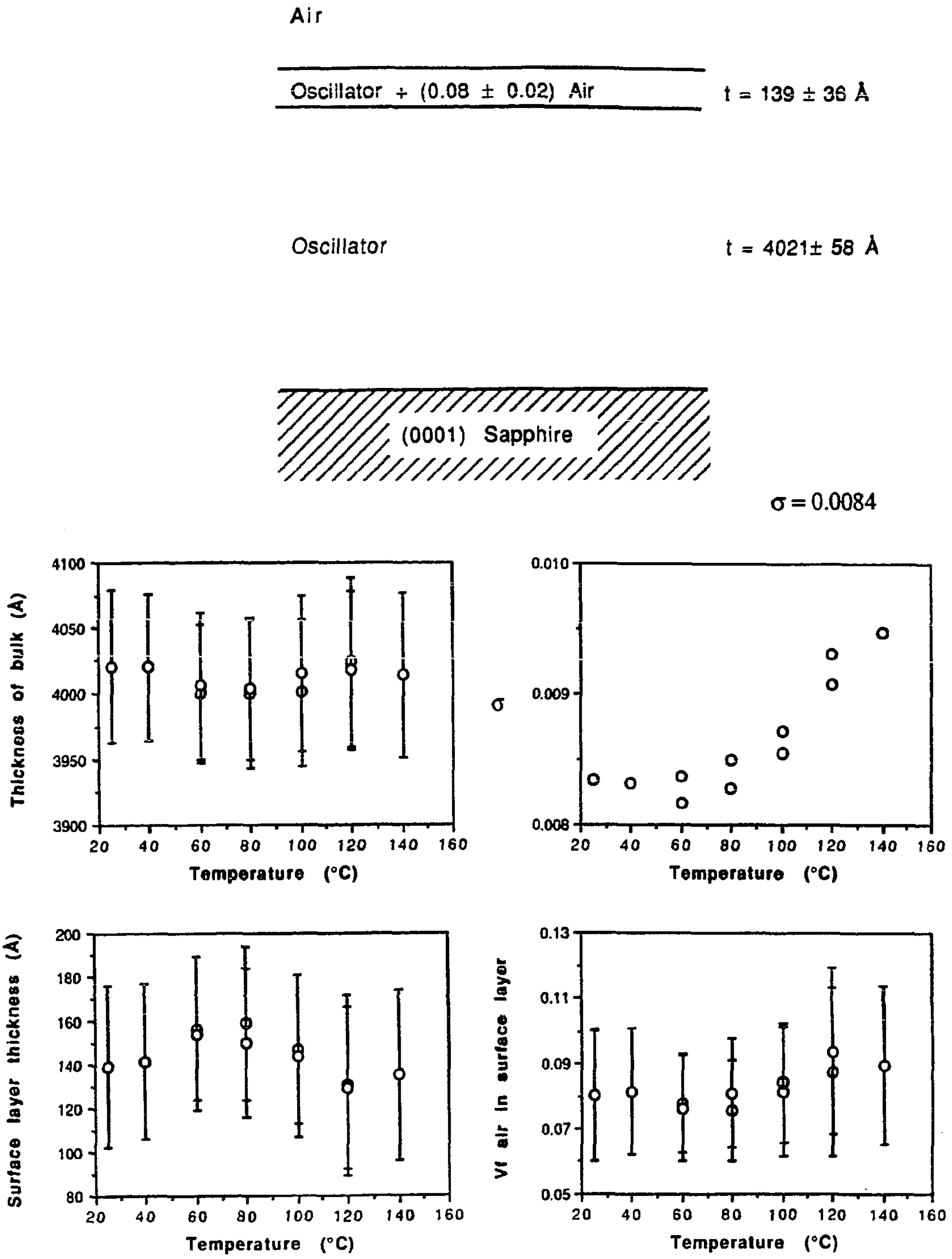

Fig. 5.1: Continued

(b)

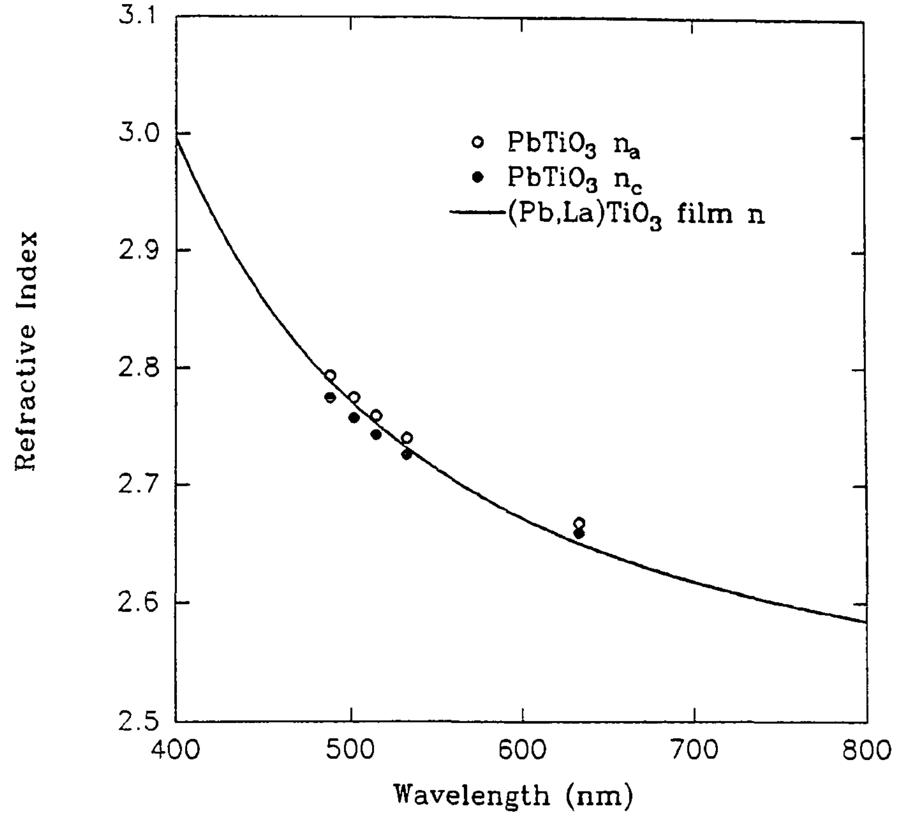

(a)

Fig. 5.2: Optical properties of an epitaxial $(Pb,La)TiO_3$ film on (0001) sapphire (a) Comparison between the ellipsometrically-derived refractive index for the film and literature data for $PbTiO_3$ (b) Optical properties of the film as a function of temperature (c) Modelled k for different spectral ranges

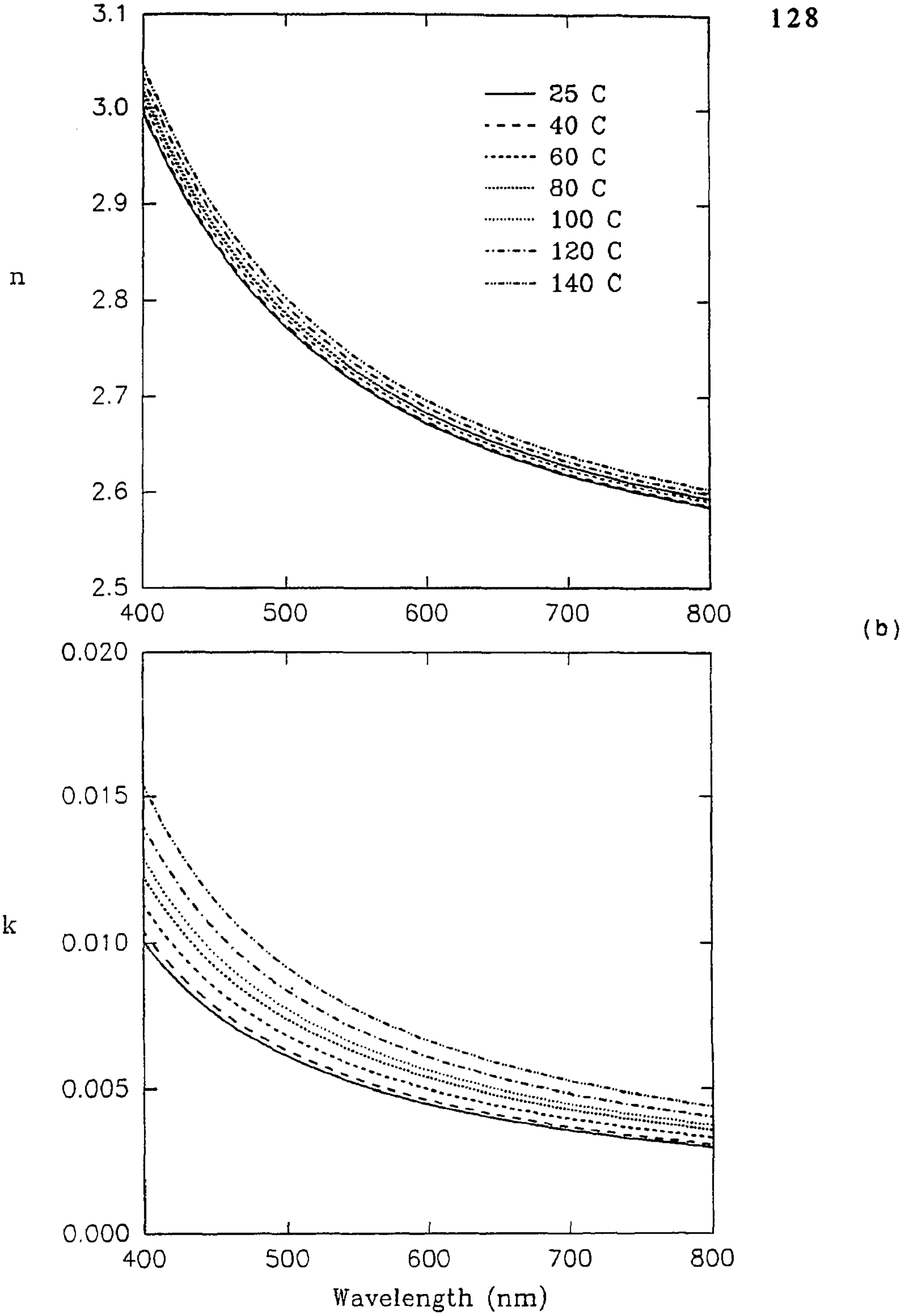

Fig. 5.2: Continued

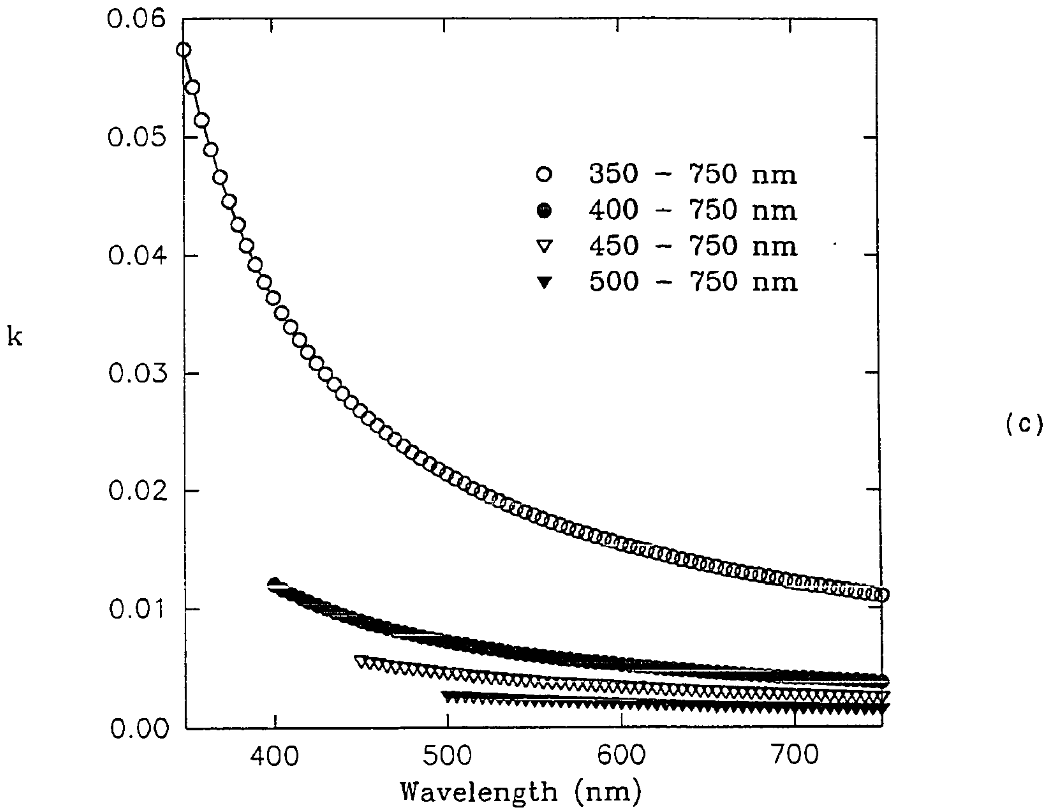

Fig. 5.2: Continued

thin layer of surface roughness, however, became indeterminate when the data set was truncated to 500-750nm. It is believed that the changes in the apparent k values for data sets with different energy ranges is due to the inability of the single oscillator model to mimic the rapid rise in optical absorption as the edge is approached, while simultaneously describing the dispersion in the refractive index correctly. In order to maintain consistency throughout this thesis, all remaining data sets for thin films were truncated to 400-800nm to strike a balance between the maximum number of data points and the elimination of the onset of absorption. This is not expected to provide any systematic errors as a function of film composition as the absorption edges of all the lead based perovskites occur at approximately the same energy (Land et al 1974).

None of the physical parameters describing the thicknesses or the void fraction of air in the surface layer show significant variation with temperature as the ferroelectric-paraelectric transition is approached (the film shows a broad dielectric maxima between ~110 and 140°C). Consequently, the two layer model is probably physically correct and not an artifact of any losses in the material associated with its ferroelectricity (such as scattering at domain walls). On the other hand, the temperature independence of all of the physical parameters suggests that intrinsic size effects, which should be tied to the polarization, and hence would vary with temperature, are not essential in fitting the optical data. This, in turn, implies that even with the relatively pristine surface of this thin film, intrinsic size effects probably do not dominate the properties of a film ~4000Å thick.

While this epitaxial lead lanthanum titanate film is nearly dense throughout its thickness (excepting the small degree of surface roughness), not all well-oriented ferroelectric films display such a high degree of homogeneity. An example of the latter possibility is the sol-gel $PbTiO_3$ film on (001) $SrTiO_3$ made at the Materials Research Laboratory by Dr. Keiko Kushida of the Hitachi Central Research Laboratory. This film was prepared from alkoxide precursors following the procedure described in the paper by Kushida et al. (Kushida et al. 1992). A 0.19 M sol to which four volume percent formamide had been added was spun onto the substrate, and the organics were removed during a 10 min 400°C pyrolysis step. Final firing was performed at 700°C for 4 hr. While the resultant X-ray pattern demonstrates excellent c-axis orientation of the $PbTiO_3$ (Fig. 5.3), an SEM micrograph shows that the film surface consists of discrete grains and is, as a result, both rough and porous (Fig. 5.4). The value for the volume fraction of porosity at the surface of the film was estimated to be near 35% from the intercept method on the SEM photograph.

This imperfect microstructure was confirmed by SE studies on the same film. Data were taken with an achromatic compensator at an incidence angle of 80°. For modelling, the data set was truncated to 400 - 800 nm to eliminate the onset of the absorption edge in $PbTiO_3$. Room temperature reference data were utilized for the $SrTiO_3$ substrate, and a polycrystalline average of reference data on $PbTiO_3$ for the film. Figure 5.5 shows the comparison between the best fit one and two layer models and the experimental data. Again, there was no indication from the ellipsometric data of any reaction layer between the film and the substrate. Although the one layer model approximates the Ψ spectrum, it is clear that the peak heights in Δ cannot be mimicked properly under the assumption that the film is homogeneous throughout its thickness. Consequently, the film seems to require at least a two layer model.

In all cases, fits to this film required a large volume fraction of air to be mixed with the optical properties of the $PbTiO_3$. This is consistent with the high degree of porosity evident in the SEM micrograph of the sample. It should also be noted that the ellipsometric study was performed "blind", so that the modelling was completed before access to the SEM photograph. While the agreement between the two characterization techniques is itself encouraging, it is especially noteworthy that reasonable results were obtained for a film with a very poor microstructure. This success may be due, in part, to the fine primary particle size (~50 - 150nm) in the film. That is close to the

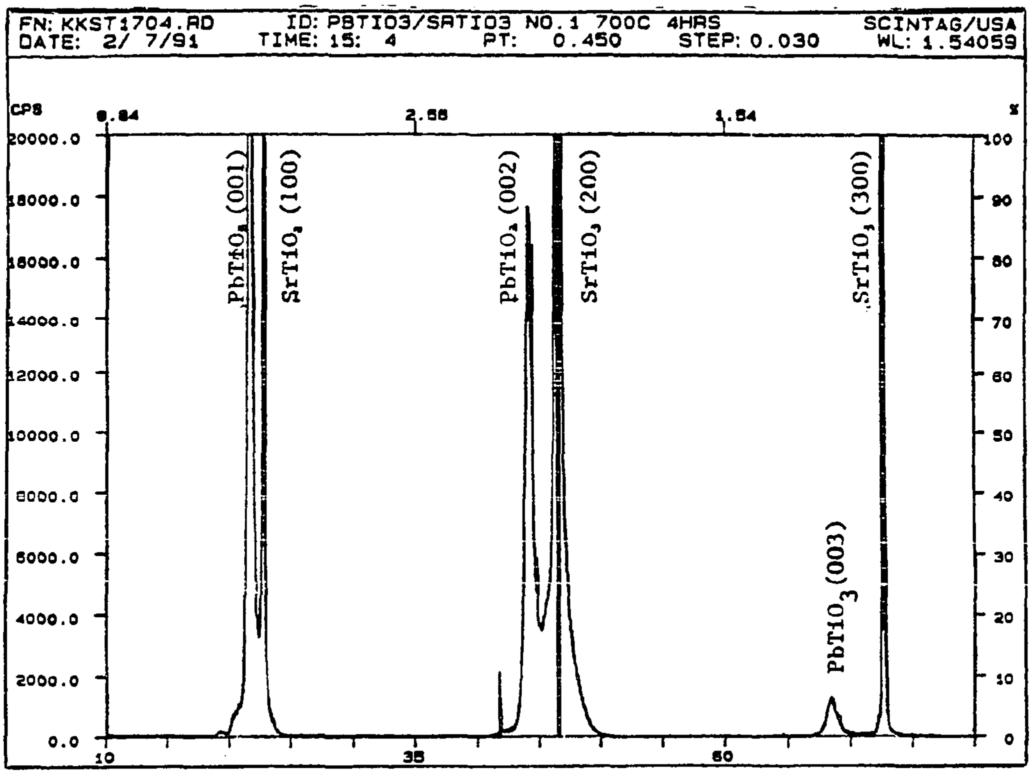

Fig. 5.3: X-ray diffraction pattern of a sol-gel $PbTiO_3$ film on (100) $SrTiO_3$. The film was annealed at 700°C for 4 hours

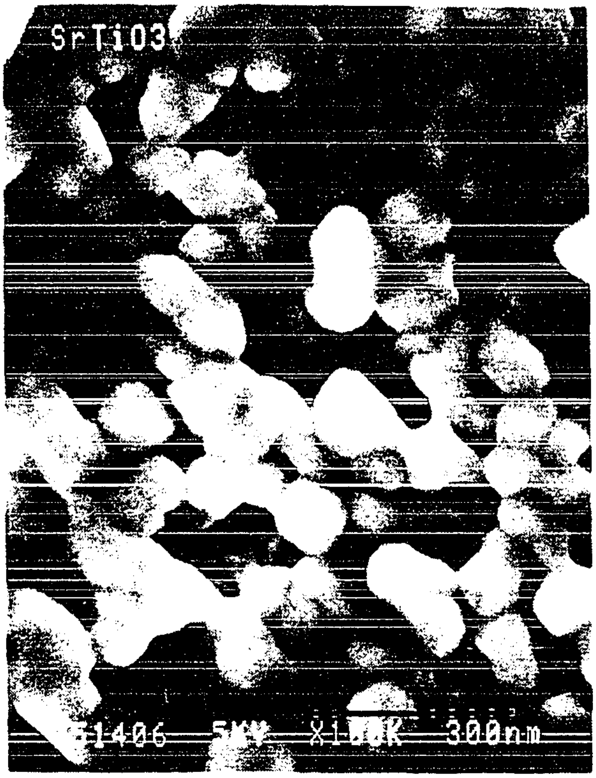

Fig. 5.4: SEM micrograph of the top surface of a well-oriented (001) $PbTiO_3$ on (100) $SrTiO_3$

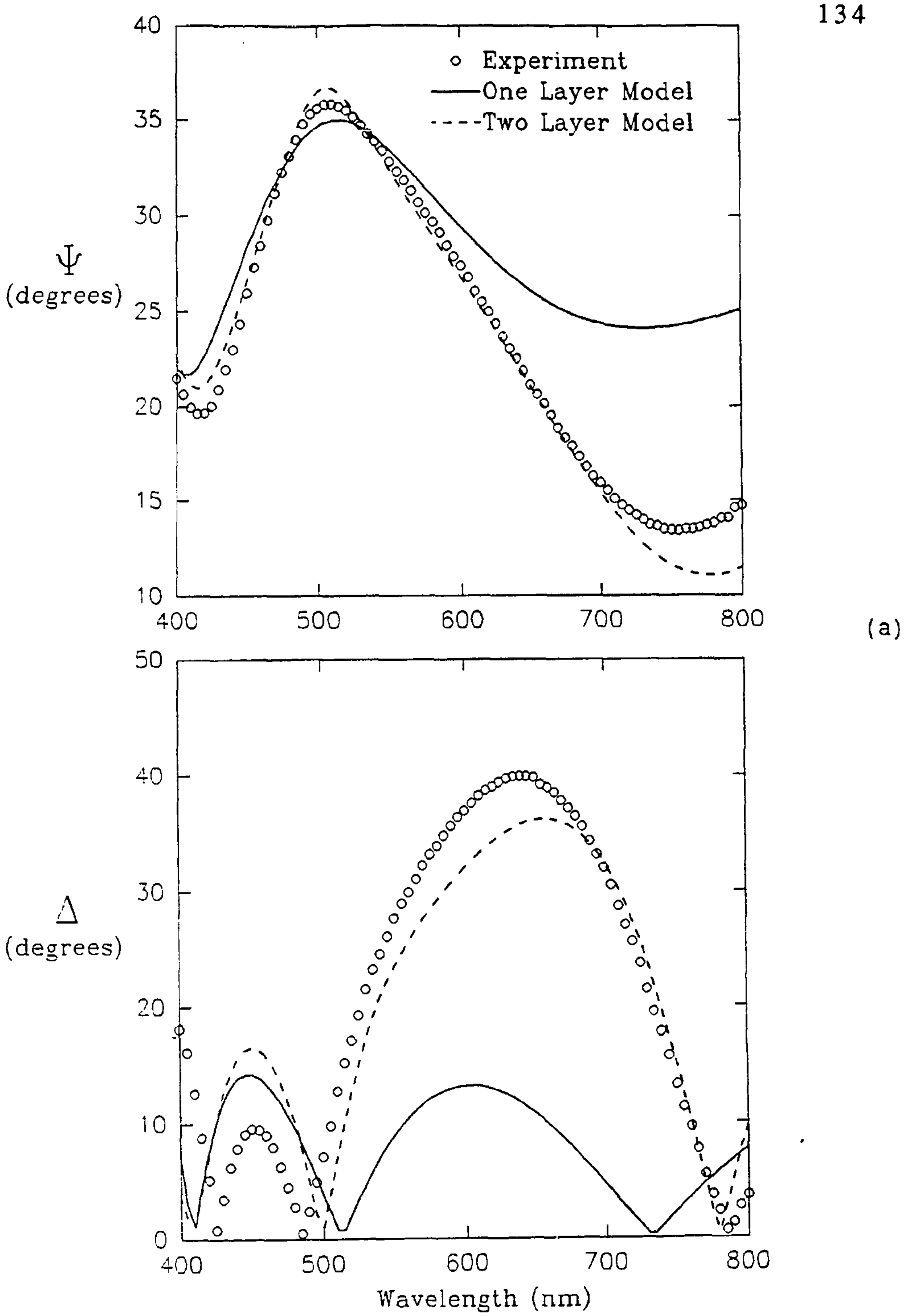

Fig. 5.5: One and two layer models for a well-oriented (001) $PbTiO_3$ on (100) $SrTiO_3$
(a) Fit to ellipsometric data (b) Models

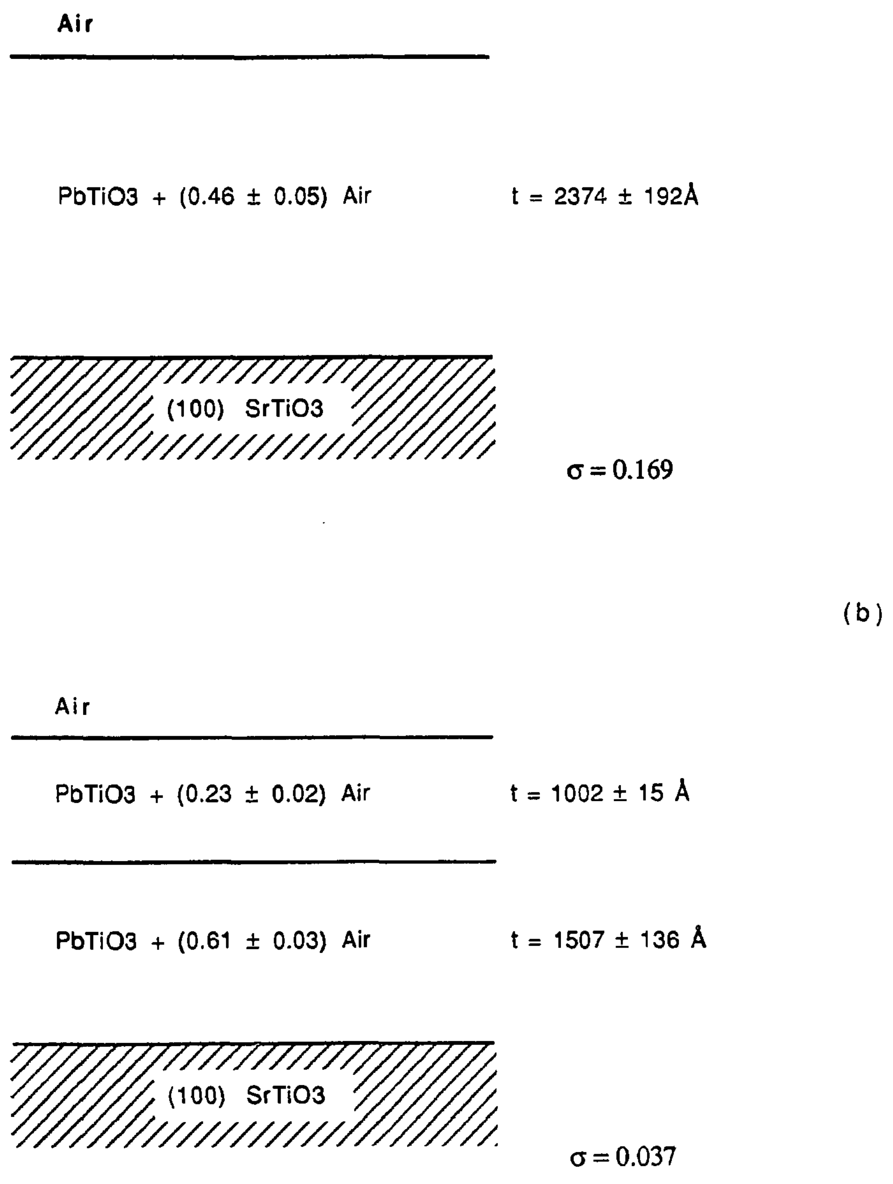

Fig. 5.5: Continued

diameter/ light wavelength ratio of ~0.25 suggested as the limit below which the Bruggeman effective medium approximation is valid in reflection measurements (Egan and Aspnes 1982).

The density of this film is much lower than those of the other sol-gel films discussed in this thesis. The principal differences in the processing between this and the other samples were the addition of formamide to the sol and the duration of the high temperature anneal. While a long anneal might be expected to increase the surface roughness as grain growth proceeded, it is unlikely that it would cause the high porosity values seen throughout the film thickness. Formamide is usually added to sol-gel formulations to control the drying by producing larger and more uniform pores. It is possible that, perhaps because of the formamide addition, the organic phase in this film was not completely removed during the pyrolysis step.

If this occurred,the film would not have collapsed completely after the pyrolysis step. Several authors have shown that when crystallization of a sol-gel film occurs before densification, the resulting film incorporates much higher porosity levels than films which are densified prior to crystallization (Keddie and Giannelis 1991). The porosity can appear either between or within individual crystallites. Consequently, it seems possible that the poor microstructure of this sol-gel $PbTiO_3$ on $SrTiO_3$ is associated largely with the processing, rather than to any inherent limitation on the density of sol-gel ferroelectric films.

It should be noted that a determination of the film inhomogeneity would be much more difficult if accurate data for Δ were not available over the full wavelength range. Consequently, use of the effective source correction and an achromatic compensator greatly extends the characterization capabilities of spectroscopic ellipsometry for transparent materials on transparent substrates. The importance of accurate measurement of Δ in depth-profiling transparent systems was previously reported by Chindaudom (Chindaudom 1991).

5.2 MIBERS PZT 50/50 Films

Stoichiometric PZT films with a Zr/Ti ratio of about 50/50 were deposited by a multi-ion-beam reactive sputtering (MIBERS) system which has been described in detail elsewhere (Hu et al. 1992). As substrates for the deposition of oriented films, both $(1\bar{1}02)$ and (0001) sapphire were used (One side polished, Union Carbide). In addition, platinum-coated silicon wafers were also utilized as substrates for some films. These substrates had a thick SiO_2 barrier layer to prevent reaction between platinum and silicon at elevated temperatures, and a thin Ti layer between the SiO_2 and the Pt to improve adhesion. Ellipsometric spectra were collected for such substrates, and the data were inverted directly to provide effective dielectric functions for the substrates.

The ferroelectric film deposition was carried out on unheated substrates without secondary ion bombardment. It was observed, however, that the substrate temperature rose to about 100°C during deposition due to intrinsic bombardment by the sputtered species. The as-deposited films were basically amorphous. Two films on sapphire and one on platinum were reserved for *in-situ* ellipsometric studies. The remaining films were heated *ex-situ* at 10°C/min to 650°C and soaked at this temperature for 2 hours. This procedure yields well-crystallized perovskite films. All films deposited on sapphire show highly oriented X-ray diffraction patterns after annealing. Films on $(1\bar{1}02)$ substrates, as seen in Fig. 5.6, were almost exclusively (101) oriented. Similarly, with (0001) substrates, the films also assumed (101) orientation, although to a lesser degree. Films on Pt-coated silicon, by contrast, had a random polycrystalline orientation.

Hysteresis loops for the films on Pt-Si were measured with sputtered gold upper electrodes.

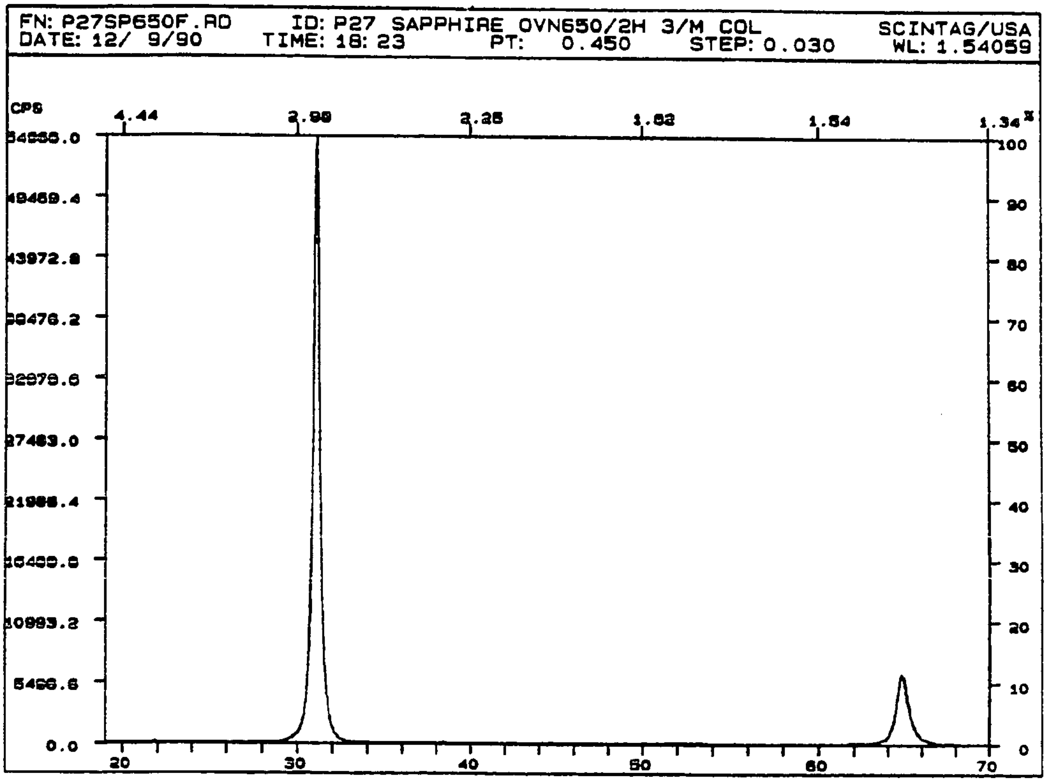

Fig. 5.6: X-ray diffraction pattern of a MIBERS 50/50 PZT film on $(1\bar{1}02)$ sapphire. Film annealed at 650°C for 2 hrs

5.2.1 Comparison between MIBERS films on Sapphire and Pt-Coated Silicon

SE measurements made on the Pt-coated Si substrates prior to film deposition showed that the surfaces of these substrates consisted of roughened platinum (typically 50-100 Å consisting of ~85% Pt and 15% air. Unfortunately, the degree of roughness changed as the substrates were heated, so the reference effective dielectric functions for the substrate itself were uncertain. This, in turn, limited the accuracy with which the refractive indices of the PZT films on Pt could be measured. No appreciable roughness could be detected for the sapphire substrates.

For the modelling, the data sets were truncated to between 400 and 800 nm in order to eliminate the onset of the fundamental absorption edge. This was necessary as the oscillator model, even with a damping term included, breaks down as the edge is approached. Results from the ellipsometric modelling obtained for the reduced data sets are shown in Table 5.1. All of the films were between 4000 and 6000 Å thick, with the majority of the film being homogeneous. In all cases, however, addition of a porous interfacial layer between the substrate and the film was essential to properly match the peak heights in both the Δ and Ψ spectra. In addition, a thin, optically lossy layer, modelled as surface roughness, improved the fit. As seen in Figure 5.7, the final fits resulted in very good matches to the experimental data. In spite of these inhomogeneous regions, the majority of the film appears to be fairly dense.

Attempts to model the bulk of the film with residual porosity were unsuccessful due to the strong correlation between the dispersion parameters and the volume fraction of air. Nevertheless, when this was tried, the volume fraction of air in the majority of the film converged to a small percentage (~2 ± 2%) and so was neglected in the first stage of the modelling. This seems justified for the film on (0001) sapphire in light of the high value for the refractive index and the low effective absorption coefficient (both

Table 5.1: Best-fit parameters for the modelling of MIBERS PZT films annealed at 650°C for 2 hours.

	Surface Roughness Vf Air	Surface Roughness Thickness (Å)	Middle Layer Thickness (Å)	Bottom Layer Vf Air	Bottom Layer Thickness (Å)	σ
PZT on (0001) Sapphire	0.07±0.02	183±52	4785±98	0.08±0.01	839±38	0.005
PZT on $(1\bar{1}02)$ Sapphire	------	------	5481±66	0.08±0.01	624±47	0.006
PZT on $(1\bar{1}02)$ Sapphire	------	-----	5803±27	0.12±0.01	538±13	0.003
PZT on Pt-coated Silicon	0.21±0.03	1092±26	5575±188	-----	-----	0.12
PZT on Pt-coated Silicon	0.15±0.02	1077±39	5220±259	0.14±0.06	563±185	0.079

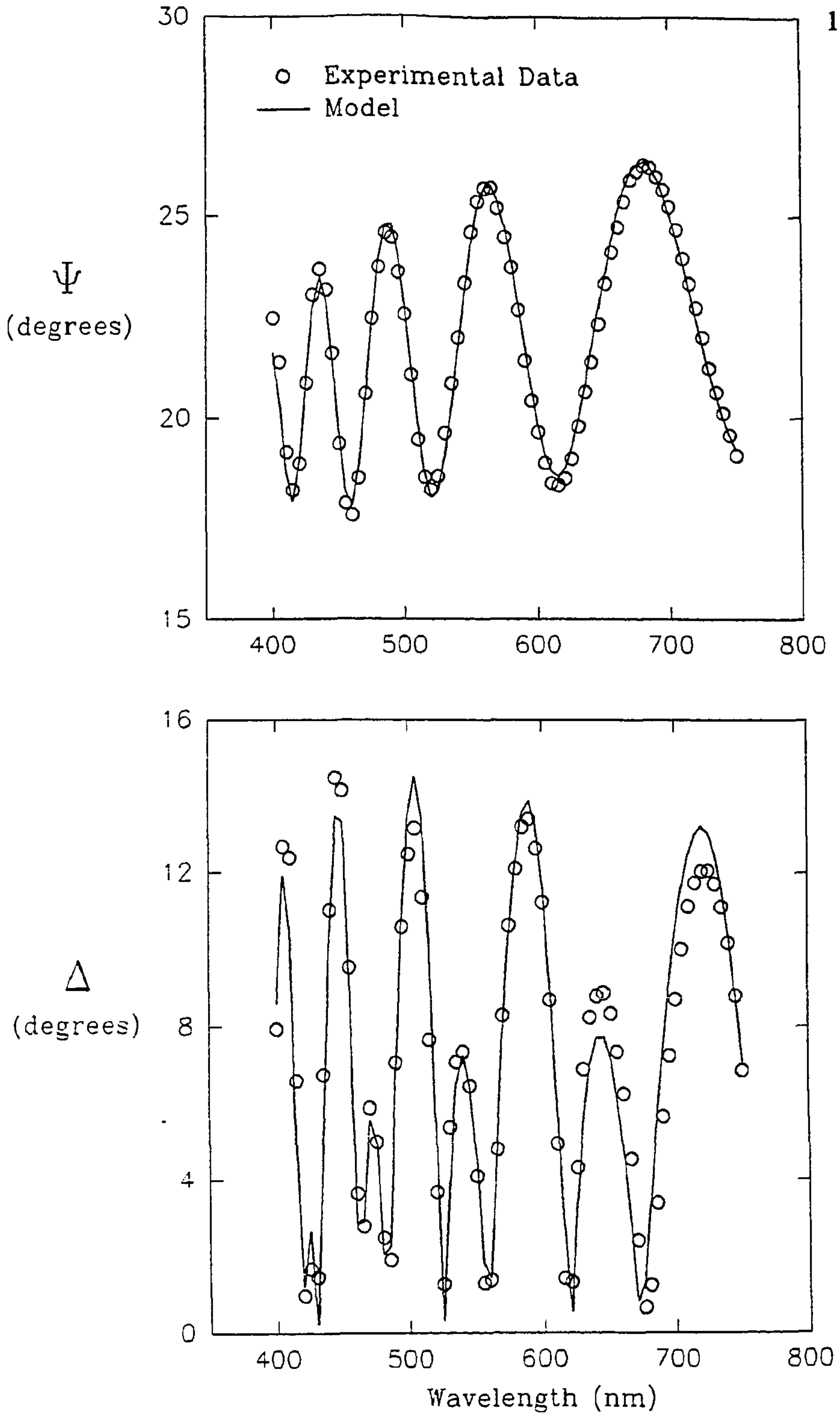

Fig. 5.7: Fit to MIBERS 50/50 PZT on (0001) sapphire.

corrected to eliminate the effect of the film inhomogeneity) obtained (see Fig. 5.8). The smaller refractive indices calculated for the films on $(1\bar{1}02)$ sapphire might be due to either the presence of residual porosity or an inability to properly account for the substrate anisotropy. When such films were fit with reference data derived from the film on (0001) sapphire, 5.7% porosity was required throughout the bulk of the film to fit the experimental data.

In comparison with Thacher's minimum deviation data on La doped PZT ceramics (Thacher 1977), the refractive indices shown in Figure 5.8 are too dispersive and in the case of the films on $(1\bar{1}02)$ substrates, too low. The apparent additional dispersion present in the MIBERS films is not an artifact of the breakdown of the oscillator model as the absorption edge is approached, but appears to be tied to the assumption of a non-zero value for the film absorption coefficient. When the current films were modelled with A(4) = 0, the oscillator position shifted from 242 nm to 213 nm, close to Thacher's value of ~212 nm for ceramics with a similar Zr/Ti ratio. Decreasing the wavelength for the oscillator position pushes the absorption edge to higher energies, lowering the dispersion and the real part of the refractive index. In Figure 5.9, it is apparent that artificially imposing a zero absorption coefficient on the PZT films used in this study, moves the derived value for the refractive index much closer to Thacher's data on PLZT throughout the visible portion of the spectrum, where minimum deviation data are very accurate. Coupled to this improvement in n, however, is a doubling of the σ parameter describing the difference between calculated and experimental Δ and Ψ values.

Unlike the lead lanthanum titanate film discussed in section 5.1, the finite values for the imaginary part of the refractive index in the MIBERS PZT films actually increased slightly as the high energy ellipsometric measurements were eliminated from the fitting. Consequently, the k values, like the additional dispersion in n, are not due to a breakdown of the oscillator model. In part, the larger k values reflect the fact that transparency in lead-based perovskites decreases as the lanthanum content is reduced.

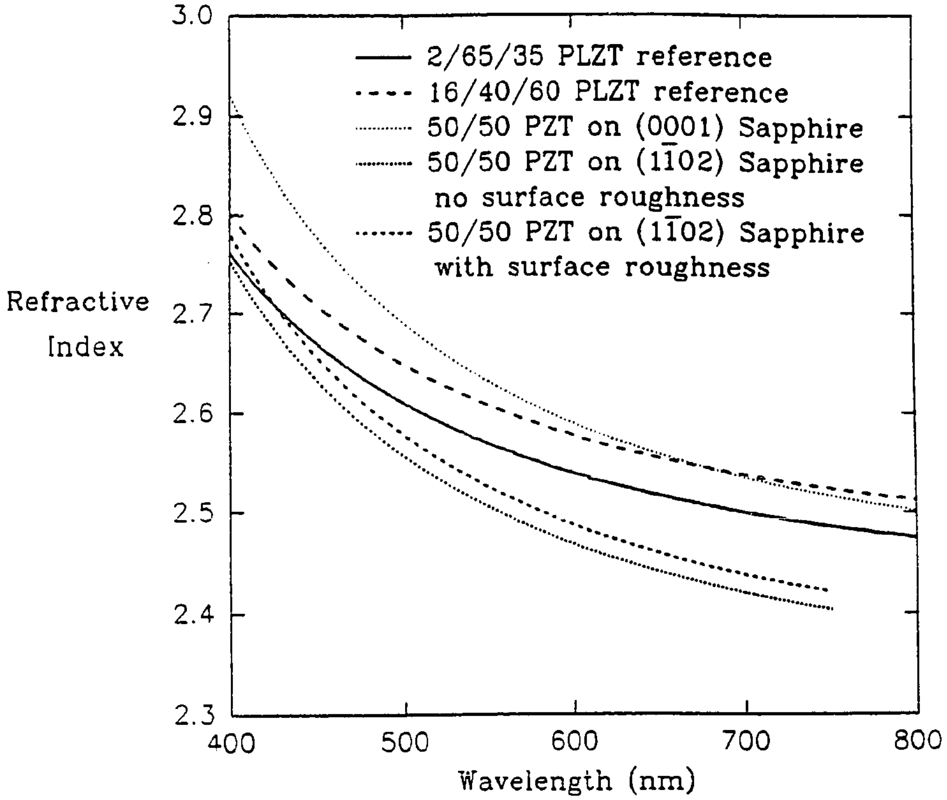

Fig. 5.8: Comparison between the refractive index of MIBERS 50/50 PZT films and PLZT ceramics. (Note: Thacher has demonstrated that the refractive index of PLZT ceramics is largely controlled by the Zr/Ti ratio, and that the La content does not change n much [Thacher 1977])

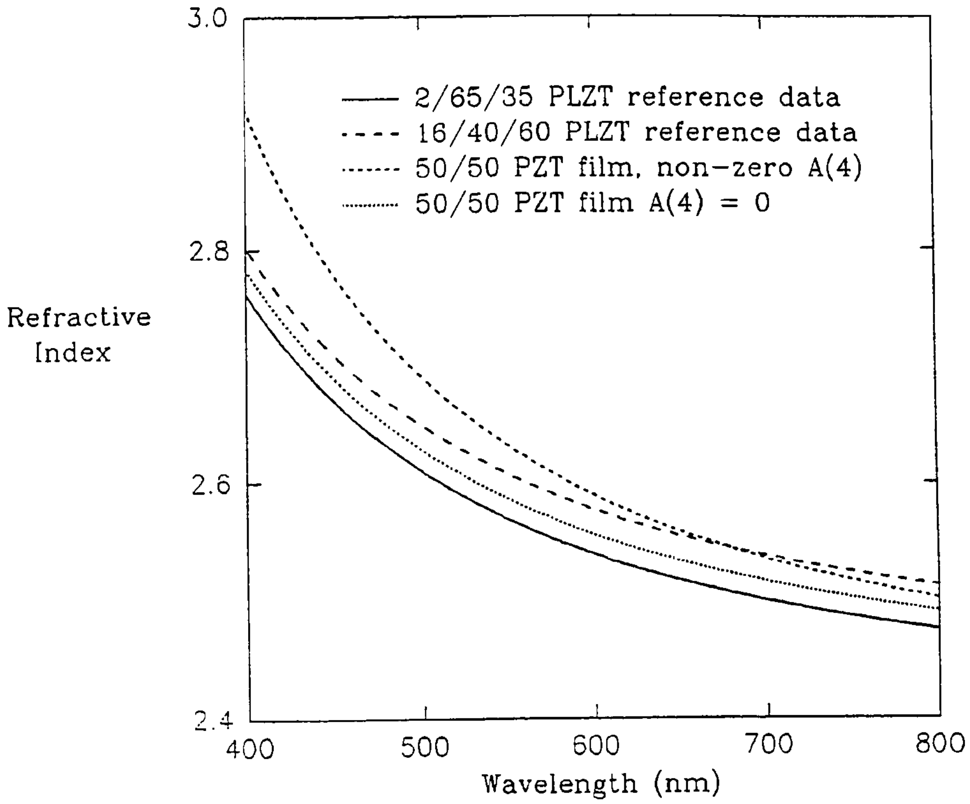

Fig. 5.9: Refractive index of a MIBERS 50/50 PZT film modelled with and without absorption

The opacity of dense, bulk PZT ceramics has been attributed to light scattering at refractive index discontinuities such as domain walls and the grain boundaries consisting of a second phase. It is likely that the same mechanisms are present in the MIBERS films. In addition, there are probably "microstructural" contributions to the effective k which arise from inhomogeneities in the film not accounted for in the modelling (i.e. scattering from distributed porosity in the bulk of the film, the presence of a lossy layer associated with either space charge formation or lead loss during firing, or the presence of additional porosity in the film not properly accounted for in the modelling). These may also influence the differences between n values modelled with and without an absorption coefficient.

Figure 5.10 shows a comparison of the cross-sections of PZT films annealed under the same conditions on Pt-coated Si and (0001) sapphire substrates. Both are densest through most of the thickness of the films, with low density layers near the substrate and some surface roughness. This observation suggests that MIBERS PZT films annealed in this way may possess the columnar or cluster morphology characteristic of many thin films (Yang 1988). For the same annealing conditions, films on Pt-coated silicon were considerably rougher than those on sapphire. That could be a result either of the higher initial degree of roughness of the sputtered Pt substrate or the higher initial PbO content in the film on platinum. As discussed by Yang et al. (1987) the roughness of a film with a columnar microstructure is dependent on the smoothness of the substrate: with rougher substrates leading to rougher films. However, Fox et al. (1992) claim that crystallization of the perovskite phase and PbO vaporization are at least as important in determining the microstructural features of annealed lead lanthanum titanate films. It was not possible to determine the refractive index of the film on platinum-coated silicon accurately due to uncertainties in the substrate optical properties. This will be discussed further in Chapter 6.

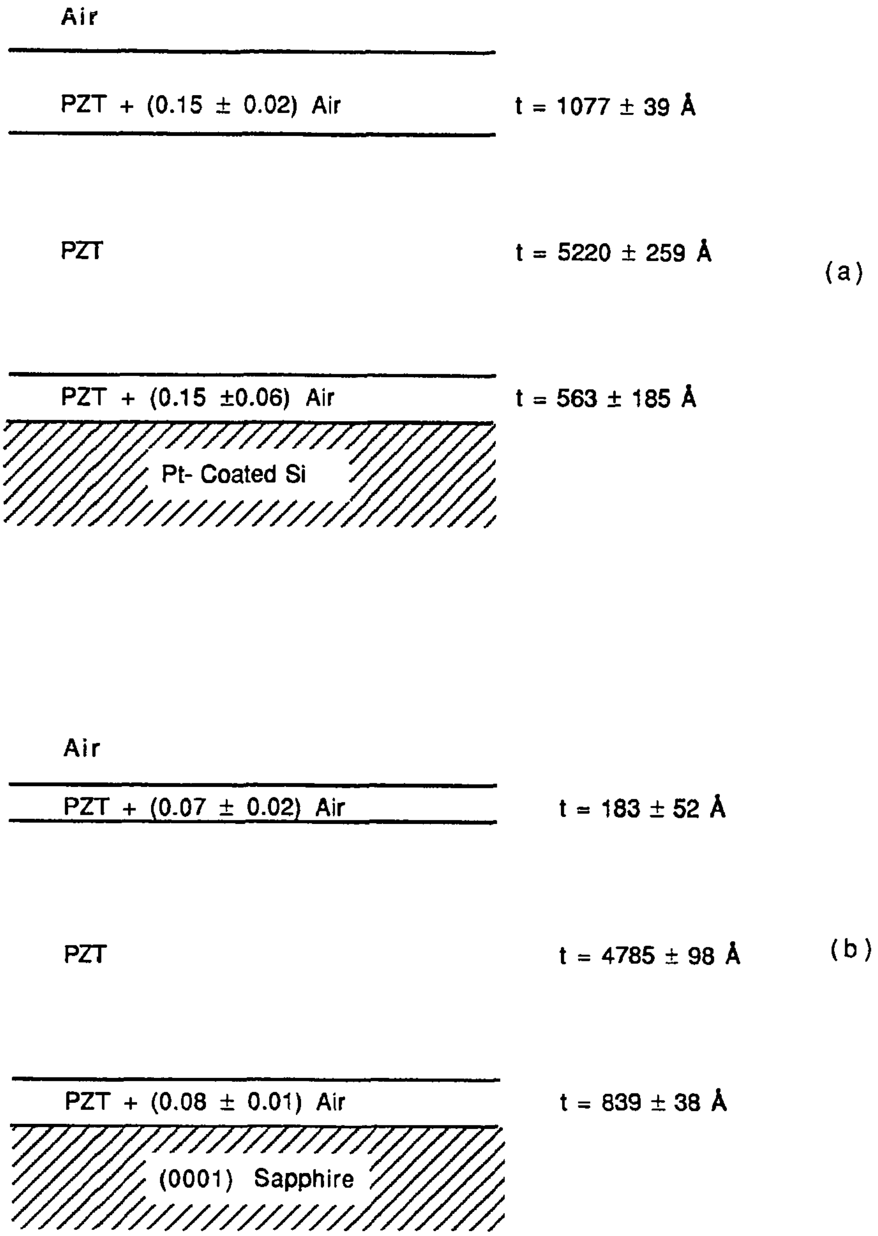

Fig. 5.10: Depth profile of the inhomogeneities in MIBERS 50/50 PZT films deposited on (a) Pt-coated silicon and (b) (0001) sapphire

5.2.2 Heating of Crystallized Films

Several crystallized MIBERS films were subsequently heated through the Curie temperature in order to examine the stability of the derived models with temperature. In most cases, no appreciable change in the modelling parameters was found between room temperature and 450°C. One example of this is found in Fig. 5.11a, where data for a film on Pt-coated silicon are presented. In one instance, however, the surface roughness of one film on $(1\bar{1}02)$ sapphire changed continuously between room temperature and 250°C, and was found to become indeterminate for temperatures ≥300°C, (Fig. 5.11b). At the same time, the "mass" for the layer of surface roughness (which is proportional to $(1\text{-}Vf_{air})^{*}$ Layer thickness) was approximately temperature independent within the 90% confidence limits, although it also became indeterminate above 250°C. True surface roughness, however, would not show any variation with temperature at such low temperatures. Consequently, on the basis of the measurements at elevated temperatures, it is clear that the layer of surface roughness is not justified in modelling the SE data. The fact that the interface roughness for the same film is nearly temperature independent suggests that the low density layer near the substrate is not an artifact of the modelling.

There are several possibilities which could be mimicked as a layer of apparent roughness which would be expected to become indeterminate as the transition temperature was approached. One of these would be the formation of a space charge layer. In order to determine whether the surface lossiness could be associated with space charge, the data for the film on the $(1\bar{1}02)$ substrate was remodelled assuming that the space charge could be regarded as a collection of free carriers. The Drude approximation was used to modify the damped oscillator describing the bulk of the film to simulate a high concentration of mobile carriers at the film surface. In order to make the model converge, it was necessary to assign the broadening parameter Γ to 0. Under

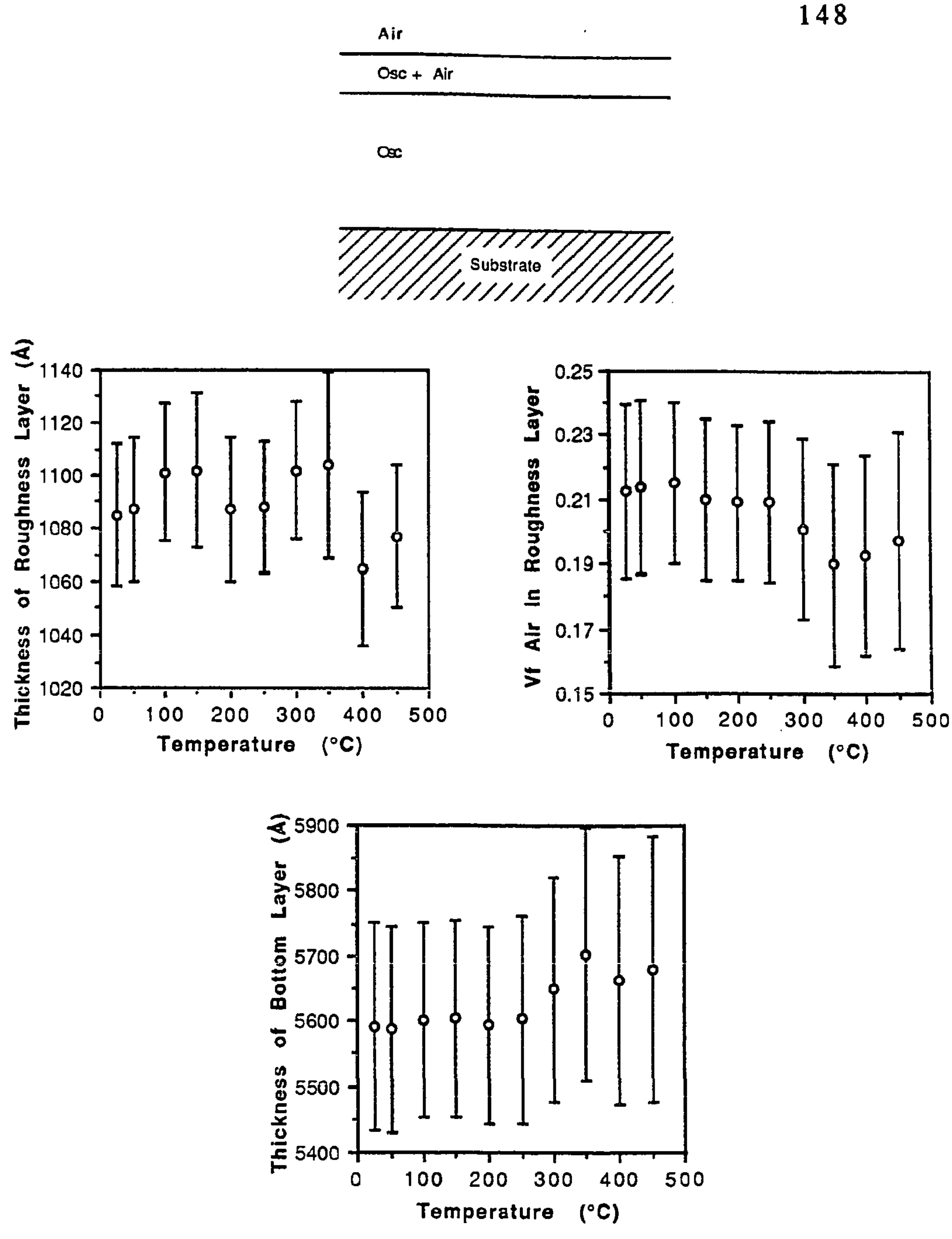

(a)

Fig. 5.11: The effect of temperature on the modelling for two crystallized MIBERS PZT films. (a) a film on Pt-coated silicon. (b) The apparent surface roughness of a film on ($1\bar{1}02$) sapphire

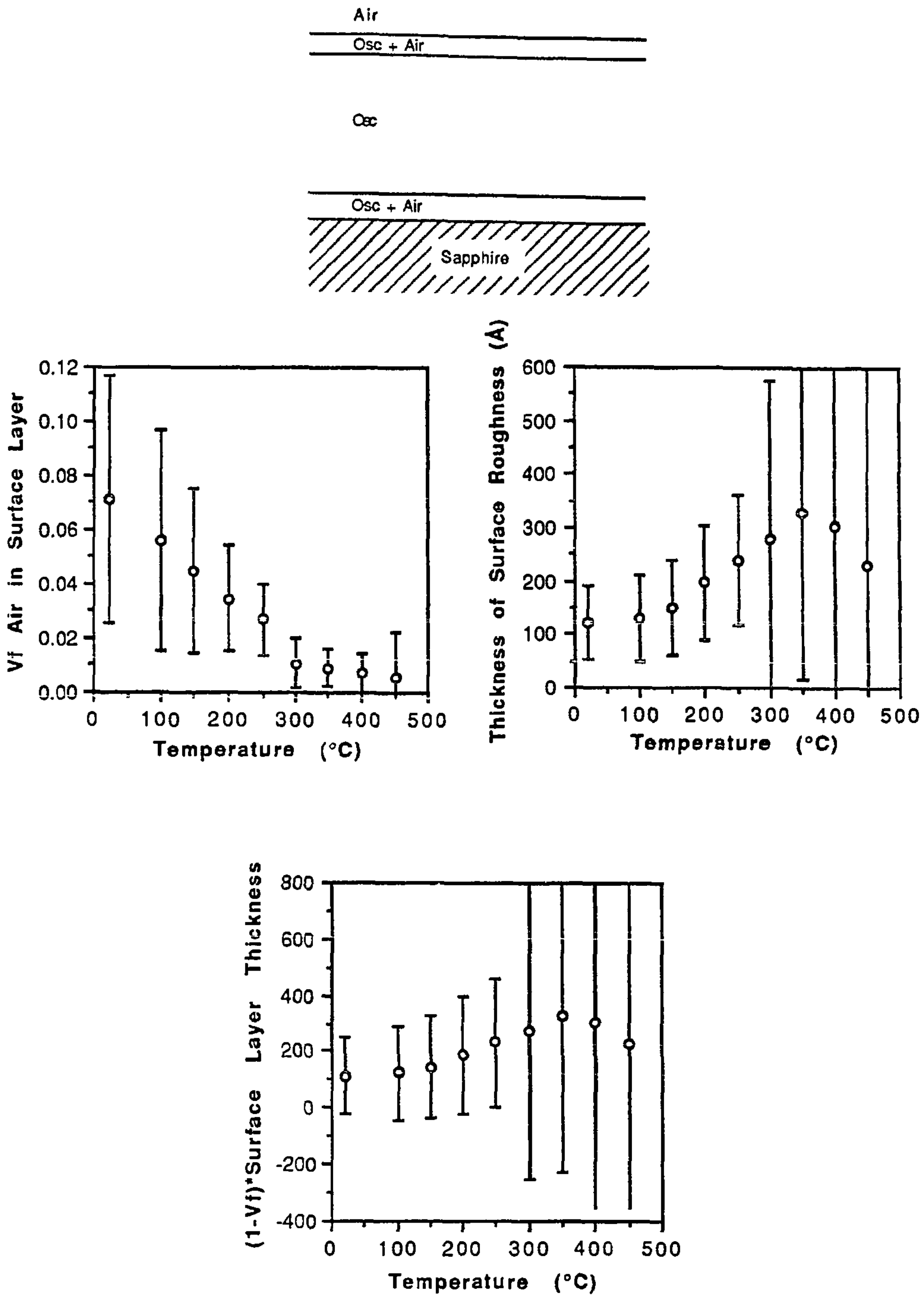

(b)

Fig. 5.11: Continued

these conditions, the best fit model consisted of a thin layer of lossy material over PZT as shown in Fig. 5.12. With increasing temperature, the lossy layer shrinks, and Ep, the parameter associated with the concentration of charge carriers, decreases, until at and above 250°C, both parameters become indeterminate. This is not unreasonable if the space charge accumulated to neutralize the polarization at the film surfaces.

A second possible explanation for the temperature dependance of the apparent optical lossiness is changes in the amount of scattering from domain or grain boundaries. Within a grain, PZT is optically anisotropic below the Curie temperature, with a static birefringence of ~0.02 - 0.04 at room temperature (Fushimi and Ikeda 1965). Grain boundaries and domain walls (except for those which separate 180° domains) thus demarcate regions where the optic axes are aligned differently. The resulting refractive index discontinuity at the boundaries scatter and depolarize light (Land and Thacher 1969). With increasing temperature the birefringence of each domain decreases, until at the Curie point, the material reverts to optical isotropy, and the extra scattering disappears.

In light of the small grain size of the PZT in the MIBERS films, the contribution to scattering from the domain walls was assumed to be small in comparison to the scattering from the grain boundaries (Land and Thacher 1969). Unfortunately, there is currently no acceptable means of calculating the effect that depolarization of the incident light beam (due to scattering) should have on ellipsometric data. Thus, it is possible that the loss of the apparent roughness in the MIBERS film could be traced to grain boundary scattering, though the very thin interaction length would imply that scattering should not be significant.

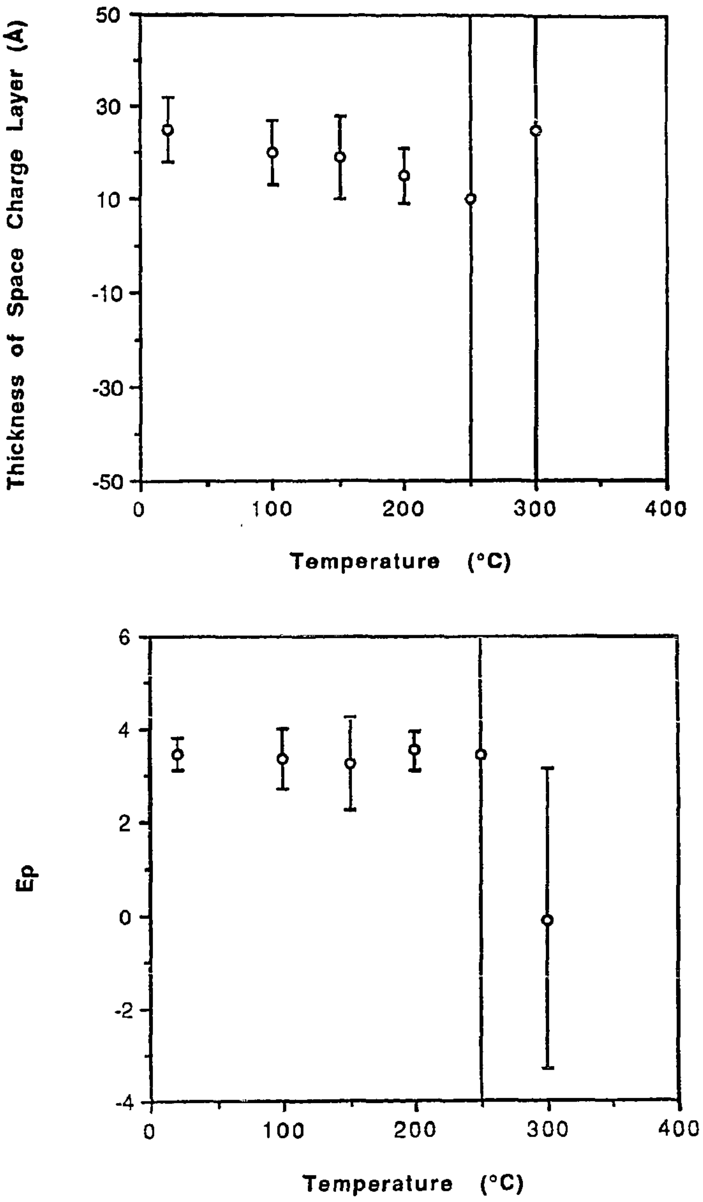

Fig. 5.12: Modelling the MIBERS film on $(1\bar{1}02)$ sapphire with space charge

5.2.3 Heating of as-Deposited Films

MIBERS 50/50 PZT films deposited at room temperature without secondary ion bombardment on $(1\bar{1}02)$ sapphire and Pt-coated silicon were obtained from Hongxing Hu of the Materials Research Laboratory of Penn State University prior to any post-deposition heat-treatment. Annealing of these films was performed *in-situ* in the ellipsometer to determine whether the inhomogeneities seen in films crystallized conventionally were generated during the deposition itself, or whether they were fostered by the annealing. The results reported here will be primarily for the film on sapphire, as in this case, all changes in the spectra with temperature could be attributed unambiguously to the film. Nevertheless, the results seem consistent with those for the film on Pt-coated silicon as well.

For the film on sapphire, all SE measurements were made with the compensator, and the data collected at an angle of incidence of 80° were corrected for residual wavelength-dependent errors in the compensator optics using the effective source correction described in section 2.2.2.3. Data were taken for different annealing temperatures at 50°C intervals between 25 and 600°C. Between room temperature and 350°C, data were collected at the annealing temperature. Above 400°C, however, the film was heated to the desired temperature, soaked for half an hour, and cooled below 300°C for measurement. In all cases, the film was heated to the previous annealing temperature at 5°C/min, and then raised from there to the new annealing temperature at 2°C/min. Cooling was done at 5°C/min until the furnace could no longer follow. The data were modelled using room temperature data for the dielectric function of sapphire. This was not a significant source of error since the temperature dependence of the optical properties of sapphire is very slight.

Figure 5.13 shows the ellipsometric spectra collected during the annealing of the film on sapphire. The data can visually be broken into three regimes. At low

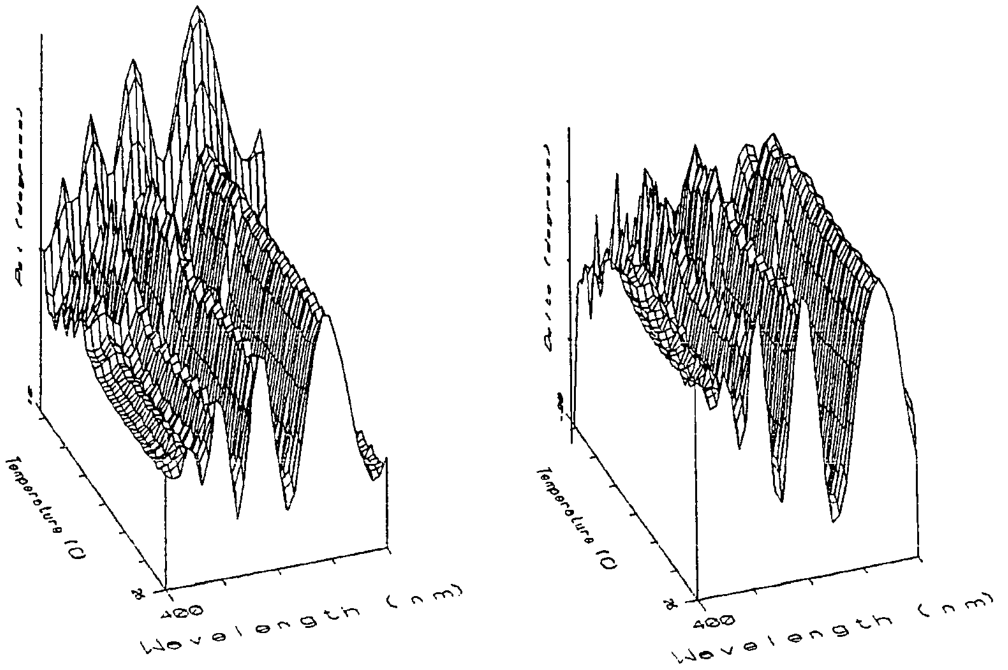

Fig. 5.13: Ellipsometric data for the annealing of an as-deposited MIBERS PZT film

temperatures the interference oscillations are damped strongly at short wavelengths. As shown in Fig. 5.14, however, this additional damping disappears between 450° and 500°C without a major shift in the position of the maxima and minima in the Δ and Ψ curves. Little change occurs from this temperature until 600°C, which appears to mark a transition between the second and third regions. The latter, as illustrated with the data after the 650°C anneal, is characterized by higher Ψ values.

It was not possible to model the full spectra at low temperatures with a single oscillator, as that did not mimic the abrupt decrease in damping below 500nm. A much better fit could be achieved by mixing the oscillator with reference data for rf sputtered lead oxide (Harris et al. 1979) (see Fig. 5.15). For all low temperature data, reference data for rf sputtered PbO provided a better fit than did data for evaporated PbO, largely because the band gap was shifted 0.6 eV lower in energy. No explanation for the disparity in the dielectric functions of the two was given by Harris et al. (Harris et al. 1979), though one possibility would be the presence of mixed valence states in the sputtered PbO (Ennos 1962). Fits to as-deposited films on sapphire substrates were not improved significantly by the addition of surface roughness or a gradient in the PbO content to the model. Similarly, due to the strong correlation between the void volume fraction and the PbO content, it was not possible to achieve reproducible fits with low density regions near the film-substrate interface. No evidence for low density regions near the substrate were found in Fox's work on as-deposited MIBERS lead lanthanum titanate films (Fox 1992).

The volume fraction of PbO remained approximately constant at lower temperatures, but beginning at 450°C, successively lower V_f were required to match the ellipsometric spectra. Fig. 5.16 shows the best-fit models for 450 and 500°C; the modelling is improved by allowing the lead "loss" to begin at the film surface and move progressively through the film thickness (see Fig. 5.16). Over the same temperature range, the film changed from an orange color to pale yellow.

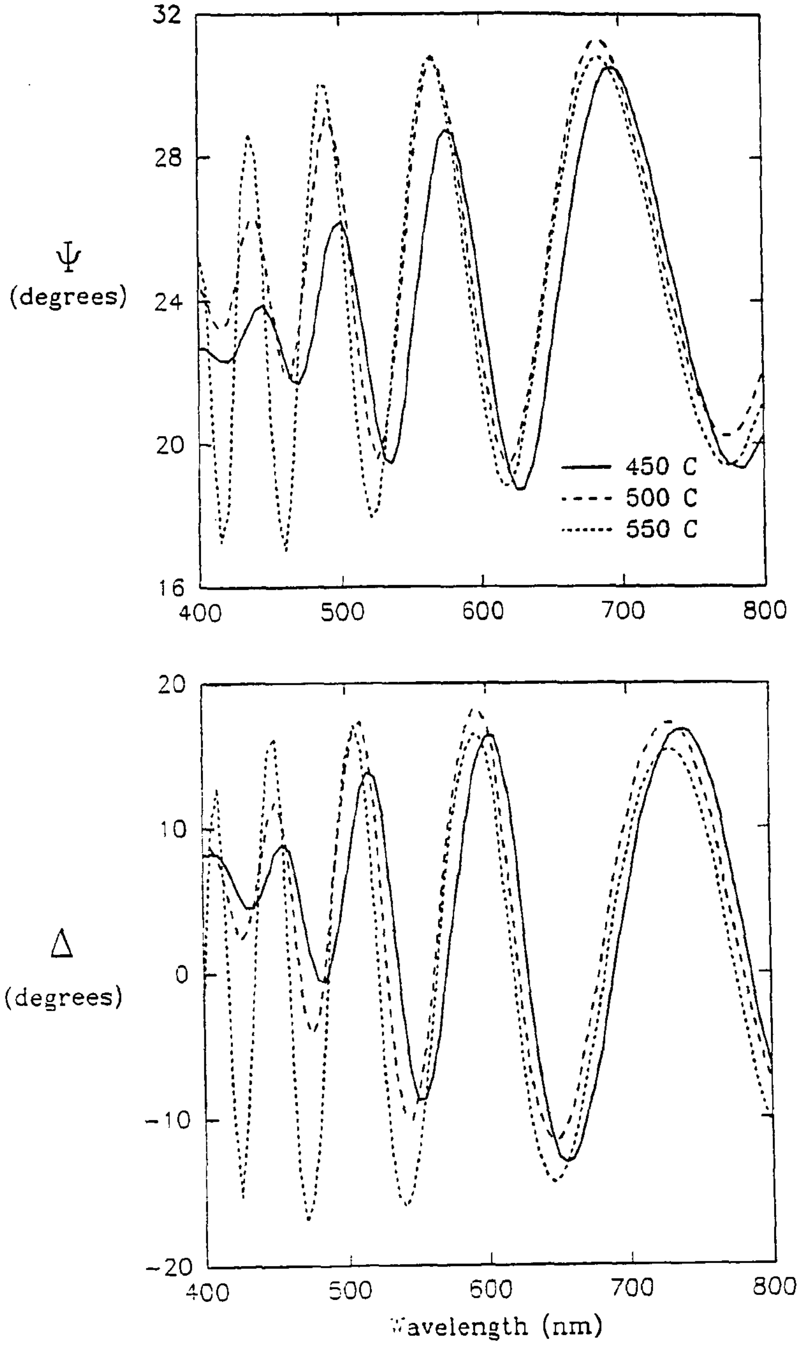

Fig. 5.14: Annealing of an as-deposited MIBERS PZT film showing a decrease in the high energy damping at 500°C

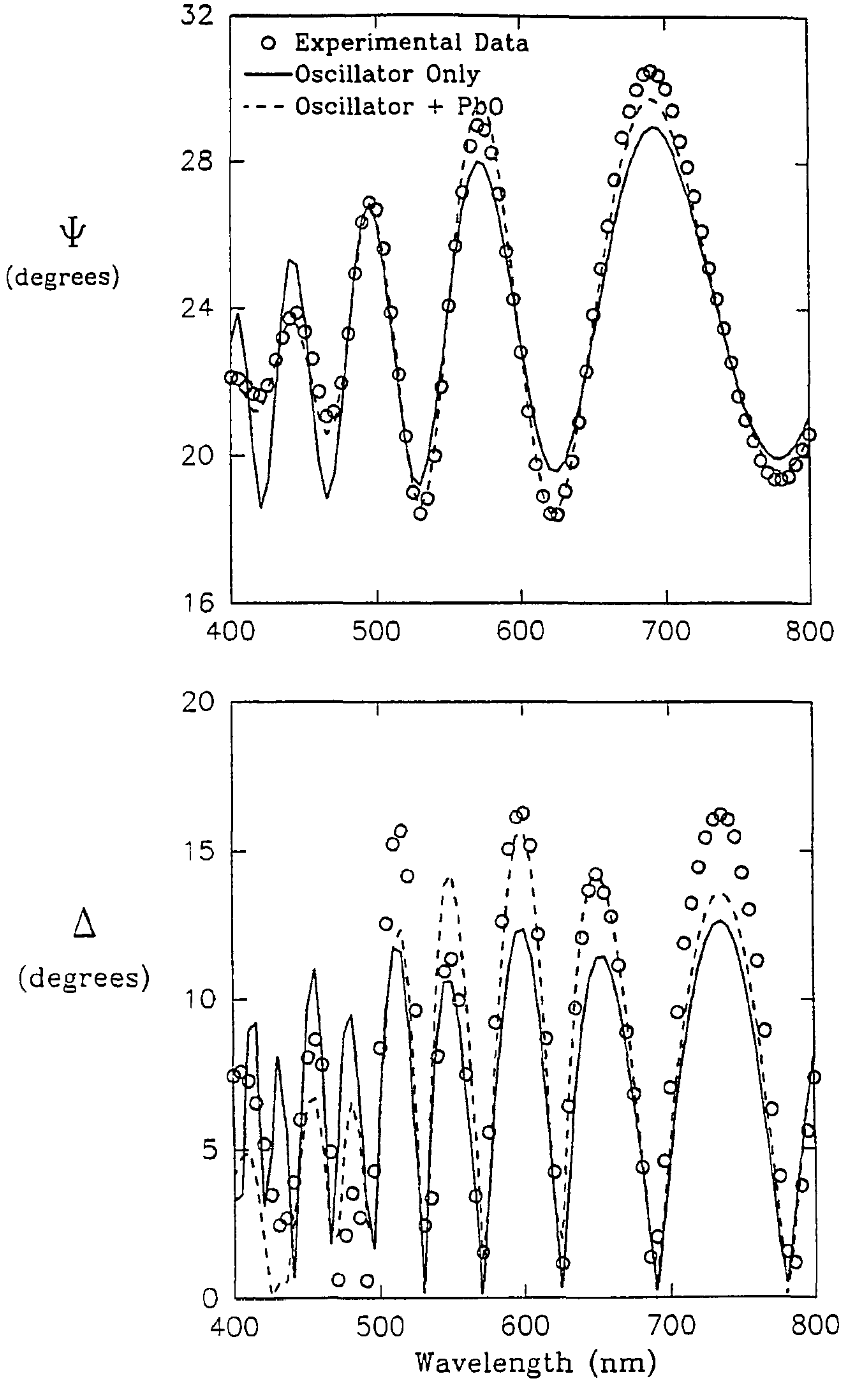

Fig. 5.15: Fit to room temperature data for an as-deposited MIBERS 50/50 PZT film on sapphire with and without rf sputtered PbO

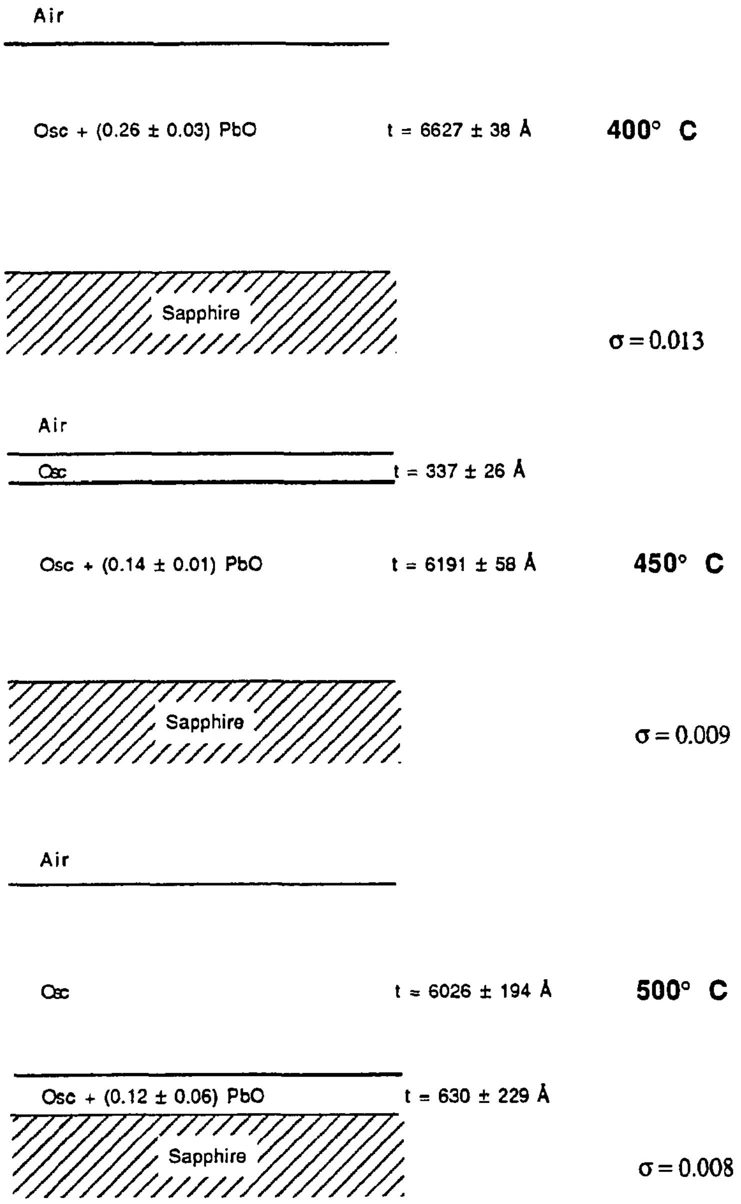

Fig. 5.16: Best fit models for intermediate temperature anneals of an as-deposited MIBERS PZT 50/50 on sapphire

Two possibilities would account for these changes. First, following composition analysis of as-deposited and annealed films, Fox et al. (1992) concluded that as-deposited MIBERS lead lanthanum titanate thin films contain excess PbO which is removed during high temperature annealing. The onset temperature at which this was projected to occur was 490 ± 50°C. While this temperature is lower than that reported for PbO loss from bulk $PbTiO_3$ samples (Holman and Fulrath 1973), it is in good agreement with the SE experiments. Secondly, the lead oxide, rather than being vaporized, could at ~450°C revert to a less lossy species. Thus, the increase in transparency at low wavelengths could be associated either with a homogenization of the lead oxidation state or with the incorporation of the lead species into a more transparent phase (like that of evaporated PbO or the perovskite). It is not possible to distinguish between these two mechanisms on the basis of the SE data and it is also possible that both are operative.

At 550°C the experimental data could be fit well with a two layer model consisting of a "dense" underlayer 4920Å thick surmounted by 820Å of surface roughness (5.9% air). As shown in Fig. 5.17, the extent of the inhomogeneities becomes more pronounced for anneals above 550°C. Again, as opposed to the samples annealed only at 650°C for 2 hrs (i.e. those not exposed to extended periods at intermediate temperatures), no low-density layer near the film/substrate interface was required. It is also likely that the void concentration varies more smoothly with depth than is shown in Fig. 5.17 (and elsewhere in this chapter). However, attempts to add additional layers to model gradations in the void profile resulted in increased values for the correlation coefficients and the 90% confidence intervals.

Between the 500 and 550°C anneals, the film refractive index also increased markedly (see Fig. 5.18). This is most likely associated with the crystallization of the perovskite phase. X-ray diffraction patterns following the 600 and 650°C anneals confirmed that the film had converted to the perovskite structure with a very high

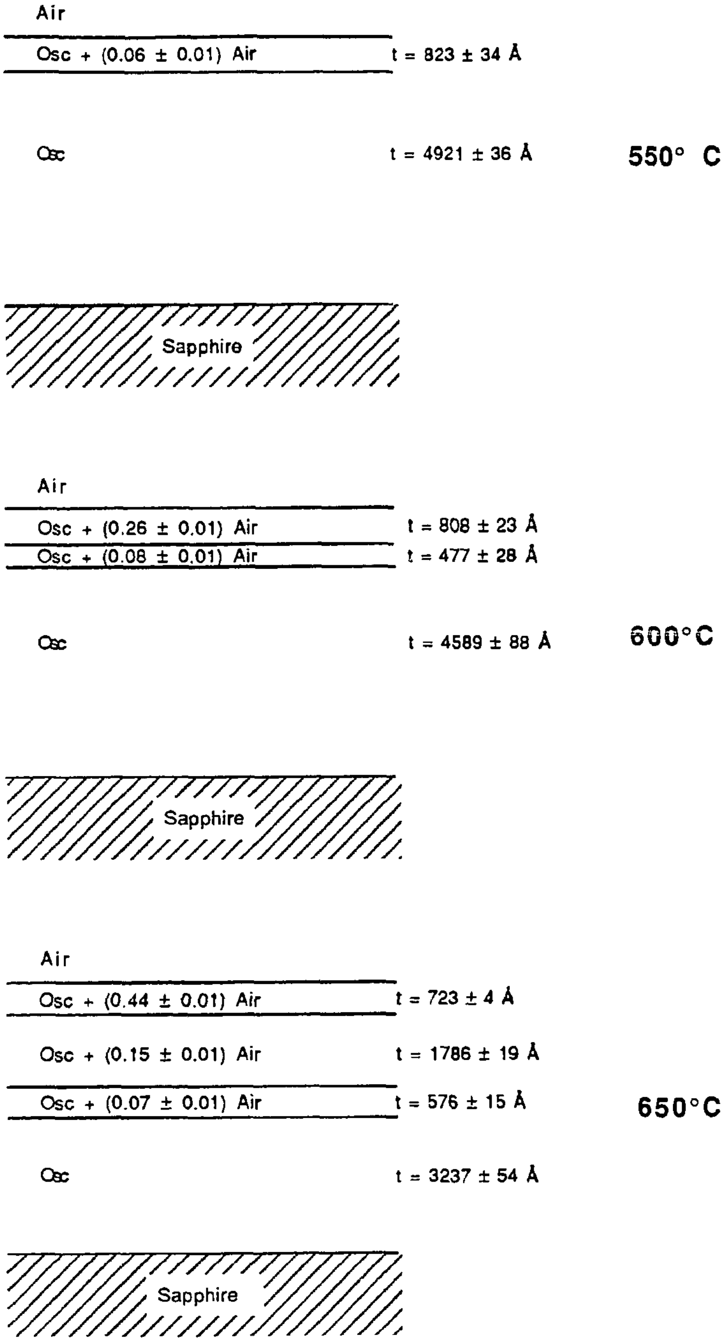

Fig. 5.17: Evolution of microstructure with temperature during high temperature annealing of an as-deposited MIBERS PZT film on sapphire *in-situ* in the ellipsometer

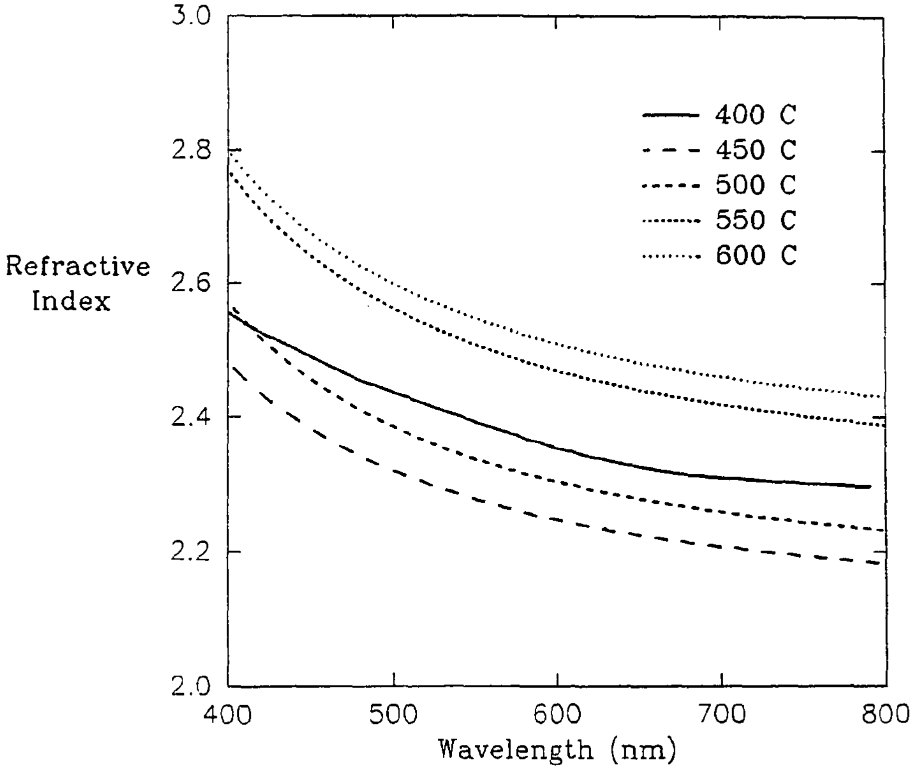

Fig. 5.18: Refractive index of an as-deposited MIBERS PZT film on sapphire as a function of annealing temperature

degree of <110> orientation. Fig. 5.18 also shows that the refractive index remains reasonably constant for all fits above 550°C; the slight drop at 650°C is probably associated with the fact that the "dense" bottom layer of the PZT contains some residual porosity.

In summary, Fig. 5.19 shows values of σ versus annealing temperatures for the different models discussed in the above paragraphs. As discussed by An et al. (1990), regions where σ begins to increase abruptly mark transitions from one model to the next. Shown in part b of that same figure is the proposed reaction scheme for changes occurring in a MIBERS film deposited at room temperature.

5.2.4 Role of Annealing Profile in Controlling Inhomogeneities in MIBERS Films

In comparing the microstructures of MIBERS PZT films annealed in different ways, it is clear that while the inhomogeneity profiles are consistent for samples given identical annealing schedules, they are strongly dependent on variations in the heating cycle. This is clearly seen in Fig. 5.20, which shows the SE-determined depth profiles for films annealed at 650°C for 2 hrs with and without extended lower temperature soaks. It is interesting that for samples annealed *in-situ* in the ellipsometer the major changes in the film inhomogeneities were coincident with the crystallization of the perovskite phase. This suggests that while the initial microstructure of a vapor-deposited film is controlled by factors such as substrate temperature, gas pressure, and adatom mobility (Messier 1984), the final appearance is also a function of any post-deposition processes involving diffusion. Thus, in ferroelectric films, elimination of excess PbO, reaction with the substrate, crystallization of either the pyrochlore or perovskite phases, and grain growth could successively alter the film microstructure. Additional support for this hypothesis is given by Fox et al. (1992), who used scanning

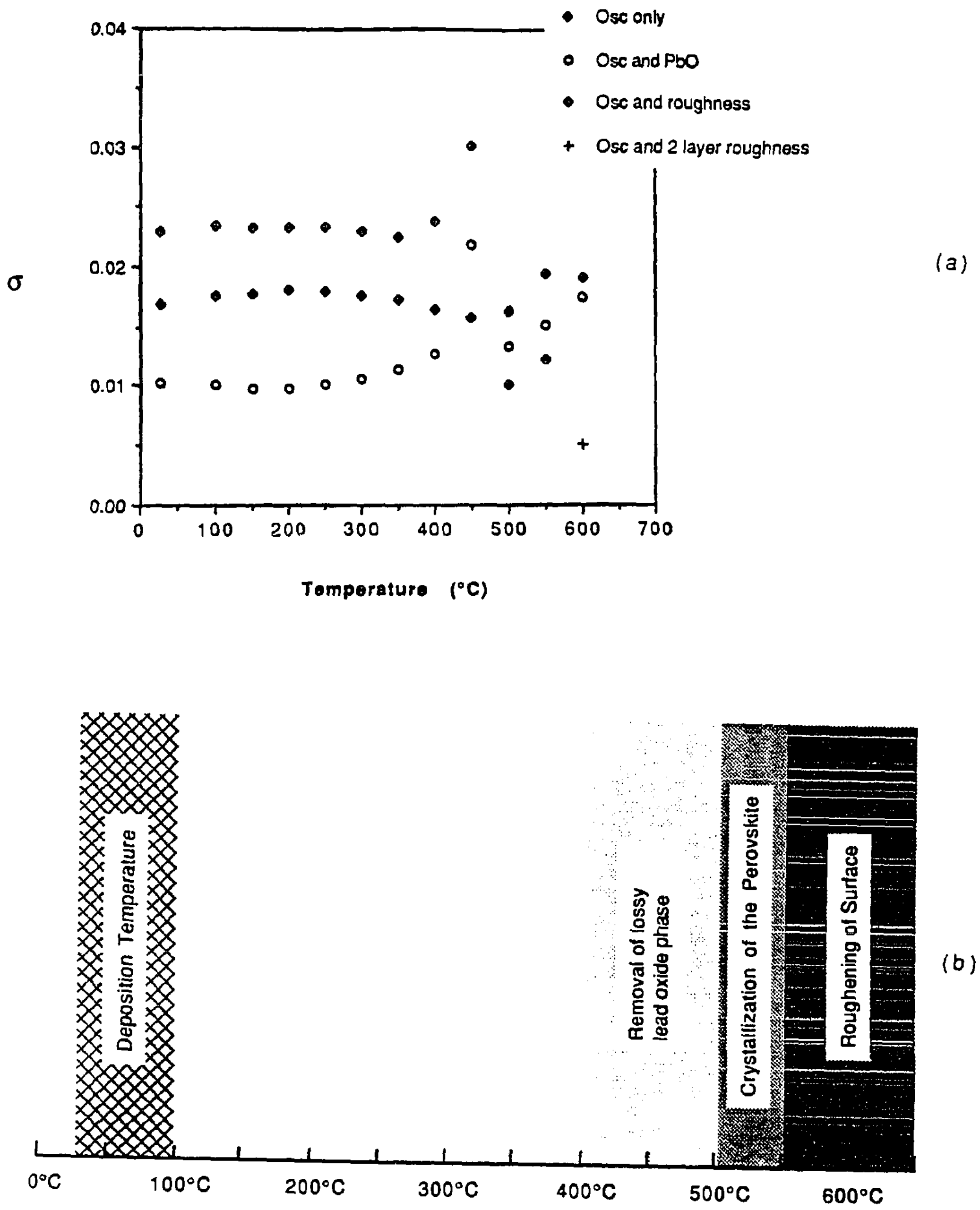

Fig. 5.19: *In-situ* annealing of a MIBERS PZT 50/50 film on sapphire (a) σ vs. temperature (b) Reaction scheme for the annealing

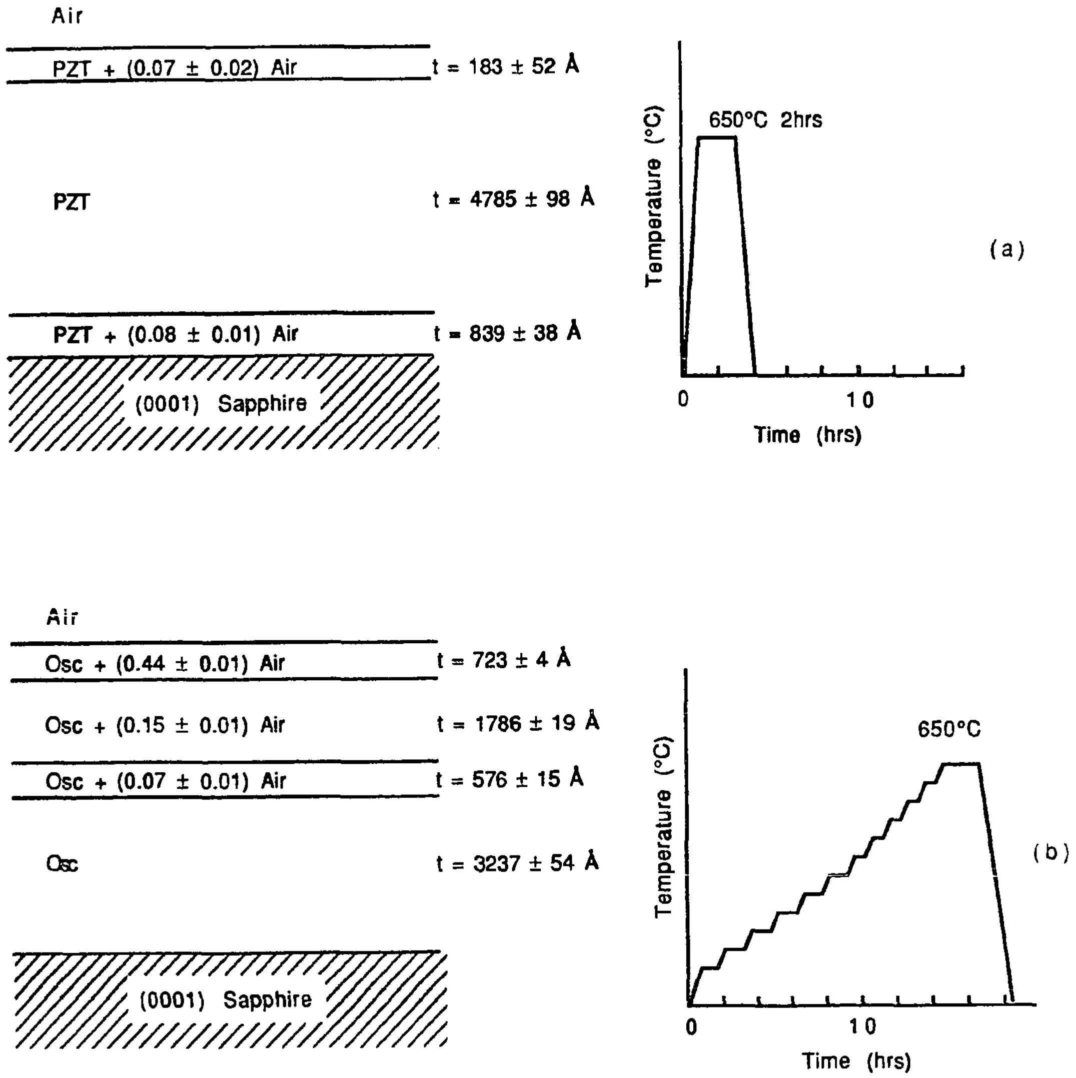

Fig. 5.20: Final microstructures of MIBERS PZT films on sapphire annealed at 650°C for 2 hrs (a) without and (b) with extended annealing at lower temperatures. The annealing profile shown for (b) is simplified

electron microscopy to follow the microstructural evolution of MIBERS lead lanthanum titanate films. In that work it was found that the dominant mechanisms affecting the final microstructure were introduction of porosity associated with the evolution of excess PbO and loss of the fibrous structure of as-deposited films due to nucleation and growth of the perovskite phase. It was also believed that the primary microstructural relics of the as-deposited microstructure were cluster boundaries.

It is demonstrated in section 5.2.5 that inhomogeneities in the microstructure, especially those associated with low density regions, alter the net coercive field, dielectric constant and remanent polarization of ferroelectric films. Given the dependence of the microstructure on the details of the post-deposition annealing profile observed here, it is clear that two films of the same composition, crystal structure, and thickness, which were annealed at the same peak temperature, could nevertheless still possess considerably different electrical properties. Consequently, post-deposition annealing should be considered an important variable in both the microstructure and property development of ferroelectric films.

It is also clear that the reasons for the discrepancies between the properties of the two aforementioned films would not be detected by X-ray diffraction. This clearly establishes the need for microstructure-sensitive characterization techniques in the study of ferroelectric films for device applications. Spectroscopic ellipsometry should be useful in this regard.

5.2.5 Influence of Inhomogeneities on the Electrical Properties of Films

As discussed in section 5.2.1, many ferroelectric films grown with the MIBERS technique possess low density regions near the film/substrate interface which are consistent with the appearance of either clustering or columns in the annealed film. Such a defective layer should be expected to alter the apparent electrical properties of the film. Indications of this can be seen experimentally in the hysteresis loops of a MIBERS film grown without bombardment and a sol-gel PZT which was shown to have a more homogeneous depth profile by spectroscopic ellipsometry. Both films have higher E_c values than would be expected for bulk ceramics of the same composition, probably as a result, in part, of the fine grain size of the films. Nevertheless, it is apparent that the vapor-deposited film possesses a higher coercive field and a more severe tilt to the "vertical" sides of the loop than does the chemically prepared one. An attempt was made to model the hysteresis loop of the MIBERS film to determine whether these differences could be attributed to the ellipsometrically characterized heterogeneities.

To model the effect that embedded porosity of this type would have on the apparent electrical properties of the film, the following approximation was considered. If a representation of a columnar microstructure is subdivided into elements vertically, then most segments contain dense PZT in series with a low dielectric constant layer (see Fig. 5.21). It is assumed here that the upper electrode is conformal, so that the surface roughness does not strongly influence the apparent electrical properties of the film. Given these conditions, the net capacitance of one element can be expressed as

$$\frac{1}{C} \propto \frac{\varepsilon_2 (d - x) + \varepsilon_1 x}{\varepsilon_1 \varepsilon_2}$$

where ε_1 and ε_2 denote the dielectric constants of the dense and the defective regions respectively, d is the total film thickness, and x is the thickness of the low density material. For this geometry,the ratio of the actual coercive field of the dense PZT to the apparent coercive field of the element is

$$\frac{E_{c(1)}}{E_c} = \frac{\dfrac{V_1}{d-x}}{\dfrac{V}{d}} = \frac{\varepsilon_2 d}{\varepsilon_2 (d - x) + \varepsilon_1 x}$$

It is also assumed that there are no forces (such as stress) acting to depole the film. While some depolarization will occur in actual samples, tilting the lines bounding the

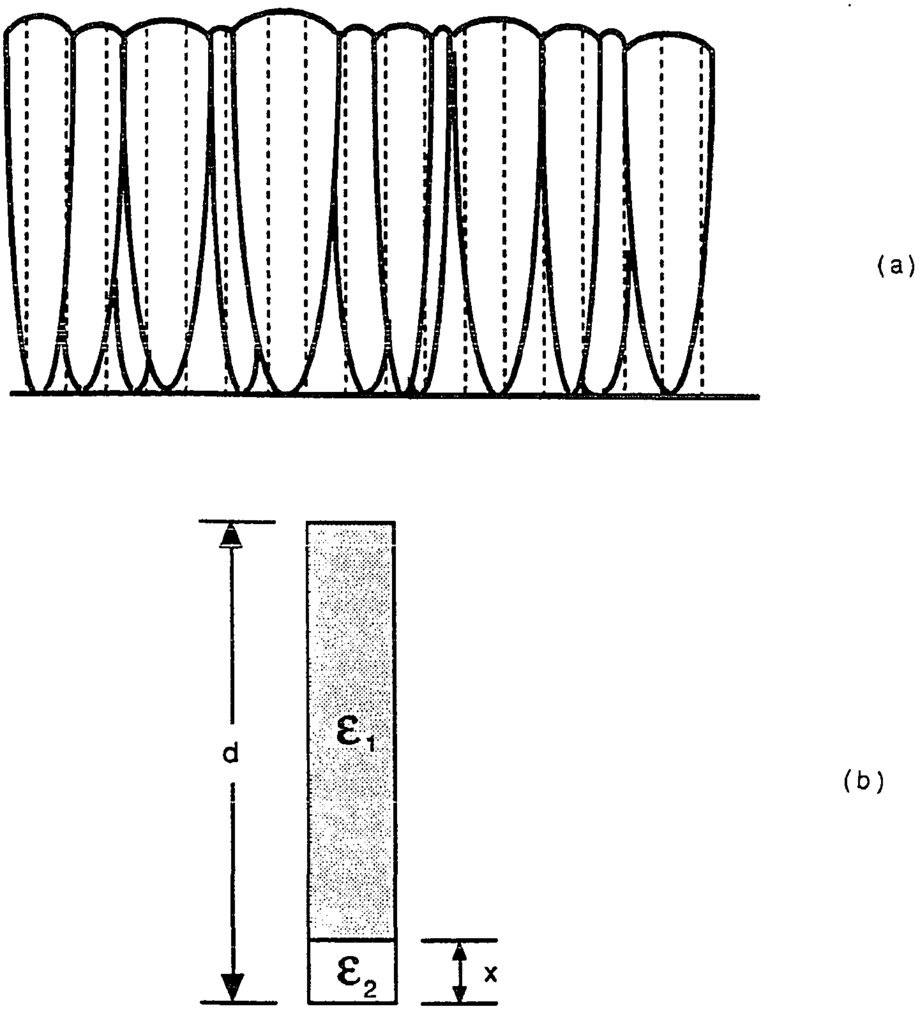

Fig. 5.21: Geometry used for modelling the effect of inhomogeneities on the electrical properties of ferroelectric thin films. (a) A two-dimensional representation of columnar growths subdivided vertically into elements. (b) One element of the above structure

top and bottom of the hysteresis loops, that will not alter the basic conclusions of this argument.

In vapor-deposited materials, the dielectric constant and the thickness of the defective material would be expected to vary locally as nucleation and growth commenced, leading to a distribution in the capacitances and coercive fields of the different subelements. The absence of a well-defined coercive field, in turn, leads to a loss in the squareness of the hysteresis loop, which is one of the desired attributes for the model. As a first approximation, the dielectric constant and coercive field for the dense fine-grained PZT were assigned to the values from the sol-gel film, i.e. $\varepsilon_1 = 1300$, and $E_{c(1)} = 40$kV/cm. To mimic the slope of the sides of the hysteresis loop for a 6000Å thick MIBERS film, the coercive fields for the elements were divided into equal steps between 40 and 110kV/cm. This gives the right slope and correctly predicts the average value for E_c (~75kV/cm). The shape of the derived hysteresis loop is also in reasonable agreement with the experimental data.

To further check the validity of this model, the net dielectric constant for a film 6000Å thick with a 600Å thick low density layer near the substrate was also calculated. The coercive field distribution described above requires dielectric constant values for the bottom layer to vary between 70 and 1300. This leads to a net dielectric constant for the film of 770, reasonably close to the experimentally observed value of ~850 for films deposited without bombardment (Hu et al. 1992). The volume fraction of air in the bottom layer of each element needed to cause the assumed coercive field distribution was also calculated using the logarithmic and series approximations for the dielectric constant of a composite. These values bracket the average volume fraction of air derived from the SE determination. This is also reasonable. Consequently, this model provides a good approximation for the observed electrical properties of some types of inhomogeneous ferroelectric films.

The role of inhomogeneities in controlling the observed low and high field electrical properties of ferroelectric films also explains much of the variability reported in the literature for these properties. As the degree and types of inhomogeneities present in the film are controlled by the preparation conditions, it is not surprising that films prepared in different ways display widely disparate dielectric constants and hysteresis loops. In all cases heterogeneities within the film would be expected to increase the coercive field value. When a distribution of coercive fields in present, the hysteresis loop would be both significantly broadened and tilted to the right. Again, these observations are consistent with reported data on ferroelectric thin films.

Moreover, depending on the distribution of porosity in the film, the coercive field of some regions could be so high as to make them practically unswitchable, lowering the apparent polarization for the film. Thus it is possible that highly crystalline films could display apparent remanent polarizations significantly below that expected for the bulk ceramic material. This would occur despite the fact that if the film could be fully switched, the remanent polarization would be 99.2% of the bulk value for the case where the bottom 600Å (of a film 6000Å thick) was, on average, 92% dense.

Finally, defective regions in the film could serve as pinning sites for domain wall motion. This, in turn, could influence both aging and fatigue in ferroelectric films. Consequently, deposition techniques which facilitate production of films which are highly homogeneous, in addition to being highly crystalline, may be essential in the preparation of optimum films for device applications.

5.2.6 Role of Inhomogeneities on Apparent Size Effects in Ferroelectric Films

Any film which contains low density regions near the substrate should also be expected to display marked extrinsic size effects. Thus, for the MIBERS films discussed above, and for other vapor-deposited films grown under low adatom mobility conditions, as the total film thickness is decreased, the defective layer contributes a larger fraction to the overall properties.

Consider, for example, the simplified model for the MIBERS film discussed in the previous section, where the first 600Å of perovskite has a lower density than the remainder of the film. As before, the dielectric constant of the defective region will be distributed between 70 and 1300, so that the hysteresis loop of the film has the proper shape. If this initial layer is kept constant while the total film thickness of the film is varied, then the hysteresis loops become progressively broader and more tilted as d is decreased (see Fig. 5.22). At the same time, the net dielectric constant drops off markedly, even though ε for the solid phase remains unchanged. Thus, an infinitely thick film would be essentially undisturbed by the anomalous layer, and would have a well-defined coercive field and dielectric constant equivalent to the values for a bulk, fine-grained ceramic. For thinner films, however, both ε and E_c diverge from the bulk values. The decrease in dielectric constant for thinner films shown in Fig. 5.22 is also in agreement with a variety of experimental studies (Gitel'son et al. 1977, Udayakumar et al. 1990).

Fig. 5.22 is drawn with each film thinnest films showing the maximum value for the remanent polarization. If the low density layer is, on average, 92% dense (i.e. the ellipsometrically determined value), this is a good approximation, even for the 1000Å thick film, since the effective remanent polarization is calculated to be 95.2% of the bulk value. As the film thickness increases, the maximum P_r value rapidly approaches 100% of the bulk value. However, this marks the limiting value for P_r assuming that full switching of the film could be achieved. In practice, it is more likely that given the presence of high local coercive fields in the thinner films, some areas of the film would become unswitchable, and the measured remanent polarization would be lowered.

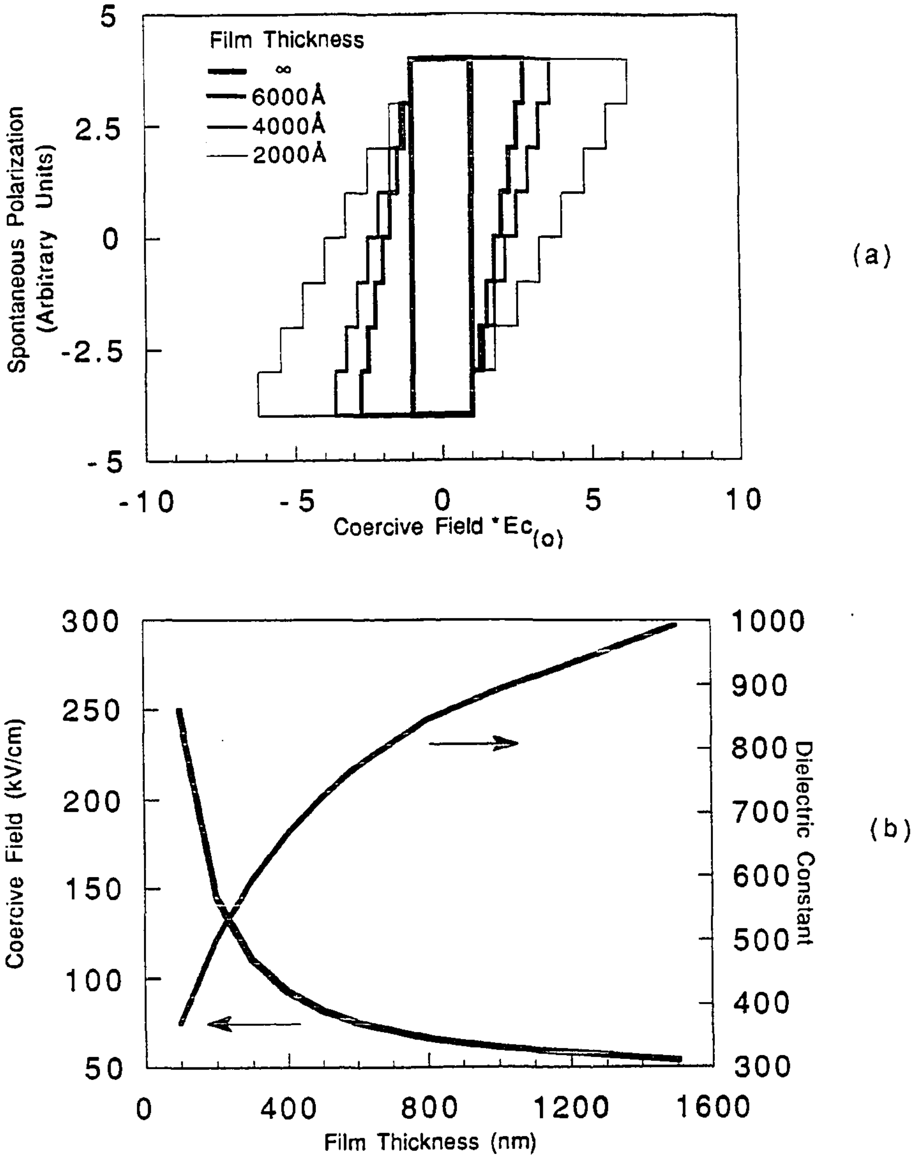

Fig. 5.22: The effect of a 600Å thick low density layer near the substrate on the electrical properties of ferroelectric thin films. (a) Variation in the hysteresis loop with the total film thickness. (b) Variation of the dielectric constant and the coercive field with film thickness. Limiting values are $\varepsilon = 1300$ and $E_c = 40$kV/cm for a homogeneous, fine-grained film on a Pt-coated silicon substrate

The sensitive dependence of the apparent size effects on the initial stages of the film microstructure would also explain why films prepared under different conditions demonstrate different properties as a function of thickness. Spectroscopic ellipsometry offers one of the few means through which depth profiles of inhomogeneities in thin film samples can be characterized non-destructively, and so should be useful in resolving many of the residual questions about structure-microstructure-property relationships in ferroelectric films.

5.3 Annealing of Sol-gel Thin Films

Sol-gel PZT films with a 52/48 Zr/Ti ratio were prepared by Jiayu Chen of the Penn State Materials Research Laboratory from alkoxide precursors. A large platinum-coated silicon wafer (obtained from Ramtron Corporation) was spin-coated with the stock solution and was rapidly heated to ~200 °C for 1-2 min. This flash heating was intended to vaporize the solvent, densify the deposit, and prevent the cracks which would otherwise appear in thick sol-gel films. The process was repeated 6 times to build up a layer ~4000Å thick. The wafer was subsequently cut into several sections so that the effect of varying thermal treatments on film density and homogeneity could be determined on samples with identical preparation history.

5.3.1 Slow Anneal

One section of this film and a similar sample deposited on $(1\bar{1}02)$ sapphire were annealed *in-situ* in the ellipsometer. The only difference between the two specimens was that the film on silicon was heated to ~ 200°C after spinning, whereas the film on sapphire was pyrolyzed at 400°C. As described in Chapter 2, the samples were aligned at room temperature on the ellipsometer sample mount and the furnace was assembled with the sample in place. SE data were first taken at room temperature. Without changing the sample position, the film was heated to 100°C at the rate of 2°C/min, realigned (to counteract drift in the screws controlling the angle of the sample mount) and remeasured. This process was repeated at 50°C temperature increments.

It was found that for the film heat-treated at 200°C, Δ and Ψ changed continuously at low temperatures due to structural and chemical changes in the film. To minimize errors associated with these continuous changes, below 400°C the temperature was stabilized at the target temperature and maintained for 15 minutes before SE data were taken. Although this slowed down the rate of change in the ellipsometric parameters, continuous changes occurred in a film held at 200°C for 12 hours. Consequently, the models of the lower temperature data on that film do not constitute equilibrium structures, but rather, distinct points during the burnout process . The film pyrolyzed at 400°C, as expected, was fully collapsed, and did not show any marked changes in the film structure or optical properties below the burnout temperature.

At higher temperatures the changes in both films were so rapid that Δ and Ψ were not observed to change at all with time. This is consistent with the observation that crystallization of the perovskite phase is completed within 10 seconds at 550°C during rapid thermal annealing of PZT films (Chen et al. 1992). Below 450°C, the ellipsometric spectra were taken at the annealing temperature. Above 500°C, however, furnace glow interfered with the reflected beam, so the films were cooled rapidly to 350°C for measurement. Plots of Δ and Ψ spectra against temperature are shown in Fig. 5.23.

The resulting curves were then modelled using room-temperature reference data for the platinum-coated silicon and sapphire substrates. For low temperatures, the experimental curves could be fit well by allowing both the thickness of the film and its optical properties to vary. In contrast to the MIBERS PZT films, no lossy PbO was

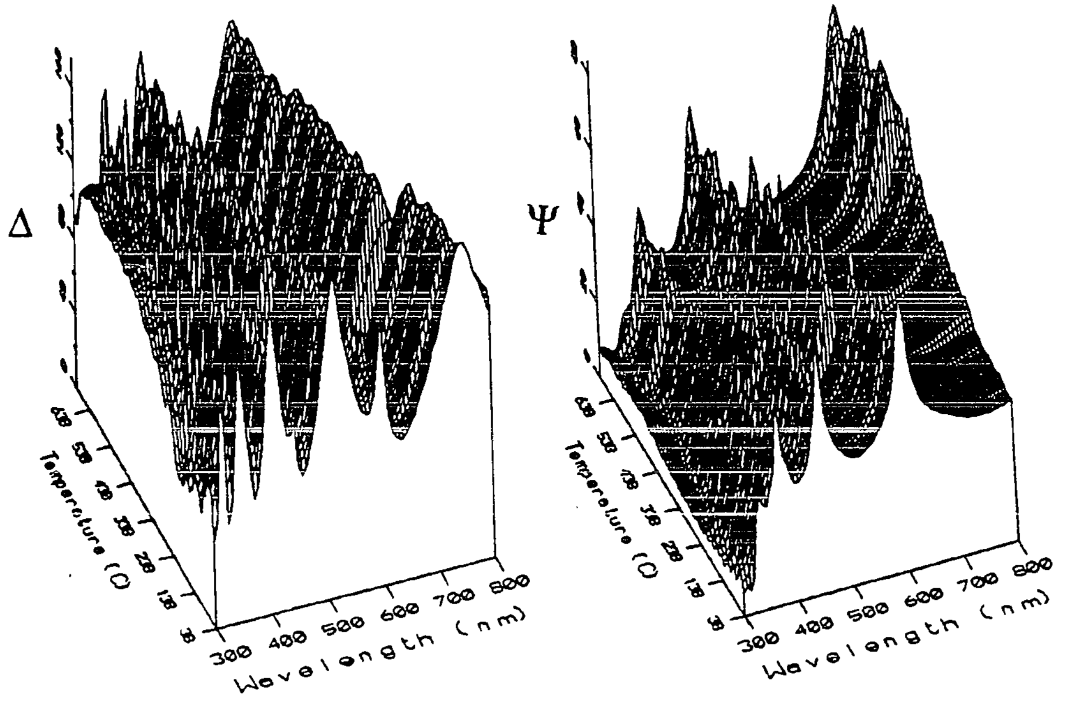

Fig. 5.23: Δ and Ψ as a function of wavelength and temperature during annealing of a sol-gel film on Pt-coated silicon

required for as-deposited films. As shown in Fig. 5.24, the film on Pt/Si began to collapse at 200°C, and had essentially reached its final thickness at ~300°C. This temperature range was also marked by a substantial increase in the oscillator strength and position describing the effective film refractive index. The film on sapphire, having been pyrolyzed at higher temperatures, did not show any substantial changes in the film thickness at those temperatures (Fig. 5.25). Below 350°C, the refractive index of the film on sapphire was both low (~2.25 at 550nm as compared to ~2.5 for the perovskite phase) and nearly temperature independent. As this film does not undergo a significant collapse in thickness at any temperature, this low refractive index is probably associated with the lack of crystallinity rather than low density.

For the films on both sapphire and platinum-coated silicon, sigma began to rise above its average value at low temperatures for anneals between 350° and 400°C. As discussed by An et al. (An et al. 1990) in *in-situ* spectroscopic ellipsometric measurements, transitions between different models are indicated by places where sigma begins to diverge from a steady or constant value. Additional analysis of the experimental data suggests that for the PZT films, these changes did not correspond to the generation of surface roughness, interface porosity, or increased absorption in the film. At 450°C and above, however, the ongoing increase in sigma could be eliminated by allowing a progressive roughening of the surface of the film on sapphire. This continued until 550°C, above which the volume fraction of air in and the thickness of the roughness layer were temperature independent. The change in the microstructure was coupled with a marked increase in the film refractive index between 500 and 600°C (see Fig. 5.26). In independent X-ray studies on films prepared in the same manner, the perovskite phase was shown to crystallize in this temperature range (Chen et al. 1992).

These changes were more difficult to follow for the film on platinum-coated silicon. As for the film on sapphire, there is an increase in σ at 550°C, suggesting the

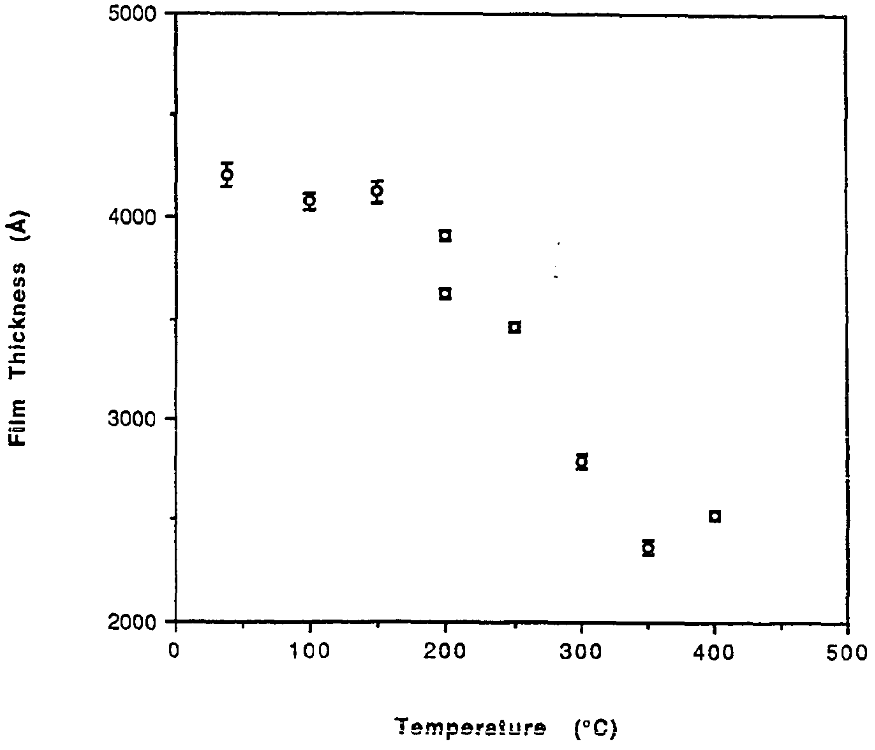

Fig. 5.24: Film thickness as a function of annealing temperature: sol-gel PZT on Pt-coated silicon

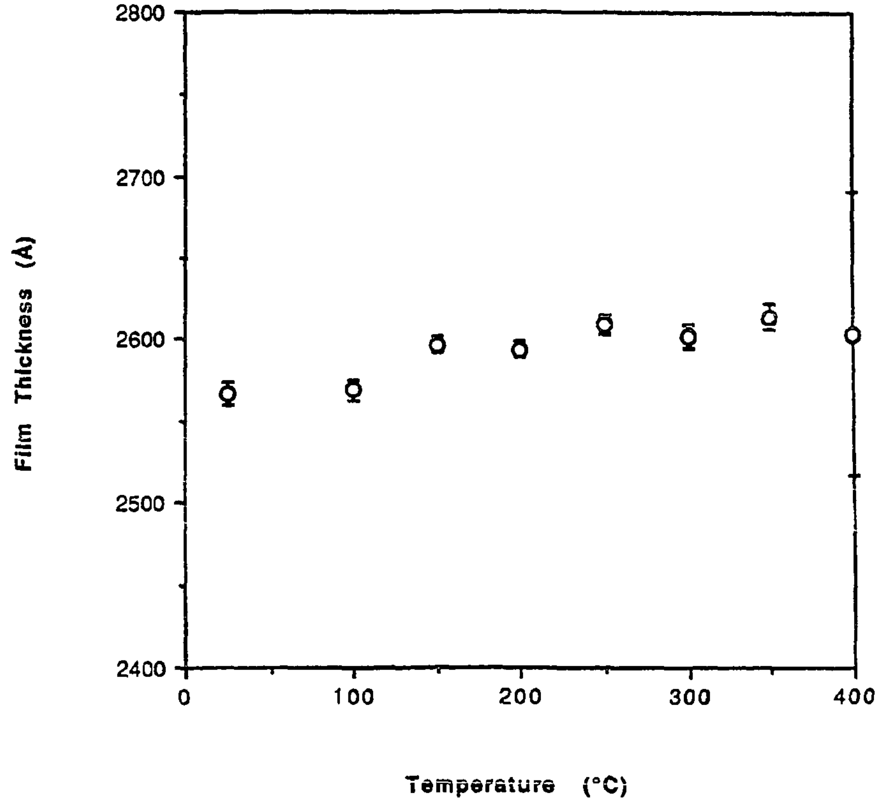

Fig. 5.25: Film thickness as a function of annealing temperature: sol-gel PZT on sapphire

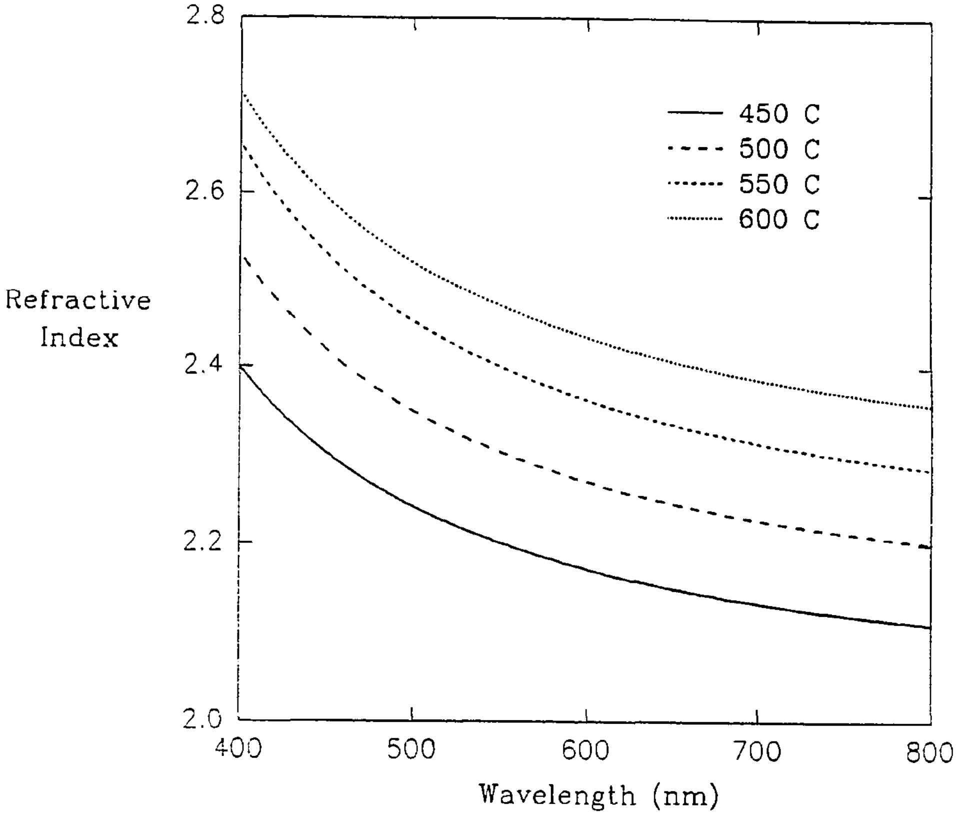

(a)

Fig. 5.26: Modelling for a sol-gel PZT film on sapphire as a function of annealing temperature (a) Refractive index and (b) depth profile of the film

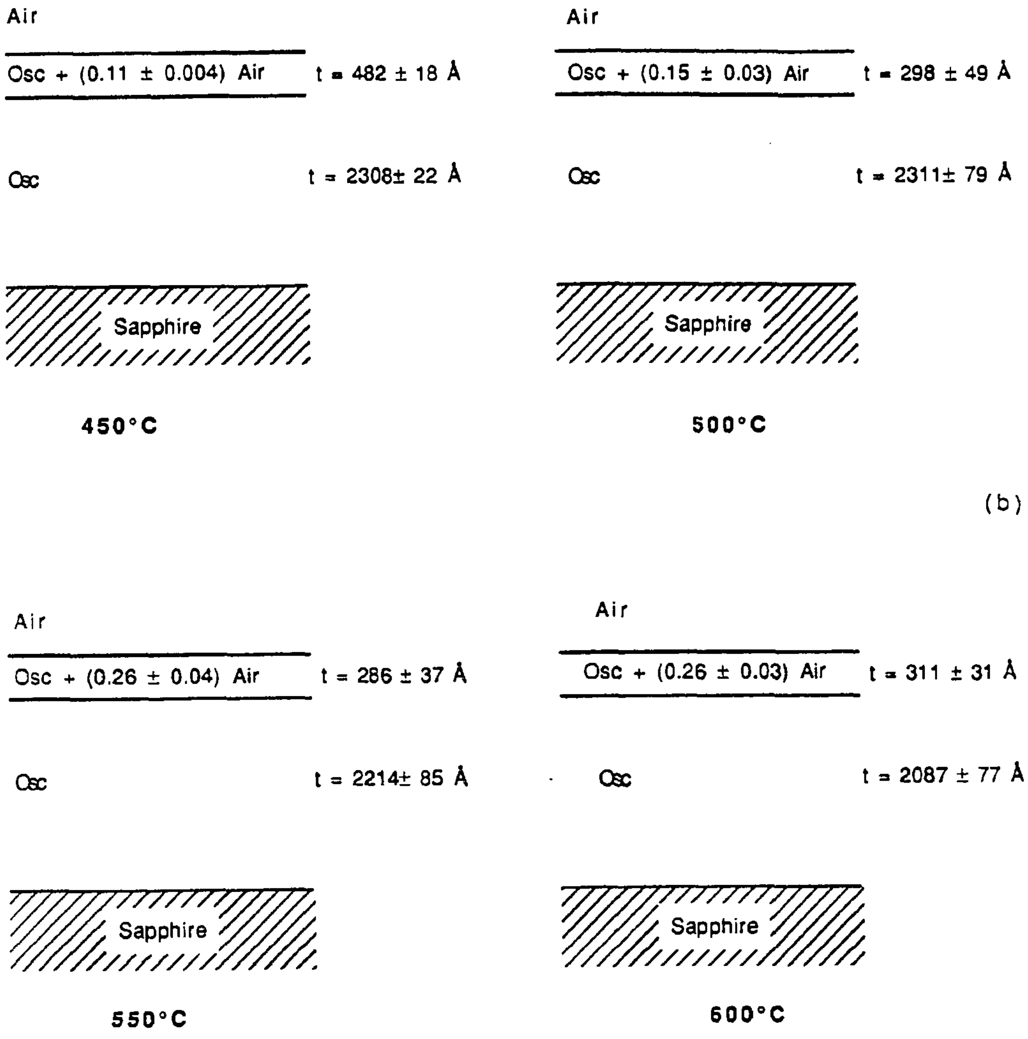

(b)

Fig. 5.26: Continued

need for a more complex model. While an increase in surface roughness and refractive index of the film partially counteracted the rise in σ, larger improvements were obtained by allowing the substrate optical properties to undergo a simultaneous change. As will be discussed in section 5.3.2, the ellipsometric spectra for a substrate exposed to the same temperature profile undergo a notable transformation at the same temperature. Pt and Si are known to form a silicide at temperatures between 500 and 600°C (Lue et al. 1987, Hung and Mayer 1986), so this change was modelled by allowing some a-Si to mix with the reference data for the substrate. Under those conditions, however, determination of the exact microstructure or optical properties of the film annealed at (or above) this temperature was not possible, given the large number of unknowns in both the film and substrate properties. This prohibited an estimation of the bulk density of the film, a measurement of the degree of surface roughness, and a determination of whether the Si in the substrate formed a thin oxide layer between the ferroelectric film and the electrode.

Schematics describing the proposed set of reactions occurring during the annealing of 52/48 PZT films on sapphire and platinum are shown in Figs. 5.27 and 5.28 respectively.

The X-ray diffraction pattern of this film after completion of the heating run showed that the film consisted largely of a crystalline perovskite phase with a small amount of poorly crystallized pyrochlore.

5.3.2 Platinum-Coated Silicon Substrates

In order to determine if, in fact, reactions occur within the substrate itself at elevated temperatures, Pt-coated silicon wafers were obtained from two different sources (Ramtron and Nova) for *in situ* measurements during annealing in the ellipsometer. Both sets of samples consisted of silicon wafers with a thermally grown

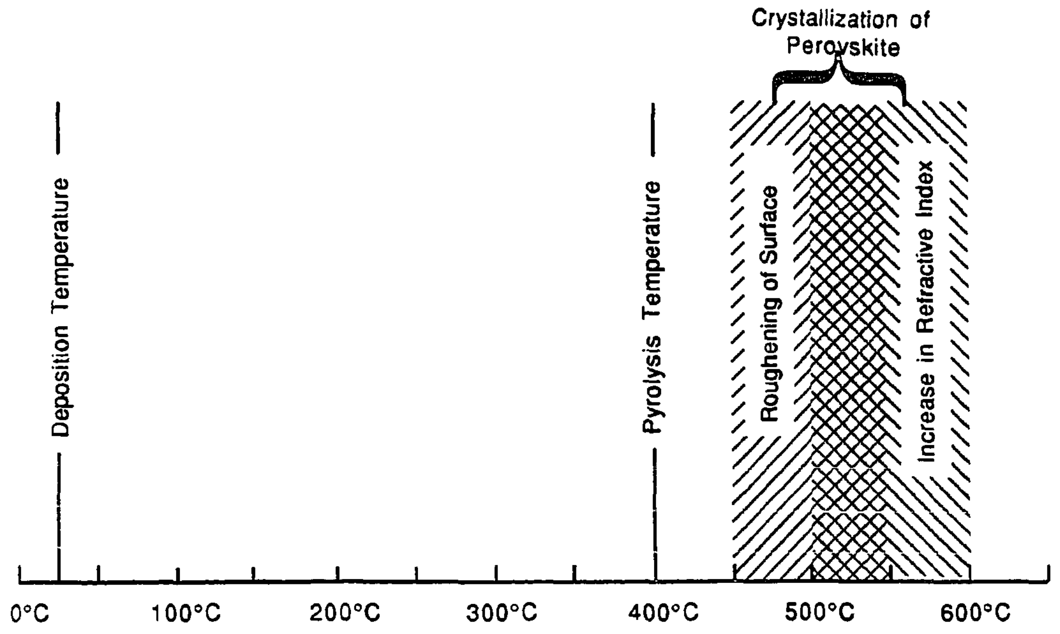

Fig. 5.27: Reaction scheme for the annealing of a sol-gel PZT film on sapphire

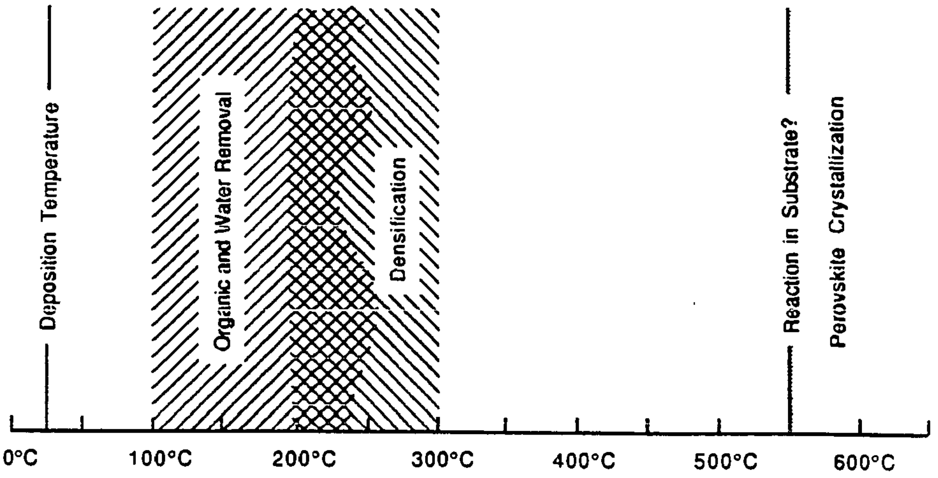

Fig. 5.28: Reaction scheme for the annealing of a sol-gel PZT on Pt-coated silicon

oxide, a thin titanium intermediate film and a sputtered platinum layer. The wafers were cut to a suitable sample size, (1.5 x 1cm), for SE measurements , and experimental data sets were collected every 50°C between room temperature and 600°C. The heating rate used throughout was 2°C/min. For temperatures above 450°C, the sample was held at the desired temperature for half an hour and cooled for measurement.

Fig. 5.29 shows the experimental spectra for Δ and Ψ as a function of temperature. Data taken prior to heating could be modelled well as a layer of roughened platinum on platinum. As the penetration depth of visible light in platinum is only about one hundred Ångstroms, it was not possible to characterize any of the layers buried deeper in the substrate. At comparatively modest temperatures, (~250°C) the microstructure of the platinum gradually altered, apparently due to coarsening of the metal grains. Nevertheless, for temperatures below 500°C, the rough surface of the platinum could be treated as a mixture of platinum and air.

Above this temperature, however, substantial changes in the ellipsometric spectra occur as is evident from Fig. 5.29. Moreover, by 550°C, the curves for Δ and Ψ have both developed interference oscillations, implying formation of a transparent/translucent film on the platinum surface. This appearance of these oscillations was confirmed on a sample heated *ex-situ* using the same temperature profile. Attempts to model the data with combinations of Pt, PtO, and air were unsuccessful.

Additional evidence for some type of reaction in annealed substrates is apparent in the high resolution SEM micrographs taken by Glen Fox at the Oak Ridge National Laboratory facilities. Shown in Fig. 5.30 are micrographs of the substrate before and after annealing to 650°C for 20 minutes. In addition to the growth of the platinum grains, scattered dark patches appear on the annealed sample.

Of the components present in the substrate, the experimental data were best fit by allowing some silicon to intermix with the platinum at the top surface of the

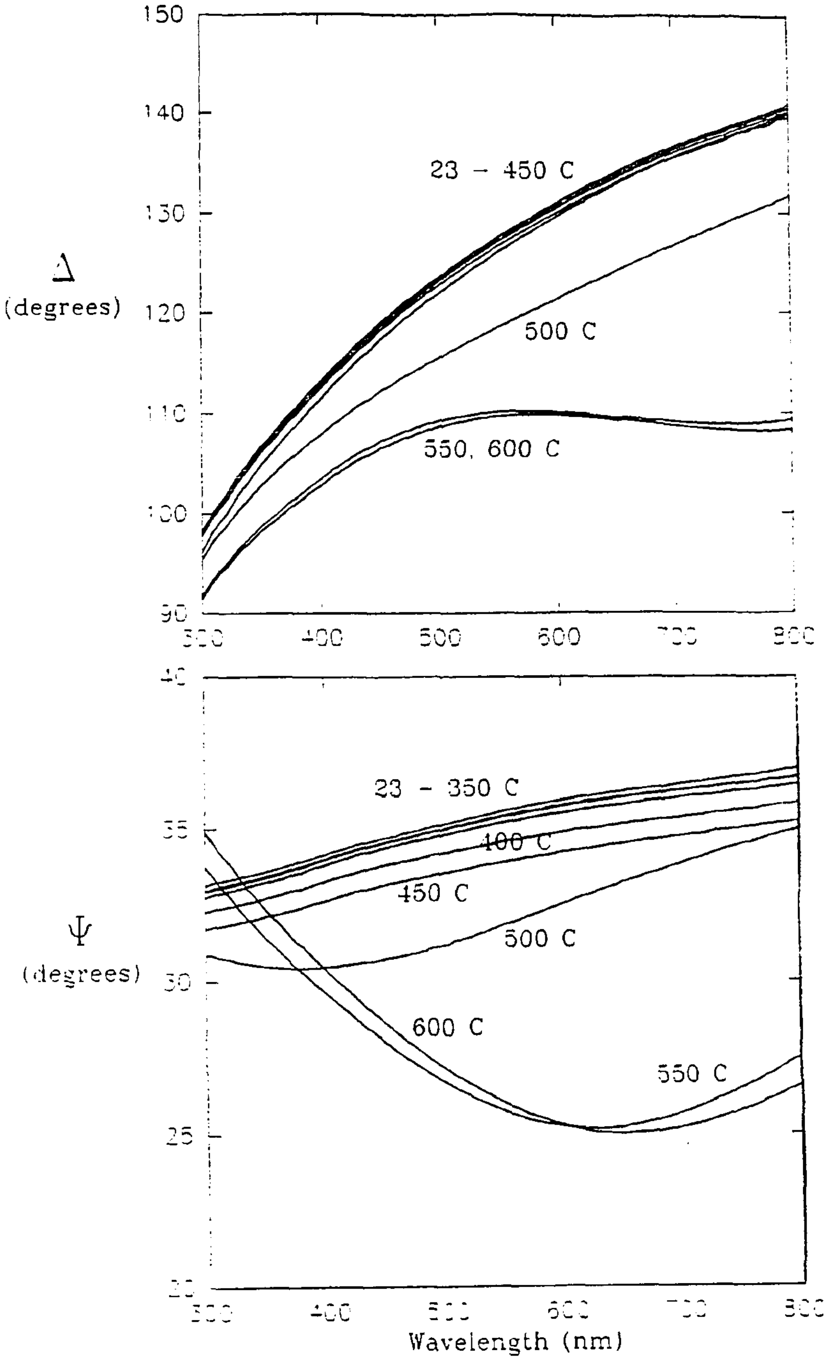

Fig. 5.29: Ellipsometric data for the annealing of a Pt-coated silicon substrate

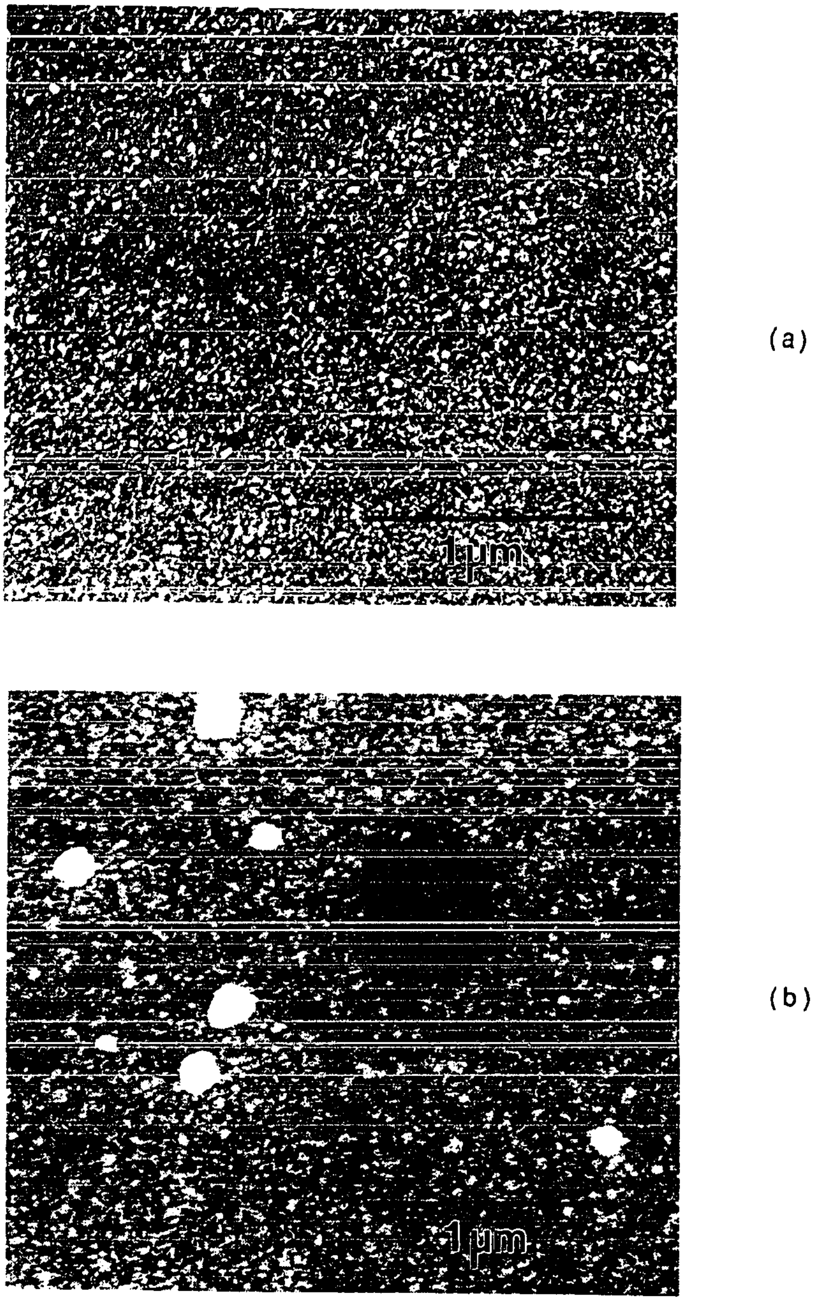

Fig. 5.30: SEM micrographs of a Pt-coated silicon substrate (a) before and (b) after annealing at 650°C for 20 min. Courtesy of G. Fox

substrate. The transparent overlayer causing the interference fringes could then be modelled by assuming that the newly exposed silicon is oxidized. A second possible reaction has been suggested in recent studies on the thermal stability of Pt/Ti/SiO_2/Si substrates, where it was shown that on annealing, Ti can diffuse to the wafer surface (Hren et al. 1992, Bruchhaus et al 1992). On reaching air, it oxidizes. While the ellipsometric spectra are fit better by a model using porous SiO_2 on PtSi than a low density layer of TiO_2 on platinum, the composition of the surface layer on the substrate cannot be determined unambiguously from the optical data.

A model incorporating a reaction between the Pt and the Si is shown along with the fit to the experimental data in Fig. 5.31. The comparatively poor fit may be associated with the patchiness of the reaction zones and the use of a-Si dielectric functions rather than those of PtSi for the fitting. Nevertheless, the fit is considerably better than those which do not account for some type of reaction between the substrate components.

Reactions between platinum and silicon have been well-documented in the literature. Hung and Mayer, for example, report that when no barrier layer is present between the semiconductor and the metal, silicon becomes mobile at temperatures above 500°C and diffuses into the platinum, forming a stable silicide. The kinetics of the silicidation are relatively rapid. Consequently, silicon begins to migrate through an 1150Å Pt-Ti alloy overlayer at 550°C and a homogeneous distribution of silicon in the metal is achieved after ~30 minutes at 625°C (Hung and Mayer 1986). The reported reaction temperatures for the formation of the silicide are consistent with the results for the commercial Pt-coated Si substrates.

It has also been demonstrated by a number of authors that metal silicides form an oxide layer at elevated temperatures (Frampton et al. 1986, Lue et al. 1986, 1987). For silicides with a high degree of metallic content, such as PtSi (Lue et al. 1987) the oxidation is considerably more rapid than that shown by semiconducting oxides like

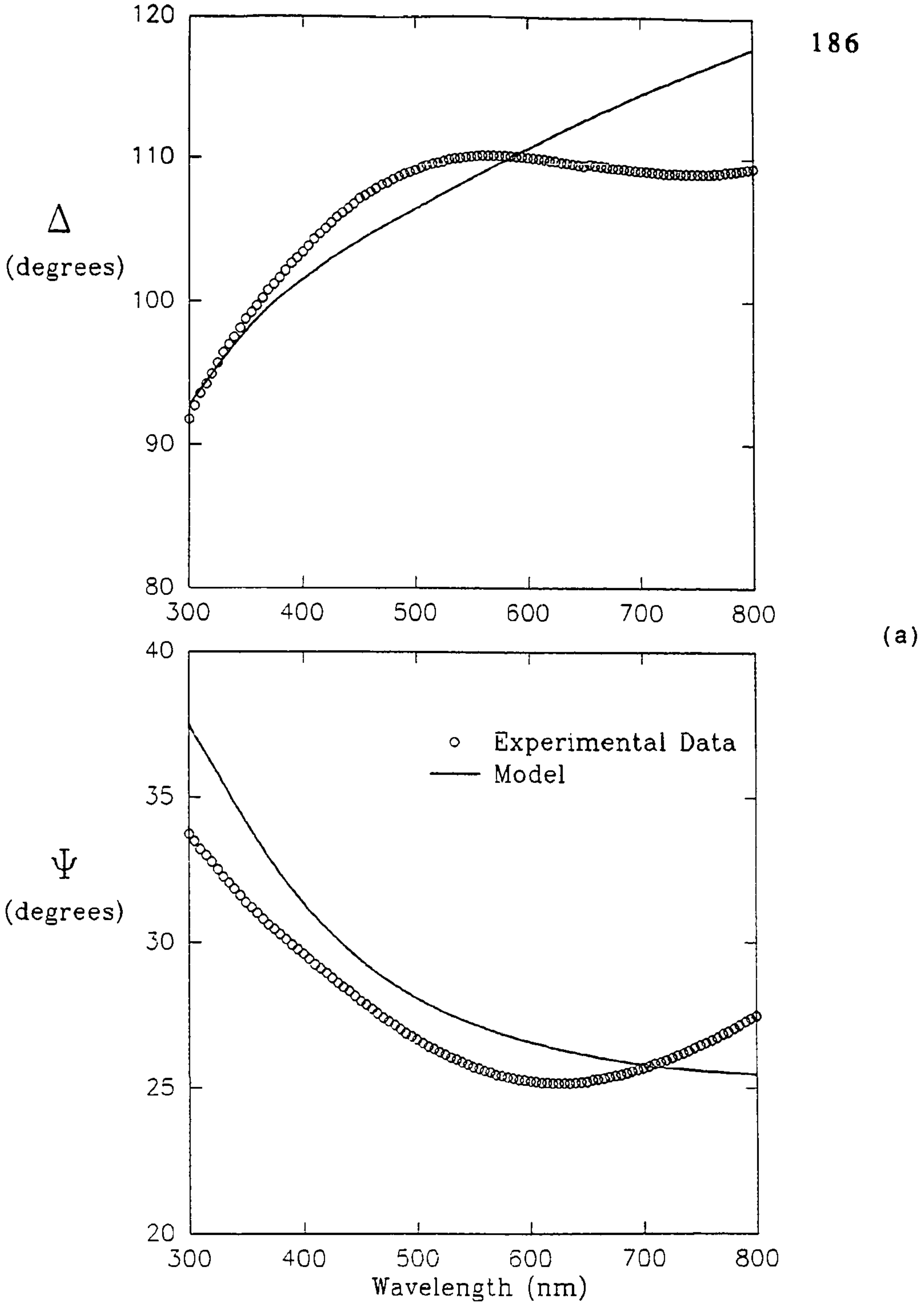

Fig. 5.31: Modelling for a Pt-coated silicon substrate heated to 550°C. (a) Comparison of experimental and modelled spectra. (b) Models

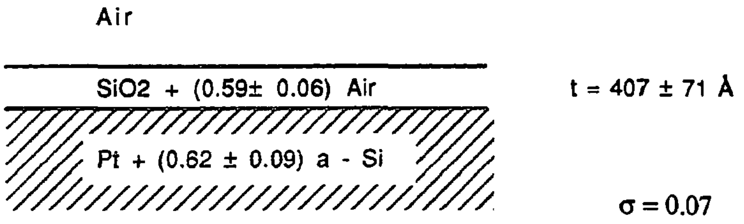

(b)

Fig. 5.31: Continued

Ir_3Si_5 (Frampton et al. 1986). Rutherford backscattering has been used to confirm that on a variety of silicides the passivating oxide is purely SiO_2 (Frampton et al. 1986). Again, this is consistent with the current spectroscopic ellipsometry studies.

It is not clear from these experiments whether the silicon diffused up through the SiO_2 barrier layer or along the edges and surface of the wafer. It has been shown by Taubenblatt and Helms that when Ti and Si are separated by a layer of silicon carbide, diffusion of the silicon at high temperatures occurs only through defective areas in the carbide barrier layer. On reaching the surface, the silicide formation continued laterally, leading to local reaction zones and pitting under the defect as silicon is progressively depleted (Taubenblatt and Helms 1986). It is possible that at some point in the processing of the Pt-coated Si substrates used in this thesis, defects were introduced into the SiO_2 barrier layer which permitted a similar situation to occur. A nonuniform reaction of this type would account for the patchiness of the reaction observed in SEM micrographs on these samples. The second possibility, surface diffusion of the silicon, could easily occur, given the high mobility of silicon above 500°C.

The reaction in the substrate is apparently slowed by the deposition of another film on the platinum surface. Thus, the amount of silicon required in the substrate to fit the experimental data was significantly lower for a substrate with a PZT film on top than for a substrate annealed prior to deposition. The reaction was also less important for substrates held at elevated temperatures comparatively short times. Substrates heated quickly to 600°C and held only 0.5 hr did not show the onset of interference fringes characteristic of a transparent overlayer. Nevertheless, even thin or patchy layers of SiO_2 between the electrode and a ferroelectric film would result in an increase in the apparent coercive field and a decrease in the apparent dielectric constant of the film.

5.3.3 Extended Anneal at 600°C

Measurements on the dielectric constant as a function of frequency on the same sol-gel PZT films have shown that there is a high-frequency roll-off in the dielectric constant of films fired at high temperatures (Chen et al. 1992). In an attempt to determine the mechanism causing this phenomenon, a second piece of the sample was examined by SE at several points during an extended anneal at 600°C.

After 0.5hr at 600°C, the film had collapsed to its final thickness, and the high refractive index suggests that the perovskite phase is both well-crystallized and fairly dense. The best fit model of the film consisted of two layers, with the majority of the film surmounted by a thin overlayer of surface roughness. With increased annealing time, there was no systematic change in the film microstructure, and all of the parameters describing the depth profile remained approximately constant for all subsequent heat treatments. In order to eliminate some of the uncertainty in the refractive index determination, the film depth profile was fixed for all times > 0.5 hr, and the film was modelled by permitting the oscillator describing the optical properties to vary. For all of the microstructures chosen, the refractive index was found to change regularly as the annealing time increased.

As shown in Fig. 5.32, after 0.5 hr the film refractive index began dropping for longer anneals. Given the volatility of lead at these temperatures, it seems possible that this is associated with the depletion of lead from the film surface. Lead volatility has previously been proposed to explain the formation of an electrically lossy layer in series with the remainder of the film at elevated temperatures (Chen et al. 1992). As these types of changes could have a substantial effect on the use and stability of ferroelectric films for memory applications, further study of these phenomenon to elucidate the mechanisms for the variations in ε, tanδ, n, and k with firing time would be fruitful.

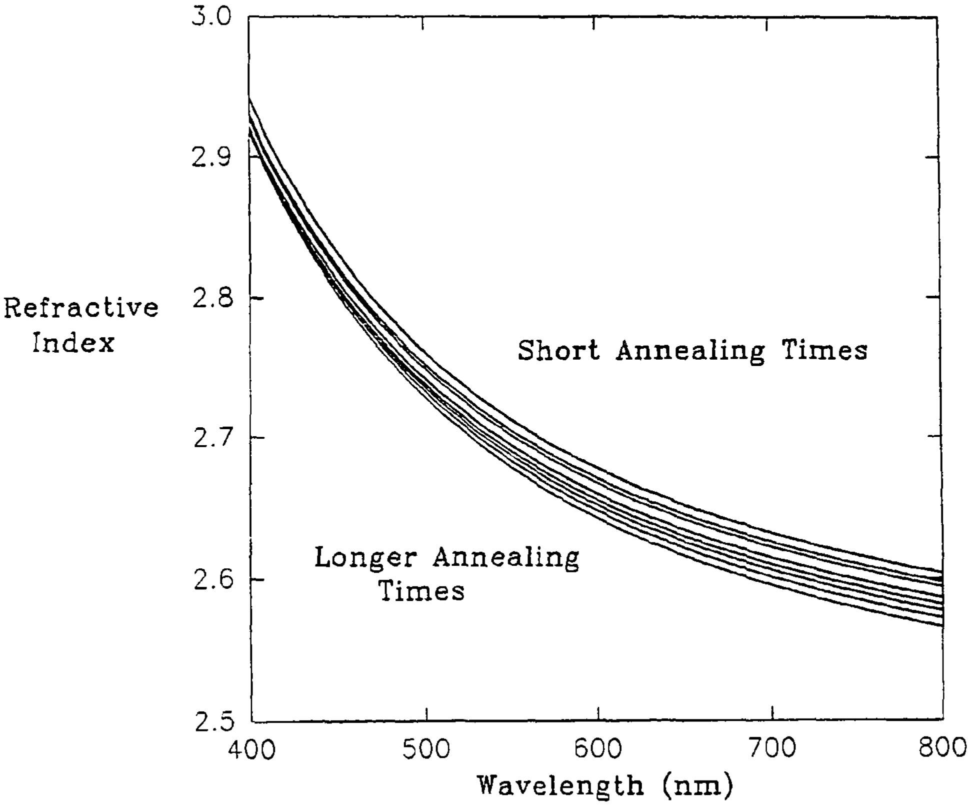

Fig. 5.32: Evolution of the modelled refractive index for a 52/48 sol-gel PZT film with annealing time at 600°C. The microstructure was held fixed for all models.

5.4 PZT Films as a Function of Thickness

In order to study the role of thickness on the properties of ferroelectric films, a series of sol-gel PZT films on Pt-coated silicon substrates were obtained from K.R. Udayakumar of the Materials Research Laboratory at Penn State University. The starting solution was a 0.5 Molar alkoxide similar to that used for the films in section 5.3. Further details concerning the sol preparation are given in the paper by Udayakumar et al. (1990). The solution was spun onto cleaned substrates at 4000 rpm. After each coating, the film was heated to drive off the solvent and partially densify the film. The process was repeated to build up films one to nine layers thick. To more fully explore the lower thickness range, the starting solution was diluted to 0.25M and 0.125M, and films of one to four layers were also prepared.

Two sections were broken from each 0.5M wafer. After heating to 400°C at a rate of 20°C/min in a covered alumina crucible, they were held for 15 minutes at 400°C to remove any residual organic phase. One piece was then heated at the same rate for a one hour hold at 700°C to crystallize and densify the perovskite phase. The second piece was annealed at 600°C. Both samples were furnace cooled. Ellipsometric spectra were collected at room temperature at an angle of incidence of 70°. Modelling was performed by allowing both the heterogeneity profile and the optical properties of the film to vary. Reference data on the platinum-coated silicon substrates were used throughout. As expected, the total film thickness scaled with the number of layers spun on, with each layer contributing ~470Å for the 0.5 Molar solution. For most of the samples, no evidence was found for density gradients through the film thickness due to the original film layering. This is consistent with cross-sectional SEM photographs, which do not demonstrate lamellae within the film (Kushida et al. 1992).

Both sets of films could be fitted with a two layer model, using a "dense" layer for the bulk of the film topped by a layer of surface roughness (typically ~400-600 Å thick with 30 - 45% air). The two layer model consistently provided a better fit to the experimental data than did a homogeneous model for films >1300Å thick. Above this limit there was no systematic variation in the calculated refractive index with the film thickness (see Fig. 5.33 for a plot of the oscillator strength as a function of the number of layers.). For films <1000Å, however, the roughness and the optical properties of the film were strongly correlated, and it was not possible to simultaneously depth profile the inhomogeneities and the optical properties of the film. When modelled with a single unknown layer, the result was a substantial increase in the apparent optical absorption and considerable uncertainty in the refractive index of the film. This precluded investigation of intrinsic size effects in ferroelectric films prepared using these annealing profiles.

It is believed that the correlation between the roughness and the apparent optical properties of the thin ferroelectric films was exacerbated by uncertainties in the substrate dielectric function. Thus, while use of a transparent substrate might mitigate the difficulties associated with the determination of the film refractive index, to circumvent the problem during SE characterization of ferroelectric films on platinum-coated silicon substrates, thicker or smoother samples should be utilized. When the film optical properties are known *a priori*, however, this problem does not arise and spectroscopic ellipsometry should be useful in characterizing the inhomogeneities of much thinner films.

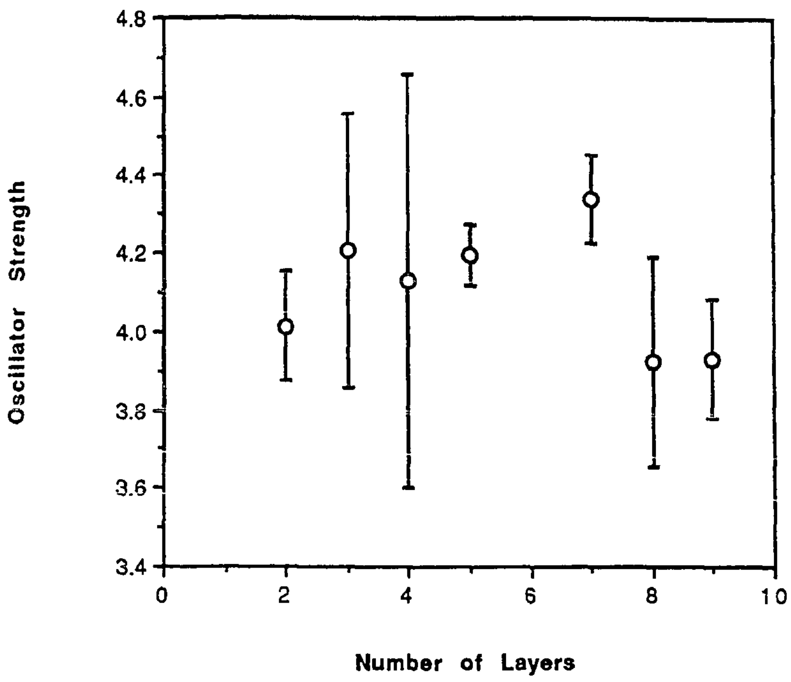

Fig. 5.33: Oscillator strength as a function of the number of layers in sol-gel PZT films on Pt-coated silicon

CHAPTER 6

DISCUSSION AND CONCLUSIONS

6.1 Spectroscopic Ellipsometry as a Characterization Tool for Ferroelectric Materials

It has been demonstrated in this thesis that spectroscopic ellipsometry is a useful characterization tool for the study of bulk and thin film ferroelectrics. In particular, the combination of high sensitivity to surface structure and the ability to depth profile the optical properties and inhomogeneities in transparent systems can be utilized to investigate intrinsic and extrinsic contributions to size effects in this class of materials. Computer code necessary for modelling the phenomena of interest in anisotropic stratified materials was also developed.

To facilitate these studies, two heating chambers were built for the ellipsometer to carry out measurements as a function of temperature on both single crystal and thin film specimens. A windowless design was utilized so that no additional wavelength-dependent errors were introduced into the system. This precluded the need for additional calibration procedures for the ellipsometer, and permitted the measurement accuracy to be maintained for temperatures up to 350°C. Above 400°C, interference between glow from the furnace and the signal reflected from the sample was detected, limiting the accuracy for *in-situ* high temperature measurements. This difficulty could be circumvented by annealing the sample at the desired temperature and cooling below 350°C prior to collecting the ellipsometric spectra. In this way, the temperature capabilities for the ellipsometer were extended to 650°C.

This system was used to track changes in the optical properties of bulk and thin film ferroelectrics with temperature. It was also possible to follow changes in the optical properties and physical structure of thin films during the annealing process.

Similarly, depth profiles of the inhomogeneities of films prepared under different conditions could be evaluated readily. In light of the relationship between structural inhomogeneities and the net electrical properties of ferroelectric films, it is imperative that some means of microstructure characterization be employed in assessing the role of preparation conditions on film quality. It has been demonstrated here that spectroscopic ellipsometry can be utilized for this purpose. These capabilities, coupled with the comparative speed and non-destructive nature of the technique, make it attractive for a variety of research and development applications.

6.2 Surface Studies on Bulk Ferroelectric Materials

Spectroscopic ellipsometry was subsequently applied to the investigation of the surface layers present on a top-seeded grown $BaTiO_3$ crystal and its variation with temperature. Not surprisingly, the optical data was influenced by the surface preparation conditions. Consequently, in describing intrinsic or extrinsic size effects in the electrical properties of ferroelectric crystals, it is important to detail the sample processing.

For a mechanically polished crystal, the data could be described by adding a low dielectric constant layer to the surface of the $BaTiO_3$. It is believed that this low K layer is associated with mechanical damage to the crystal structure, probably through amorphization, roughness, and incorporation of second phases into the near surface region. With careful preparation (final polish 0.05µm γ-Al_2O_3 in a non-aqueous medium) the depth of the optically determined anomalous layer could be less than 200Å on average. Given the damage produced by mechanically polishing the surfaces of both single crystal $BaTiO_3$ and ceramic PLZT samples, care should be exercised in interpreting size-dependent phenomena displayed by ferroelectrics exposed to high stress operations such as polishing or milling.

Chemical etching of the crystal was shown to roughen the surface, but again, the depth of the damaged layer could be made quite thin with an $HCl:H_2O_2:H_2O$ etchant (<300Å). Dissolution of the titanium was found to be much slower than the alkaline earth cation in most acids, however, and it is expected that much of the literature data on etched $BaTiO_3$ was influenced by a non-stoichiometric surface layer.

There is no convincing optical evidence for thick layers of space charge on top-seeded grown $BaTiO_3$ single crystals. This is in contrast to previously reported data on Remeika crystals grown in a KF flux. It is believed that this discrepancy is due to the much lower levels of impurities in the top-seeded crystals.

In summary, the anomalous layers detected optically at the surface of unelectroded $BaTiO_3$ crystals are thinner than the majority of the experimentally determined "surface layer" thicknesses reported in the literature. It is believed that this is due to a combination of careful surface preparation and the increased purity of top-seeded grown crystals relative to the butterfly twins on which many early experiments were performed. It also appears that for bulk ferroelectric materials, like the thin film samples investigated, the major contributions to deviations from ideal ellipsometric spectra are tied to damage or defects introduced during processing. Similarly, it is believed that many of the surface and size effects reported in the literature are not due to intrinsic limitations on the stability of ferroelectricity in insulating specimens. This is encouraging as it suggests that given careful preparation procedures, it should be possible to prepare functional ferroelectric devices down to very small sizes.

6.3 Spectroscopic Ellipsometry Studies on Ferroelectric Thin Films

It has been shown in this thesis that spectroscopic ellipsometry can be utilized to characterize the structural inhomogeneities in ferroelectric thin films. Some degree of heterogeneity was found in most of the films examined; in all cases these were more important in modelling the ellipsometric spectra than were intrinsic size effects. The presence of microstructural imperfections is not necessarily linked to the existence of defects in the crystal structure of ferroelectric films. As a result, well-crystallized, and even well-oriented films can display poor microstructures, as exemplified in a gross fashion by the sol-gel $PbTiO_3$ film on $SrTiO_3$ discussed in section 5.1 and less dramatically by the MIBERS PZT films on sapphire described in section 5.2.

A model was developed to approximate the effect that such local density variations should have on the net electrical properties of an otherwise perfect film. Depending on the configuration of the embedded porosity, it was demonstrated that structural inhomogeneities can profoundly alter the dielectric constant, coercive field, and remanent polarization of ferroelectric films. Effects of this type are expected to be especially pronounced in vapor-deposited films with columnar or cluster microstructures and low density sol-gel films.

Due to the relationship between the film microstructure and the net electrical properties, any systematic variations in the density with film thickness, like those associated with columnar growth, will cause changes in the net film properties as a function of thickness. This mechanism is expected to be responsible for the majority of apparent size effects reported in the literature. Consequently, in examining the properties of ferroelectric films, and especially in considering the variation in properties with film thickness, it is imperative that some structure-sensitive technique, like microscopy or spectroscopic ellipsometry, be utilized.

No evidence was found for a reaction between PZT or PLT films and $SrTiO_3$ or Al_2O_3 single crystal substrates at typical processing temperatures. Similarly, no reaction layer between platinum coated silicon substrates and lead-based perovskite films was positively identified by spectroscopic ellipsometry, although the possibility of forming a thin insulating film on the surface of the substrate itself during prolonged heating above 500°C was discussed. It is expected that if a film was deposited on a platinum coated silicon substrate without an SiO_2 barrier layer separating the metal and the semiconductor, however, a standard annealing profile would cause formation of a platinum silicide within the substrate itself, and a subsequent reaction between the silicide and the lead in the film to form a lead silicate glass.

This thesis has also demonstrated that spectroscopic ellipsometry can track the evolution of crystallinity and structural inhomogeneity during annealing of as-deposited films. One of the advantages of performing these studies on transparent materials is that the entire depth of the film can be sampled (and characterized) at once. In this work, crystallization of the perovskite phase was shown to be largely complete after half an hour at 550°C for both MIBERS and sol-gel PZT 50/50 films. For the prolonged heating cycles utilized during *in-situ* annealing of the ferroelectric films, roughening of the film surface was coincident with this crystallization, and can probably be attributed to the growth of crystal nuclei. In addition, lower temperature phenomena like burnout of organic phases, film densification, and changes in the lead species present could be identified.

It was found that the final microstructures of MIBERS PZT films is dependent on the details of the annealing process. Thus, while the depth profile of film inhomogeneities was consistent for films given the same annealing schedule, changes in the annealing resulted in considerable modification of the final density distribution. Even films annealed at the same peak temperature, but which were exposed to intermediate temperatures for different lengths of time, displayed this type of behavior. Consequently, while the final film microstructure may be influenced by the as-deposited state, it will not necessarily be controlled by the deposition parameters.

This has several important consequences in terms of processing ferroelectric films for device applications. First, as the net electrical properties depend on the inhomogeneities present in the film, it implies that the film electrical properties are a function of the annealing schedule. Second, evaluation of annealing schedules should be conducted in light of structural information for the film (i.e. from microscopy or spectroscopic ellipsometry) in addition to the X-ray diffraction information. Third, some limited property tuning may be possible given proper control of the annealing process. In particular, porosity profiles could be tailored to permit control or grading of the film properties (i.e. structural or optical) through the thickness. One area in ceramic materials in which this type of control might be interesting is in the preparation of functionally gradient materials or in ceramic membranes.

6.4 Ambiguities in the Characterization of Transparent Ferroelectric Materials by Spectroscopic Ellipsometry

Nevertheless, there are still some residual difficulties in the technique that must be considered. While spectroscopic ellipsometry is a very powerful tool for the characterization of insulating thin film materials, it remains an indirect technique. Consequently, in order to determine the true optical properties of a thin film, any sources of changes in the <u>effective</u> optical properties, such as the presence of low density regions or mobile charge, must be correctly accounted for in the modelling. This is clearly pointed up in the room temperature data on the MIBERS 50/50 PZT film on ($1\bar{1}02$) sapphire. Shown in Fig. 6.1 are the fits for two and three layer models describing the system. From this data alone the surface roughness model appears to be justified. However, as described in section 5.2.2, on heating the film, the apparent roughness disappeared gradually with increasing temperature. Such a result is physically unrealistic. Moreover, the changes in the calculated film index behave more systematically as a function of temperature with the two as opposed to the three layer model. Thus, the presence of surface roughness, which appeared to be a reasonable possibility on the basis of the room temperature data, is not sustained by the SE

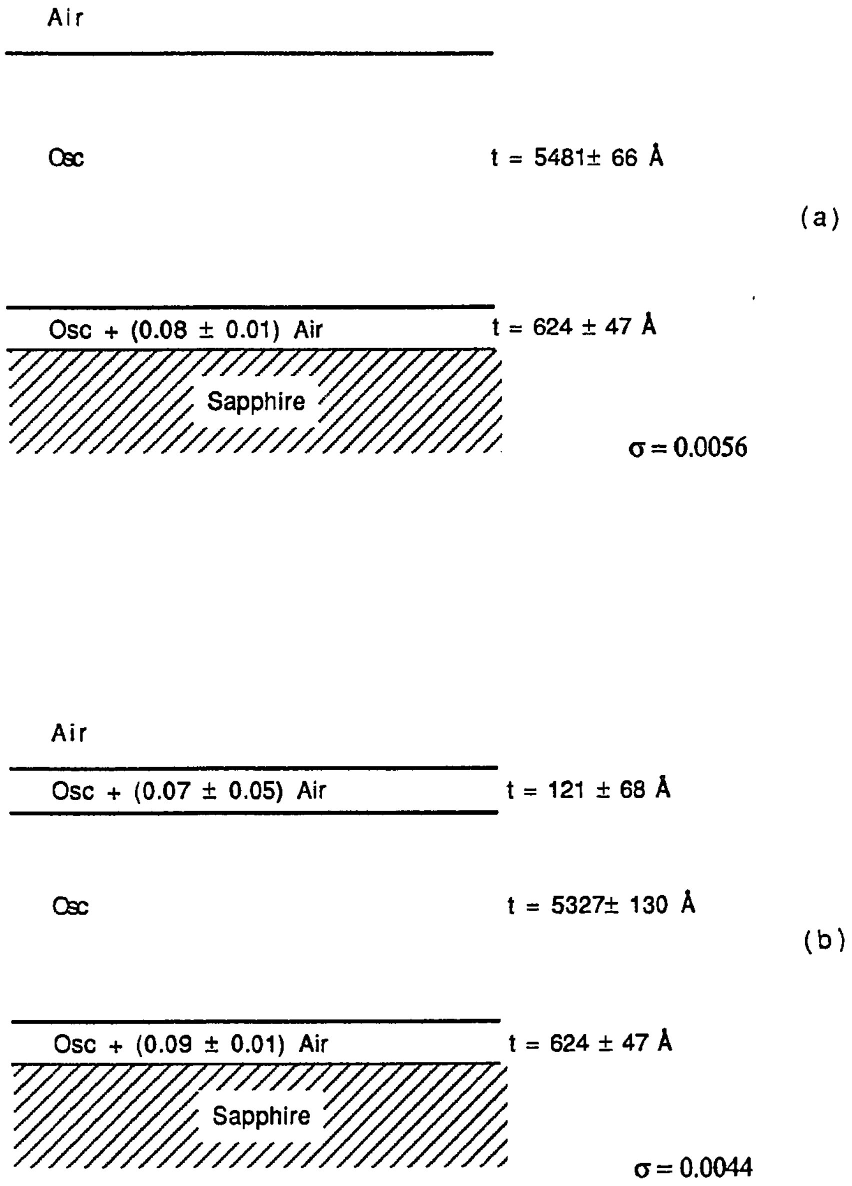

Fig. 6.1: Models for a MIBERS PZT film on $(1\bar{1}02)$ sapphire. (a) Two and (b) three layer models

measurements as a function of temperature. Similarly, while room temperature measurements on a well-poled $BaTiO_3$ crystal could be modelled well with only surface roughness, higher temperature modelling demonstrate marked changes in the apparent roughness, indicating the existence of some phenomenon not properly accounted for in the modelling. A full characterization of ferroelectric materials by spectroscopic ellipsometry, then, in some instances requires measurements as a function of temperature to distinguish the true microstructure from phenomena such as space charge layers, additional scattering due to domain walls, etc..

6.5 Unresolved Difficulties in Determining the Optical Properties of Transparent Materials and Films

While some of the ambiguities in the characterization of ferroelectric films can be alleviated by utilizing temperature as an additional experimental parameter, there remain additional unresolved difficulties which complicate the determination of the refractive index and dispersion of transparent materials by spectroscopic ellipsometry. Included among these are the inability to completely decouple the optical properties of the film from its microstructure, the effect of grain size and roughness on the polarization state of the reflected beam, uncertainties in the substrate optical properties, and the breakdown of standard models for the dispersion of the refractive index as the absorption edge is approached.

The first of these difficulties concerns the fact that small changes in the microstructure and small changes in the refractive index can have similar effects on the Δ and Ψ data, and so the two cannot be decoupled completely. Especially problematic is the high degree of correlation between the general level of the refractive index (parameter A(2) from the dispersion equation given in section 3.4.1.2) and the volume fraction of incorporated porosity through the bulk of the film.

Examples of this type of behavior include the MIBERS films on $(1\bar{1}02)$ sapphire previously discussed in section 5.2.1 and the very thin sol-gel films on platinum-coated silicon substrates considered in section 5.4. In fits on the MIBERS film in which the optical properties of the film were allowed to vary and the majority of the film was assumed to be dense, the microstructure shown in part a of Fig. 6.2 was obtained. However, an equally good fit could be achieved by fixing the volume fraction of air incorporated in the bulk of the film to some small number and again varying the optical properties of the film. Figure 6.3 shows a comparison of the two fits to the experimental data and the calculated refractive indices of the two models. It is not possible to distinguish the better of the two possibilities by varying the measurement temperature or the angle of incidence. The best means of resolving this ambiguity is to compare the calculated refractive indices to values obtained from the literature in transmission experiments. For the MIBERS film, the refractive index matches literature values well when the film is assumed to contain ~ 5.7% residual porosity. It is important to note that even when there is some ambiguity in the SE characterization of transparent films, the gross features of the microstructure, such as the presence of either surface roughness or interfacial porosity, can still be determined. In effect, what is characterized is the relative density of the film as a function of depth, rather than the absolute density. It is believed that this type of correlation between microstructure and derived optical properties accounts for the remaining discrepancies between the refractive indices of oxide and fluoride films determined by Chindaudom and those reported in the literature for bulk samples (Chindaudom 1991). Consequently, unless some corroborating evidence is presented, the "dense" regions in transparent films should not be referred to as "void-free".

Another factor which limits the accuracy of the determined values for the film refractive index is uncertainty in the substrate optical properties. This error source is also tied to the indirect nature of the modelling process. During modelling of thin film

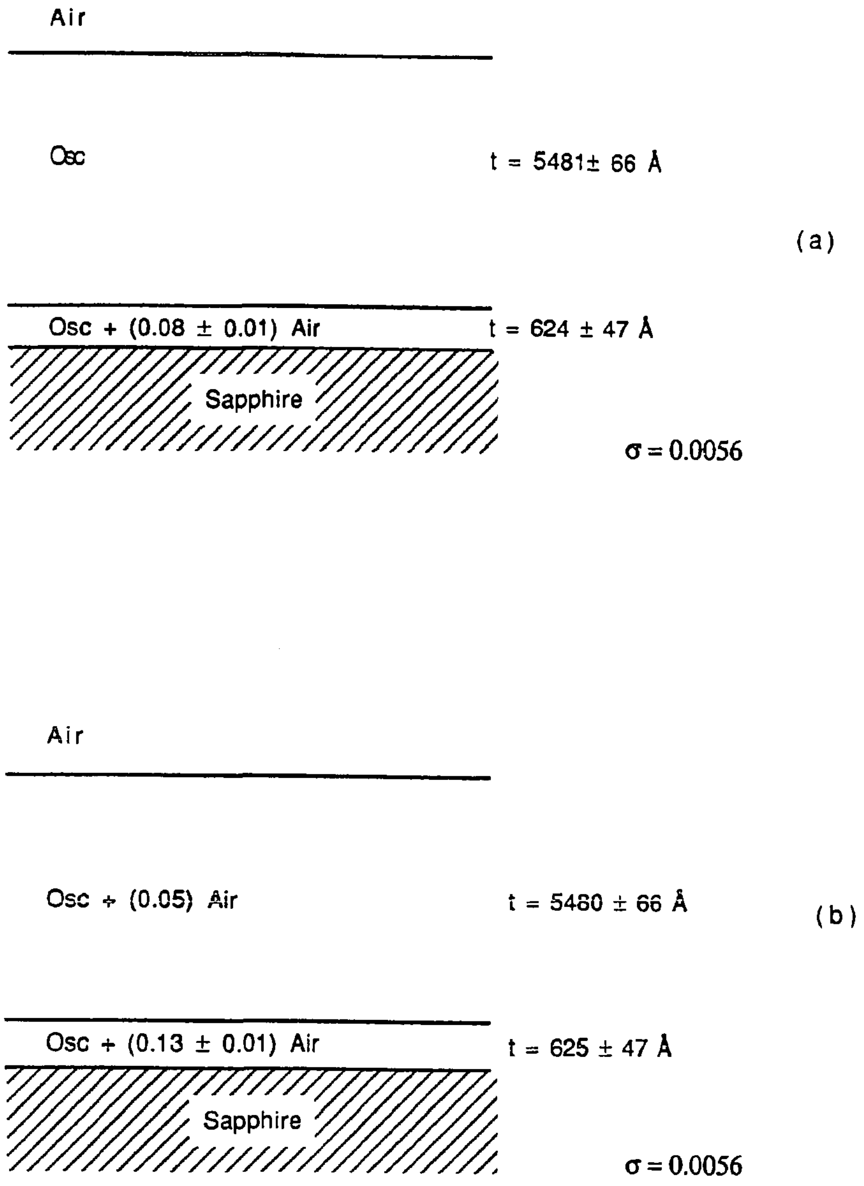

Fig. 6.2: Models for a MIBERS PZT film on $(1\bar{1}02)$ sapphire with (a) and without (b) voids in the majority of the film. (c) Fit to the experimental data

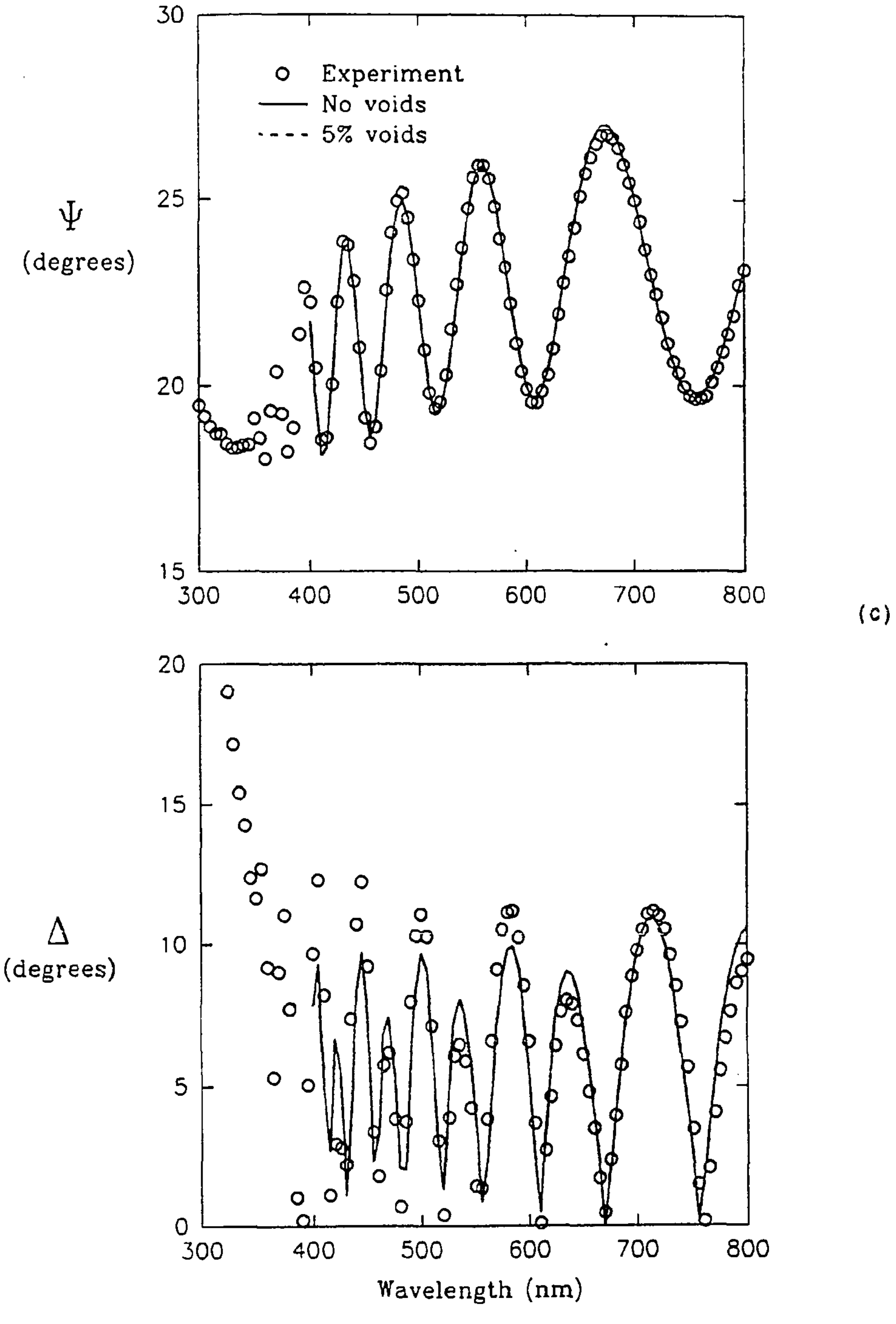

Fig. 6.2: Continued

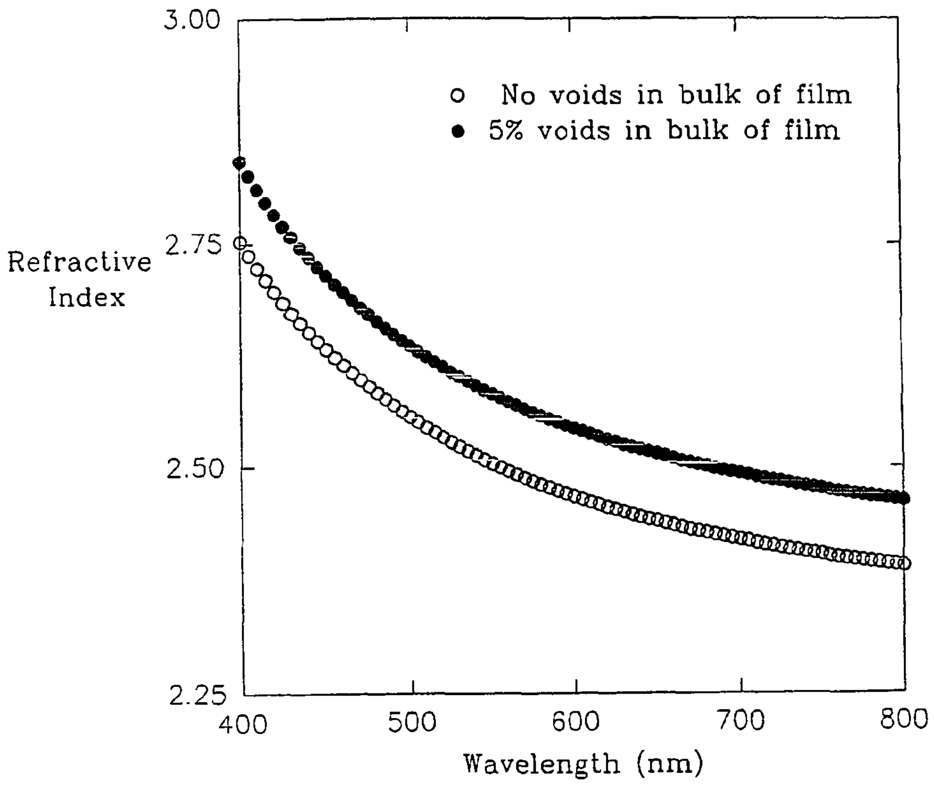

Fig. 6.3: Refractive index of a MIBERS PZT 50/50 film on (1$\bar{1}$02) sapphire modelled with and without voids in the majority of the film

SE data, the sigma value is largely controlled by the interference fringes present in the data. As these fringes are a result of the difference between the dielectric functions of the substrate and the film, any errors in the effective optical properties on the substrate causes the error minimization routine to compensate by shifting the output values for the film optical properties.

This point can be illustrated with the ellipsometric data for ferroelectric films on Pt-coated silicon substrates. As discussed in section 5.3.2, many platinum-coated silicon substrates undergo irreversible changes in their effective optical constants as a function of temperature. Consequently, it was not always possible to utilize initial data for the substrate to characterize the film/substrate system throughout the processing of the ferroelectric. When, however, the substrate dielectric function was permitted to vary to mimic these changes, the resultant uncertainty in substrate properties led to unrealistic values for the refractive index of the ferroelectric (i.e. well above the values for a dense ceramic of the same composition). A second consequence of this type of error is that it precludes an accurate determination of the absolute film density.

A third source of error in the determination of the optical constants of either transparent samples is the breakdown in the Sellmeier oscillator model as the absorption edge is approached. While the Sellmeier oscillator is an adequate description of the dielectric function dispersion far from the absorption edge, at the onset of significant absorption, it does not mimic the abrupt rise in Δ well. In previous ellipsometric studies on transparent films/transparent substrate systems utilizing accurate data for both Δ and Ψ, only materials with near zero absorption coefficients throughout the wavelength range of interest were characterized (Chindaudom 1991) and this effect did not serve as a significant error source. As most ferroelectric materials have absorption edges in the near UV, however, this becomes progressively more troublesome. In this work, this was found to be particularly problematic in the characterization of surface layers on monolithic transparent materials. To minimize this problem, data sets were truncated to eliminate the onset of the absorption edge. Nevertheless, the values for the absorption in thin films were also affected by this as described in section 5.1. In future studies it would be useful to develop a better approximation for the optical properties of transparent materials near the absorption edge.

Fourthly, finite wavelength effects may act as another error source in the SE characterization of some ferroelectric thin films. If the grain size of a particulate compact is comparable to the wavelength of light, the assumptions underpinning the static effective medium approximations are no longer fulfilled, and use of the standard Bruggeman effective medium theory can lead to significant error incorporation (Egan and Aspnes 1982). This error source should be important only when some major structural feature in the films is on the order of the wavelength of the light (i.e. for a poorly densified film which is composed of discrete particles of the right size, or in a very rough film where the roughness meets the same criterion). In a dense film, a fairly smooth one, or in any situation where the effective medium approximation is not required during modelling, this will not contribute to the error. Most of the films in this thesis should not be susceptible to this error source. Nevertheless, in a simultaneous determination of the optical properties and the inhomogeneities of some films, this can also lead to errors in the calculated refractive index. As a result, SE data on transparent films should be coupled with additional information from microscopy in characterization of a completely unknown film system.

6.6 Future Work

It has been demonstrated during the course of this work that spectroscopic ellipsometry can be utilized to study several problems of interest in the characterization and processing of insulating materials. Consequently, in addition to the possibility of future studies on ferroelectric materials (covered in the second half of this section) there are many areas in the broader field of ceramic and glass science which would be interesting to address with this technique. Among these are the characterization of optical coatings, *in-situ* studies on structure and microstructure development during annealing of as-deposited thin films, investigation of nucleation and growth mechanisms for thin films, the measurement of active optical property coefficients in thin film samples, and the study of surface modification in bulk glass and ceramic specimens. From an industrial standpoint, spectroscopic ellipsometry is also interesting as an in-line diagnostic tool for either process monitoring or quality control in device manufacture.

As discussed by Chindaudom (Chindaudom 1991), spectroscopic ellipsometry offers a unique opportunity to simultaneously determine the optical properties and homogeneity of dielectric thin films. An understanding of the role of film processing (through its effect on the microstructure) in controlling the real and imaginary parts of the apparent refractive index would be particularly helpful in the design and manufacture of antireflection coatings and filters for optical applications. In addition to providing a means to optically characterize thin films intended for optical applications, this also permits the study of the high frequency dielectric function for materials which cannot be prepared as transparent single crystals or ceramics.

While the technique can be applied in its current form to many technologically interesting materials and systems, there are also several fronts for research in the characterization of dielectric thin films. One of these would be to determine if spectroscopic ellipsometry is sufficiently sensitive to accurately depth-profile graded refractive index optics. A second attractive area for study would be to investigate the sensitivity of ellipsometry in the detection of absorbing species, like coloring ions, in glasses. In particular, it would be very useful to know whether "k" values due to the colorant in colored thin film dielectrics could be unambiguously separated from the apparent "k" associated with the film microstructure.

Spectroscopic ellipsometry should also be useful in the study of nucleation, growth, and structural and microstructural changes in dielectric thin films. As has been demonstrated by Collins et al. for semiconducting and metallic materials (An et al. 1990), if the standard detection system of a rotating polarizer spectroscopic ellipsometer is replaced with an optical multichannel analyzer, complete ellipsometric spectra can be collected in 40 ms. This is sufficiently rapid to permit real-time control of vapor-deposited thin film deposition. Moreover, subsequent modelling of the data contains information on the mechanism of growth (layer-by-layer or island), the nucleation density, coalescence of nuclei, and the film density (An et al. 1990). Following deposition, the continual evolution of the film structure can be evaluated during *in-situ* annealing of either vapor- or liquid- deposited films. These capabilities could be applied widely to study densification, crystallization, and microstructure development in thin films with different compositions. Such studies would be especially beneficial in examining the relative importance of film deposition and the annealing profile in determining the net film properties.

It should also be possible to use ellipsometry to measure optical property coefficients in thin films, provided the magnitude of the effect is large enough to produce a measurable change in either the refractive index or the absorption coefficient. Of particular importance here would be the first and second order electrooptic and magnetooptic effects. Again, one of the attractive features of utilizing ellipsometry for this purpose is its ability to separate the effect of microstructure from the measured property coefficients.

Finally, spectroscopic ellipsometry could be utilized to study surface modified glasses and ceramics. Chemical strengthening of glass surfaces typically involves replacing modifier cations near the surface with either larger or more cations so that the surface is forced into compression. As this would be accompanied by a simultaneous alteration in the near surface refractive index, it should be possible to follow the strengthening process with ellipsometry. Chemical weathering of glass and ceramic surfaces is also an important field of study. As leaching of alkali cations from the exposed surface should also result in a measurable change in the refractive index, kinetics studies on the weathering process could be initiated using spectroscopic ellipsometry. A third area which could be interesting is the study of highly reflective plate glasses for buildings. These materials are typically soda-lime-silica float glasses which have been electrolytically treated to produce small metal droplets in the top several hundred Ångstroms of the surface (Loukes 1991). Here, a means of determining the volume fraction of the included phase and its depth profile would be useful in modelling the net optical properties of the glass.

To a limited extent, spectroscopic ellipsometry may also be useful in investigating the surfaces of materials underneath electrodes. As the penetration depth of light in metals is quite small, special samples with semi-transparent top electrodes would have to be prepared to conduct studies of this type. Nevertheless, if the sample surface can be probed, it may be possible to examine phenomena like electrode delamination in capacitor and actuator materials. This would be particularly useful if such studies were conducted as a function of both the environment and the applied field. Similarly, with a micro-imaging ellipsometer (Beaglehole 1988) it might also be possible to study local reliability problems like electrode migration during aging of capacitors.

In the area of ferroelectric materials and films, there are also several possibilities for future work. One aspect which would be interesting to pursue is a further elaboration of the properties of the anomalous layers on single crystal and ceramic ferroelectrics. In particular, it would be useful to ally the SE data with more quantitative information on the sample surface composition, like that obtained from

Auger electron spectroscopy. This would help eliminate ambiguities associated with the origin of the low K layers on $BaTiO_3$ which result from most surface preparation techniques. In addition, as discussed in section 3.4.5, ellipsometry becomes insensitive to gradients in the polarization in $BaTiO_3$ when the decay length is <~100Å. One of the features that makes such phenomena difficult to detect is that when the optic axis is perpendicular to the surface, the Δ and Ψ parameters are not particularly sensitive to values for the extraordinary index. Unfortunately, in $BaTiO_3$ only the extraordinary refractive index is polarization dependent. To confirm the results on $BaTiO_3$, then, it would be ideal to investigate a system where the ordinary refractive index also depends on the spontaneous polarization. This, in turn, would make optical detection of changes in the polarization near the surface of the ferroelectric easier. Ideally the material chosen should also be optically uniaxial to facilitate modelling. Possible candidates include $PbTiO_3$ and $LiTaO_3$. The former in particular is especially attractive as the ordinary index is a strong function of the polarization and the birefringence is comparatively small.

Another candidate for single crystal studies is the family of strontium barium niobates (SBN). In these materials, the barium to strontium ratio can be adjusted to alter the spontaneous polarization and the transition temperatures in these materials. The optical properties are comparable to those of barium titanate. Of particular interest in this family is the rapid domain pinning demonstrated by the single crystals. Typically, after several cycles through the hysteresis loop the domains cannot be reoriented with an applied electric field, and the remanent polarization drops to a fraction of its initial value (Cline 1977). It has been suggested that this is a function of space charge accumulation at the surface of the crystals (Cross 1991). Spectroscopic ellipsometry should be capable of distinguishing whether, in fact, the pinning is due strictly to a surface phenomenon, and if so, what the mechanism for the pinning is. As SBN is a candidate material for holographic storage, an understanding of the mechanism for domain pinning will also be important in the fixing of holographic memories. From a fundamental standpoint, such extensive space charge migration would permit verification of the expected relationship between the degree of internal compensation of the spontaneous polarization and the value for the surface polarization.

Another area in which further study would be useful is the role of thickness on the properties of ferroelectric thin films. As discussed in section 5.4, this would best be approached by investigation of films on single crystal substrates like MgO, sapphire, or a single crystal perovskite. This would be advantageous in two ways. First, in such a study, the refractive index of the film should be fairly close to that of the substrate so that the small perturbations in the complex reflectivity due to size effects in the thin films are not completely overwhelmed by strong interference-induced oscillations in Δ and Ψ. Secondly, high quality, oriented films on single crystal substrates can be prepared. This would minimize the dependence of the results on extrinsic size effects. Good results could probably be obtained with the rf sputtered lead lanthanum titanate films on sapphire examined in section 5.1. Ideally, the composition of the film should be chosen so that the ferroelectric-paraelectric transition could be tracked as a function of film thickness. This, in turn, would help to resolve the mechanism for the loss of ferroelectricity at small dimensions.

To elucidate the role of electrical boundary conditions on the properties of ferroelectrics as a function of size, similar studies should be repeated on films electroded on one or both surfaces. In particular, this should permit the role of depolarizing fields and space charge layers to be examined for thin film samples. Moreover, as thin films are not as susceptible to thermal shock and fracture on traversing the ferroelectric-paraelectric phase transition, it should be possible to determine for each film the complex reflectivity expected in the non-ferroelectric phase. These spectra should then serve as references for the ideally terminated films. Changes in Δ and Ψ on passing through the phase transition could then be related to changes in the electrical boundary conditions. This, in turn, should help clarify which mechanisms are responsible for deviations from bulk properties.

As most practical applications of ferroelectric materials require electroding of the device, such experiments would also lead to guidelines on the changes that should be expected in device properties as a function of thickness. One particular property which ellipsometry should be capable of measuring is the electrooptic coefficient. Experimentally, this would involve only monitoring changes in Δ and Ψ as an electric field is applied across the film. This is especially interesting as it exploits the precision of ellipsometry rather than its absolute accuracy, increasing by an order of magnitude the sensitivity to changes in the film optical properties. Similar studies have been initiated at Sandia National Laboratories (Land and Dimos 1991) with a single wavelength ellipsometer. Land and Dimos have demonstrated that large changes in Δ and Ψ can be induced with an applied electric field, but due to their wavelength limitations, they are not capable of measuring the film's refractive index, its thickness, or the extent of inhomogeneity in the film. With a spectroscopic ellipsometer, those difficulties would be eliminated. As one of the major interests in ferroelectric films stems from the possibility of using them as electrooptic switches, a survey of the changes that should be expected in the electrooptic coefficients as a function of thickness would be of practical interest. Again, due to the depth profiling capabilities of the spectroscopic ellipsometry, the roles of intrinsic and extrinsic contributions to changes in the electrooptic coefficient as a function of size could be decoupled.

It would also be instructive to compare the ellipsometric studies with Raman scattering results on the same samples. Raman scattering is a sensitive method for determining the soft mode behavior in ferroelectric systems, and as such, would serve as an independent verification for the presence or absence of ferroelectricity in very thin films. Such results would be an interesting complement to the work reported by Ishikawa et al. (1988) on the ferroelectric-paraelectric transition in fine ferroelectric particles, and would act as a springboard for discussions on the differences between size effects in zero (particulate) and two dimensional (film) systems.

Another interesting set of experiments which should be performed on the electroded films involves monitoring Δ and Ψ as the film is cycled repeatedly through the hysteresis loop. As in the SBN single crystals, when the polarization direction of most lead zirconate titanate films has been reversed a sufficient number of times, the domains pin, and the magnitude of the remanent polarization decays. Eventually, if the cycling is continued, the films either break down electrically and short through the film thickness, or lose enough of the reversible polarization that they are no longer useful for information storage. This places a serious limitation on the utilization of ferroelectric films for memory applications. Several mechanisms have been proposed to explain the fatigue demonstrated during cycling of the films. Among these is the postulation that the fatigue is associated with the generation of a space charge layer (Duiker et al. 1990). However, there are currently no data available on either how or how quickly the charge accumulates. Spectroscopic ellipsometry may provide a means to determine whether charge migration is, in fact, responsible for the poor cycling behavior of ferroelectric films. Similarly, other possible contributions, including the formation of microcracks, or separation of the electrode from the film surface (Johnson et al. 1990), should also be readily detectable.

Finally, it would be interesting to study materials which can be field-forced from the antiferroelectric to the ferroelectric state. In the lead zirconate - lead zinc niobate solid solution some compositions remain ferroelectric when the field is removed and persist in that state until converted back to the antiferroelectric phase by a reversed electric field. As an antiferroelectric does not have a net polarization which must be compensated at the surface, the depolarization energy contribution to the free energy of the system disappears (Binder 1981). Due to the continued presence of the bare surface and correlation energy terms, however, the sublattice polarization still decays at the surface. In this case, however, the decay is not modulated by depolarization fields, and so Binder predicts the polarization decay length will be longer than for the ferroelectric case (1981). The ability to measure these two numbers on the same sample should allow verification of Binder's hypothesis.

REFERENCES

H. Adachi, T. Mitsuyu, O. Yamazaki, and K. Wasa, "Ferroelectric (Pb,La)(Zr,Ti)O_3 epitaxial thin films on sapphire grown by rf-planar magnetron sputtering," *J. Appl. Phys.* **60** [2] 736-741 (1986).

V. Afanasjev, S. Korpela, and T. Tuomi, "The influence of surface layers on the measured refractive index of ferroelectric materials studied by means of spectroscopic ellipsometry," *Ferroelectrics* **65** 175-180 (1985).

D. Allara and A. Parikh, Polymer Science Department, The Pennsylvania State University, private communication, 1989.

I. An, H. V. Nguyen, N. V. Nguyen, and R. W. Collins, "Microstructural evolution of ultrathin amorphous silicon films by real-time spectroscopic ellipsometry," *Phys. Rev. Lett.* **65** [18] 2274-2277 (1990).

G. Arlt, D. Hennings, and G. de With, "Dielectric properties of fine-grained barium titanate ceramics," *J. Appl. Phys.* **58** [4] 1619-1625 (1985).

N. W. Ashcroft and N. D. Mermin, *Solid State Physics,* Holt, Rinehardt, and Winston, Philadelphia, 1976.

D. E. Aspnes, "Effects of component optical activity in data reduction and calibration of rotating- analyzer ellipsometers," *J. Opt. Soc. Am.* **64** [6] 812-819 (1974).

D. E. Aspnes and A. A. Studna, "High precision scanning ellipsometer," *Appl. Opt.* **14** [1] 220-228 (1975).

D. E. Aspnes and A. A. Studna, "Chemical etching and cleaning procedures for Si, Ge, and some III-V compound semiconductors," *Appl. Phys. Lett.* **39** [4] 316-318 (1981).

D. E. Aspnes, A. A. Studna, and E. Kinsbron, "Dielectric properties of heavily doped crystalline and amorphous silicon from 1.5 to 6.0 eV," *Phys. Rev.* **B29** [2] 768-779 (1984).

R. Bachmann and K. Barner, "Stable suspensions of ferroelectric $BaTiO_3$ particles," *Sol. State Comm.* **68** [9] 865-869 (1988).

C. F. Baes, Jr. and R. E. Mesmer, *The Hydrolysis of Cations*, John Wiley and Sons, New York, 1976.

J. C. Bailar Jr., T. Moeller, J. Kleinburg, C. O. Guss, M. E. Castellion, and C. Metz, *Chemistry, 2nd Ed.,* Academic Press, New York, 1984.

N. P. Bansal and A. L. Sandkuhl, "Chemical durability of high-temperature superconductor $YBa_2Cu_3O_{7-x}$ in aqueous environments," *Appl. Phys. Lett.* **52** [4] 323-325 (1988).

I. P. Batra, P. Wurfel, and B. D. Silverman, "Depolarization field and stability considerations in thin ferroelectric films," *J. Vac. Sci. Technol.* **10** [5] 687-692 (1973a).

I. P. Batra, P. Wurfel, and B. D. Silverman, "Phase transition, stability, and depolarization field in ferroelectric thin films," *Phys. Rev.* **B8** [7] 3257-3265 (1973b).

D. Beaglehole, "Performance of a microscopic imaging ellipsometer," *Rev. Sci. Instrum.* **59** [12] 2557-2559 (1988).

P. Beauvillain, C. Chappert, J. P. Renard, C. Marliere, and D. Renard, "Magnetic interaction between ultrathin nickel films through a gold interlayer," in *Magnetic Thin Films, 1986,* Edited by R. Krishnan, les editions de physique, France, 1986.

A. E. Berkowitz, W. J. Schuele, and P. J. Flanders, "Influence of crystallite size on the magnetic properties of acicular γ - Fe_2O_3 particles," *J. Appl. Phys.* **39** [2] 1261-1263 (1968).

P. J. Besser, J. E. Mee, P. E. Elkins, and D. M. Heinz, "A stress model for heteroepitaxial magnetic oxide films grown by chemical vapor deposition," *Mat. Res. Bull.* 6 1111-1124 (1971).

V. G. Bhide, R. T. Gondhalekar, and S. N. Shringi, "Surface layers on ferroelectric $BaTiO_3$ crystals," *J. Appl. Phys.* **36** [12] 3825-3833 (1965).

K. Binder, "Surface effects on phase transitions in ferroelectrics and antiferroelectrics," *Ferroelectrics* **35** 99-104 (1981).

S. V. Biryukov, V. M. Mukhortov, A. M. Margolin, Yu. I. Golovko, I. N. Zakharchenko, V. P. Dudkevich, and E. G. Fesenko, "Phase transitions in polycrystalline and heteroepitaxial ferroelectric films," *Ferroelectrics* **56** 115-118 (1984).

M. Blackman and A. E. Curzon, "On the size dependence of the melting and solidification temperatures of small particles of tin," *Structure and Properties of Thin Films*, pp. 217-222. Wiley, New York, 1959.

B. T. Boiko, A. T. Pugachev, and Y. M. Bratsykhin, "Melting of subcritically thin condensed films of indium," *Sov. Phys. - Sol. State* **10** [12] 2832-2834 (1969).

J. P. Borel, "Thermodynamic size effect in and structure of metallic clusters," *Surface Science* **109** 1-9 (1981).

L. Bretherick, *Hazard in the Chemical Laboratory*, the Royal Society of Chemistry, London, 1986.

R. Bruchhaus, D. Pitzer, O. Eibl, U. Scheithauer, and W. Hoesler, "Investigation of Pt bottom electrodes for "in-situ" deposited $Pb(Zr,Ti)O_3$ thin films," preprint 1992.

Ph. Buffat and J.-P. Borel, "Size effect on the melting temperature of gold particles," *Phys. Rev.* **A13** [6] 2287-2298 (1976).

V. I. Bukatyi, Yu. V. Goncharov, V. N. Krasnopevtsev, A. M. Shaiduk, V. P. Lushev, A. A. Pavlenko, and M. G. Potapov, "Study of the temperature dependence of the refractive index of sapphire," *Opt. Spectrosc. (USSR)* **56** [3] 283-285 (1984).

G. Burns and F. H. Dacol, "$BaTiO_3$ as a biased paraelectric," *Jap. J. Appl. Phys.* **24** suppl. 24-2 649-650 (1985).

I. Camlibel, M. DiDomenico, Jr., and S. H. Wemple, "Dielectric properties of single-domain melt-grown $BaTiO_3$," *J. Phys. Chem. Solids* **31** 1417-1419 (1970).

T. Chainer, Y. Morii, and H. Kojima, "Size effects in superfluid ^3He," *Phys. Rev.* **B21** [9] 3941-3944 (1980).

J. Chen, K. R. Udayakumar, K. G. Brooks, and L. E. Cross, "Rapid thermal annealing of sol-gel derived lead zirconate titanate thin films," submitted (1992).

P. Chindaudom, *Characterization of Inhomogeneous Transparent Thin Films on Transparent Substrates by Spectroscopic Ellipsometry,* Ph.D. Thesis, The Pennsylvania State University, 1991.

A. G. Chynoweth, "Surface space-charge layers on barium titanate," *Phys. Rev.* **102** [3] 705-714 (1956).

T. W. Cline, *Domain Contributions to the Dielectric Response in Ferroelectric Crystals,* Ph.D. thesis, The Pennsylvania State University 1977.

CRC Handbook of Laser Science and Technology, Vol. 3, Edited by M. J. Weber, CRC Press.

R. Comes, M. Lambert, and A. Guinier, "The chain structure of $BaTiO_3$ and $KNbO_3$," *Sol. State Comm.* **6** 715-719 (1968).

L. E. Cross, private communication, 1991.

L. E. Cross, "Relaxor ferroelectrics," *Ferroelectrics* **76** [3-4] 241-267 (1987).

A. Croteau, S. Matsubara, Y. Miyasaka, and N. Shohata, "Ferroelectric $Pb(Zr,Ti)O_3$ thin films prepared by metal target sputtering," *Jpn. J. Appl. Phys.* **26** suppl. 26-2, 18-21 (1987).

B. D. Cullity, *Introduction to Magnetic Materials,* Chap. 11. Addison-Wesley Publishing Company, Reading, Mass., 1972.

J. M. M. de Nijs and A. van Silfhout, "Systematic and random errors in rotating-analyzer ellipsometry," *J. Opt. Soc. Am.* **5** [6] 773-781 (1988).

J. L. Devore, *Probability and Statistics for Engineering and the Sciences* Chapter 9. Brooks/Cole Publishing Company, Monterey, California, 1982.

S. K. Dey and R. Zuleeg, "Sol-gel ferroelectric thin films merged with GaAs JFET memory technology," *ISAF 1990 abstracts,* 12.2 (1990).

M. DiDomenico, Jr. and S. H. Wemple, "Optical properties of perovskite oxides in their paraelectric and ferroelectric phases," *Phys. Rev.* **166** [2] 565-576 (1968).

R. H. Doremus, D. Murphy, N. P. Bansal, W. A. Lanford, and C. Burman, "Reaction of zirconium fluoride glass with water: kinetics of dissolution," *J. Mat. Sci.* **20** 4445-4453 (1985).

S. Ducharme, J. Feinberg, and R. R. Neurogaonkar, "Electrooptic and piezoelectric measurements in photorefractive barium titanate and strontium barium niobate," *IEEE J. Quantum Elec.* **QE-23** [12] 2116-2121 (1987).

V. P. Dudkevich, V. A. Bukreev, Vl. M. Mukhortov, Yu. I. Golovko, Yu. G. Sindeev, V. M. Mukhortov, and E. G. Fesenko, "Internal size effect in condensed $BaTiO_3$ ferroelectric films," *phys. stat. sol. (a)* **65**, 463-467 (1981).

H.M. Duiker, P. D. Beale, J. F. Scott, C. A. Paz-Araujo, B. M. Melnick, J. D. Cuchiaro, and L. D. McMillan, "Fatigue and switching in ferroelectric memories: Theory and experiment," *J. Appl. Phys.* **68** [11] 5783-5791 (1990).

W. G. Egan and D. E. Aspnes, "Finite-wavelength effects in composite media," *Phys. Rev.* **B26** [10] 5313-5320 (1982).

J. M. Eldridge and D. W. Dong, "The growth of thin PbO layers on lead films," *Surf. Sci.* **40** 512-530 (1973).

F. L. English, "Electron-mirror microscopy study of $BaTiO_3$ surface layers," *J. Appl. Phys.* **39** [7] 3231-3236 (1968).

A. E. Ennos, "Optical properties of evaporated lead monoxide films," *J. Opt. Soc. Am.* **52** [3] 261-264 (1962).

V. E. Fertman, *Magnetic Fluids Guidebook: Properties and Applications*, Hemisphere Publishing Corp., Philadelphia, 1990.

P. W. Forsbergh, Jr., "Effect of two-dimensional pressure on the Curie point of barium titanate," *Phys. Rev.* **93** [4] 686-692 (1954).

G. R. Fox, J. H. Adair, and R. E. Newnham, "Effects of pH and H_2O_2 upon coprecipitated $PbTiO_3$ powders: I. Properties of as-precipitated powders," *J. Mat. Sci.* **25** 3634-3640 (1990).

G. R. Fox, S. B. Krupanidhi, K. L. More, and L. F. Allard, "Composition/structure/property relations of multi-ion-beam reactive sputtered lead lanthanum titanate thin films: Part I: Composition and structure analysis," submitted to *J. Mat. Res.* (1992).

R. D. Frampton, E. A. Irene, and F. M. d'Heurle, "The measurement of effective complex refractive indices for selected metal silicides," *J. Appl. Phys.* **59** [3] 978-980 (1986).

M. H. Francombe and S. V. Krishnaswamy, "Growth and properties of piezoelectric and ferroelectric films," *J. Vac. Sci. Technol.* **A8** [3] 1382-1390 (1990).

K. G. Frase, E. G. Liniger, and D. R. Clarke, "Environmental and solvent effects on yttrium barium cuprate ($Y_1Ba_2Cu_3O_x$)," *Advanced Ceramic Materials* **2** [3B] special issue on ceramic superconductors, 698-700 (1987).

E. Furman, *Dielectric Breakdown and Related Properties of Lead Lanthanum Zirconate Titanate 9.5/65/35*, Ph.D. Thesis, The Pennsylvania State University, 1987.

S. Fushimi and T. Ikeda, "Optical study of lead zirconate-titanate," *J. Phys. Soc. Jpn.* **20** [11] 2007 -2012 (1965).

V. G. Gavrilyachenko, R. I. Spinko, M. A. Martynenko, and E. G. Desenki, "Spontaneous polarization and coercive fields of lead titanate," *Sov. Phys. - Sol. State* **12** [5] 1203 - 1204 (1970).

V. L. Ginzburg and L. P. Pitaevskii, "On the theory of superfluidity," *Sov. Phys. JETP* 34 [7], number 5, 858-861 (1958).

V. L. Ginzburg, "Some remarks on phase transitions of the second kind and the microscopic theory of ferroelectric materials," *Sov. Phys. - Sol. State* **2** [9] 1824-1834 (1961).

A. A. Gitel'son, A. M. Lerer, V. S. Mikhalevskii, V. M. Mukhortov, and S. V. Orlov, "Physical properties of (Ba,Sr)TiO_3 ferroelectric thin films in weak electric fields," *Sov. Phys. Sol. State* **19** [7] 1121-1124 (1977).

N. T. Gladkich, R. Niedermayer, and K. Spiegel, "Nachweis großer schmelzpunktserniedrigungen bei dünnen metallschichten," *phys. stat. sol.* **15** 181-191 (1966).

G. Godefroy, C. Dumas, P. Lompre, and A. Perrot, "Crystal growth and characterization of two kinds of Fe doped $BaTiO_3$ single crystals, " *Ferroelectrics* 37 725-728 (1981).

J. H. Greiner, "Oxidation of lead films by rf sputter etching in an oxygen plasma," *J. Appl. Phys.* 45 [1] 32-37 (1974).

K. M. Gustin, "Optical characterization of low-index transparent thin films on transparent substrates by spectroscopic ellipsometry," *Appl. Opt.* **26** [18] 3796-3802 (1987).

E. Guyon and C. D. Mitescu, "Comparative study of size effects in solid and liquid films," *Thin Solid Films* **12** 355-366 (1972).

E. P. Harris, P. S. Hauge, and C. J. Kircher, "Optical properties of ultrathin PbO layers grown on Pb films," *Appl. Phys. Lett.* 34 [10] 680-682 (1979).

I. Hlasnik et al., "Properties of superconducting NbTi superfine filament composites with diameters <~0.1 µm," *Cryogenics* **25** 558-565 (1985).

R. L. Holman and R. M. Fulrath, "Intrinsic nonstoichiometry in the lead zirconate-lead titanate system determined by Knudsen effusion," *J. Appl. Phys.* **44** [12] 5227-5236 (1973).

P. D. Hren, H. Al-Shareef, S. H. Rou, A. I. Kingon, P. Buaud, and E. A. Irene, "Hillock formation in plainum films," preprint from the Spring 1992 MRS Meeting.

H. Hu, V. Kumar, and S. B. Krupanidhi, "Multi-ion beam reactive sputter deposition of ferroelectric $Pb(Zr,Ti)O_3$ thin films," *J. Appl. Phys.* **71** 376(1992a).

L. S. Hung and J. W. Mayer, "Interactions of four metallic compounds with Si substrates," *J. Appl. Phys.* **60** [3] 1002-1008 (1986).

M. Ido, "Fluctuation effect on the Knight shift of superconducting Al fine particles," *J. Phys. Soc. Jpn.* **41** [2] 412-418 (1976).

K. Iijima, Y. Tomita, R. Takayama, and I. Ueda, "Preparation of c-axis oriented $PbTiO_3$ thin films and their crystallographic, dielectric, and pyroelectric properties," *J. Appl. Phys.* **60** [1] 361-367 (1986).

K. Ishikawa, K. Yoshikawa, and N. Okada, "Size effect on the ferroelectric phase transition in $PbTiO_3$ ultrafine particles," *Phys. Rev.* **B37** [10] 5852-5855 (1988).

I. I. Ivanchik, "The macroscopic theory of ferroelectrics," *Sov. Phys. - Sol. State* **3** [12] 2705-2712 (1962).

I. S. Jacobs and C. P. Bean, "Fine particles and exchange anisotropy (Effects of finite dimensions and interface on the basic properties of ferromagnets)," in *Magnetism Vol. III: Spin Arrangements and Crystal Structure, Domains, and Micromagnetics*, edited by G. T. Rado and H. Suhl. Academic Press, NY 1963.

B. Jaffe, W. R. Cook Jr., and H. Jaffe, *Piezoelectric Ceramics*, Academic Press Ltd., India, 1971.

G. E. Jellison, Jr. and F. A. Modine, "Two-channel polarization modulation ellipsometer," *Appl. Opt.* **29** [7] 959-974 (1990).

G. E. Jellison, Jr. and B. C. Sales, "Determination of the optical functions of transparent glasses by using spectroscopic ellipsometry," *Appl. Opt.* **30** [30] 4310-4315 (1991).

M. A. Jeppesen, "Some optical, thermo-optical, and piezo-optical properties of synthetic sapphire," *J. Opt. Soc. Am.* **48** [9], 629-632 (1958).

Q. Jiang, private communication (1990).

D. J. Johnson, D. T. Amm, E. Griswold, K. Sreenivas, G. Yi, and M. Sayer, "Measuring fatigue in PZT thin films," *Mat. Res. Soc. Symp. Proc. Vol. 200: Ferroelectric Thin Films*, Edited by E. R. Myers and A. I. Kingon. Materials Research Society, Pittsburgh, PA, 1990.

A. R. Johnston, "Dispersion of electro-optic effect in $BaTiO_3$," *J. Appl. Phys.* **42** [9] 3501-3507 (1971).

S. Jyomura, I. Matsuyama, and G. Toda, "Effects of the lapped surface layers on the dielectric properties of ferroelectric ceramics," *J. Appl. Phys.* **51** [11] 5838-5844 (1980).

W. Kanzig, "Space charge layer near the surface of a ferroelectric," *Phys. Rev.* **98** 549- 550 (1955).

J. L. Keddie and E. P. Giannelis, "Effect of heating rate on the sintering of titanium dioxide thin films: competition between densification and crystallization," *J. Am. Ceram. Soc.* **74** [1] 2669-2671 (1991).

L. P. Kholodenko, "A theory of domainless, nonhomogeneous, spontaneous polarization of ferroelectric plates near the Curie point," *Sov. Phys. - Sol. State* **5** [3] 660-667 (1963).

R. J. King and M. J. Downs, "Ellipsometry applied to films on dielectric substrates," *Surf. Sci.* **16**, 288-302 (1969).

K. Kinoshita and A. Yamaji, "Grain-size effects on dielectric properties in barium titanate ceramics," *J. Appl. Phys.* **47** [1] 371-373 (1976).

C. Kittel, "Theory of the structure of ferromagnetic domains in films and small particles," *Phys. Rev.* **70** [11,12] 965-971 (1946).

L. H. Kjaldman, J. Kurkijarvi, and D. Rainer, "Suppression of P-wave superfluidity in long, narrow pores," *J. Low Temp. Phys.* **33** [5/6] 577-587 (1978).

E. F. Kneller and F. E. Luborsky, "Particle size dependence of coercivity and remanence of single-domain particles," *J. Appl. Phys.* **34** [3] 656-658 (1964).

W. Kleeman, F. J. Shafer, and D. Rytz, "Crystal optical studies and spontaneous polarization in $PbTiO_3$," *Phys. Rev.* **B34** [11] 7873-7879 (1986).

R. Kretschmer and K. Binder, "Surface effects on phase transitions in ferroelectrics and dipolar magnets," *Phys. Rev.* **B20** [3] 1065-1076 (1979).

M. Kriss and I. Rudnick, "Size effects in He II as measured by fourth sound," *J. Low. Temp. Phys.* **3** 339-357 (1970).

S. B. Krupanidhi, private communication.

A. X. Kuang, L. S. Wu, and Q. F. Zhou, "$PbTiO_3$ thin film prepared by sol-gel process," *ISAF 1990 abstracts*, X.34 (1990).

O. Kubo, T. Ido, H. Yokoyama, and Y. Koike, "Particle size effects on magnetic properties of $BaFe_{12-2x}Ti_xCo_xO_{19}$ fine particles," *J. Appl. Phys.* **57** [1] 4280-4282 (1985).

K. Kushida, K. R. Udayakumar, S. B. Krupanidhi, and L. E. Cross, "Origin of orientation in sol-gel derived lead titanate films," submitted to *J. Am. Ceram. Soc.* (1992).

M. Lambert and R. Comes, "The chain structure and phase transition of $BaTiO_3$ and $KNbO_3$," *Sol. State Commun.* **7** 305-308 (1969).

C. E. Land and D. Dimos, "Electrooptic effects and photosensitivities of PLZT thin films," 93rd Annual American Ceramic Society Meeting, Cincinnati, Ohio (1991).

C. E. Land, P. D. Thacher, and G. H. Haertling, "Electrooptic Ceramics," in *Applied Solid State Science: Advances in Materials and Device Research Vol. 4*, Edited by R. Wolfe. Academic Press Inc., New York, 1974.

C. E. Land and P. D. Thacher, "Ferroelectric ceramic electrooptic materials and devices," *Proc. IEEE* **57** [5] 751-768 (1969).

S. B. Lang and D. K. Das-Gupta, "Laser-intensity-modulation method: A technique for determination of spatial distributions of polarization and space charge in polymer electrets," *J. Appl. Phys.* **59** [6] 2151-2160 (1986).

M. H. Lee, A. Halliyal, and R. E. Newnham, "Poling studies of piezoelectric composites prepared by coprecipitated $PbTiO_3$ powder," *Ferroelectrics* **87** 71-80 (1988).

T. N. Lezgintseva, "Concerning the structure of surface layers in $BaTiO_3$ crystals," *Sov. Phys. - Sol. State* **7** [4] 785-788 (1965).

M. E. Lines and A. M. Glass, *Principles and Applications of Ferroelectrics and Related Materials*, Clarendon Press, Oxford, 1977.

M. Loposzko, M. Pawelczyk, M. Urbanska, and Z. Surowiak, "Diffuse phase transitions in thick ferroelectric $Ba(Ti_xSn_{1-x})O_3$ films of perovskite-type structure," *Thin Solid Films* **69** 339-345 (1980).

D. G. Loukes, "Electrolytic surface modification of float glass using molten metal electrodes," *Glass Tech.* **32** [6] 187-199 (1991).

J. T. Lue, S. J. Mu, and I. C. Wu, "Ellipsometry and structure studies of chromium, molybdenum, and platinum silicides," *Phys. Rev.* **B36** [3] 1657-1661 (1987).

J. T. Lue, H. W. Chen, and S. I. Lew, "Optical constants of palladium silicides measured by a multiple-wavelength ellipsometer," *Phys. Rev.* **B34** [8] 5438-5442 (1986).

I. H. Malitson, "Refraction and dispersion of synthetic sapphire," *J. Opt. Soc. Am.* **52** [12] 1377-1379 (1962).

I. H. Malitson, "Interspecimen comparison of the refractive index of fused silica," *Opt. Soc. Am.* **55**, 1205 (1965).

G. R. Mariner, *Characterization of Nonabsorbing Surfaces and Interfaces by a Rotating-Analyzer Automated Ellipsometer*, Ph.D. thesis, The Pennsylvania State University, 1981.

P. J. McMarr, *Characterization of Surfaces, Thin Films, and Ion-Implanted Silicon by Spectroscopic Ellipsometry*, Ph.D. thesis, The Pennsylvania State University, 1985.

R. Messier, "Toward quantification of thin film morphology," *J. Vac. Sci. Technol.* **A4** [3] 490-495 (1986).

R. Messier, A. P. Giri, and R. A. Roy, "Revised structure zone model for thin film physical structure," *J. Vac. Sci. Technol.* **A2** [2] 500-503 (1984).

D. Miller, *Synthesis and Properties of Barium Titanate Nanocomposites*, Ph.D. thesis, The Pennsylvania State University, 1991.

R. C. Miller and A. Savage, "Motion of 180° domain walls in $BaTiO_3$ under the application of a train of voltage pulses," *J. Appl. Phys.* **32** [4] 714-721 (1961).

R. C. Miller and A. Savage, "Asymmetric hysteresis loops and the pyroelectric effect in barium titanate," *J. Appl. Phys.* **30** [6] 808-811 (1959).

H. Nagata, M. Watanabe, H. Sakai, and Y. Kubota, "Thin film ferroelectrics of PZT system by sol-gel processing," *ISAF 1990 abstracts*, X.1 (1990).

T. Nagatomo and O. Omoto, "Preparation of $BaTiO_3$ films by rf sputtering and their crystallographic, dielectric, and optical properties," *Jpn. J. Appl. Phys.* **26** suppl. 26-2, 11-14 (1987).

S. Naka, F. Nakakita, Y. Suwa, and M. Inagaki, "Change from metastable cubic to stable tetragonal form of submicron barium titanate," *Bull. Chem. Soc. Japan* **47** [5] 1168-1171 (1974).

S.F. Nee and H. E. Bennett, "Ellipsometric characterization of optical constants for transparent materials," *SPIE Properties and Characteristics of Optical Glass* **970** 62-69 (1988).

T. Okamura, M. Adachi, T. Shiosaki, and A. Kawabata, "Epitaxial growth of ferroelectric $Pb(Zr_{0.9}Ti_{0.1})O_3$ films by reactive sputtering of multi metal target," *ISAF 1990 abstracts*, X.5 (1990).

M. Okuyama and Y. Hamakawa, "Preparation and basic properties of $PbTiO_3$ ferroelectric thin films and their device applications," *Ferroelectrics* **63** 243-252 (1985).

A. N. Parikh and D. L. Allara, "Quantitative determination of molecular structure in multilayered thin films of biaxial and lower symmetry from photon spectroscopies. I. Reflection infrared vibrational spectroscopy," *J. Chem. Phys.* **96** [2] 927 - 945 (1992).

A. Paul, "Chemical durability of glasses; a thermodynamic approach," *J. Mat. Sci.* **12** 2246-2268 (1977).

D.A. Payne, "Integration of ferroelectric materials on semiconductors by sol-gel methods," *ISAF 1991 Abstracts* 12.1 (1990).

M. Prutton, *Thin Ferromagnetic Films*, Butterworth and Co. Ltd., Washington, 1964.

H. Rawson, *Properties and Applications of Glass*, Elsevier, New York, 1980.

K. Saegusa, W. E. Rhine, and H. K. Bowen, "Preparation of $Pb_xBa_{1-x}TiO_3$ and the effect of composition and the size of the crystallite on the crystal phase," preprint from 1989 Am. Cer. Soc. annual meeting.

G. A. Samara, "Pressure and temperature dependence of the dielectric properties and phase transitions of the ferroelectric perovskites: $PbTiO_3$ and $BaTiO_3$," *Ferroelectrics* **2** 277- 289 (1971).

H. Schlosser and M. E. Drougard, "Surface layers on barium titanate single crystals above the Curie point," *J. Appl. Phys.* **32** [7] 1227-1231 (1961).

M. Schoijet, "On the anomalous crystallographic properties of small barium titanate particles," *Brit. J. Appl. Phys.* **15** 719-723 (1964).

G. M. Sessler, J. E. West, and G. Gerhard, "High-resolution laser-pulse method for measuring charge distributions in dielectrics," *Phys. Rev. Lett.* **48** [8] 563-566 (1982).

K. Sreenivas and M. Sayer, "Characterization of $Pb(Zr,Ti)O_3$ thin films deposited from multi-element metal targets," *J. Appl. Phys.* **64** [3] 1484-1493 (1988).

Struers Metallographic Equipment Catalog

E. C. Subbarao, M. C. McQuarrie, and W. R. Buessem, "Domain effects in polycrystalline barium titanate," *J. Appl. Phys.* **28** [10] 1194-1200 (1957).

Z. Surowiak, A. M. Margolin, I. N. Zakharchenko, and S. V. Biryukov, "The influence of structure on the piezoelectric properties of $BaTiO_3$ and $(BaSr)TiO_3$ thin films with a diffuse phase transition," *Thin Solid Films* **176** 227-246 (1989).

M. Takagi, "Electron-diffraction study of liquid-solid transition in thin metal films," *J. Phys. Soc. Jpn.* **9** [3] 359-363 (1954).

M. Tanaka and G. Honjo, "Electron optical studies of barium titanate single crystal films," *J. Phys. Soc. Japan* **19** [6] 954-970 (1964).

M. A. Taubenblatt and C. R. Helms, "Interaction of Ti with C- and SiC-contaminated Si surfaces," *J. Appl. Phys.* **59** [5] 1992-1997 (1986).

P. D. Thacher, "Refractive index and surface layers of ceramic $(Pb,La)(Zr,Ti)O_3$ compounds," *Appl. Opt.* **16** [12] 3210-3213 (1977).

J. A. Thornton, "High rate thick film growth" *Ann. Rev. Mater. Sci.* **7** 239-260 (1977).

Yu. Ya. Tomashpolski, E. N. Lubnin, and M. A. Sevostianov, "Auger spectroscopy of surface layers in ferroelectrics," *Ferroelectrics* **22** 785-786 (1978).

Yu. Ya. Tomashpol'skii, E. N. Lubnin, and M. A. Sevost'yanov, "The nature of the surface layers of ferroelectric films," *Sov. Phys. Crystallogr.* **23** [5] 573-576 (1978).

Yu. Ya. Tomashpolski, "Structure studies of ferroelectric vacuum deposits," *Ferroelectrics* **7** 253-255 (1974a).

Yu. Ya. Tomashpolski, M. A. Sevostianov, M. V. Pentegova, L. A. Sorokina, and Yu. N. Venevtstev, "Ferroelectric vacuum deposits of complex oxide structure type," *Ferroelectrics* **7** 257-258 (1974b).

L. L. Tongson, A. S. Bhalla, and L. E. Cross, "Studies of ferroelectric surfaces using ion beam and chemical etching techniques," *Ferroelectrics* **36** 471-474 (1981).

T. Toyoda, "The temperature dependence of the optical dispersion parameters in $SrTiO_3$ and TiO_2," *J. Phys.D: Appl. Phys.* **18** L129 - L134 (1985).

S. Triebwasser, "Space charge fields in $BaTiO_3$," *Phys. Rev.* **118** [1] 100-105 (1960).

A. V. Turik, "The problem of the surface layer in barium titanate single crystals," *Sov. Phys. Sol. State.* **5** [9] 1748 - 1750 (1964).

K. Uchino, E. Sadanaga, K. Oonishi, T. Morihashi, and H. Yamamura, "Particle/grain size dependence of ferroelectricity," *Ceram. Trans.* **8** 107-115 (1990).

K. R. Udayakumar, J. Chen, S. B. Krupanidhi, and L. E. Cross, "Sol-gel derived PZT thin films for switching applications," paper presented at ISAF 1990 (1990).

B. L. Utech, *The Effect of Solution Chemistry on Barium Titanate Ceramics*, M.S. thesis, The Pennsylvania State University, 1990.

O. G. Vendik, I. G. Mironenko, and L. T. Ter-Martirosyan, "Size effects in dynamic polarization in displacive ferroelectrics," *Sov. Phys. - Sol. State* **26** [10] 1864-1867 (1984).

D. Viehland, S. J. Jang, L. E. Cross, and M. Wuttig, "Freezing of the polarization fluctuations in lead magnesium niobate relaxors," *J. Appl. Phys.* **68** [6] 2916-2921 (1990).

J. H. P. Watson, "Critical magnetic field and transition temperature of synthetic high-field superconductors," *Phys. Rev.* **148** [1] 223-230 (1966).

S. H. Wemple, "Polarization fluctuations and the optical-absorption edge in $BaTiO_3$," *Phys. Rev.* B2 [7] 2679-2689 (1970).

S. H. Wemple, M. DiDomenico, Jr., and I. Camlibel, "Dielectric and Optical Properties of Melt-Grown $BaTiO_3$," *J. Phys. Chem. Solids* **29** 1797-1803 (1968).

W. A. Weyl and E. C. Marboe, *The Constitution of Glasses: A Dynamic Interpretation*, John Wiley and Sons, Inc., New York, 1967.

M. C. Wittels and F. A. Sherrill, "Fast neutron effects in tetragonal barium titanate," *J. Appl. Phys.* **28** [5] 606-609 (1957).

Z. Wu and M. Sayer, "Properties of sol-gel processed PLZT (2/54/46) thin films," *ISAF 1990 abstracts*, X.6 (1990).

P. Wurfel and I. P. Batra, "Depolarization-field-induced instability in thin ferroelectric films - experiment and theory," *Phys. Rev. B* **8** [11] 5126- 5133 (1973).

P. Wurfel, I. P. Batra, and J. T. Jacobs, "Polarization instability in thin ferroelectric films," *Phys. Rev. Lett.* **30** [24] 1218-1221 (1973).

Y. Yamada, G. Shirane, and A. Linz, "Study of Critical Fluctuations in $BaTiO_3$ by Neutron scattering," *Phys. Rev.* **177** [2] 848-857 (1969).

O. Yamaguchi, A. Narai, T. Komatsu, and K. Shimizu, "Crystallization and transformation of distorted cubic $PbTiO_3$," *J. Am. Ceram. Soc.* **69** [10] C256-C257 (1986).

E. Yamaka, H. Watanabe, H. Kimura, H. Kanaya, and H. Okhuma, "Structural, ferroelectric, and pyroelectric properties of highly c-axis oriented $Pb_{1-x}Ca_xTiO_3$ thin film grown by radio-frequency magnetron sputtering," *J. Vac. Sci. Technol.* **A6** [5] 2921-2928 (1988).

B. Yang, *Spectroscopic Ellipsometry and Computer Simulation Studies of Thin Film Morphology Evolution*, Ph.D. Thesis, The Pennsylvania State University, 1988.

B. Yang, B. L. Walden, R. Messier, and W. B. White, "Computer simulation of the cross-sectional morphology of thin films," *SPIE 821: Modelling of Optical Thin Films* 68-76 (1987).

P. Yeh, "Electromagnetic propagation in birefringent layered media," *J. Opt. Soc. Am.* **69** [5] 742-756 (1979).

P. Yeh, "Optics of anisotropic layered media: a new 4 x 4 matrix algebra," *Surf. Sci.* **96** 41-53 (1980).

J. E. Yehoda, B. Yang, K. Vedam, and R. Messier, "Investigation of the void structure in amorphous germanium thin films as a function of low-energy ion bombardment," *J. Vac. Sci. Technol* **A6** [3] 1631-1635 (1988).

G. Yi, Z. Wu. and M. Sayer, "Preparation of $Pb(Zr,Ti)O_3$ thin films by sol gel processing: Electrical, optical, and electro-optic properties," *J. Appl. Phys.* **64** [5] 2717-2724 (1988).

G. Yi and M. Sayer, "Sol-gel processing of complex oxide films," *Cer. Bull.* **70** [7] 1173-1179 (1991).

S.-G. Yoon, H. Y. Lee, and H. G. Kim, "Compositional analysis of lead titanate thin films by Auger electron spectroscopy and their electrical properties," *Thin Solid Films* **171** 251- 262 (1989).

APPENDIX A

COMPUTER CODE FOR MODELLING ANISOTROPIC STRATIFIED MATERIALS

```
C      ************************************************************
C THIS PROGRAM IS SET UP TO TAKE EXPERIMENTAL PSI AND/OR DELTA
C VALUES AND CALCULATE THE BEST FIT TO A USER DEFINED DISPERSION
C RELATION.  MULTIPLE ANISOTROPIC LAYERS ARE HANDLED USING ELL_SIM,
C A PROGRAM WRITTEN BY ATUL PARIKH AND D. ALLARA
C SPACE CHARGE IS HANDLED AS IN ASPNES' PAPER ON HEAVILY
C DOPED SEMICONDUCTORS

C  SO FAR ANY OSCILLATOR UTILIZED IS ISOTROPIC 8- 28- 1990
C
C      ************************************************************

   EXTERNAL TRY

    INTEGER*4 M,N,IXJAC,NSIG,MAXFN,IOPT,I,INFER,IER,NOL,JJ,KK
    INTEGER*4 NSET, NPT, NUMCOM, COMNUM, COMP1(7), COMP2(7), III
    INTEGER*4 NSTEP(25), HOLD,JJJ, NOCOMP, NN, OSC, J, K, II
   INTEGER*4 INDEX, SPCHRG, EQ, SPOSC, tYcD
        REAL*8  PARM(4),XJAC(570,20),XJTJ(210),WORK(1500),TEMP(25),
   C EPS,DELTA,SGN,SSQ,ABS,TANPSI(285),COSDEL(285),AI(4),tau,
  C CONF,SIGMA, LAM,RES1,RES2, T(10), FV, EP, PI
      REAL*8  LAMBDA(100),THETAD,X(25),F(570),AZI,CPSI,CDEL
     REAL*8  XMIN(25),XSTEP(25), TPSI, TDEL, PARAM(20)
    REAL SIGMIN,temper
       COMPLEX*16  HEPS(4,4,10),subeps(2,4,100)
    CHARACTER*15 FILNAM
    CHARACTER*6 COMLBL
    COMMON /COM1/ SUBEPS, COMP1, COMP2, SPCHRG, eq, osc,SPOSC
    COMMON /ZSQ/ COSDEL,TANPSI,NPT, NOL, X, NSTEP,TYCD
    COMMON /FLA/AI,LAMBDA, NOCOMP
    COMMON /ERR/ CONF,SIGMA

       PI  =  3.14159265
    m=165
    IXJAC = 570

     WRITE(*,*) 'INPUT FILENAME?'
     READ(*,*) FILNAM
    OPEN (UNIT = 3, FILE = FILNAM)
     READ(3,*) IOPT
    IF (IOPT .EQ. 2) THEN
        READ(3,*) PARM(1)
        READ(3,*) PARM(2)
        READ(3,*) PARM(3)
        READ(3,*) PARM(4)
    END IF
```

```
         READ (3,*) FILNAM
      OPEN (UNIT = 7, FILE = FILNAM)
         READ (3,*) FILNAM
      OPEN (UNIT = 11, FILE = FILNAM)

       read (3,*) NSIG
        read(3,*) temper
         READ(3,*) NOCOMP
         READ (3,*) tYcD

      EPS = 1.D-6
      DELTA = 1.D-6
      MAXFN = 1000

       READ(3,*) NSET
      K = 1
      DO 1,J=1,NSET
         READ(3,*) FILNAM
            WRITE(7,*) FILNAM
        OPEN (UNIT = 8, FILE = FILNAM)
           read (8,*,end = 25) AI(J)
             WRITE(*,*)  AI(J)
        DO 50 I=1,M
           READ(8,*,END = 25) CDEL,CPSI,LAMBDA(I)
             if (tYcD .eq. 1) then
               COSDEL(K) = DCOS(CDEL * PI /180.)
                TANPSI(K) = DTAN(CPSI * PI /180.)
            elseif (tYcD .eq. 0 .OR. TYCD .eq. 2) then
             COSDEL(K) = CDEL
              TANPSI(K) = CPSI
            end if
          K = K+1
50      CONTINUE
25       CLOSE (UNIT = 8)
            IF (J .EQ. 1) THEN
               NPTOLD = I - 1
           ELSE
               NPT = I - 1
              IF (NPT .NE. NPTOLD) THEN
                 WRITE(*,*) 'NUMBER OF POINTS IN DIFFERENT DATA SETS
   1                   NOT MATCHED'
                    STOP
              END IF
            END IF
1     CONTINUE

       M = K-1

C        READ IN REFERENCE OPTICAL PROPERTIES
         SPCHRG = 0
         SPOSC = 0
         osc = 0
         READ(3,*) NUMCOM
```

```
       write(*,*)  numcom
       DO 14 I = 1, NUMCOM
         READ(3,*)  COMNUM, COMLBL, FILNAM
          write(7,*)  comnum,  comlbl
         IF (COMLBL .EQ. 'SPCHRG' .OR. COMLBL .EQ. 'SPOSC') THEN
           WRITE(7,*) 'GRID LIMITS ON EP AND TAU'
            DO 11 ii = 1,2
                 READ(3,*)  XMIN(20+ii),  XSTEP(20+ii),  NSTEP(20+ii)
                 WRITE(7,*)  XMIN(20+ii),  XSTEP(20+ii),  NSTEP(20+ii)
11          CONTINUE
           IF (COMLBL .EQ. SPCHRG) THEN
             SPCHRG = COMNUM
           ELSE
             SPOSC = COMNUM
           END IF
         ELSEIF (COMLBL .EQ. 'OSC') THEN
            READ(3,*) EQ
           WRITE(*,*) 'OSCILLATOR NUMBER = ',EQ
           WRITE(7,*) 'OSCILLATOR NUMBER = ',EQ
            write(*,*) 'GRID LIMITS ON OSC'
            write(7,*) 'GRID LIMITS ON OSC'
            DO 65 I = 0,5
                 READ(3,*)  xmin(15+i),  xSTEP(15+I),  Nstep(15+I)
                  write(7,*)  xmin(15+i),  xSTEP(15+I),  Nstep(15+I)
                  write(*,*)  xmin(15+i),  xSTEP(15+I),  Nstep(15+I)
65          CONTINUE
           OSC = COMNUM
         END IF
         IF (COMLBL .NE. 'OSC' .AND. COMLBL .NE. 'SPOSC') THEN
           OPEN (UNIT = 10, FILE = FILNAM)
           DO 12 J = 1,M/NSET
             READ(10,*, END = 13) SUBEPS(1, COMNUM, J),
     C      SUBEPS(2, COMNUM, J)
12        CONTINUE
13         CLOSE (UNIT = 10)
         END IF
14     CONTINUE


C MULTIPLY M*2 TO ACCOUNT FOR DELTA AND PSI BEING INDEPENDENT
       M=M*2
       IF (M .GT. IXJAC) THEN
         WRITE(*,*) 'TOO MANY DATA POINTS'
       ELSE
       WRITE(*,*) 'NUMBER OF DATA POINTS = ',M
         WRITE(7,*) 'NUMBER OF DATA POINTS = ', M
       END IF


C      READ IN GEOMETRY
       DO 16 I = 1,7
          READ(3,*, ERR = 17, END = 17) COMP1(I),COMP2(I),XMIN(2*I-1),
     1     XSTEP(2*I-1),  NSTEP(2*I-1),  XMIN(2*I),  XSTEP(2*I),  NSTEP(2*I)
```

```
          write(7,15) COMP1(I),COMP2(I),XMIN(2*I-1),XSTEP(2*I-1),
     1    NSTEP(2*I-1), XMIN(2*I), XSTEP(2*I), NSTEP(2*I)

          write(*,15) COMP1(I),COMP2(I),XMIN(2*I-1),XSTEP(2*I-1),
     1    NSTEP(2*I-1), XMIN(2*I), XSTEP(2*I), NSTEP(2*I)

15    format(1x,i1,3x,i1,3x,f8.3,3x,f8.3,3x,i2,3x,f9.3,3x,f9.3,3x,i2)
16    CONTINUE
17    CLOSE (UNIT = 3)
      NOL = I - 1
      WRITE(*,*) 'NOL = ',NOL
     N = NOL*2

      AZI = 0.d0

C
C***********************************************************************
C START GRID SEARCH
C***********************************************************************
     SigMin = 1.0e+30


C INITIALIZE EPS
      DO 200 I=1,4
       DO 201 J=1,4
        DO 202 K=1,10
          HEPS(I,J,K) = (0.D0,0.D0)
202    CONTINUE
201   CONTINUE
200   CONTINUE


      WRITE(7,*) 'GRID SEARCH LIMITS'

     CONF = 1.
       IF (osc .NE. 0) THEN
         DO 38 K = 0,5
           IF (NSTEP(15+K) .GE. 0) THEN
           CONF = CONF*(NSTEP(15+K) + 1)
           END IF
38       CONTINUE
       END IF
       IF (SPCHRG .NE. 0 .OR. SPOSC .NE. 0) THEN
         DO 39 K = 1,2
           IF (NSTEP(20+K) .GE. 0) THEN
           CONF = CONF*(NSTEP(20+K) + 1)
           END IF
39       CONTINUE
       END IF
      DO 40 K = 1,2*NOL
          if (nstep(k) .GE. 0) then
         CONF = CONF*(NSTEP(K)+1)
          end if
```

```
40    CONTINUE
        write(*,*) 'number of steps = ', conf
        write(*,*) 'Program in progress - please do not disturb'

      NN = 0
      DO 700 JJ = 1, CONF
         INDEX = JJ
      IF (SPCHRG .NE. 0 .OR. SPOSC .NE. 0) THEN
         DO 705 K = 1, 2
            IF (NSTEP(20+K) .LE. 0) THEN
               X(20+K) = XMIN(20+K)
           ELSE
               HOLD = MOD(INDEX, (NSTEP(20+K)+1))
               X(20+K) = XMIN(20+K) + XSTEP(20+K) * HOLD
               INDEX = INDEX / (NSTEP(20+K) + 1)
           END IF
705      CONTINUE
        END IF
       IF (osc .NE. 0) THEN
          DO 707 K = 0,5
            IF (NSTEP(15+K) .LE. 0) THEN
               X(15+K) = XMIN(15+K)
           ELSE
               HOLD = MOD(INDEX, (NSTEP(15+K)+1))
               X(15+K) = XMIN(15+K) + XSTEP(15+K) * HOLD
               INDEX = INDEX / (NSTEP(15+K) + 1)
           END IF
707      CONTINUE
        END IF
        DO 710 K = 1,N
            IF (NSTEP(K) .LE. 0) THEN
               X(K) = XMIN(K)
           ELSE
               HOLD = MOD(INDEX, (NSTEP(K)+1))
               X(K) = XMIN(K) + XSTEP(K) * HOLD
               INDEX = INDEX / (NSTEP(K) + 1)
           END IF
710      CONTINUE
        SIGMA = 0.

         DO 750 II = 1,M/2, 3
            K = II/NPT
            KK = II - K*NPT
           IF (KK .EQ. 0) THEN
               KK = NPT
           END IF
            NN = (II - 1)/NPT
         THETAD = AI(NN+1)
            LAM = LAMBDA(KK)*10.
           IF (SPCHRG .NE. 0 .OR. SPOSC .NE. 0) THEN
              Ep = x(21)
              Tau = X(22)
           END IF
```

```
*************************************************************
C CALCULATE THE THICKNESSES OF EACH LAYER TAKING CARE THAT THE LAYERS FROM
C THE SPACE CHARGE AND THE GEOMETRICAL LAYERS ARE RECONCILED
*************************************************************

          DO 760 I =1,NOL
             T(I) = X(I*2)
            FV = X(2*I - 1)
            CALL SETEPS(I,KK,HEPS,FV,EP,TAU,LAMBDA(KK),X)
760       CONTINUE
        CALL ELLSIM(HEPS,T,NOL,CPSI,CDEL,AZI,THETAD,LAM)
            if (nocomp .eq. 0 .and. cdel .gt. 90.) then
                cdel =180. - cdel
            end if

            if (tYcD .eq. 1) then
              TPSI = DTAN (CPSI * PI /180.)
             TDEL = DCOS (CDEL * PI /180.)
            RES1 = TANPSI(II) - TPSI
             RES2 = COSDEL(II) - TDEL
            elseif (tYcD .eq. 0) then
            RES1 = TANPSI(II) - cPSI
             RES2 = COSDEL(II) - cDEL
            elseif (tYcD .eq. 2) then
            RES1 = TANPSI(II) - cPSI
             RES2 = 0.D0
            end if

          SIGMA= SIGMA + RES1**2 + RES2**2
750       CONTINUE

         IF (MOD(JJ,20) .EQ. 0) THEN
             WRITE(*,*) JJ,' / ',CONF
        end if

        IF (SIGMA .LT. SigMin) THEN
          SigMin = Sigma
             DO 720 I = 1, 25
                 TEMP(I) = X(I)
720        CONTINUE
              WRITE(*,*) 'SSQMIN = ', SIGMIN
          END IF
700   CONTINUE


*************************************************************
* ECHO Grid Search Results to M2O File
*************************************************************

        write(7,*) 'best FILM GEOMETRY after grid search'
        write(7,*) 'com1   com2   Vf          Thickness'
        do 600 i = 1, nol
           write(7,610) comp1(i), comp2(i), temp(2*i - 1), temp(2*i)
```

```
600    continue
610    format (' ', i1, 5x, i1, 5x, f8.3, 5x, f9.3)

       if (OSC .ne. 0) then
         write(7,*) 'best OSCILLATOR parameters after grid search'
         do 612 i = 0, 5
            write(7,615) (temp(15 + i))
612      continue
615       format(' ',f11.3)
       end if

       if (SPCHRG .ne. 0) then
         write(7,*) 'best SPACE CHARGE parameters after grid search'
         do 620 i = 1, 2
            write(7,630) (temp(20 + i))
620      continue
630       format(' ',f11.3)
       end if


* TAKE THICKNESS AND VOLUME FRACTION OF UNVARIED GEOMETRIC PARAMETERS
* OUT FROM THE X VECTOR SO THAT ZXSSQ WON'T HAVE TO DEAL WITH THEM

*******************************************************************
* Set all free parameters to value that yields smallest sigma
*******************************************************************
        J = 1
      DO 41 I = 1,2*NOL
         IF (NSTEP(I) .NE. 0) THEN
          PARAM(J) = TEMP(I)
            J = J+1
         END IF
41    CONTINUE
        IF (OSC .NE. 0) THEN
          DO 42 I = 0,5
            IF (NSTEP(15+I) .NE. 0) THEN
               PARAM(J) = TEMP(15+I)
                J = J+1
            END IF
42        CONTINUE
        END IF
        IF (SPCHRG .NE. 0 .OR. SPOSC .NE. 0) THEN
          DO 43 I = 1,2
            if (nstep(20+i) .ne. 0) then
              PARAM(J) = TEMP(20+I)
             J = J+1
            end if
43        CONTINUE
        END IF
        N = J-1
        WRITE(*,*) 'N = ', N

      CONF = 1.67
```

```
      WRITE(*,*) 'STARTING ITERATION'

****************************************************************
C CALL ZXSSQ TO FIT VARIABLES
****************************************************************
C
     CALL ZXSSQ(TRY,M,N,NSIG,EPS,DELTA,MAXFN,IOPT,PARM,PARAM,SSQ,
    C         F,XJAC,IXJAC,XJTJ,WORK,INFER,IER)

      SIGMA = DSQRT(SSQ/(M - N))

C
C
****************************************************************
C OUTPUT THE VALUES FROM ZXSSQ
****************************************************************


       WRITE(7,*)
           WRITE(7,9250) iopt,infer
          IF (infer .EQ. 0) WRITE(7,9260) IER
            WRITE (7,9270) nsig,work(3),eps,delta,work(1)
              WRITE (7,9280) MaxFn,Work(2),Parm(1),Work(4),Parm(2)
             WRITE (7,9290) Parm(3),Parm(4),Work(5)


9250    Format(//,25x,' IMSL Routine Input and Output',//,
    1      13x,'Algorithm Used: ',I1,/
    2     ' Convergence Criterion Met: ',I1)

9260    Format(17x,'Error Code: ',I3)

9270     Format(/,5x,'Parameter  ',28x,'INPUT',10x,'OUTPUT',/,
     1       ' Sig Digits in parameters',15x,I3,17x,F7.3,/,
     2      ' Rel Diff in e on Succ Iter',12x,E10.3e2,/,
     3       ' Norm of Gradient an Minimum',12x,E10.3e2,10x,E10.3e2,//)

9280    Format( ' Max Num of Func Evaluations',12x,I6,14x,F6.0,/,
     1       ' Marquardt Parameter',20x,E10.3e2,10x,E10.3e2,/,
    2      ' MP Scaling Factor  ',20x,E10.3e2)

9290     Format( ' Maximum  MP',29x,E10.3e2,/,
    1       ' Central => Forward Diff ',15x,E10.3e2,/,
    2       ' Number of Iterations   ',15x,F6.0)


       WRITE(7,*) 'SIGMA AFTER ITERATION = ',SIGMA
         DO 110 I=1,N
             WRITE(7,*) 'PARAM(',I,')= ',PARAM(I)
110     CONTINUE
        CALL ERRBAR(XJAC,M,N,7,PARAM)
      CLOSE (UNIT = 7)
```

```
C CALCULATE DELTA AND PSI FOR THE FINAL MODEL AND WRITE TO AN OUTPUT FILE

        J = 1
          DO 1016 I = 1, 2*NOL
            IF (NSTEP(I) .NE. 0) THEN
               X(I) = PARAM(J)
              J = J+1
            END IF
1016     CONTINUE
        IF (OSC .NE. 0) THEN
           DO 1020 I = 0,5
              IF (NSTEP(15 + I) .NE. 0) THEN
                  X(15 + I) = PARAM(J)
                 J = J + 1
               END IF
1020      CONTINUE
        END IF
        IF (SPCHRG .NE. 0 .OR. SPOSC .NE. 0) THEN
           DO 1030 I = 1,2
              if (nstep(20+i) .ne. 0) then
                X(20 + I) = PARAM(J)
                J = J + 1
             end if
1030      CONTINUE
        END IF


        DO 1040 II = 1,M/2
           K = II/NPT
           KK = II - K*NPT
           IF (KK .EQ. 0) THEN
              KK = NPT
           END IF
            NN = (II - 1)/NPT
         THETAD = AI(NN+1)
            LAM = LAMBDA(KK)*10.
           IF (SPCHRG .NE. 0 .OR. SPOSC .NE. 0) THEN
               Ep = x(21)
              Tau = X(22)
           END IF
             DO 1060 I =1,NOL
                T(I) = X(I*2)
               FV = X(2*I - 1)

               CALL SETEPS(I,KK,HEPS,FV,EP,TAU,LAMBDA(KK),X)
1060       CONTINUE

          CALL ELLSIM(HEPS,T,NOL,CPSI,CDEL,AZI,THETAD,LAM)
              if (nocomp .eq. 0 .and. cdel .gt. 90.) then
                    cdel =180. - cdel
              end if
               WRITE(11,*) LAMBDA(KK), CDEL, CPSI, THETAD
```

```
1040  CONTINUE
      CLOSE (UNIT = 11)

   END



* * * * * * * * * * * * * * * * * * * * * * * * * * * * * * * * * * * * * * * * * * * * * * * * * * * * * * * * * * * * * * * * *
C
C USER DEFINED SUBROUTINE THAT DEFINES THE RESIDUALS BETWEEN
C THE EXPERIMENTAL AND CALCULATED DATA UTILIZING ELL_SIM
C
* * * * * * * * * * * * * * * * * * * * * * * * * * * * * * * * * * * * * * * * * * * * * * * * * * * * * * * * * * * * * * * * *


     SUBROUTINE TRY(PARAM,M,N,F)
       INTEGER*4 M,N,I,NOL,NPT, KK, II,JJJ,COMP1(7), COMP2(7), K, J
     INTEGER*4 NOCOMP, NN, III, spchrg, SPOSC,TYCD
     INTEGER*4 EQ, OSC, NSTEP(25)
       REAL*8 TANPSI(285),COSDEL(285),PI,THETAD, TAU,EP,PARAM(20)
         REAL*8  LAMBDA(100),T(10),LAM,X(25),F(570),CPSI,CDEL,AZI
      REAL*8  FV, AI(4), TDEL, TPSI
        COMPLEX*16   HEPS(4,4,10),SUBEPS(2,4,100)
     COMMON /COM1/ SUBEPS, COMP1, COMP2, SPCHRG, eq, osc, SPOSC
     COMMON /ZSQ/COSDEL,TANPSI,NPT, NOL, X,NSTEP,TYCD
     COMMON /FLA/AI,LAMBDA, NOCOMP
C
      DO 15 I = 1,4
        DO 10 J = 1,4
          DO 5 K = 1, 10
             HEPS(I,J,K) = (0.D0, 0.D0)
5           CONTINUE
10      CONTINUE
15    CONTINUE
      AZI = 0.d0

      NN = 1
      PI  =  3.14159265
      J = 1
      DO 16 I = 1, 2*NOL
        IF (NSTEP(I) .NE. 0) THEN
            X(I) = PARAM(J)
           J = J+1
        END IF
16    CONTINUE
      IF (OSC .NE. 0) THEN
         DO 20 I = 0,5
            IF (NSTEP(15 + I) .NE. 0) THEN
                 X(15 + I) = PARAM(J)
                J = J + 1
              END IF
20       CONTINUE
      END IF
```

```
        IF (SPCHRG .NE. 0 .OR. SPOSC .NE. 0) THEN
           DO 30 I = 1,2
              if (nstep(20+i) .ne. 0) then
                X(20 + I) = PARAM(J)
                J = J + 1
             end if
30         CONTINUE
        END IF

       DO 750 II = 1,M/2
          K = II/NPT
          KK = II - K*NPT
         IF (KK .EQ. 0) THEN
              KK = NPT
         END IF
          NN = (II - 1)/NPT
        THETAD = AI(NN+1)
          LAM = LAMBDA(KK)*10.
         IF (SPCHRG .NE. 0 .OR. SPOSC .NE. 0) THEN
            Ep = x(21)
            Tau = X(22)
         END IF

*******************************************************************
C CALCULATE THE THICKNESSES OF EACH LAYER TAKING CARE THAT THE LAYERS FROM
C THE POLARIZATION GRADIENT AND THE GEOMETRICAL LAYERS ARE RECONCILED
*******************************************************************
           DO 760 I =1,NOL
              T(I) = X(I*2)
              FV = X(2*I - 1)

            CALL SETEPS(I,KK,HEPS,FV,EP,TAU,LAMBDA(KK),X)
760      CONTINUE

        CALL ELLSIM(HEPS,T,NOL,CPSI,CDEL,AZI,THETAD,LAM)
           if (nocomp .eq. 0 .and. cdel .gt. 90.) then
                 cdel =180. - cdel
           end if

            if (tYcD .eq. 1) then
               TPSI = DTAN (CPSI * PI /180.)
               TDEL = DCOS (CDEL * PI /180.)
              F(II) = TANPSI(II) - TPSI
                F(II + M/2) = COSDEL(II) - TDEL
             elseif (tYcD .eq. 0) then
              F(II) = TANPSI(II) - cPSI
                F(II + M/2) = COSDEL(II) - cDEL
             elseif (tYcD .eq. 2) then
              F(II) = TANPSI(II) - cPSI
                F(II + M/2) = 0.D0
            end if

750     CONTINUE
```

```
RETURN
END

SUBROUTINE EFFMED(E,EH,FV)

 REAL*8 FV,FILL, E1, E2

COMPLEX*16 EH(2),E,INSIDE,RHO, HOLD, EIGHT, FOUR

    EIGHT = (8.0D0, 0.0D0)
    FOUR = (4.0D0, 0.0D0)

 IF (FV.EQ.0.0) THEN
    E = EH(1)

 ELSEIF (FV .ne. 0.0) THEN
   FILL = FV
       E1 = DREAL(EH(1))
       E2 = DIMAG(EH(1))
        EH(1) = DCMPLX(E1, -1.*E2)
       E1 = DREAL(EH(2))
       E2 = DIMAG(EH(2))
        EH(2) = DCMPLX(E1, -1.*E2)

            RHO = (3.0*(1.0-FILL)-1.0)*EH(1) + (3.0*FILL-1.0)*EH(2)
       HOLD = EH(1) * EH(2)
      INSIDE = RHO*RHO + HOLD * EIGHT
   INSIDE = CDSQRT(INSIDE)
     IF (DIMAG(INSIDE) .LT. 0.0) INSIDE = -INSIDE
      E = (RHO+INSIDE)/FOUR
      E1 = DREAL(E)
      E2 = DIMAG(E)
       E = DCMPLX(E1, -1.*E2)
  End if

RETURN
END


    SUBROUTINE SETEPS(I,KK,HEPS,FV,EP,TAU,LAMBDA,X)

    INTEGER I,LAYCNT,KK,COMP1(7), COMP2(7),JJJ,SPCHRG,eq,osc
    INTEGER *4 SPOSC
    REAL*8 E1, E2, EP, TAU, NRG, LAMBDA, FV, abc(6), X(25)
    COMPLEX*16  HEPS(4,4,10),SUBEPS(2,4,100),EH(2),E, SPCEPS
    COMPLEX*16 TIMAG
 COMMON /COM1/ SUBEPS,COMP1,COMP2,SPCHRG, eq, osc, SPOSC

    TIMAG = (0.D0, 1.D0)
    NRG = 1239.8537/LAMBDA
    IF (COMP1(I) .EQ. SPCHRG .OR. COMP1(I) .EQ. SPOSC) THEN
      SPCEPS = EP**2 / (NRG*(NRG + TIMAG * TAU + 1.D-5))
     E1 = DREAL(SPCEPS)
```

```
         E2 = DIMAG(SPCEPS)
         SPCEPS = DCMPLX(E1, -1.*E2)
        ELSE
         SPCEPS = (0.D0, 0.D0)
        END IF
        JJJ = 1
        DO 10 J = 1,2
          IF (COMP1(I) .EQ. OSC .OR. COMP1(I) .EQ. SPOSC) THEN
            do 7 ij = 0,5
               abc(1+ij) = x(15+ij)
7           continue
            CALL DISEQS (EH(1), LAMBDA, EQ, ABC)
             EH(2) = SUBEPS(J, COMP2(I), KK)
          ELSE
             EH(1) = SUBEPS(J, COMP1(I), KK)
             EH(2) = SUBEPS(J, COMP2(I), KK)
          END IF
           EH(1) = EH(1) - SPCEPS
          CALL EFFMED(E, EH, FV)
           E1 = DREAL(E)
           E2 = DIMAG(E)
            HEPS(JJJ,JJJ,I) = DCMPLX(E1,E2)
           JJJ = 3
1 0     CONTINUE
        HEPS(2,2,i)  =  HEPS(1,1,i)

        RETURN
        END


        SUBROUTINE DISEQS (E, LAM1, EQ, A)

     INTEGER*4 EQ, I

      REAL*8 E1, E2, LAM2, A(6), LAM1, DENOM
     REAL*8 NE, NO, N, HW

     COMPLEX*16 E, Timag

       PARAMETER(HW = 1239.8116)

        TIMAG = (0.D0, 1.D0)
       LAM2 = LAM1 * LAM1
       E2 = 0.0

        GOTO (1, 2, 3, 4, 5, 6, 7, 8, 9, 10) EQ


1   0   E1 = A(1) + A(2) * LAM2 / (LAM2 - A(3) * A(3))
    1             + A(4) * LAM2 / (LAM2 - A(5) * A(5))
    2             + A(6) * LAM2 / (LAM2 - A(7) * A(7))
      GOTO 100
```

```
2  0   E1 = A(1) + A(2) / (LAM2 - A(3) * A(3))
   1            + A(4) / (LAM2 - A(5) * A(5))
   2            + A(6) / (LAM2 - A(7) * A(7))
  GOTO 100

3  0   NE = A(1) + A(2) * LAM2 / (LAM2 - A(3) * A(3))
   1            + A(4) * LAM2 / (LAM2 - A(5) * A(5))

   0   NO = A(6) + A(7) * LAM2 / (LAM2 - A(8) * A(8))
   1            + A(9) * LAM2 / (LAM2 - A(10) * A(10))

     N = (DSQRT(NE) + 2.0 * DSQRT(NO)) / 3.0
    E1 = N * N
   GOTO 100

4  0   NE = A(1) + A(2) / (LAM2 - A(3) * A(3))
   1            + A(4) / (LAM2 - A(5) * A(5))

   0   NO = A(6) + A(7) / (LAM2 - A(8) * A(8))
   1            + A(9) / (LAM2 - A(10) * A(10))

     N = (DSQRT(NE) + 2.0 * DSQRT(NO)) / 3.0
    E1 = N * N
   GOTO 100

5  0   NE = A(1) + A(2) / (LAM1 - A(3))
   1            + A(4) / (LAM1 - A(5))

   0   NO = A(6) + A(7) / (LAM1 - A(8))
   1            + A(9) / (LAM1 - A(10))

     N = (NE + NO) / 2.0
    E1 = N * N
   GOTO 100

6       N = A(1) + A(2) / DEXP(A(3)*DLOG(LAM1/1000.0 - A(4)))
    E1 = N * N
   GOTO 100

C   THIS EQUATION ADDED AND DEBUGGED 24APR90
 7      NE = A(3)**2 - (HW/LAM1)**2
        NO = NE**2 + (A(4)*HW/LAM1)**2

        E1 = A(1) + A(2)*A(2)*NE/NO
        E2 = A(2)**2 * A(4) * HW / ( LAM1 * NO )

   GOTO 100
```

```
8   0   E = A(1) + A(2) * LAM2 / (LAM2 - A(3) * A(3)
  1          - 2.*TIMAG*a(4)*lam1  +  1.D-6)
       E1 = DREAL(E)
       E2 = DIMAG(E)

       GOTO 100

9        denom = A(2)**2 - 1.537455e6 / LAM2
       E1 = A(1) * A(2) / DENOM + 1.
      e2 = 0.d0

     goto 100

10   0   E = 1.0 + A(1) * LAM2 / (LAM2 - A(2) * A(2) - TIMAG*a(3)*lam1
  1          + 1.D-6)
       E1 = DREAL(E)
       E2 = DIMAG(E)

       GOTO 100

 100     E = DCMPLX(E1,-1.*E2)
 101    CONTINUE


    RETURN
    END



C$   NOFLOATCALLS
c$    DEBUG
*       22:25:43   3/1/1989
***************************************************************
     SUBROUTINE ELLSIM(EPS,T,M,DPSI,DDELTA,PHID,THETAD,lambda)

      INTEGER K,I,J,M,IER,KOUNT1,KOUNT2
     DOUBLE PRECISION THETAR,PHIR,DIFF
      DOUBLE PRECISION CR(5),CI(5)
       REAL*8 T(10),LAMBDA,PI,THETAD,PHID,DELTA,PSI
     COMPLEX  A,B,C,D,E,F,G,H
           COMPLEX  P(4,4,10),Q(4,4,10),DY(4,4,10),DYINV(4,4,10)
            COMPLEX*16  PR(4,4,10),TLP(4,4,10),TRM(4,4,10),EPS(4,4,10)
        COMPLEX*16 TPREV(4,4,10),TPROD(4,4,10),ALPHA,BETA,ZO(4)
       COMPLEX*16 GAMA(5,10),GAMMA(4,10),COEFF(5)
     COMPLEX IM,DEN,SUM,COUNT
       COMPLEX AMINV(4,4),AFINV(4,4)
          COMPLEX  AMP(4,4),AF(4,4),RF(4,4),AM(4,4),S,P1SUM(4)
     DOUBLE PRECISION DIFFE,TEMP
          COMPLEX  P2SUM(4),PP(4,4,10),PPP(4,4,10),P3SUM(4)
     DOUBLE PRECISION DDELTA,DPSI,ELLIPA,ELLIPB
```

```
*************************************************************
         IM=CMPLX(0.D0,1.D0)
          PI=3.141592653598D0
*************************************************************
          PHIR=PI*PHID/180.D0
        THETAR=PI*THETAD/180.D0

         ALPHA=cmplx(DSIN(THETAR)*DCOS(PHIR),0.D0)
          BETA=cmplx(DSIN(THETAR)*DSIN(PHIR),0.D0)

*************************************************************
*       i n i t i a l i z a t i o n

4000       DO 140 I=1,4
         DO 150 J=1,4
        IF (I.EQ.J)THEN
           TPREV(I,J,M)=CMPLX(1.d0,0.d0)
       ELSE
           TPREV(I,J,M)=CMPLX(0.d0,0.d0)
       ENDIF
150      CONTINUE
140      CONTINUE

C      WRITE(*,*) 'GIVE UPPER AND LOWER SELN. BOUNDS(1E-6,-1E-6)'
C      READ(*,*) Y,Z
      Y = 1.E-3
       Z = -1.E-1

          DO 1000 K=M,1,-1

*************************************************************
C      THIS SECTION OF THE PROGRAM DEFINES SIMPLIFIED NOMENCLATURE
C      BY LUMPING THE CONSTANTS IN THE MATRIX DESCRIBING THE WAVE
C      EQUATION IN THE MOMENTUM SPACE
*************************************************************
           A=EPS(1,1,K)-BETA**2
         B=EPS(1,2,K)+ALPHA*BETA
           C=EPS(2,2,K)-ALPHA**2
              D=EPS(3,3,K)-ALPHA**2-BETA**2
         E=EPS(1,3,K)
       F=ALPHA
         G=EPS(2,3,K)
       H=BETA


*************************************************************
C THE MATRIX EXPANSION GIVES A QUARTIC IN GAMA C0+C1*GAMA+C2*GAMA**2
C  +C3*GAMA**3+C4*GAMA**4
C      WHERE THE CONSTANTS OF THE POLYNOMIAL ARE LUMPED
C      AND ARE DEFINED BELOW
C     COEFF(1) = COEFFICIENT OF THE HIGHEST ORDER TERM
```

```
           COEFF(5)=A*D*C-A*G*G-B*B*D+B*E*G*2.0-C*E*E
             COEFF(4)=-2.0*A*G*H+B*E*H+B*F*G+B*E*H+B*F*G-2.0*C*E*F
            COEFF(3)=-A*D-A*H*H+B*H*F+E*E+B*F*H-F*F*C-C*D+G*G
        COEFF(2)=2.0*G*H+2.0*E*F
      COEFF(1)=H*H+D+F*F

*****************************************************************
C     THE QUARTIC EQUATION IS SOLVED IN THE SUBROUTINE
C      QUARTIC AND THE ROOTS GAMA(I),I=1,2,3,4 ARE CALLED
C     BACK TO THE MAIN
       DO 160 I=1,5
         CR(I)=REAL(COEFF(I))
         CI(I)= DIMAG(COEFF(I))
160     CONTINUE

      TEMP=0.D0
       DO 170 I=1,4
         TEMP=TEMP+CI(I)**2
170     CONTINUE


      CALL ZCPOLY(COEFF,4,ZO,IER)

         GAMA(1,K)=ZO(1)
         GAMA(2,K)=ZO(2)
         GAMA(3,K)=ZO(3)
         GAMA(4,K)=ZO(4)
**************************************

C DIVIDE NUMBER LINE INTO SECTIONS OVER WHICH DIFFERENT SOLUTIONS APPLY
      KOUNT1=1
      KOUNT2=1
       DO 300 J=1,4
                P(1,J,K)=D*(C-GAMA(J,K)**2)-(G+H*GAMA(J,K))**2
              P(2,J,K)=(G+H*GAMA(J,K))*(E+F*GAMA(J,K))-B*D
               P(3,J,K)=B*(G+H*GAMA(J,K))-(C-GAMA(J,K)**2)*
     1   (E+F*GAMA(J,K))

         P1SUM(J)=CMPLX(0.d0,0.d0)
         DO 310 I=1,3
             P1SUM(J)=P1SUM(J)+P(I,J,K)**2
310      CONTINUE

           PP(1,J,K)=(G+H*GAMA(J,K))*(E+F*GAMA(J,K))-B*D
             PP(2,J,K)=(A-GAMA(J,K)**2)*D-(E+F*GAMA(J,K))**2
             PP(3,J,K)=B*(E+F*GAMA(J,K))-(A-GAMA(J,K)**2)*(G+H*GAMA(J,K))

         P2SUM(J)=CMPLX(0.d0,0.d0)

         DO 307 I=1,3
             P2SUM(J)=P2SUM(J)+PP(I,J,K)**2
```

```
307      CONTINUE
          DIFFE=0.D0
             DIFFE=CABS(P1SUM(J))-CABS(P2SUM(J))
       IF (DIFFE .LE.Y)THEN
         IF(DIFFE .LT.Z)THEN
               IF(REAL(GAMA(J,K)).GT.0.D0)THEN
               DO 4 I=1,3
                   PPP(I,1,K)=PP(I,J,K)
4                 P3SUM(1)=P2SUM(J)
                GAMMA(1,K)=GAMA(J,K)
            ELSE
               DO 7 I=1,3
                     PPP(I,2,K)=PP(I,J,K)
7                   P3SUM(2)=P2SUM(J)
                GAMMA(2,K)=GAMA(J,K)
            ENDIF
        ELSE

            IF(REAL(GAMA(J,K)).GE.0.D0)THEN
            IF(KOUNT1.EQ.1)THEN
               DO 8 I=1,3
                     PPP(I,1,K)=PP(I,J,K)
                   P3SUM(1)=P2SUM(J)
8                KOUNT1=2
                GAMMA(1,K)=GAMA(J,K)
            ELSE
               DO 11 I=1,3
                     PPP(I,3,K)=P(I,J,K)
11                    P3SUM(3)=P1SUM(J)
                GAMMA(3,K)=GAMA(J,K)
            ENDIF
          ELSE
            IF(KOUNT2.EQ.1)THEN
               DO 9 I=1,3
                    PPP(I,2,K)=PP(I,J,K)
                  P3SUM(2)=P2SUM(J)
9               KOUNT2=2
                GAMMA(2,K)=GAMA(J,K)
            ELSE
               DO 12 I=1,3
                    PPP(I,4,K)=P(I,J,K)
12                   P3SUM(4)=P1SUM(J)
                GAMMA(4,K)=GAMA(J,K)
            ENDIF
          ENDIF
         ENDIF
       ELSE
              IF(REAL(GAMA(J,K)).GT.0.D0)THEN
              DO 16 I=1,3
                  PPP(I,3,K)=P(I,J,K)
16                P3SUM(3)=P1SUM(J)
               GAMMA(3,K)=GAMA(J,K)
```

```
      ELSE
        DO 17 I=1,3
          PPP(I,4,K)=P(I,J,K)
17         P3SUM(4)=P1SUM(J)
         GAMMA(4,K)=GAMA(J,K)
       ENDIF
   ENDIF
300  CONTINUE

     DO 319 J=1,4
      GAMA(J,K)=GAMMA(J,K)
      DO 320 I=1,3
         P(I,J,K)=PPP(I,J,K)/CSQRT(P3SUM(J))
320   CONTINUE


      DO 325 I=1,3
        IF (CABS(P(I,J,K)).LT.1D-8) THEN
         P(I,J,K)=CMPLX(0.D0,0.D0)
     ELSE
     ENDIF
325   CONTINUE
319  CONTINUE
**********************************************************************
C    THE MAGNETIC Q VECTOR HAS BEEN COMPUTED HERE
     DO 324 J=1,4
         Q(1,J,K)=BETA*P(3,J,K)-GAMA(J,K)*P(2,J,K)
         Q(2,J,K)=GAMA(J,K)*P(1,J,K)-ALPHA*P(3,J,K)
         Q(3,J,K)=ALPHA*P(2,J,K)-BETA*P(1,J,K)
     DO 326 I=1,3
        IF (CABS(Q(I,J,K)).LT.1D-8) THEN
         Q(I,J,K)=CMPLX(0.D0,0.D0)
     ELSE
     ENDIF
326   CONTINUE

324   CONTINUE


**********************************************************************
C     THE DYNAMIC MATRICES ARE DEFINED HERE


     DO 400 J=1,4
        DY(1,J,K)=P(1,J,K)
        DY(2,J,K)=Q(2,J,K)
        DY(3,J,K)=P(2,J,K)
        DY(4,J,K)=Q(1,J,K)
400   CONTINUE
******************************************************************
C     THE PROPAGATION MATRIX IS DEFINED HERE
C     GAMA SCALED TO INVERSE DISTANCE UNITS
```

```
        DO 410 I=1,4
410          GAMA(I,K)=2.D0*PI*GAMA(I,K)*T(K)/LAMBDA
C       WRITE(10,*) 'PROPAGATION MATRIX'

         DO 420 I=1,4
          DO 430 J=1,4
           IF(I.EQ.J) THEN
              PR(I,J,K)=CDCOS(-GAMA(I,K))-IM*CDSIN(-GAMA(I,K))
          ELSE
              PR(I,J,K)=DCMPLX(0.D0,0.D0)
          ENDIF
430        CONTINUE
420      CONTINUE
**************************************************************
C      THIS SECTION OF THE PROGRAM COMPUTES THE TRANSFER MATRX
C      FOR THE LAYER IN QUESTION
       CALL INVERSE(DY,DYINV,K)
1000    CONTINUE


        K=M

3000          CALL SMLTP(DYINV,DY,TLP,K,4)
          IF (K .EQ.M) THEN
              DO 500 I=1,4
              DO 510 J=1,4
                TRM(I,J,K)=TLP(I,J,K)
510           CONTINUE
500           CONTINUE
          ELSE
              CALL MMLTP(TLP,PR,TRM,K,4)
           CONTINUE
          ENDIF
**************************************************************
C      THIS SECTION OF THE PROGRAM EFFECTS THE PRODUCT OF THE
C      TRANSFER MATRICES FOR ALL BIREFRIGENT LAYERS

         CALL MMLTP (TRM,TPREV,TPROD,K,4)
          DO 520 I=1,4
          DO 530 J=1,4
530             TPREV(I,J,K-1)=TPROD(I,J,K)
520        CONTINUE
           K=K-1
          IF(K.GT.1) GO TO 3000

**************************************************************
C      THE TERMINATING SECTION OF THE COMPUTATIONS CALCULATES THE
C      REFLECTANCE AND TRANSMITTANCE CHARACTERISTICS OF THE BIREFRINGENT
C       ANISOTROPIC MEDIUM
```

```
       DO 600 I=1,4
       DO 610 J=1,4
        AM(I,J)=TPREV(I,J,1)
610    CONTINUE
600    CONTINUE

C     THIS SECTION OF THE CODE COMPUTES THE AMPLITUDES
C     KNOWING THE SAME AT THE EXIT
        AMP(1,1)=CMPLX(1.0,0.0)
        AMP(2,1)=CMPLX(0.0,0.0)
        AMP(3,1)=CMPLX(1.0,0.0)
        AMP(4,1)=CMPLX(0.0,0.0)

C THIS ROUTINE DOES MATRIX-VECTOR MULTIPLICATION

          DEN=AM(1,1)*AM(3,3)-AM(1,3)*AM(3,1)

           RF(1,1)=(AM(2,1)*AM(3,3)-AM(1,3)*AM(3,1))/DEN
C           RF(1,2)=(AM(4,1)*AM(3,3)-AM(4,3)*AM(3,1))/DEN
C           RF(2,1)=(AM(1,1)*AM(2,3)-AM(2,1)*AM(1,3))/DEN
           RF(2,2)=(AM(1,1)*AM(4,3)-AM(4,1)*AM(1,3))/DEN

         ELLIPA=REAL(RF(2,2)/RF(1,1))
         ELLIPB=AIMAG(RF(2,2)/RF(1,1))
       DELTA=DATAN(ELLIPB/ELLIPA)
         PSI=DATAN(SQRT(ELLIPA**2+ELLIPB**2))
       IF(ELLIPA.LT.0.D0) DELTA=DELTA+PI
       DDELTA=180.D0*DELTA/PI
        DPSI=180.D0*PSI/PI
        IF (DDELTA .GT. 0. .AND. DDELTA .LT. 180.) THEN
          DDELTA = 180. - DDELTA
        ELSEIF (DDELTA .GT. 180. .AND. DDELTA .LT. 270.) THEN
          DDELTA = DDELTA - 180.
        ELSEIF (DDELTA .GT. -90. .AND. DDELTA .LT. 0.) THEN
          DDELTA = 180. + DDELTA
        END IF

      RETURN
      END


*************************end    of    program**************************


      SUBROUTINE MMLTP(A,B,C,K,N)
          COMPLEX*16   A(4,4,10),B(4,4,10),C(4,4,10),SUM
      INTEGER KK,N,J,K,I

C     A=PRE MATRIX FOR MULTIPLICATION
C     B=POST MATRIX TO BE MULTIPLIED TO PRE MATRIX
C     A= M*N ARRAY
```

```
        SUM=DCMPLX(0.D0,0.D0)
       DO 10 KK=1,N
       DO 20 I=1,N
       DO 30 J=1,N
          SUM=SUM+A(I,J,K)*B(J,KK,K)
30     CONTINUE
        C(I,KK,K)=SUM
        SUM=DCMPLX(0.D0,0.D0)
20     CONTINUE
10     CONTINUE
      RETURN
      END
*************************************************************

       SUBROUTINE SMLTP(A,B,C,K,N)
          COMPLEX  A(4,4,10),B(4,4,10)
         COMPLEX*16  C(4,4,10),SUM
       INTEGER K,N,KK,K1
C       A=PRE MATRIX FOR MULTIPLICATION
C       B=POST MATRIX TO BE MULTIPLIED TO PRE MATRIX
C       A= M*N ARRAY
        SUM=DCMPLX(0.D0,0.D0)
        K1=K-1
       DO 10 KK=1,N
       DO 20 I=1,N
       DO 30 J=1,N
          SUM=SUM+A(I,J,K1)*B(J,KK,K)
30     CONTINUE
        C(I,KK,K)=SUM
        SUM=DCMPLX(0.D0,0.D0)
20     CONTINUE
10     CONTINUE
      RETURN
      END
*************************************************************

       SUBROUTINE INVERSE(A,B,K)
        INTEGER IER,K,J,I,IJOB
          COMPLEX  A(4,4,10),B(4,4,10)
         COMPLEX*16 SAVEA(4,4),BTWO(4,4)
        COMPLEX BHOLD(4,1)
       DOUBLE PRECISION WA(4)
        DO 20 I=1,4
         DO 30 J=1,4
           SAVEA(I,J)=A(I,J,K)
         IF (I.EQ.J) THEN
             BTWO(I,J)=DCMPLX(1.D0,0.D0)
        ELSE
             BTWO(I,J)=DCMPLX(0.D0,0.D0)
        ENDIF
30      CONTINUE
20     CONTINUE
C CALL ROUTINE ONCE TO FACTOR THE MATRIX
```

```
        CALL LEQT1C(SAVEA,4,4,BTWO,4,4,0,WA,IER)
        IF (IER .EQ. 129) THEN
          WRITE(*,*) 'LECT1C MATRIX IS SINGULAR'
       END IF
C CALL ROUTINE 4 MORE TIMES TO COMPUTE THE INVERSE COLUMN BY COLUMN
        DO 50 I=1,4
         DO 49 J=1,4
            B(I,J,K) = BTWO(I,J)
49       CONTINUE
50      CONTINUE
       RETURN
       END


       subroutine ERRBAR(XJAC,NPTS,NPARM,M2O,PARAM)

        INTEGER*4 N,M,I,K,M2O,npts,nparm
           REAL*8  XJAC(570,20),A(20,20),DXX(20),CONF,XX(20),PARAM(20),
    C        SIGMA,hold(20)

        INTEGER*4 CMPINX(20)
        CHARACTER*2 CMPLBL(20)
       COMMON /ERR/CONF,SIGMA

         WRITE(*,9320)

           Call InvM(XJAC,a,nPts,nParm)
          IF (nPts .LT. 0.0) THEN
             WRITE(m2o,9340)
             WRITE(6  ,9340)
         ENDIF

           WRITE(m2o,9310)

          j = 1
           DO 1150 k = 1, NPARM
             I = NPARM*3 + k

C CALCULATE UNCERTAINTY FOR EACH VARIABLE

              CMPINX(J) = j
    0       IF (nPts .GT. 0)
     1            dXX(j) = conf*Sigma*dSqrt(Dabs(XJAC(j,j)))

                XX(j) = Param(j)
               CMPLBL(J) = 'XX'
                j = j +1
C           ENDIF

1150       CONTINUE
```

```
              WRITE(m2o,9350) (CmpLbl(j),CmpInx(j),j=1,nParm)

       DO 1600 i=1,nParm
        do 1620 j = 1,nParm
              hold(j) = xjac(i,j)/dSqrt(dabs(xjac(i,i)*xjac(j,j)))
1620     continue
          Write(m2o,9330) i,(hold(j) ,j = 1,nParm)
1600  CONTINUE

          WRITE(m2o,9240) Sigma

          DO 1350 i = 1,NParm
             WRITE(m2o,9230) i,XX(i),dXX(i)
1350      CONTINUE

9010      Format(' # Data Points: ',I3,5x,'Data in: ',A2,5x,
    1       'Ang Inc: ',F4.1,5x,'Modeling: ',A6,/)

9230       Format(2x,I2,3x,F8.4,' ± ',e15.8)

9240       Format(//,5x,'After Iteration Sigma = ',F8.5,/)

9310        Format(//,5x,'Correlation  Matrix',/,3x)

9320        Format(/,5x,'Inverting  Matrix',/)

9330        Format(I2,11(1x,F6.3))

9340       Format(/,5x,'Jacobian is Singular!?!',/)

9350         Format(3x,100(1x,A2,'-',I2,1x))

      RETURN
      End


      SUBROUTINE INVM(Y,A,NPTS,N)

         REAL*8 Y(570,20),D,B(20)
        Real*8 A(20,20)
        INTEGER*4 i,j,k,INDX(20),Npts,n


       Do 50 i=1,n
         Do 50 j=1,n
           A(i,j) = 0.0
          Do 50 k=1,nPts
                 A(i,j)=A(i,j)+Y(k,i)*Y(k,j)
50    Continue

       Do 100 i=1,n
        Do 150 j=1,n
          Y(i,j)=0.0
```

```
150     Continue
       Y(i,i) = 1.0
100    Continue


        call ludcmp(a,n,indx,d)
       IF (d .eq. 0.0) then
         nPts =  -nPts
      ENDIF
       do 170 j=1,n
        do 210 i = 1,n
210             b(i) = y(i,j)
          call lubksb(a,n,indx,b)
        do 220 i = 1,n
            y(i,j) = b(i)
              write(*,*) 'y in columns',y(i,j)
220       continue
170      continue

    RETURN
    END

    SUBROUTINE LUBKSB(A,N,INDX,B)

      INTEGER*4 ii,i,ll,j,n
     INTEGER*4 INDX(n)

       REAL*8  A(20,20),B(20),sum


      II=-1
     DO 12 I = 1, N
        LL=INDX(I)
        SUM=B(LL)
          B(LL)=B(I)
        IF (II.NE.0) THEN
            DO 11 J = II, I-1
                 SUM = SUM-A(i,j)*B(J)
 11         CONTINUE
        ELSE IF (SUM.NE.0.0) THEN
           II=I
        ENDIF
         B(I)=SUM
 12  CONTINUE

      DO 14 I= N, 1, -1
         SUM=B(I)
        IF (I.LT.N) THEN
            DO 13 J= I+1, N
                   SUM=SUM-A(i,j)*B(J)
 13         CONTINUE
        ENDIF
           B(I)=SUM/A(i,i)
```

```
 14 CONTINUE
    RETURN
    END

    SUBROUTINE LUDCMP(A,N,INDX,D)

      INTEGER*4 i,j,k,imax,n
     INTEGER*4 INDX(n)

       REAL*8  A(20,20),vv(20)
      REAL*8 aamax,D,sum,dum,tiny

      PARAMETER (TINY=1.0D-20)
     D=1.0

     DO 12 I = 1, N
       AAMAX=0.0
        DO 11 J= 1, N
             IF (ABS(A(i,j)).GT.AAMAX) AAMAX=DABS(A(i,j))
 11     CONTINUE
       IF (AAMAX.EQ.0.0) THEN
          D=0.0
         RETURN
       ENDIF
        VV(I) = 1.0/AAMAX
 12  CONTINUE

     DO 19 J = 1, N
        IF (J.GT.1) THEN
            DO 14 I = 1, J-1
               SUM=A(I,J)
             IF (I.GT.1) THEN
                DO 13 K = 1, I-1
                     SUM=SUM-A(I,K)*A(K,j)
 13            CONTINUE
                A(I,J)=SUM
             ENDIF
 14        CONTINUE
       ENDIF
       AAMAX=0.0
        DO 16 I = J, N
            SUM=A(I,j)
          IF (J.GT.1) THEN
              DO 15 K = 1, J-1
                   SUM=SUM-A(I,K)*A(K,J)
 15           CONTINUE
              A(I,J)=SUM
          ENDIF
            DUM=VV(I)*ABS(SUM)
          IF (DUM.GE.AAMAX) THEN
             IMAX=I
            AAMAX=DUM
          ENDIF
```

```
16     CONTINUE
       IF (J.NE.IMAX) THEN
          DO 17 K = 1, N
             DUM=A(IMAX,K)
              A(IMAX,K)=A(J,K)
             A(J,K)=DUM
17        CONTINUE
          D=-D
           VV(IMAX)=VV(J)
       ENDIF
        INDX(J)=IMAX
       IF (J.NE.N) THEN
            IF (A(J,J).EQ.0.0) A(J,J)=TINY
           DUM=1.0/A(J,J)
          DO 18 I=J+1,N
              A(I,J)=A(I,J)*DUM
18        CONTINUE
       ENDIF
19   CONTINUE
      IF (A(N,N).EQ.0.0) A(N,N)=TINY
     RETURN
     END
```

APPENDIX B

ALGORITHM FOR POLARIZATION GRADIENT MODELLING

```
C      ****************************************************
C THIS PROGRAM IS SET UP TO TAKE EXPERIMENTAL PSI AND/OR DELTA
C VALUES AND CALCULATE THE BEST FIT TO A USER DEFINED DISPERSION
C RELATION.  MULTIPLE ANISOTROPIC LAYERS ARE HANDLED USING ELL_SIM,
C A PROGRAM WRITTEN BY ATUL PARIKH AND D. ALLARA


C  THIS PROGRAM CALCULATES THE REFLECTION FROM A ROUGH BATIO3 SURFACE
C  WITH A POLARIZATION GRADIENT

C      ****************************************************

    EXTERNAL TRY

     INTEGER*4 M,N,IXJAC,NSIG,MAXFN,IOPT,I,INFER,IER,NOL,JJ,KK
     INTEGER*4 NSET, NPT, NUMCOM, COMNUM, COMP1(4), COMP2(4), III
    INTEGER*4 NLAYPG, HOLD,JJJ, NOCOMP, NN
    INTEGER*4 INDEX, GRAD,LAYCNT, IJ
        REAL*8 AI(4),tau,Po, P(0:100),
    C CONF, LAM,T(100), FV, d(0:100),STEP
       REAL*8 LAMBDA(91),THETAD,X(20),F(570),AZI,CPSI,CDEL, LD,REDGE
      REAL*8  sumt, temp1, alaypg,c
      REAL*8 LTU, Tc, theta, psquare, Ps0, Pmax,LAMH,LAML
     REAL temper
         COMPLEX*16  HEPS(4,4,100),subeps(2,4,91), PGEPS(2,100)
    CHARACTER*15 FILNAM
    CHARACTER*6 COMLBL
    COMMON /COM1/ SUBEPS, COMP1, COMP2, GRAD, PGEPS

        PI  =  3.14159265
      Tc = 135.
      theta = 112.
       ps0 = 0.1827206


      WRITE(*,*) 'INPUT FILENAME?'
      READ(*,*) FILNAM
     OPEN (UNIT = 3, FILE = FILNAM)

        READ  (3,*)  FILNAM
      OPEN (UNIT = 7, FILE = FILNAM)
        READ  (3,*)  FILNAM
      OPEN (UNIT = 11, FILE = FILNAM)

       read(3,*) temper
        PSQUARE  =  (2. + dSQrt(4. - 3.*(Temper - THETA)/(TC - THETA)))/
```

```
      C        3.*PS0**2
        Pmax = Dsqrt (PSQUARE)
          READ(3,*) NOCOMP

            WRITE(*,*) 'INPUT NUMBER OF INCIDENCE ANGLES'
             READ(*,*) NSET
            DO 22 I = 1,NSET
              WRITE(*,*) 'INCIDENT ANGLE'
                READ(*,*) AI(I)
22          CONTINUE
            WRITE(*,*) 'INPUT LOW WAVELENGTH'
             READ(*,*) LAML
            WRITE(*,*) 'INPUT HIGH WAVELENGTH'
             READ (*,*) LAMH
             WRITE(*,*) 'INPUT STEP'
             READ(*,*) STEP
            M = 1
            DO 23 LAM = LAML,LAMH,STEP
              LAMBDA(M) = LAM
              M = M + 1
23          CONTINUE
             M = M - 1


C          READ IN REFERENCE OPTICAL PROPERTIES
           GRAD = 0
           READ(3,*) NUMCOM
           DO 14 I = 1, NUMCOM
             READ(3,*)  COMNUM, COMLBL, FILNAM
               write(7,*)  comnum,  comlbl
             IF (COMLBL .EQ. 'GRAD') THEN
                WRITE(7,*) 'GRID LIMITS ON TAU AND PO'
                 READ(3,*) NLAYPG
                 DO 11 ii = 1,2
                      READ(3,*) X(18+ii)
                      WRITE(7,*) X(18+ii)
11             CONTINUE
               GRAD = COMNUM
             ELSE
               OPEN (UNIT = 10, FILE = FILNAM)
               DO 12 J = 1,M
                  READ(10,*, END = 13) SUBEPS(1, COMNUM, J),
      C         SUBEPS(2, COMNUM, J)
12            CONTINUE
13             CLOSE (UNIT = 10)
             END IF
14         CONTINUE

           IF (M .GT. 600) THEN
             WRITE(*,*) 'TOO MANY DATA POINTS'
             STOP
           ELSE
          WRITE(*,*) 'NUMBER OF DATA POINTS = ',M
```

```
         WRITE(7,*) 'NUMBER OF DATA POINTS = ', M
        END IF


C       READ IN GEOMETRY
        DO 16 I = 1, 9
          READ(3,*, ERR = 17, END = 17) COMP1(I),COMP2(I),X(2*I-1),
     1    X(2*I)

            write(7,15)  COMP1(I),COMP2(I),X(2*I-1),X(2*I)

            write(*,15)  COMP1(I),COMP2(I),X(2*I-1),X(2*I)

15      format(1x,i1,3x,i1,3x,f8.3,3x,f8.3)
16      CONTINUE
17     CLOSE (UNIT = 3)
        NOL = I - 1
        WRITE(*,*) 'NOL = ',NOL

        AZI = 0.d0


C INITIALIZE EPS
      DO 200 I=1,4
       DO 201 J=1,4
        DO 202 K=1,100
           HEPS(I,J,K) = (0.D0,0.D0)
202     CONTINUE
201    CONTINUE
200   CONTINUE


        write(*,*) 'Program in progress - please do not disturb'

        TAU = X(19)
        Po = X(20)/100.
        tflag = 0
        DO 350 I = 1, NOL
         IF ((COMP1(I) .EQ. grad) .AND. TFLAG .EQ. 0) THEN
            alaypg = dreal(nlaypg)
            DO 300 ij=0, nlaypg
               c  =  dreal(ij)
               P(ij)  =  (Pmax  -  Po)/alaypg*c  +  Po
               if  (ij  .eq.  nlaypg)  then
                 D(ij)  =  1.0D6
               else
                  D(ij)   =   -1.*tau*dlog((Pmax  -  P(ij))/(Pmax  -  Po))
               end if
               WRITE(*,*)  IJ,  D(IJ)
300        CONTINUE
           TFLAG = 1
          END IF
350    CONTINUE
```

```
C CALCULATE DELTA AND PSI AND WRITE TO AN OUTPUT FILE

      DO 1000, J = 1,NSET
      THETAD = AI(J)
        DO 1040 KK = 1,M
          LAM = LAMBDA(KK)*10.
         TFLAG = 0

         DO 1050 I = 1, NOL
            IF ((COMP1(I) .EQ. grad) .AND. TFLAG .EQ. 0) THEN
            DO 1055 ij=0, nlaypg
              CALL OPTPROP(P(ij),PGEPS,LAMBDA(kk),IJ + 1)
1055       CONTINUE
             TFLAG = 1
            END IF
1050     CONTINUE

         SUMT = 0.
          laycnt = 0
         TFLAG = 0
         I = 1

         DO WHILE (I .LE. NOL)
          LTU = 0
            LD  =  X(I*2)
            FV  =  X(2*I  -  1)

          IF ((COMP1(I) .EQ. GRAD) .AND. (TFLAG .EQ. 0)) THEN
               DO  1065  ij=  0,  Nlaypg-1
               TFLAG = 1
               IF (COMP1(I) .EQ. GRAD) THEN
                DO WHILE (TFLAG .EQ. 1)
                 TFLAG = 0
                    REDGE  =  (D(IJ)  +  D(IJ  +  1))/2.
                   IF (REDGE .GT. LD) THEN
                    REDGE = LD
                    TFLAG = 1
                   END IF
                   LAYCNT = LAYCNT + 1
                   T(LAYCNT) = REDGE - SUMT
                   SUMT = REDGE
                 CALL SETEPS(i,IJ,KK,HEPS,LAYCNT,FV)
            WRITE(*,*)  LAYCNT,T(LAYCNT),HEPS(3,3,LAYCNT)
                   LTU = LTU + T(LAYCNT)
                   IF (TFLAG .EQ. 1) THEN
                     I = I + 1
                     LTU = 0
                      LD  =  LD  +  X(2*I)
                      FV  =  X(2*I  -1)
                     IF (COMP1(I) .NE. GRAD) THEN
                      TFLAG = 0
                     END IF
                   END IF
```

```
                  REPEAT
                 END IF
1065            CONTINUE
                 TFLAG = 1
               END IF
               IF ((I .LE. NOL) .AND. (LTU .LT. X(2*I))) THEN
                 LAYCNT = LAYCNT + 1
                  T(LAYCNT) = X(2*I) - LTU
                 CALL SETEPS(I,IJ,KK,HEPS,LAYCNT,FV)
                   WRITE(*,*) LAYCNT, T(LAYCNT), HEPS(3,3,LAYCNT)
               END IF

               I = I+1
              REPEAT

        CALL ELLSIM(HEPS,T,LAYCNT,CPSI,CDEL,AZI,THETAD,LAM)
            if (nocomp .eq. 0 .and. cdel .gt. 90.) then
               cdel =180. - cdel
           end if
            WRITE(11,*) LAMBDA(KK), CDEL, CPSI, THETAD
              WRITE(*,*) LAMBDA(KK), CDEL, CPSI, THETAD

1040    CONTINUE
1000  CONTINUE
      CLOSE (UNIT = 11)

    END


    SUBROUTINE EFFMED(E,EH,FV)

     REAL*8 FV,FILL, E1, E2

    COMPLEX*16 EH(2),E,INSIDE,RHO, HOLD, EIGHT, FOUR

       EIGHT = (8.0D0, 0.0D0)
       FOUR = (4.0D0, 0.0D0)

     IF (FV.EQ.0.0) THEN
        E = EH(1)

     ELSEIF (FV .ne. 0.0) THEN
       FILL = FV
          E1 = DREAL(EH(1))
          E2 = DIMAG(EH(1))
           EH(1) = DCMPLX(E1, -1.*E2)
          E1 = DREAL(EH(2))
          E2 = DIMAG(EH(2))
           EH(2) = DCMPLX(E1, -1.*E2)

              RHO = (3.0*(1.0-FILL)-1.0)*EH(1) + (3.0*FILL-1.0)*EH(2)
          HOLD = EH(1) * EH(2)
         INSIDE = RHO*RHO + HOLD * EIGHT
```

```
      INSIDE = CDSQRT(INSIDE)
        IF (DIMAG(INSIDE) .LT. 0.0) INSIDE  = -INSIDE
          E = (RHO+INSIDE)/FOUR
          E1 = DREAL(E)
          E2 = DIMAG(E)
           E = DCMPLX(E1, -1.*E2)

    End if

  RETURN
  END


       SUBROUTINE SETEPS(I,IJ,KK,HEPS,LAYCNT,FV)

       INTEGER I,IJ,KK,LAYCNT, COMP1(4), COMP2(4), JJJ, GRAD
       REAL*8 E1, E2
       COMPLEX*16  HEPS(4,4,100),PGEPS(2,100),SUBEPS(2,4,91),EH(2),E
     COMMON /COM1/ SUBEPS,COMP1,COMP2,GRAD,PGEPS

       JJJ = 1
       DO 10 J = 1,2
         IF (COMP1(I) .EQ. GRAD) THEN
             EH(1) = PGEPS(J,IJ+1)
         ELSE
             EH(1) = SUBEPS(J, COMP1(I), KK)
         END IF
          EH(2) = SUBEPS(J, COMP2(I), KK)
         CALL EFFMED(E, EH, FV)
          E1 = DREAL(E)
          E2 = DIMAG(E)
           HEPS(JJJ,JJJ,LAYCNT) = DCMPLX(E1,E2)
           JJJ = 3
10     CONTINUE
       HEPS(2,2,LAYCNT) = HEPS(1,1,LAYCNT)

       RETURN
       END


       SUBROUTINE OPTPROP(P, PGEPS, LAMBDA, I)

       INTEGER I
       real*8  LAMea,den1a,den1c,denom2,c2a,c2c,c1a,c1c,
    c  kc,ka,nc,na,Se,Sg,Ge,Gg,LAMg,BIREF, LAMBDA,P, e1, e2,
    c  LAMec,nasquare,ncsquare,hold1a,hold1c,hold2
      COMPLEX*16  NE,PGEPS(2,100),NO

C      calculate no,ne,ko,ke from dispersion relation
      SE = 147.86017
       Sg = .15448901e-3
     LAMg = 137.7
      Ge = .134186e-1
```

```
 Gg = -.25997685e-1
LAMea = 301.27191
BIREF = 254.79467
LAMec = LAMea - BIREF*P**2

     hold1a = 1.- (LAMea/lambda)**2
     hold1c = 1. - (LAMec/lambda)**2
     hold2 = 1. - (LAMg/lambda)**2
      den1a = hold1a**2 + (2.D0*Ge*LAMea/lambda)**2
      den1c = hold1c**2 + (2.D0*Ge*LAMec/lambda)**2
      denom2 = hold2**2 + (2.D0*Gg*LAMg/lambda)**2
      c2a = 1. + Se*1.d-7*LAMea**2*hold1a/den1a
    c2a = c2a + Sg*LAMg**2*hold2/denom2
      c2c = 1. + Se*1.d-7*LAMec**2*hold1c/den1c
    c2c = c2c + Sg*LAMg**2*hold2/denom2
     c1a = Ge*Se*1.d-7*LAMea**3/lambda/den1a
    c1a = c1a + Gg*Sg*LAMg**3/lambda/denom2
      c1c = Ge*Se*1.d-7*LAMec**3/lambda/den1c
    c1c = c1c + Gg*Sg*LAMg**3/lambda/denom2
        nasquare = 1./2.*(c2a + DSqrt(c2a**2 + 4.*c1a**2))
        ncsquare = 1./2.*(c2c + Dsqrt(c2c**2 + 4.*c1c**2))
  na = Dsqrt(nasquare)
  nc = Dsqrt(ncsquare)
 ka = c1a/na
   if (ka .lt. 0) ka = 1.e-6
 kc = c1c/nc
   if (kc .lt. 0) kc = 1.e-6

     no = Dcmplx(na,ka)
    ne = Dcmplx(NC,KC)
   PGEPS(1,I) = NO**2
      e1 = dreal(pgeps(1,i))
      e2 = dimag(pgeps(1,i))
       pgeps(1,i) = dcmplx(e1, -1.*e2)
   PGEPS(2,I) = NE**2
      e1 = dreal(pgeps(2,i))
      e2 = dimag(pgeps(2,i))
       pgeps(2,i) = dcmplx(e1, -1.*e2)
  RETURN
  END
```

VITA

Susan McKinstry was born in Syracuse, New York, on March 3, 1965. She and her family subsequently moved to northeastern Pennsylvania, where she graduated from Conestoga Senior High School in June 1983. Following this, she enrolled at The Pennsylvania State University in August 1983, where she received Bachelor and Master of Science degrees in Ceramic Science in May 1987, with a specialty in electronic ceramic materials. She has published several articles in professional journals and is a member of the American Ceramic Society, the Materials Research Society, and Keramos.